

# UC Berkeley

## UC Berkeley Electronic Theses and Dissertations

### Title

Dispenser Printed Zinc Microbattery with an Ionic Liquid Gel Electrolyte

### Permalink

<https://escholarship.org/uc/item/93w7b723>

### Author

Ho, Christine Chihfan

### Publication Date

2010

Peer reviewed|Thesis/dissertation

Dispenser Printed Zinc Microbattery with an Ionic Liquid Gel Electrolyte

By

Christine Chihfan Ho

A dissertation submitted in partial satisfaction of the  
requirements for the degree of

Doctor of Philosophy

In

Engineering – Materials Science and Engineering

in the

Graduate Division

of the

University of California, Berkeley

Committee in charge:

Professor James W. Evans, Chair

Professor Paul K. Wright

Professor Fiona M. Doyle

Fall 2010



## Abstract

Dispenser Printed Zinc Microbattery with an Ionic Liquid Gel Electrolyte

by

Christine Chihfan Ho

Doctor of Philosophy in Materials Science and Engineering

University of California, Berkeley

Professor James W. Evans, Chair

Rapid trends show a steady decrease in electronic device form factors, which are miniaturizing and flattening, while demonstrating an increase in device functionality, requiring complex and exacting power needs. This movement has motivated a shift in energy storage design and manufacture to accommodate novel and unconventional materials, new device geometries, and non-traditional fabrication methods. A combination of these strategies will lead to a revolution in the way energy storage components are designed, integrated, and utilized in electronic devices.

In this work, we present one possible strategy combining a materials innovation with simple engineering methods to fabricate and integrate batteries directly onto a device. A novel ionic liquid gel electrolyte compatible with zinc-metal oxide battery systems was synthesized. This gel electrolyte properties and its compatibility with the electrodes, current collector materials, packaging, and substrates were investigated.

A simple, low-cost, solution-based printing method for integrating energy storage components directly onto a device is demonstrated with a direct write dispenser printing system. The dispenser printer is able to pattern “inks” into multilayer devices with custom dimensions.

Printed  $1\text{ cm}^2$  zinc-metal oxide microbatteries utilizing the ionic liquid gel electrolyte were fabricated and then various device quantities such as its storage capacity, power performance, self-discharge, and other properties were characterized. Prospective applications of this printable battery include flexible electronics and applications that need highly customized integrated or miniature energy storage such as printed circuit boards, permanent power supplies for autonomous wireless sensors, and active RFID tags.

There are so many things I am grateful for, and so many who I am beholden to.  
I endeavor to enjoy unconditionally those things, and to thank personally those who I  
appreciate and love.

# Contents

<b>Contents</b>	<b>ii</b>
<b>List of Figures</b>	<b>vi</b>
<b>List of Tables</b>	<b>xviii</b>

## **1. Introduction to Energy Storage for Miniature Wireless Sensor Nodes**

1.1 INTRODUCTION .....	1
1.1.1 <i>Battery Operating Principles</i> .....	2
1.1.2 <i>Electrochemical Capacitor Operating Principles</i> .....	3
1.1.3 <i>Comparison of Energy Storage Devices</i> .....	4
1.2 MICROPOWER SUPPLIES FOR WIRELESS SENSOR DEVICES .....	5
1.2.2 <i>Materials Considerations for Microbatteries</i> .....	11
1.2.3 <i>Geometry and Processing Considerations for Microbatteries</i> .....	13
1.3 IMPLEMENTATIONS OF 2D MICROBATTERIES .....	14
1.3.1 <i>Thin Film Solid-State Microbatteries</i> .....	15
1.3.2 <i>Thick Film Microbatteries</i> .....	18
1.3.3 <i>Concluding Remarks for 2D Microbatteries</i> .....	25
1.4 THREE-DIMENSIONAL MICROBATTERIES .....	26
1.4.1 <i>3D Microbattery Architectures With A Discontinuous Element</i> .....	28
1.4.2 <i>3D Microbattery Architectures With Continuous Elements</i> .....	34
1.4.3 <i>Prospects for Three-Dimensional Microbattery Implementation</i> .....	37
1.5 ELECTROCHEMICAL MICROCAPACITORS .....	39
1.5.1 <i>Electrochemical Capacitor Materials</i> .....	39
1.5.2 <i>Microcapacitor Prototypes</i> .....	40
1.5.3 <i>Conclusions and Prospects for Microcapacitors</i> .....	43
1.6 CONCLUSION .....	44
1.7 REFERENCES .....	44

## **2. Direct write dispenser printing**

2.1 PRINTING PROCESS AND EQUIPMENT .....	52
2.2 COMPATIBLE MATERIALS .....	54
2.2.1 <i>Characterizing Ink Viscosity</i> .....	55
2.3 POST-PROCESSING .....	58
2.4 ARCHITECTING STRUCTURES .....	58
2.5 CONCLUDING REMARKS .....	60
2.6 REFERENCES .....	60

## **3. Gel Electrolyte Design and Characterization**

3.1 IONIC LIQUID ELECTROLYTES – AN INTRODUCTION .....	61
3.2 DESIGN OF A ZINC ION CONDUCTING IONIC LIQUID ELECTROLYTE .....	62
3.2.1 <i>Electrochemical Potential Stability</i> .....	62
3.2.2 <i>Ionic Electrolyte Transport Properties</i> .....	63

3.2.3 Zinc Electrodeposition and Dissolution .....	67
3.3 DESIGN OF A ZINC ION CONDUCTING IONIC LIQUID GEL ELECTROLYTE.....	69
3.3.1 Gel Electrolyte Morphology .....	69
3.3.2 Gel Electrolyte Transport Properties .....	71
3.4 CONCLUDING REMARKS .....	73
3.5 REFERENCES .....	73
<b>4. Gel Electrolyte Compatibility With the Anode</b>	
4.1 GEL ELECTROLYTE COMPATIBILITY WITH A ZINC ANODE .....	75
4.1.1 The Zinc and Gel Electrolyte Interface.....	75
4.1.2 Zinc Electrodeposition and Dissolution .....	79
4.1.3 Electrodeposit Morphology .....	80
4.2 GEL ELECTROLYTE COMPATIBILITY WITH PRINTED ZINC ANODES.....	82
4.2.1 Printed Zinc Electrode Fabrication.....	82
4.2.2 Measuring Printed Zinc Film Electrical Resistance.....	83
4.2.3 Measuring Printed Zinc Electrode Electrochemical Impedance.....	85
4.2.4 Zinc Electrodeposition and Dissolution from Printed Electrodes.....	87
4.3 CONCLUDING REMARKS .....	88
4.4 REFERENCES .....	89
<b>5. Gel Electrolyte Compatibility with Transition Metal Oxide Cathodes</b>	
5.1 GEL ELECTROLYTE COMPATIBILITY WITH PRINTED VANADIUM PENTOXIDE CATHODES .....	91
5.1.1 A Review of Multivalent Ion Insertion into Vanadium Pentoxide Materials... 91	
5.1.2 Synthesis of a Vanadium Pentoxide Printable Electrode .....	92
5.1.3 Detecting Zinc Ion Electrochemical Insertion.....	93
5.1.4 Measuring Galvanostatic Cyclability .....	94
5.1.5 Tailoring the Electrode Capacity using Dispenser Printing .....	95
5.1.6 Comparing the Electrochemical Capacity of $V_2O_5$ Ambigel and Crystalline Powders .....	97
5.2 COMPATIBILITY WITH PRINTED MANGANESE DIOXIDE CATHODES.....	98
5.2.1 Synthesis of a Printed Manganese Dioxide Electrode.....	98
5.2.2 Detecting Zinc Ion Electrochemical Insertion in the Printed Manganese Dioxide Electrode .....	99
5.2.3 Galvanostatic Characterization of the Printed Manganese Dioxide Electrode.....	101
5.2.4 Electrochemical Impedance Spectroscopy .....	108
5.3 CONCLUDING REMARKS .....	112
5.4 REFERENCES .....	112
<b>6. Current Collectors and Other Microbattery Constituents</b>	
6.1 CURRENT COLLECTOR REQUIREMENTS AND POTENTIAL MATERIALS.....	114
6.2 PRINTABLE SILVER CURRENT COLLECTOR .....	115
6.3 PRINTABLE NICKEL CURRENT COLLECTOR.....	117
6.3.1 Electrochemical Stability.....	117

6.3.2 Printed Current Collector Processing Considerations .....	117
6.4 OTHER MICROBATTERY CONSTITUENTS .....	119
6.4.1 Substrate Materials.....	119
6.4.2 Packaging Materials.....	119
6.5 CONCLUDING REMARKS .....	120
6.6 REFERENCES .....	121
<b>7. Printed Microbatteries: Device Fabrication and Testing</b>	
7.1 MICROBATTERY FABRICATION .....	122
7.2 MICROBATTERY DEVICE CHARACTERIZATION.....	123
7.2.1 Galvanostatic Characterization.....	123
7.2.2 Self-Discharge Characterization .....	127
7.2.3 Preliminary Failure Analysis.....	139
7.3 CONCLUDING REMARKS.....	141
7.4 REFERENCES .....	142
<b>8. Applications and Prospects for Dispenser Printed Microbatteries</b>	
8.1 “PRINTING ON GREEN” .....	144
8.2 HYBRID MICROPOWER SUPPLIES .....	145
8.3 CONFORMAL PRINTING .....	146
8.4 LOCAL ENERGY STORAGE – AN OPPORTUNITY IN CREATING A NEW DESIGN PARADIGM .....	147
8.5 FLEXIBLE ELECTRONICS .....	148
8.6 CONCLUSIONS .....	149
8.7 REFERENCES .....	149
<b>9. Appendix: Experimental Methods and Derivations</b>	
9.1 RHEOMETRY .....	151
9.1.1 Rotating Parallel Plate Rheometer.....	151
9.1.2 Cone-Plate Viscometer .....	152
9.1.3. Dispenser Printer Deposition Capabilities.....	152
9.2 VOLTAMMETRY .....	156
9.2.1 Linear Sweep Voltammetry.....	156
9.2.2 Cyclic Voltammetry.....	157
9.3 ELECTROCHEMICAL IMPEDANCE SPECTROSCOPY .....	159
9.3.1 EIS Equivalent Electrical Circuit Modeling.....	161
9.4 GALVANOSTATIC AND POTENTIOSTATIC TECHNIQUES.....	169
9.4.1 Galvanostatic Cycling.....	169
9.4.2 Restricted Diffusion Method .....	170
9.4.3 Galvanostatic Intermittent Titration Technique (GITT).....	172
9.4.4 Rate Performance .....	176
9.4.5 Self-Discharge .....	176
9.5 X-RAY DIFFRACTION.....	180
9.6 ELECTRICAL RESISTANCE .....	181
9.7 ELECTRON DISPERSIVE X-RAY SPECTROSCOPY .....	182



9.8 IMAGING .....	182
9.9 REFERENCES .....	182

# List of Figures

## Chapter 1

1.1. Battery schematic.....	2
1.2. Discharge behavior of batteries with (a) invariant cell potential or (b) sloped cell potential. ....	3
1.3. Electrochemical capacitor schematic.....	4
1.4. Discharge potential of capacitor scales linearly with charge extracted. ....	5
1.5. Ragone plot comparing energy storage devices [Kötz <i>et al.</i> , 2000]. ....	6
1.6. Ambient intelligence devices categorized according to power consumption and functionalities (adapted from [Snijders, 2005]). ....	8
1.7. Visual representation demonstrating the diminishing discrepancy between the power demanded by a microwatt node and the power generated by energy harvesters. Any discrepancy will need to be addressed with an energy storage component.....	9
1.8. Power profile exhibiting one duty cycle of a prototypical wireless sensor device [Ho, <i>et al.</i> , 2009] .....	10
1.9. Volumetric energy densities of various commercial batteries as a function of cell volume. Batteries surveyed include lithium and lithium-ion chemistries with various cell geometries (adapted from [Lai, <i>et al.</i> , 2010]) .....	15
1.10. (left) Two-dimensional planar and (right) stacked microbattery configuration	15
1.11. Thin film microbattery structure [Bates, <i>et al.</i> , 2000]. ....	17
1.12. Array of thin film microfabricated microbatteries [Song, <i>et al.</i> , 2009] .....	17
1.13. A monolithic solid-state battery formed by (a) cold pressing and sintering a stack of electrodes and ceramic electrolyte, (b) polishing the electrodes to the desired thickness and sputtering current collectors at each end, and (c) cutting the monolithic microbattery into a desired shape to be embedded into a substrate [Birke, <i>et al.</i> , 1999].....	18
1.14. Microfabricated Zn-NiOOH planar microbattery with thick film electrodeposited electrodes [Humble, <i>et al.</i> , 2001] .....	20
1.15. Schematic of flow-based direct write printing .....	22
1.16. Flow-based printed interdigitated, planar lithium-ion electrode array [Dokko, <i>et al.</i> , 2007].....	22

1.17. Schematic of matrix-assisted pulsed laser evaporation (MAPLE) direct write deposition [Pique, <i>et al.</i> , 2003].	24
1.18. Planar (left) concentric circle and (right) interdigitated zinc-silver oxide alkaline microbatteries fabricated using laser direct write [Arnold, <i>et al.</i> , 2007].	24
1.19. Stacked lithium-ion microbattery embedded in a substrate using laser direct write fabrication [Sutto, <i>et al.</i> , 2006].	25
1.20. Three-dimensional microbattery architectures with at least one discontinuous component: (a) regular arrangements of interdigitated anode and cathode cylinders or (b) interdigitated electrode plate arrays distributed in an electrolyte; (c) electrolyte coated anode cylinders dispersed in a continuous phase of cathode material. Note (a) and (c) do not display current collectors [Long, <i>et al.</i> , 2004].	28
1.21. Three-dimensional microbattery architectures where the electrodes and electrolyte are each continuous phases: (a) a 2D stacked battery configuration that is folded into a 3D architecture; (b) a periodic and (c) an aperiodic scaffold (composed of cathode material conformably coated with a thin electrolyte) back-filled with anodic material occupying the free volume. Note that (b) and (c) do not display current collectors [Long, <i>et al.</i> , 2004].	29
1.22. (left) Fabrication process of interdigitated Ni-Zn post electrode microbattery. (1) Silicon mold is micromachined with high aspect ratio trenches (2) nickel and zinc are selectively electrodeposited into the mold (3) silicon mold is removed and nickel hydroxide is conformally coated onto the nickel electrodes (4) microbattery is defined by epoxy walls and filled with aqueous alkaline electrolyte. (right) Micrographs of (a) the nickel and zinc electrodeposited posts and (b) a nickel post; (c) a nickel post coated with nickel hydroxide [Chamran, <i>et al.</i> , 2006].	30
1.23. (a) Interlaced electrode rods separated by a porous silicon mold. (b-c) Top and cross-section views of the silicon mold [Rippenbein, <i>et al.</i> , 2009].	31
1.24. (a) Schematic of a C-MEMS fabricated interdigitated electrode post array of pyrolyzed carbon anodes and polymer cathode coatings of dodecylbenzenesulfonate- doped polypyrrole (PPYDBS). Micrographs (b-c) show an array of interdigitated carbon anodes and thick polymer coated cathodes [Min, <i>et al.</i> , 2008].	32
1.25. Super ink jet printed Zn-Ag <sub>2</sub> O post electrode arrays. (a-b) silver pillars are printed on a substrate. (c) When submerged in an alkaline electrolyte with dissolved zinc oxide, an applied electric field causes silver to oxidize at the positive electrode while zinc electrodeposits on the negative electrode, assembling a microbattery in its charged state. Micrographs of (d) an electrode array and (e) printed silver posts [Ho, <i>et al.</i> , 2009].	33
1.26. Concentric battery (a) schematic of the cross section of a perforated substrate with high aspect ratio holes that are conformably coated with continuous, thin films of current collector, cathode, and electrolyte layers. The anode is back-filled into	

the open volume. (b,c) Micrographs of the perforated substrate and (d) 3D enhanced microbattery with graphite filled microchannel volume [Nathan, <i>et al.</i> , 2005 and Golodnitsky, <i>et al.</i> , 2006].	34
1.27. Schematic of textured silicon substrate conformably coated with a lithium-ion thin film battery layers [Niessen, <i>et al.</i> , 2008].	35
1.28. (a) Three-dimensional interpenetrating lithium-ion microbattery. A three-dimensional ordered macroporous (3DOM) carbon anode monolith is coated with a polymer electrolyte film, then (b) back-filled with a vanadium pentoxide ambigel cathode [Ergang, <i>et al.</i> , 2007].	36
1.29. Aperiodic sponge microbattery assembled from (a) a manganese oxide cathode ambigel coated with a (b) continuous polymer electrolyte and back-filled with (c) ruthenium oxide anode material [Rolison, <i>et al.</i> , 2009].	37
1.30. Schematic of thin film electrochemical capacitor.	41
1.31. Schematics (a-b) and micrographs (c-d) of origami folded supercapacitors [In, <i>et al.</i> , 2006].	42
1.32. Ink-jet printed carbon supercapacitor electrodes on gold, interdigitated current collectors [Pech, <i>et al.</i> , 2009].	42
1.33. Cross section micrograph of a dispenser printed stacked, carbon electrochemical capacitor [Ho, <i>et al.</i> , 2006].	43

## Chapter 2

2.1. A comparison of the processing steps involved in subtractive microfabrication (left) and additive direct write printing (right).	53
2.2. Schematic of direct write dispenser printing.	54
2.3. Examples of syringe tips and corresponding inner diameter dimensions compatible with dispenser printing.	54
2.4. (left) Dispenser printer schematic and (right) image of laboratory setup.	55
2.5. Schematic of ink synthesis for dispenser printing.	55
2.6. Viscosity with respect to applied shear rate for composite slurry and polymer solution inks. The ranges of shear rates and corresponding printed feature sizes applied by the dispenser printer are bracketed for both inks.	56
2.7. Image of drop extruded from dispenser printer needle hovering above substrate.	57
2.8. (a-c) Dispenser printing procedure for the fabrication of a multilayer device.	58

2.9. (a-d) Other capabilities using dispenser printing including (a) 3D polymer molds, (b) back-filling the molds, (c) precise deposition of magnetic ink on the ends of MEMS cantilever beams [Leland, <i>et al.</i> , 2009] and (d) the fabrication of thermoelectric grid devices [Chen, <i>et al.</i> , 2009].	59
--	----

### Chapter 3

3.1. Electrochemical potential stability ionic liquid electrolytes with 0 to 0.75 M zinc salt concentrations. The occurrence of a large magnitude current density corresponds to electrolyte decomposition. Scan rate of 5mV/s used with positive polarization direction.	63
3.2. The ionic conductivity and viscosity of BMIM <sup>+</sup> Tf <sup>-</sup> ionic liquid electrolytes as a function of zinc solute concentrations.	64
3.3. The diffusion coefficients of zinc ions in BMIM <sup>+</sup> Tf <sup>-</sup> ionic liquid electrolytes as a function of zinc solute concentrations.	65
3.4. Comparison of the ionic conductivities of zinc and lithium ion – ionic liquid electrolytes as a function of solute concentration in the BMIM <sup>+</sup> Tf <sup>-</sup> ionic liquid.	66
3.5. Comparison of diffusion coefficient of zinc and lithium ions in ionic liquid electrolytes as a function of solute concentration in the BMIM <sup>+</sup> Tf <sup>-</sup> ionic liquid.	66
3.6. Zinc deposition (negative potentials) and dissolution (positive potentials) from an ionic liquid electrolyte with 0.75 M zinc salt. Scan rate of 10 mV/s. The initial polarization direction was towards more positive potentials.	67
3.7. Voltammograms of ionic liquid electrolytes with zinc salt concentrations ranging from 0 to 0.75 M. Scan rate of 10 mV/s. The initial polarization direction was towards more positive potentials.	68
3.8. Cyclic behavior of the peak zinc dissolution current densities measured from ionic liquid electrolytes with zinc salt concentrations of 0 to 0.75 M. The anodic current density values were extracted from repeated cyclic voltammogram tests using the experimental parameters described in Figure 3.7.	69
3.9. (a-d) Micrographs of ionic liquid gel electrolytes showing the morphological changes in the film with decreasing ionic liquid electrolyte swelled into the polymer.	70
3.10. Average gel grain sizes with varying concentrations of PVDF-HFP in the ionic liquid gel electrolyte.	70
3.11. X-ray diffraction scans for ionic liquid gel films with increasing polymer concentration (from 25 to 100 %). Arrows direct the eye along peak features that evolve over the varying gel compositions, corresponding to the crystalline nature of the film.	71

3.12. Room temperature ionic conductivities of gels with varying ionic liquid concentrations in PVDF-HFP. ....	72
3.13. Viscosities of the gel electrolyte constituents .....	72

## Chapter 4

4.1. The electrochemical impedance spectra for gel electrolyte films sandwiched between two blocking stainless steel electrodes in comparison with two non-blocking zinc electrodes. Cells were swept with a $V_{AC}$ of 10 mV from 1 MHz to 1 Hz with 0V DC bias.....	76
4.2. Electrochemical impedance spectra of a cell monitored through the course of 36 hours. The cell contained a gel electrolyte film sandwiched between two zinc foil electrodes. The change in morphology of the spectra can be attributed to the increased interfacial impedance over time. Cells were swept with a $V_{AC}$ of 10 mV from 1 MHz to 1 Hz with 0V DC bias.....	77
4.3. Interfacial impedances of $BMIM^+Tf^-$ gel films with varying zinc solute concentrations. Interfacial impedance measurements were derived from electrochemical impedance spectra (EIS) tests. Cells were allowed to stabilize for 24 hours after assembly and then were swept with a $V_{AC}$ of 10 mV from 1 MHz to 1 Hz with 0V DC bias.....	78
4.4. Zinc deposition (negative potentials) and dissolution (positive potentials) from an ionic liquid gel electrolyte with 0.5 M zinc solute concentration. Scan rate of 10 mV/s. The initial polarization direction was towards more positive potentials.....	79
4.5. Voltammograms comparing the zinc deposition and dissolution behaviors from an ionic liquid or gel electrolyte. Both the ionic liquid and gel electrolyte had a zinc solute concentration of 0.5 M. Scan rate of 10 mV/s. The initial polarization direction was towards more positive potentials. ....	80
4.6. A dendrite study induced by galvanostatic cycling of a cell containing 0.5 M zinc solute in $BMIM^+Tf^-$ ionic liquid electrolyte sandwiched by two zinc foil electrodes. An applied current density of $1.67 \text{ mA/cm}^2$ is applied for 5 minutes in both the positive and negative direction, and the resulting cell potential is measured. Note that the experiment was interrupted at $t=11.5 \text{ hr}$ and resumed within 15 minutes. ....	81
4.7. Zinc foil dendrite study in ionic liquid electrolyte. (a) Two foil electrodes are separated by a 2mm gap and covered with ionic liquid electrolyte. After rapid galvanostatic cycling, (b-d) mossy growth is visible especially at the interfaces between the electrolyte and zinc foils.....	82
4.8. (a-b) Micrographs comparing the morphologies of (a) a gel electrolyte film and (b) zinc electrodeposits from a gel electrolyte onto a zinc foil.....	83

4.9. Micrograph of a printed film containing 10 $\mu\text{m}$ zinc particles held together with PVDF-HFP polymer binder. ....	83
4.10. Electrical resistances of printed films with varying weight percents of zinc powder in PVDF-HFP polymer binder .....	84
4.11. Electrical resistances of printed films with varying weight percents of acetylene black conductive carbon powder mixed into a slurry of zinc powder in a PVDF-HFP polymer binder (original composition of slurry before addition of acetylene black was 92.7 wt.% zinc powder and 7.3 wt.% PVDF-HFP). ....	84
4.12. Electrochemical impedance spectrum and equivalent circuit model fit of planar pair of printed zinc-carbon electrodes covered in a printed gel electrolyte. From the equivalent circuit fit, the cell's solution resistance $R_{\text{solution}}=55.4 \Omega$ , surface film resistance $R_{\text{surface}}=54.4 \text{ k}\Omega$ , surface film constant phase element $Q=24.7 \text{ S}\cdot\text{s}$ , and Warburg diffusion element $W= 4.4 \text{ kS}\cdot\text{s}^{1/2}$ . ....	85
4.13. Equivalent circuit model for a test structure containing two printed composite zinc-carbon electrodes covered in a gel electrolyte. ....	86
4.14. The impedance spectra of two test structures containing zinc electrodes in foil or printed form. Both test structures were symmetric and planar cells covered by gel electrolyte.....	86
4.15. Zinc deposition (negative potentials) and dissolution (positive potentials) from an ionic liquid gel electrolyte with printed zinc-carbon composite electrodes. Scan rate of 10 mV/s. The initial polarization direction was towards more positive potentials .....	87
4.16. Voltammograms comparing the zinc deposition and dissolution behaviors from an ionic liquid gel electrolyte with foil and printed electrodes. Scan rate of 10 mV/s. The initial polarization direction was towards more positive potentials. ....	88

## Chapter 5

5.1. Micrograph of the cross-section of a printed $\text{V}_2\text{O}_5$ ambigel film and gel electrolyte .....	93
5.2. Voltammogram for a printed $\text{V}_2\text{O}_5$ ambigel electrode, printed gel electrolyte, and zinc foil electrode cell on a nickel substrate. Upon a decreasing voltage sweep, zinc ions insert into the $\text{V}_2\text{O}_5$ material, while with increasing voltage, zinc ions extract from the electrode structure. Scan rate of 1 mV/s. The initial polarization direction was towards more positive potentials. ....	94
5.3. Discharge cell potential of a $\text{V}_2\text{O}_5$ ambigel electrode, gel electrolyte, and zinc foil electrode on a nickel substrate. Cell was discharged at a C/3 rate. ....	95
5.4. The cell potential of a cell containing a $\text{V}_2\text{O}_5$ ambigel electrode, gel electrolyte, and zinc foil electrode on a nickel foil substrate due to galvanostatic cycling. Approximately C/3 charge and discharge rates were used. ....	96

5.5. The cyclic progression of the discharge capacity of a cell containing a V <sub>2</sub> O <sub>5</sub> ambigel electrode, gel electrolyte, and zinc foil electrode on nickel substrate due to galvanostatic cycling. A C/3 discharge rate was used. ....	96
5.6. The discharge cell potentials of three test cells with 15, 30, and 45 μm thick V <sub>2</sub> O <sub>5</sub> ambigel dispenser printed electrodes. A 0.1 mA/cm <sup>2</sup> discharge current density was applied to all cells. The corresponding discharge capacities are 0.29, 0.58, and 0.89 mAh/cm <sup>2</sup> . ....	97
5.7. Commercial MnO <sub>2</sub> powder incorporated into a printed film .....	98
5.8. Voltammogram for a printed MnO <sub>2</sub> electrode, printed gel electrolyte, and zinc foil electrode cell. Upon a decreasing voltage sweep, zinc ions insert into the MnO <sub>2</sub> material, while with increasing voltage, zinc ions extract from the electrode structure. Scan rate of 1 mV/s. The initial polarization direction was towards more positive potentials. ....	99
5.9. Comparison of the voltammograms for test cells with a printed MnO <sub>2</sub> electrode and printed V <sub>2</sub> O <sub>5</sub> electrode, For both voltammograms the scan rate of 1 mV/s was used. The initial polarization direction was towards more positive potentials. ....	100
5.10. (a-c) Energy dispersive x-ray spectroscopy (EDS) scans for (a) a freshly printed MnO <sub>2</sub> film, (b) a freshly printed MnO <sub>2</sub> film on a gel electrolyte backing, and (c) a MnO <sub>2</sub> film on a gel electrolyte backing after 20 galvanostatic cycles against a zinc foil electrode (zinc foil was removed from the cell during the EDS experiment).....	102
5.11. The first eleven galvanostatic cycles of a cell containing a printed MnO <sub>2</sub> composite electrode, gel electrolyte, and zinc foil electrode. A C/5 discharge rate was used. Between cycle 7 and cycle 9 a significant discharge capacity increase is observed. ....	103
5.12. A comparison of the potential of a printed MnO <sub>2</sub> electrode, gel electrolyte, and zinc foil electrode cell. The galvanostatic charge (increasing cell potential) and discharge (decreasing cell potential) potentials of the third and eleventh cycle are compared.....	104
5.13. Galvanostatic intermittent titration technique (GITT) procedure: current is applied for 30 minutes to a cell, then held at open circuit for 5 hours while the cell potential is monitored. ....	105
5.14. The equilibrium potential as a function of depth of discharge and stoichiometry for a cell comprised of a printed MnO <sub>2</sub> electrode, gel electrolyte, and zinc foil electrode from GITT measurements. ....	105
5.15. The equilibrium potential as a function of depth of charge for a cell comprised of a printed MnO <sub>2</sub> electrode, gel electrolyte, and zinc foil electrode from GITT measurements.....	107



5.16. The equilibrium potentials as a function of depth of charge (for a cell comprised of a printed MnO <sub>2</sub> electrode, gel electrolyte, and zinc foil electrode from GITT measurements. The equilibrium cell potentials with respect to the discharge capacity (negative depth of charge) and charge capacity (positive depth of charge) are plotted for the first two cycles. ....	107
5.17. Electrochemical impedance spectrum of a printed MnO <sub>2</sub> electrode, gel electrolyte, and zinc foil cell at 1.555 V with equivalent circuit model fit. The EIS scans were recorded at the equilibrium potential of the cell with an AC input amplitude of 5 mV and a frequency sweep between 0.01 to 10 <sup>6</sup> Hz. From the equivalent circuit model fit, R <sub>solution</sub> =239.6 Ω, R <sub>surface</sub> =9.86 kΩ, R <sub>charge transfer</sub> =49.5 kΩ. All fit parameters are listed in Chapter 9, Table 9.2. ....	108
5.18. Equivalent circuit model for a printed MnO <sub>2</sub> electrode, gel electrolyte, and zinc foil cell. ....	109
5.19. The first and last discharge impedance spectra corresponding to equilibrium cell potentials of 1.555 V and 1.248 V. The cell that was probed contained a printed MnO <sub>2</sub> electrode, gel electrolyte, and zinc foil electrode. The EIS scans were recorded at the equilibrium potential of the cell with an AC input amplitude of 5 mV and a frequency sweep between 0.01 to 10 <sup>6</sup> Hz. ....	111
5.20. A comparison of the charge impedance spectra corresponding to equilibrium cell potentials of 1.267, 1.393, and 1.620 V. The cell that was probed contained a printed MnO <sub>2</sub> electrode, gel electrolyte, and zinc foil electrode. The EIS scans were recorded at the equilibrium potential of the cell with an AC input amplitude of 5 mV and a frequency sweep between 0.01 to 10 <sup>6</sup> Hz. ....	111
5.21. Equilibrium cell voltage, charge transfer resistance, and exchange current density of a cell containing a printed MnO <sub>2</sub> electrode, gel electrolyte, and zinc foil electrode. The charge transfer resistances and exchange current densities were calculated from equivalent circuit models used to fit electrochemical impedance spectra (EIS) measurements. The EIS scans were recorded at the equilibrium potential of the cell with an AC input amplitude of 5 mV and a frequency sweep between 0.01 to 10 <sup>6</sup> Hz. ....	112

## Chapter 6

6.1. Voltammograms of symmetric cells containing two adjacently printed current collector films covered in a printed gel electrolyte. The electrochemical instabilities of silver and nickel in the gel electrolyte correspond with the magnitude of current density detected for a given potential. Scan rate of 10 mV/s. The initial polarization direction was towards more positive potentials. ....	116
6.2. Micrograph showing silver dendrite formation along the interface between the printed silver (black) and the gel electrolyte (yellow). ....	116
6.3. (a-c) Nickel films containing spherical, flake, and fiber particles dispersed in a polymer binder. ....	118

6.4. Cross section of a printed test structure comprising of polymer printed on top of a printed nickel fiber film. The polymer ink percolated through the printed nickel film, forming a uniform layer of polymer underneath it and displacing it from the substrate the nickel film was printed on (glass substrate was removed to image the printed films).....	118
6.5. Barrier material permeabilities quantified by water vapor transmission rates (WVTR – g/m <sup>2</sup> /day). Available barrier materials and corresponding device moisture exposure tolerances are listed. For the printed microbattery developed in this work, we hypothesize that the minimum permeability requirement is approximately 10 <sup>-3</sup> g/m <sup>2</sup> /day (adapted from [Lewis, 2006]).....	130

## Chapter 7

7.1. Dispenser printing procedure for stacked zinc, gel electrolyte, and manganese dioxide microbattery on a nickel foil substrate.....	122
7.2. Micrograph of the cross section of a zinc, gel electrolyte, and manganese dioxide printed microbattery. The nickel foil substrate was removed so that the printed structure could be imaged. ....	123
7.3. Cell potential of a printed zinc, gel electrolyte, and MnO <sub>2</sub> microbattery as a function of percent depth of galvanostatic discharge. The discharge rate was C/3. ....	124
7.4. The galvanostatic cycling of a printed zinc, gel electrolyte, and MnO <sub>2</sub> microbattery at a C/5 rate. Activation of the battery occurred within the first 15 cycles. After more than 70 cycles no signs of performance degradation is visible ...	124
7.5. Percent of maximum discharge capacity extracted from the printed microbattery as a function of discharge current density .....	125
7.6. Printed microbattery discharge times as a function of discharge power density ....	126
7.7. Ragone plot illustrating the affect of the discharge power density on the achievable energy density of a printed microbattery for deep discharges .....	127
7.8. A series of self-discharge routines of the printed microbattery after charging. Potential decay at open circuit is plotted with respect to time.....	129
7.9. A series of self-discharge routines of the printed microbattery after charging. Potential decay at open circuit is plotted with respect to the logarithm of time..	130
7.10. A series of self-discharge routines of the printed microbattery after charging. Potential decay at open circuit is plotted with respect to the square root of time	131

7.11. Magnitudes of self-discharge of the printed microbattery due to charging. The slope of the potential decay at open circuit is plotted with respect to the logarithm of time as a function of cell potential.....	131
7.12. A series of self-recovery routines of the printed microbattery after discharging. Potential recovery at open circuit is plotted with respect to time .....	132
7.13. A series of self-recovery routines of the printed microbattery after discharging. The potential recovery of the battery at open circuit is plotted with respect to the logarithm of time .....	133
7.14. A series of self-recovery routines of the printed microbattery after discharging. Potential recovery at open circuit is plotted with respect to the square root of time .....	133
7.15. Magnitudes of self-recovery of the printed microbattery due to discharging. The slope of the potential recovery at open circuit is plotted with respect to the logarithm of time as a function of cell potential .....	134
7.16. The current response to potentiostatic control of a printed battery. The float current is assumed to be the steady state current achieved after holding the cell at a certain potential for extended times.....	135
7.17. The float currents for two charge cycles as a function of cell potential.....	135
7.18. The float currents for two discharge cycles as a function of cell potential .....	136
7.19. The charge passed due to leakage for two charge cycles as a function of cell potential. Measurements were extracted from float current measurements .....	137
7.20. The charge passed due to leakage for two discharge cycles as a function of cell potential. Measurements were extracted from float current measurements .....	137
7.21. The leakage power for two charge cycles as a function of cell potential. Measurements were extracted from float current measurements .....	138
7.22. The leakage power for two discharge cycles as a function of cell potential. Measurements were extracted from float current measurements .....	138
7.23. Galvanostatic cycling of a printed battery demonstrating unexpected behavior starting at $t = 47$ h and subsequently followed by the failure of the device .....	139
7.24. (a-b) Optical micrographs of gel electrolyte decomposition. (c-d) Scanning electron microscope (SEM) micrographs of gel electrolyte decomposition.....	140

- 7.25. Pinholes in the gel electrolyte result in uneven electrode and electrolyte interfaces, which result in points of failure. Magnification of a pinhole boxed in (a) is displayed in (b)..... 141

## Chapter 8

- 8.1. (a-d) “Printing on green” concept: (a) A crowded printed circuit board (PCB) has limited unoccupied substrate area, as is designated in red in (b). The dispenser printer is able to deposit a printed battery in this open space (c) and an energy storage device is integrated directly onto the PCB (adapted from [Steingart, 2006]) ..... 145
- 8.2. (a-d) An integrated hybrid power supply comprising of (a) MEMS vibration energy harvesters patterned on a silicon die. (b-d) The dispenser printer deposits a multilayer printed energy storage component in the open space surrounding the energy harvester (adapted from [Miller, *et al.*, 2009]) ..... 146
- 8.3. (a-d) The conformal printing of a microbattery on an integrated circuit board: (a) An integrated circuit board originally designed to be powered with two hearing aid batteries (connected by two gold circular traces) will be retrofit with a dispenser printed microbattery. (b) An electrical insulating layer is printed on top of the board on which (c-d) a printed microbattery is deposited ..... 147
- 8.4. Flexible dispenser printed microbatteries on a polyimide substrate. The microbatteries are composed of a nickel current collector, manganese dioxide electrode, ionic liquid gel electrolyte, and zinc electrode/current collector ..... 149

## Chapter 9

- 9.1. Rheometrics ARES parallel plate rheometer. Polymer solution or slurry is injected into the gap between the top and bottom plate [Rheometrics ARES Rheometer]152
- 9.2. A schematic of the flow down a needle. A differential shell is defined, along with the coordinate system and relevant variables ..... 153
- 9.3. Schematic of linear sweep voltammetry showing an applied sweeping potential (left) and resulting measured current (right). The current rise corresponds to the oxidation or reduction reaction of an active species at a certain potential ..... 156
- 9.4. Test cell used to measure the electrochemical potential stability of ionic liquid electrolytes. Zinc is the counter electrode while stainless steel acts as the working electrode..... 157
- 9.5. Symmetric cell probed by CV to determine properties of the electrodeposition and dissolution of zinc with the gel electrolyte ..... 157
- 9.6. Printed symmetric cell probed by CV to determine properties of the electrodeposition and dissolution of printed zinc films with the gel electrolyte.

Films were deposited adjacent to each other on a substrate such as glass and gel electrolyte was printed on top of the printed electrodes .....	158
9.7. Example voltammogram with key parameters typically characterized using CV .....	158
9.8. Test cell probed with CV used to test the electrochemical intercalation of zinc ions into a metal oxide host material .....	159
9.9. Printed symmetric cell probed by CV to determine the stability of printed current collector films with the gel electrolyte. Films were deposited adjacent to each other on a substrate such as glass, and gel electrolyte was printed on top of the printed electrodes .....	160
9.10. Nyquist plot displaying the real versus the imaginary components of the impedance of an example electrochemical system (known as Randles cell).....	161
9.11. Cell used to determine the solution resistance of an electrolyte using EIS. For the electrolytes studied, the stainless steel terminals are blocking electrodes.....	162
9.12. Galvanostatic charge and discharge of a test cell.....	170
9.13. Restricted diffusion method measures (a) the cell potential during polarization (increasing cell potential) then when it is interrupted (exponentially decaying potential). The slope of the negative natural log of the open circuit cell potential $[-\ln(\Delta\Phi)]$ with respect to time is used to determine the salt diffusion coefficient within the electrolyte.....	171
9.14 (a-b). Electrolyte concentration along the width of a cell (electrodes are situated at 0 and L) during (a) equilibrium and (b) when polarizing the cell .....	171
9.15. Galvanostatic intermittent titration technique (GITT) procedure: current is applied for 30 minutes to a cell, then held at open circuit for 5 hours while the cell potential is monitored .....	173
9.16. An example of the equilibrium cell potential of a battery using GITT protocol. Flat cell potential regions indicate phase changes in the host while diffusion coefficients can be extracted from sloped regions.....	176
9.17. An example of the open circuit potential decay of a battery measured after polarization .....	179
9.18. The current response to potentiostatic control of a printed battery. The float current is assumed to be the steady state current achieved after holding the cell at a certain potential for extended times.....	180
9.19. Test structure for measuring electrical sheet resistance using Van der Pauw's method. Contacts are made on the corners of the sample and are labeled 1-4 .....	181

# List of Tables

## Chapter 1

1.1. Summary of primary battery chemistries [Linden, <i>et al.</i> , 1995] .....	6
1.2. Selected rechargeable battery chemistries [Linden, <i>et al.</i> , 1995].....	12
1.3. Two-dimensional microbatteries summary .....	26
1.4. Three-dimensional microbattery demonstrations and performance summary ....	38
1.5. Electrochemical capacitor electrode materials .....	40
1.6. Electrochemical microcapacitor demonstrations and performance.....	44

## Chapter 2

2.1. Recipes of composite slurry and polymer solution inks used for viscosity studies .....	56
2.2. Shear rates (1/s) applied by the printer for a gel polymer ink extruded through varying needle diameters calculated as a function of the pneumatic controller applied pressure .....	57

## Chapter 5

5.1. Interlayer spacing of common forms of electrochemical insertion host materials [Braithwaite, <i>et al.</i> , 1999 and Rolison, <i>et al.</i> , 2001]. The images are illustrations of the host material structures and are not displayed to scale. ....	92
5.2. V <sub>2</sub> O <sub>5</sub> ambigel composite slurry ink formula .....	93
5.3. MnO <sub>2</sub> composite slurry ink composition.....	98

## Chapter 6

6.1. Relative conductivity normalized for volume, mass and cost of candidate current collector materials with respect to copper at room temperature .....	115
---	-----

## Chapter 7

7.1. Printed Microbattery Performance Summary – All values were derived from the maximum measured quantity in lab experiments .....	142
---	-----

## Chapter 9

9.1. Equivalent circuit elements and their impedance expressions .....	166
9.2. Equivalent circuit model fit for printed MnO <sub>2</sub> electrode, gel electrolyte, and zinc foil cells. Measurements were taken during a discharge sweep. The EIS scans were recorded at the equilibrium potential of the cell ranging between 1.555 to 1.248 V with an AC input amplitude of 5 mV and a frequency sweep between 0.01 to 106 Hz.....	167
9.3. Equivalent circuit model fit for printed MnO <sub>2</sub> electrode, gel electrolyte, and zinc foil cells. Measurements were taken during a charge sweep. The EIS scans were	

recorded at the equilibrium potential of the cell ranging between 1.267 to 1.62 V  
with an AC input amplitude of 5 mV and a frequency sweep between 0.01 to 106  
Hz..... 168

# Chapter 1

## Introduction to Energy Storage for Miniature Wireless Sensor Nodes

For over a century, batteries and electrochemical capacitors have been the mainstay energy storage component of machines, tools, and gadgets. With steady improvements and miniaturization of energy storage technology, the relationship between people and electronic devices has gradually evolved, causing modern society to develop a strong dependence on batteries and supercapacitors for the upkeep of both comforts and necessities, from powering our personal mobile phones to large industrial process equipment. Choices for the materials, design, and production of an energy storage device can vary extensively depending on a host of parameters, including an application's performance and lifetime requirements, size, cost, and of more recent concern, environmental impact. Devising power supplies for small, autonomous wireless systems has been especially challenging, providing engineers with a rich opportunity for innovation because of its stringent demands. This chapter details design considerations, reviews existing technology, and evaluates prospects for micro-energy storage devices, in particular batteries and electrochemical capacitors used in conjunction with an energy harvester(s) to provide permanent power to autonomous wireless systems.

### 1.1 Introduction

The reduction of electronic device form factors and their power demands has augmented the prospects of realizing a fully integrated microdevice platform, one with computation, communication, and sensing capabilities all enabled by a permanent power source [Warneke, *et al.*, 2001]. The implications of the widespread deployment of these devices, especially autonomous wireless sensor nodes, are pivotal to a variety of fields including emergency response [Wilson, *et al.*, 2007], structural monitoring [Paek, *et al.*, 2005], and the cost and energy-effective regulation of home, industrial, and office energy use [Ota, *et al.*, 2006], to name a few. For wireless microdevices with footprint areas occupying less than 1 cm<sup>2</sup> of a substrate, typical power demands can vary, oftentimes spanning a few orders of magnitude from microwatts ( $\mu\text{W}$ ) to milliwatts (mW) depending on the application. The need for a micropower source that can satisfy the power requirements of a wireless device within comparable geometric dimensions has incited a surge of research within the fields of microfabrication, energy harvesting, and energy storage [Roundy, *et*



*al.*, 2003]. For autonomous wireless sensors, the foremost microenergy storage devices being considered are microbatteries and electrochemical microcapacitors, and are the technologies discussed in this chapter.

### 1.1.1 Battery Operating Principles

Batteries are galvanic cells that convert chemical energy using electrochemical reactions to yield electrical energy that can be harnessed externally. They contain two chemically different electrodes sandwiching an ion-conducting electrolyte phase. At open circuit, a measurable electrical voltage develops between the electrodes due to their different electrochemical potentials. Upon electrical connection to a load, redox (reduction and oxidation) reactions take place, causing electrons to pass through an external circuit and ions to travel across the electrolyte. A spontaneous flow of electrons travels in the external circuit from the electrode with the more negative potential to the more positive electrode, and can therefore be used to power a load such as a device (see Figure 1.1). If the battery is rechargeable, the reverse reactions can be induced with a sufficient voltage able to change the electrochemical potentials of the electrodes. Depending on the type of reactions that occur, for example displacement reactions or insertion reactions [Winter, *et al.* 2004], the discharge behavior of the battery will vary (Figure 1.2), resulting in different cell potential outputs (V) with respect to the amount of charge (q) extracted from the battery, and from this relationship the amount of useful energy (E) obtained from the battery can be determined from the following expression:

$$E = \int V dq \quad (\text{Equation 1.1})$$

The energy extracted is typically reported in units of joules (J) or watt-hours (Wh). The total charge extracted from the battery, or the amount that can be stored in the cell, is known as the capacity typically reported as amp-hours (Ah) or coulombs (C). The maximum power, measured in watts (W), that can be drawn from the battery is dependent on the kinetics of the system, which can be limited by the summation of impedances in the cell, including charge transport in the electrodes and electrolyte, the rates at which reactions occur, and interfacial resistances. The power behavior of a battery can also be

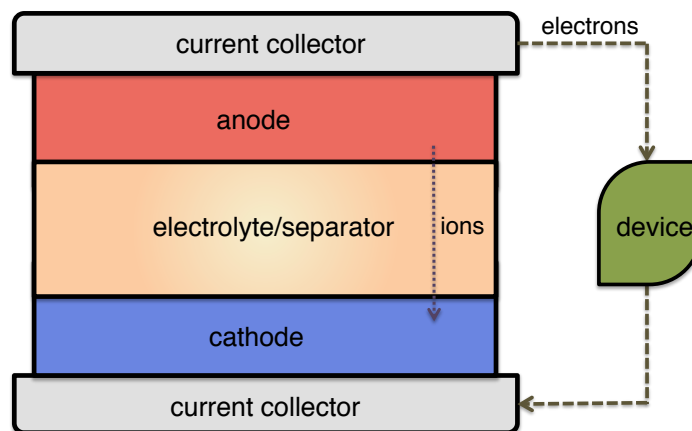


Figure 1.1. Battery schematic.

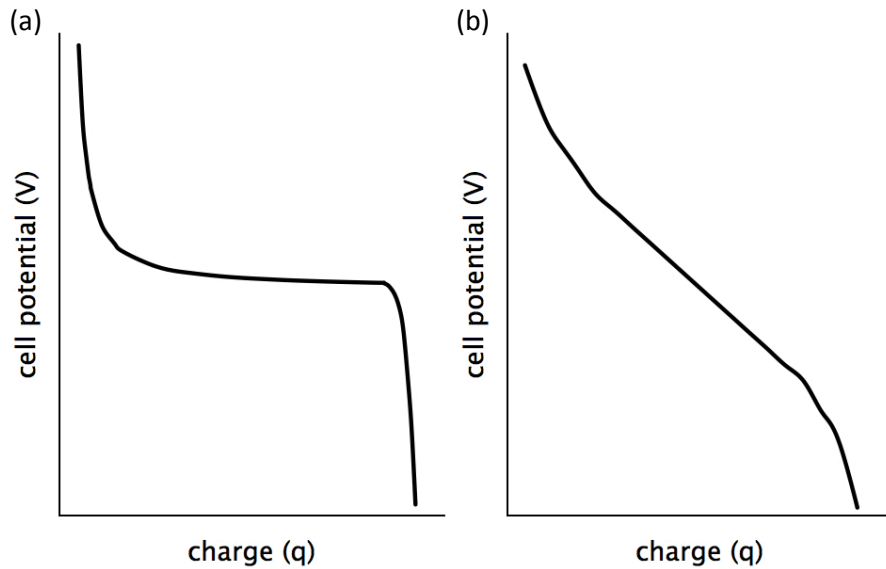


Figure 1.2. Discharge behavior of batteries with (a) invariant cell potential or (b) sloped cell potential.

characterized by its rate performance, and is evaluated by the time (in hours) it takes to deplete a device of its maximum storage capacity ( $C$ ). Note that this terminology can be confusing, as  $C$  is also used to represent Coulombs and should not be confused when referred to as a rate of charge or discharge. For example a battery that took 10 hours to completely drain was discharged at a  $C/10$  rate, while a quick discharge of  $2C$  means the battery was depleted in a half hour. Note that all the quantities listed can be normalized with respect to weight, volume, and footprint area, for example electrochemical storage energy is primarily quantified in terms of the specific energy ( $\text{Wh/g}$ ), the amount of energy stored per unit volume ( $\text{Wh/cm}^3$ ), and the energy stored per unit footprint area occupied on a substrate ( $\text{Wh/cm}^2$ ). Note that when quantifying the theoretical performances of electrochemical materials, metrics normalized with respect to weight and volume are customarily used, however when comparing microdevices, the constrained unit is most often the footprint area occupied on a substrate, and to compare across many fabrication methods, materials, and device configurations, areal metrics are preferred.

The chemistries and relative amounts of the battery components will determine its operating voltage and energy storage capacity, and along with the cell geometry and processing, will also influence the maximum power accessible. In addition to these properties, other performance metrics include the battery's lifetime (or for rechargeable batteries, its cycle life) as well as its safety and cost, all of which depend on its inherent materials properties, such as their stability and compatibility. Though batteries are straightforward conceptually, there have been numerous chemistries, geometries, and processing methods proposed [Winter, *et al.*, 2004].

### 1.1.2 Electrochemical Capacitor Operating Principles

Electrochemical capacitors, also referred to as supercapacitors, ultracapacitors, or double-layer electrochemical capacitors, are emerging as practical energy storage devices for

high power density applications. Electrochemical capacitors are similar in construction to batteries, but are typically symmetric, oftentimes as seen in commercial cells having two carbon electrodes.

Capacitors store energy by displacing electrons from one device terminal to the other, creating a charge separation that generates a potential across the device. The energy that can be stored in a capacitor is related to the amount of charge separated and the resulting voltage, which inherently is dependent on the dimensions and materials properties of the capacitor components. Electrolytic and electrochemical capacitors utilize an ionic conducting electrolyte rather than a dielectric material found in conventional ceramic capacitors, which enables greater charge separation and therefore a higher capacitance for a given voltage. Electrochemical capacitors offer the highest energy density of the different capacitors because of its high surface area electrodes that allow for greater charge storage along the interfaces between the electrode and electrolyte.

Upon applying an electric field across an electrochemical capacitor, ions in the electrolyte can dissociate and travel towards oppositely charged electrode surfaces, as illustrated in Figure 1.3. Because the mechanism of energy storage is purely electrostatic, the capacitor voltage scales linearly with charge stored, as shown in Figure 1.4. The resulting capacitance ( $C$ ), measured in farads (F), of the device can be determined from the following expression:

$$C = \frac{q}{V} \quad (\text{Equation 1.2})$$

Due to the absence of any Faradaic or chemical reactions, theoretically no irreversible phenomena occur during standard operation, therefore electrochemical capacitors should in theory operate indefinitely, and have been frequently demonstrated to cycle more than one million times.

### 1.1.3 Comparison of Energy Storage Devices

The energy and power densities of selected energy storage devices are summarized in a

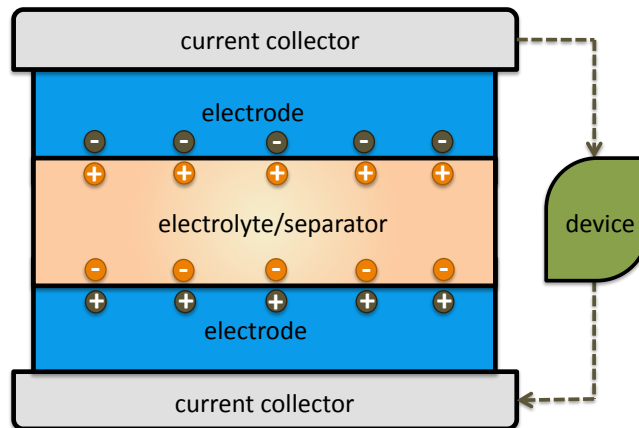


Figure 1.3. Electrochemical capacitor schematic.

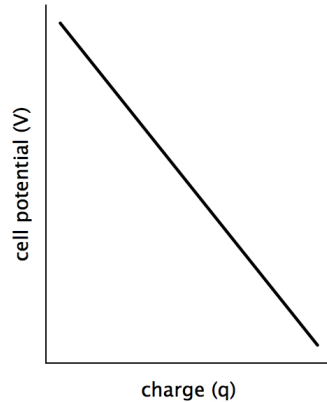


Figure 1.4. Discharge potential of capacitor scales linearly with charge extracted.

Ragone plot shown in Figure 1.5. Though the performance units in the Ragone plot are normalized with respect to weight, the illustrated trends are fairly consistent when normalized with respect to volume. The specific energies of batteries are typically one to two orders of magnitude greater than electrochemical capacitors, which can contain an order of magnitude greater specific energy than ceramic and electrolytic capacitors. The trend for power density is the reverse: ceramic and electrolytic capacitors can theoretically extract at least an order of magnitude greater power density than electrochemical capacitors, while typical batteries report power densities at least one order lower than electrochemical capacitors.

## 1.2 Micropower Supplies for Wireless Sensor Devices

Currently the most prevalently used power sources for wireless sensor platforms are primary macrobatteries (batteries greater than  $1 \text{ cm}^2$  in footprint diameter typically assembled separately of the devices they power). Primary macrobatteries are typically assembled in the charged state, utilized until completely discharged, and then disposed of. Today, these batteries are commercially offered in a variety of shapes and sizes, the smallest commercially having coin or button cell construct (about 10 mm in diameter and 5 mm thickness). For a device with relaxed size prerequisites, anticipated finite lifetimes, and/or where the replacement of its power supply is unchallenging or inexpensive, primary batteries are simple, hassle-free, and often the most cost-effective choice for a power source. Without the need for special mounting prerequisites or calibration, devices powered by primary batteries can be quickly deployed almost anywhere. Furthermore, most commercial battery chemistries offer fairly stable discharge potentials, which can be used as a direct supply voltage to a device without the need of additional regulation.

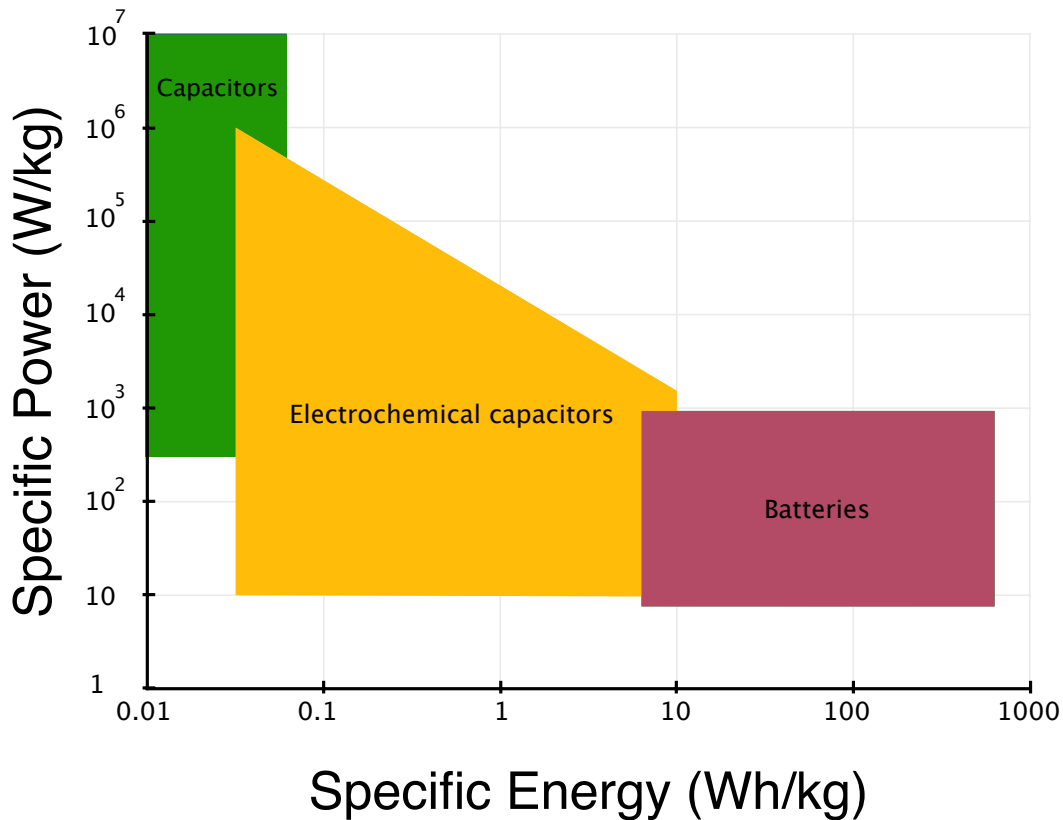


Figure 1.5. Ragone plot comparing energy storage devices [Kötz *et al.*, 2000].

Practical energy densities for various primary battery chemistries are listed in Table 1..

Table 1.1. Summary of primary battery chemistries [Linden, *et al.*, 1995]

<i>Chemistry</i>	<i>Leclanché</i>	<i>Alkaline</i>	<i>Lithium</i>	<i>Zinc-air</i>
Energy Density (Wh/kg)	85	145	230	370
Energy Density (mWh/cm <sup>3</sup> )	165	400	535	1300

For applications that require the ubiquitous and unobtrusive distribution of many autonomous wireless sensors, primary macrobatteries have proven to be unreasonably expensive and difficult to replace once depleted. Additionally, to meet extended lifetime demands, primary batteries would need to be far too large and unwieldy, and would overwhelm the total volume of a device. Permanent solutions for power sources have been proposed as viable alternatives, and a large research effort has been directed towards developing micro-scale ambient energy harvesters and complementary micro-energy storage devices. The combination of the two, known as a hybrid micropower supply, incorporates the ability to convert ambient energy (for example solar, vibrations, and thermal energy) into useful electrical energy, which is then stored in an energy reservoir until needed by the microdevice. In most environments, ambient energy is not always available, and therefore can only be harvested either periodically in recurring timescales

or in most cases, intermittently. As a consequence, an energy reservoir is necessary to provide power to the device even when ambient energy is not present, and the size of this reservoir is dictated by the energy source (the magnitude of the harvested energy and the frequency at which ambient energy is available) and on the load (the magnitude of power demanded from the device and the frequency at which this power is demanded). For environments in which energy conversion occurs effectively whenever the microdevice operates, the corresponding energy reservoir storage capacity can be minimal, and is simply limited by the maximum power required. For this case, something of minimal storage capacity such as a stand-alone capacitor may suffice. In the event that ambient energy is unavailable, a battery with higher energy storage capacity is necessary, however, a load-leveling electrochemical capacitor may also be used in conjunction to alleviate the battery from the device's exacting power demands, and as a consequence improve the battery health and life span.

In the late '70s, a growing trend towards wafer-scale fabrication of integrated circuits engendered the development of microelectromechanical systems (MEMS), elaborate devices having microscopic dimensions. The drivers that have made MEMS devices a widespread commercial success were revolutionary: MEMS technology was capable of making small, integrated systems with immense functionality using low-cost and high-throughput fabrication processes. These same drivers and the need for local and efficient energy delivery to these MEMS components have inspired research efforts towards developing power sources of comparable dimensions to MEMS devices. Microbatteries evolved from a burgeoning concept into a conceivable notion as a result of substantial developments in solid-state ion conducting materials [Kennedy, 1977], and the construction of the first solid-state microbatteries was demonstrated in the early 1980's [Creus, *et al.*, 1989]. Though most of these prototypes exhibited fairly low capacity, the demonstrations catalyzed more fervent investigations in the microbattery field. There were however many practical barriers, as intimated by Owen in 1985, "the geometry, and in particular, the dimensions of this device are alien to conventional battery production" however, he forecasted that within ten years, because of the important implications, the production of microbatteries would likely become a reality [Sequeria, *et al.*, 1985].

In this section, the application constraints, unique materials, processing, and integration considerations involved in designing rechargeable microbatteries and electrochemical capacitors are reviewed.

### **1.2.1 Power Considerations for Miniature, Autonomous Wireless Devices**

This section attempts to outline the application spaces and establish design guidelines for the development of micro-energy storage devices specifically for small and autonomous wireless sensor platforms. In particular, this section highlights the interrelated nature of all the various device components and draws attention to how any design choices may greatly affect the entire system, in particular the fabrication constraints, use, and health of the energy storage components. Trends in new design paradigms and philosophies developing in this field are also featured.

In the 1990's, the cumulative progress in computation, communication, software, data storage, displays, sensors, and microfabrication inspired a new technological concept: an intelligent, responsive, and connected network composed of integrated platforms that leveraged the advances in all of these technologies. This idea was dubbed "Ambient Intelligence" and is described in detail by Snijders [Snijders, 2005]. An ambient intelligent network is composed of a collection of three classes of devices illustrated in Figure 1.6: microwatt, milliwatt, and watt nodes. The devices are categorized according to their power consumption from microwatts to watts, and this inherently defines their appropriate power sources, processing ability, functionalities. Autonomous microwatt nodes act as distributed sensors or actuators in the network, consuming one to hundreds of microwatts of power to simply take measurements and then transmit this data. Milliwatt nodes are typically used as "relays" that receive the data transmitted by the microwatt devices and send that data further distances to a base station. This base station or watt node, which can be a desktop computer, accumulates and stores this data for review by the user and may also analyze and execute a task according to the data and the user's preferences. This work specifically concentrates on developing an autonomous and permanent power supply for microwatt nodes.

Autonomous microwatt nodes, more prevalently known as wireless sensor devices or "smart dust," are envisioned to be unobtrusive sensing and/or actuating devices that

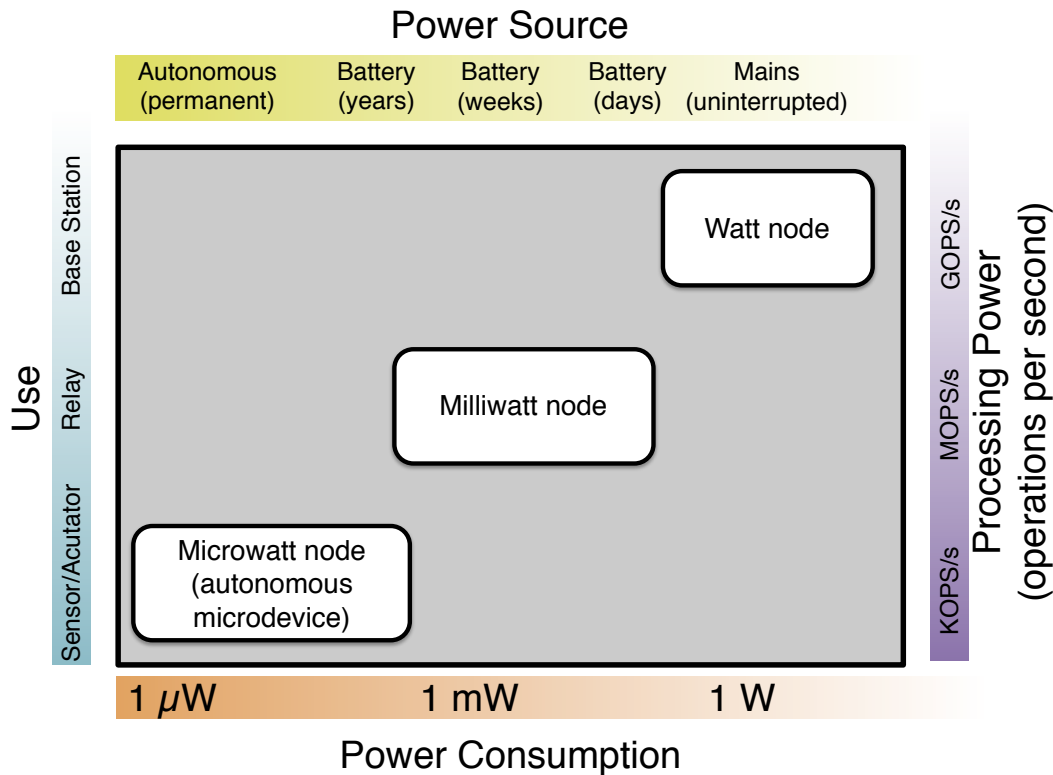


Figure 1.6. Ambient intelligence devices categorized according to power consumption and functionalities (adapted from [Snijders, 2005]).

can be dispersed through an environment such as a home, industrial factory, or even outside in a forest or desert. To create truly pervasive, integrated, and autonomous computers that can perform meaningful tasks, researchers have focused on implementing four characteristics: (1) the reduced power consumption of all computing, sensing, and communication components ( $<1$  mW average power draw) (2) the incorporation of a permanent power supply, (3) the integration of all its components on one substrate, (4) and the miniaturization ( $<1$  cm<sup>3</sup>) of the entire integrated device. Researchers have explored various strategies to implement the first characteristic including ultra low power circuit design in communication and processing protocol platforms [Otis, *et al.* 2007]. This dissertation's body of work proposes a battery chemistry and fabrication process to enable the latter three characteristics.

Presented here is an exercise in designing an energy storage device for a microwatt node. An energy storage device acts as a bridge between the input power from the energy harvesting device and the output power to the load, as illustrated by Figure 1.7. If a large disparity between the power magnitudes or a mismatch in the availability of the power exists, an energy storage device can alleviate these discrepancies by time shifting the flow of electrons from the energy harvester to the load. Design of a compatible energy storage system requires an understanding of the power usage of the entire system, and recognizing whether the system is limited by the input or output. The "power limiting" component will hence dictate the characteristics of the energy storage device. An energy harvester's output will depend heavily on its environmental calibration and the ambient energy available for conversion. Thorough reviews on the amount of energy that can

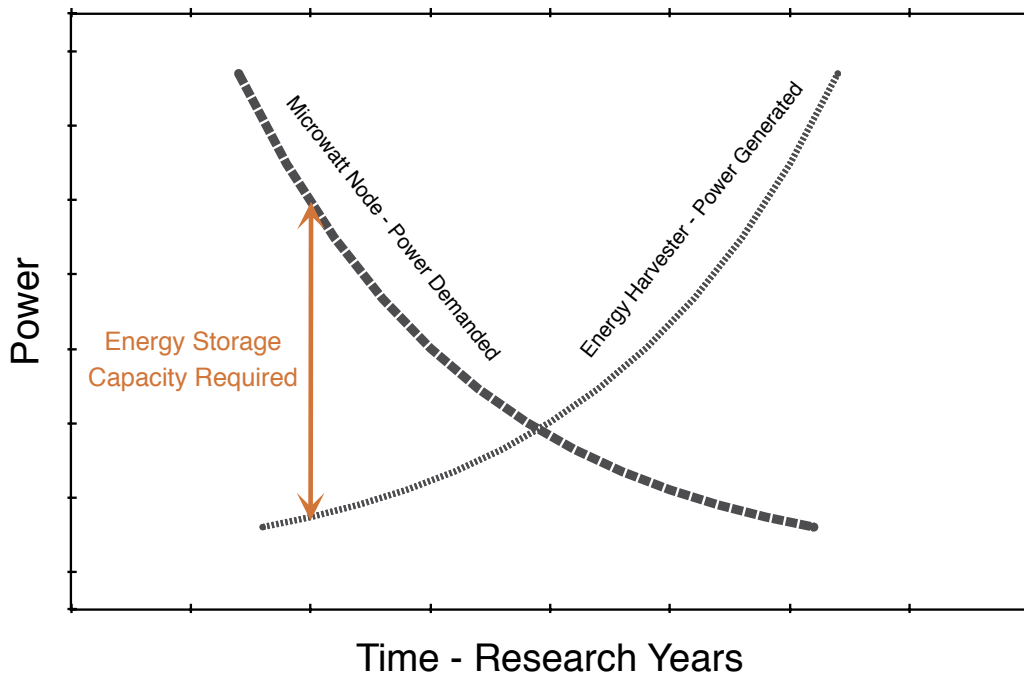


Figure 1.7. Visual representation demonstrating the diminishing discrepancy between the power demanded by a microwatt node and the power generated by energy harvesters. Any discrepancy will need to be addressed with an energy storage component.



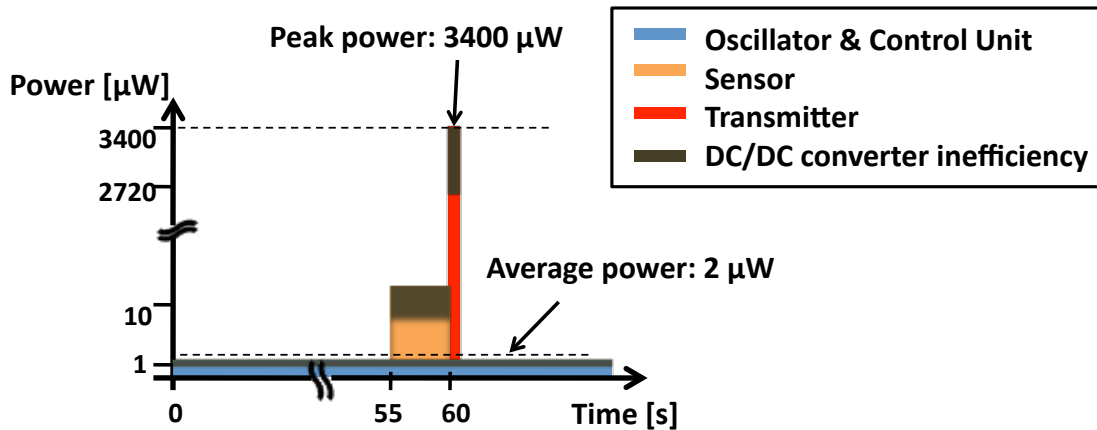


Figure 1.8. Power profile exhibiting one duty cycle of a prototypical wireless sensor device [Ho, *et al.*, 2009].

be harvested from the ambient environment and the devices that have been designed to capture that energy are provided by Roundy [Roundy, *et al.* 2003]. Depending on the ambient source, environmental calibration, and device design, harvested ambient power from 1 - 330  $\mu\text{W}/\text{cm}^3$  has been reported [Roundy, *et al.* 2003]. Additional energy storage capacity may also be needed to cope with any intermittency and unpredictability of the available ambient energy, for example a node that uses a solar cell outside would need an energy storage component designed to power the device through the night when ambient light is unavailable. In the case of an implantable glucose sensor, if a thermoelectric element is optimized to harvest energy from the temperature gradient between the skin and fat layers of the body, in normal conditions, the node may need substantially less energy storage capacity as this gradient is typically maintained [Ho, *et al.*, 2009].

Conversely, the energy storage component may depend on the demands of the node. An example power profile from a study on an implantable wireless glucose sensor is shown in Figure 1.8, however this profile could be similar for a variety of applications utilizing microwatt nodes, including distributed temperature sensors in homes or tire pressure sensors in automobiles [Ota *et al.*, 2006 and Chee, *et al.*, 2008]. The power profile captures one duty cycle that encapsulates three device functions and its corresponding power requirements. A continual power demand of less than 1  $\mu\text{W}$  is needed to maintain the control unit. This state is known as the “sleep state” when essentially all components are turned “off” except for the control unit. When a sensor measurement is required, an order of magnitude greater power draw ( $>10 \mu\text{W}$ ) is demanded for a few seconds. An even larger pulse ( $>1 \text{ mW}$ ) is demanded when the device transmits data. This routine is repeated on a user-defined schedule. The disparate power demands between the “sleep state” and the “transmit” state are difficult for any existing micro energy storage device to address within a device volume of  $< 1 \text{ cm}^3$ , and when designing an energy storage component, the load is typically limiting in most autonomous nodes. Long device lifetimes also compound the design challenges. Commonly cited desired performance metrics for microbatteries and capacitors are 1-10  $\text{mA}/\text{cm}^2$  and 1-10  $\text{mW}/\text{cm}^2$  [Dunn, *et al.*, 2008].

### 1.2.2 Materials Considerations for Microbatteries

As Owen had predicted, materials and processing innovations in the 1980's led to a few successful microbattery implementations, and eventually a variety of materials, geometries, and processing strategies were proposed and explored [Sequeria, *et al.*, 1985]. In the 90's, the field was further invigorated by the growing interest in microenergy harvesting devices and their need for secondary energy storage. Typical materials systems that have been incorporated in rechargeable microbatteries are analogous to macrobattery chemistries (batteries with footprint areas greater than 1 cm<sup>2</sup> and thicker than a few millimeters). A few candidate rechargeable microbattery chemistries are summarized in Table 1.2.

Materials efforts that have significantly contributed to micro-energy storage developments and are particularly worth discussing in detail include research on solid electrolyte and nano-dimensioned electrode materials. To avoid manufacturing and packaging complexities and to increase resiliency against extreme conditions such as shock, vibrations, and extreme temperatures, a solid or polymeric electrolyte is desired. Some of the first solid-state batteries incorporated solid, lithium-ion conducting glasses that could be deposited using physical vapor technology to form pinhole-free films with thicknesses as low as one  $\mu\text{m}$  [Duclot, *et al.*, 2001]. Most solid-state electrolyte materials are oxide-based such as lithium phosphorus oxynitride (Lipon). This glassy electrolyte is electrochemically, mechanically, and thermally very robust: it has a large potential stability between 0-5.5 V vs  $\text{Li}^+/\text{Li}$ , the mechanical strength to resist lithium dendrite propagation, and exhibits little degradation in temperatures ranging from -40 to 150 °C [Duclot, *et al.*, 2001]. The ability to deposit thin films of these solid-state electrolytes compensates for their low lithium-ion conductivity ( $< 5 \mu\text{S}/\text{cm}$ ) so that moderate to high rate performance is possible. Alternative solid-state electrolyte materials such as other oxide and sulfide glasses and glassy ceramics have also been explored.

Table 1.2. Selected rechargeable battery chemistries [Linden, *et al.*, 1995]

<b>Battery Chemistry</b>	<b>Energy Density (Wh/kg, mWh/cm<sup>3</sup>)</b>	<b>Operating Voltage (V)</b>	<b>Advantages</b>	<b>Disadvantages</b>
Nickel-Zinc (Ni-Zn)	60, 120	1.6	<ul style="list-style-type: none"> <li>• Environmentally friendly</li> <li>• High charge and discharge rates possible</li> </ul>	<ul style="list-style-type: none"> <li>• Zinc dendrites and electrode shape change reduce cycle life</li> </ul>
Rechargeable Alkaline Manganese (RAM)	145, 400	1.5	<ul style="list-style-type: none"> <li>• Environmentally friendly</li> <li>• Cheap materials costs</li> <li>• No memory effect</li> </ul>	<ul style="list-style-type: none"> <li>• Zinc dendrites and electrode shape change reduce cycle life</li> </ul>
Zinc-Silver Oxide (Zn-Ag <sub>2</sub> O)	105, 180	1.5	<ul style="list-style-type: none"> <li>• High power density</li> <li>• Low self discharge rate</li> <li>• Flat discharge potential</li> </ul>	<ul style="list-style-type: none"> <li>• Expensive silver</li> <li>• Zinc dendrites and electrode shape change reduce cycle life</li> <li>• Short wet life</li> </ul>
Lithium-ion (Li-ion)	150, 400*	3-4.2*	<ul style="list-style-type: none"> <li>• Flat discharge potentials</li> <li>• Long shelf life (&gt;10 years)</li> <li>• No memory effect</li> </ul>	<ul style="list-style-type: none"> <li>• Strict charge and discharge regulation needed</li> <li>• Moisture sensitivity and flammability risk</li> </ul>
Lithium polymer	130, 300*	3-4.2*	<ul style="list-style-type: none"> <li>• Reduced manufacturing complexity and costs</li> <li>• Increased safety</li> </ul>	<ul style="list-style-type: none"> <li>• High internal resistance</li> <li>• Strict charge and discharge regulation needed</li> </ul>

\*Values depend on electrode chemistries. Lithium-ion anodes include C<sub>6</sub>, Si. Typical cathodes: LiCoO<sub>2</sub>, LiMnO<sub>2</sub>, LiFePO<sub>4</sub>

Solid polymeric materials are also being considered as potential electrolytes for a variety of microbattery systems. In addition to the advantages of being solid-state, polymeric electrolytes are attractive because of their processing simplicity. There have been two principal materials directions in solid polymer electrolyte research, the first being the development of gel electrolytes, which swell salt solutions within amorphous regions formed by cross-linked polymer chains. Gel electrolytes tend to have moderate room temperature ionic conductivities (1 mS/cm<sup>2</sup> [Song, *et al.*, 1999]), but poor mechanical and electrochemical stability. Typical liquid components incorporated into gel electrolytes for batteries include organic solutions of ethylene or propylene carbonate, and of recent interest, ionic liquids [Fuller, *et al.*, 1998]. Ionic liquids are molten salts with high ionic conductivity, negligible vapor pressure, are non-flammable, and will become strong candidates for safe, plastic batteries if cost and large-batch processing

considerations can be addressed [Galiński, *et al.*, 2006]. The second thrust of solid polymer electrolyte research has concentrated on the development of dry polymer electrolytes, where the polymer acts both as the ion-conducting phase as well as the separator. These materials tend to be mechanically robust and can be cast very thin, but have fairly poor room temperature ionic conductivities (0.01 mS/cm [Meyer, 1998]). Dry polymer electrolytes made of nano-structured block copolymers have recently been shown to exhibit improved performance [Soo, *et al.*, 1999]. The block copolymers are able to self-organize into certain arrangements of rigid and highly ionic conductive regions, effectively decoupling the two properties within the material while significantly increasing their composite properties relative to other solid polymer electrolytes.

Significant and sometimes unexpected enhancements in performance have been observed in nano-dimensioned electrode materials. Electrode nanomaterials have oftentimes exhibited higher reaction rates due to increased electrode/electrolyte interfacial areas and shorter charge transport distances [Arico, *et al.*, 2005]; further performance enhancements may be reached with various nanoparticle morphologies, architectures, and composite materials. For example, Nam *et al.* demonstrated that with the deliberate texturing of dispersed gold nanoparticles along the length of virus-templated  $\text{Co}_3\text{O}_4$  electrode nanowires for lithium-ion batteries [Nam, *et al.*, 2006]; a significant capacity increase from 700 mAh/g to 1000 mAh/g was observed due to the gold's enhanced electrical conductivity as well as its catalytic effect on lithium-ion insertion [Nam, *et al.*, 2008]. The work by Nam, *et al.* combined two exciting fields in nanomaterial research with application to electrochemistry: first, the opportunity to explore nanoscale arrangements of materials and their performance effects, and second, it proposes a novel and simple method for using biological systems to program and self-assemble functional nanomaterials. Difficulties packing nanoparticles and the higher propensity for unwanted side reactions as a result of increased electrode/electrolyte contact areas have inhibited the adoption of some nanostructured electrode materials, however methods to curtail these problems have been proposed [Armand, *et al.*, 2008].

### **1.2.3 Geometry and Processing Considerations for Microbatteries**

Though the various battery chemistries listed in Table 1.2 differ in performance and processing, most of these chemistries have been considered or even implemented in rechargeable microbatteries largely because of the varying materials compatibilities associated with different fabrication processes. In addition, though microbattery electrode and electrolyte chemistries are in most cases indistinguishable from those of macrobatteries, the resulting microbattery performance does not usually scale proportionally because the configurations, materials deposition methods, post-processing, and packaging methods used to assemble macrobatteries and are oftentimes not feasible below the  $\text{cm}^3$  scale. For example, many lithium-ion commercial macrobattery electrodes are cast onto large substrates and then calendared, or compacted so the electrodes are pressed into a desired thickness. They are then cut into appropriate shapes and tightly rolled or folded into rigid canisters that provide both hermetic packaging and compression to the cell. For small microbatteries that are intended to be deposited directly onto a microdevice, these compression techniques and packaging processes cannot be implemented. Furthermore, on-board patterning of the microbatteries will often place temperature and other processing constraints on the fabrication method in order to

prevent damage to any neighboring components on the device. As a result, in addition to materials optimization, microbattery researchers have focused on advancing microbattery fabrication processes and novel cell geometries.

A survey by Lai, *et al.* summarized in Figure 1.9 supplements this discussion [Lai, *et al.*, 2010]. Lithium and lithium-ion battery chemistries are categorized according to traditional device geometries (prismatic, cylindrical, coin, or pouch) and their volumetric energy densities are recorded with respect to the cell volume. A linearly decreasing trend is observed for all cells, which correlates diminishing energy densities with cells of reduced volumes. If this trend were to continue to cell volumes  $< 1 \text{ mL}$  ( $1 \text{ cm}^3$ ), the projected energy density of the battery is less than  $100 \text{ Wh/L}$ , and effectively insufficient for the autonomous wireless devices. This suggests that at small device scales, a device and manufacturing vacuum exists irrespective of the energy storage materials used, and innovation in new fabrication processes and device geometries is necessary. The next two sections will discuss various research efforts to improve the performance of microbatteries, which include new fabrication strategies for both 2D and 3D geometries.

### 1.3 Implementations of 2D microbatteries

Two-dimensional microbatteries generally are cells configured from successive film depositions, either in planar or stacked arrangements as illustrated in Figure 1.10. Planar batteries are one of the simplest configurations to construct, comprising of two electrodes positioned adjacent to each other on a substrate. Since the electrodes are physically detached, a separator is not necessary. Oftentimes, planar cells are simply submerged in a liquid electrolyte or blanketed with a solid or polymer electrolyte film. The electrodes may be patterned into a variety of shapes such as square pads or more elaborate interdigitated structures, but regardless the current density distribution across each electrode varies with respect to its relative distance from the adjacent electrode. This uneven current distribution may result in unfavorable consequences especially during rapid charge and discharge, however if the internal resistances within the electrodes are minimal, reasonable performance may be achieved.

Stacked batteries are constructed by the consecutive deposition of films assembled layer-by-layer, with all films occupying the same approximate footprint area. The current distribution in a stacked cell runs through the thickness of the electrolyte/separator layer perpendicular to the electrode planes and is approximately constant, resulting in uniform performance across both electrodes; it is more suited for high rate applications in comparison to planar batteries. Furthermore, better areal energy density should be achieved with this configuration in comparison to planar microbatteries. Fabricating pinhole-free thin electrolytes/separators that can structurally support the weight and stress developed upon deposition of the electrode and current collector films has not been a trivial feat, however solid-state ionic materials and polymer electrolytes have been utilized to enable this configuration.

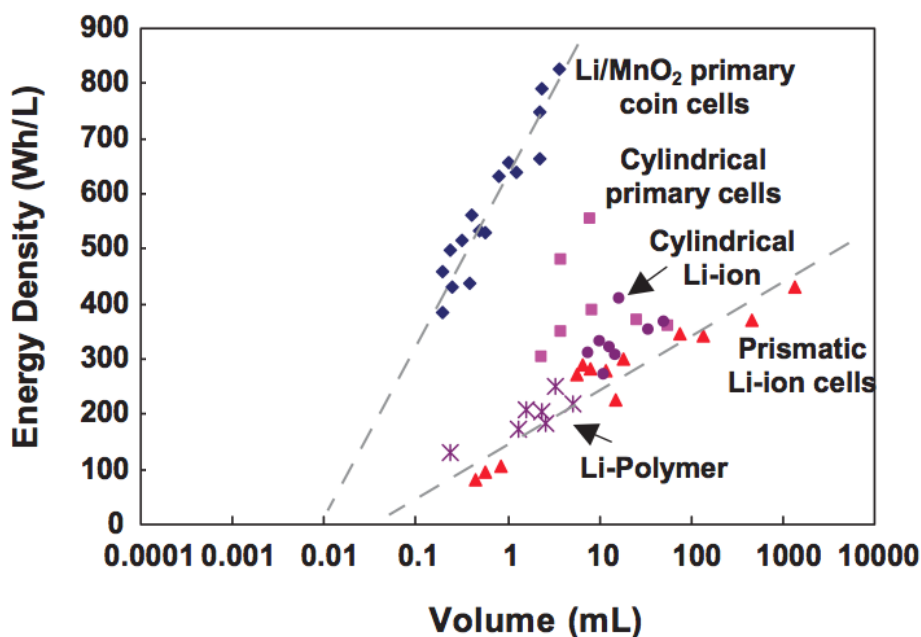


Figure 1.9. Volumetric energy densities of various commercial batteries as a function of cell volume. Batteries surveyed include lithium and lithium-ion chemistries with various cell geometries (adapted from [Lai, *et al.*, 2010]).

Two-dimensional microbatteries of both planar and stacked configurations have been constructed using a diverse spectrum of processing tools. Two-dimensional microbattery implementations are classified according to two processing strategies, from thin film to thick film microbattery deposition, and are manufactured by a variety (and in some cases a combination) of microfabrication and solutions-based processes. Prototypes of 2D microbatteries have been fabricated with wide-ranging degrees of completion, and notable efforts will be summarized and compared in the following section.

### 1.3.1 Thin Film Solid-State Microbatteries

Perhaps the most advanced implementations and extensive explorations of microbatteries have been conducted using thin film deposition methods and recently, thin film batteries have been sold commercially [Cymbet and Infinite Power Solutions]. Most thin film solid-state batteries are fabricated using physical vapor deposition (PVD) tools that deposit materials onto a substrate via condensation from its vapor phase. PVD tools that

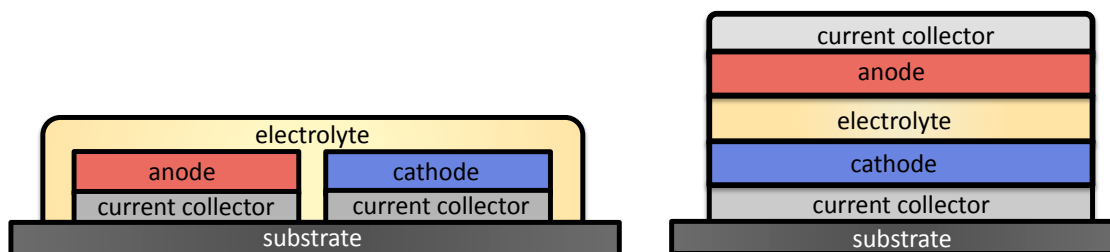


Figure 1.10. (left) Two-dimensional planar and (right) stacked microbattery configurations.

have been used for thin film batteries include sputtering and pulse laser deposition. Researchers at Oak Ridge National Laboratory (ORNL) have demonstrated stacked lithium-ion thin film microbatteries in which all components, including the current collectors, electrodes, electrolyte, and protective packaging, were deposited using thin-film techniques (see Figure 1.11) [Bates, *et al.*, 2000 and Dudney 2005]. Each of the layers can be successively deposited as conformal films, and depending on the deposition parameters, the film thicknesses range between sub-micron to a few micrometers. The deposited films are usually very uniform, and as a result, consistent current and charge distributions occur across the whole device. Commercial thin film batteries are typically a few  $\text{cm}^2$  in footprint area with capacities ranging from  $10 \mu\text{Ah}/\text{cm}^2$  to  $1 \text{mAh}/\text{cm}^2$ , however the thin film processes can be modified to deposit batteries with active areas under  $1 \text{mm}^2$  (Figure 1.12) [Song, *et al.*, 2009 and Kushida, *et al.*, 2002]. Because the fabrication tools used to build these microbatteries are compatible with standard microfabrication methods, it is conceivable that thin film microbatteries can be deposited while concurrently also patterning other wafer-scale components onto the same substrate. Multiple thin film microbatteries can be patterned in series and parallel configurations to match voltage and current requirements [West, *et al.*, 2002], and the integration of localized energy storage components can be achieved to provide efficient power delivery for discrete on-chip components such as integrated circuits.

Though microbatteries and macrobatteries share common electrode chemistries, their electrochemical performances can differ quite significantly depending on the materials processing methods and parameters used. In general, the as-deposited PVD electrode films are homogenous in composition, lacking binders and additives. The dense films are amorphous until annealed between  $300\text{-}1000^\circ\text{C}$ . The resulting crystalline films are microstructurally robust and exhibit rapid lithium-ion diffusion, leading to excellent cycle lives ( $> 1,000$  deep cycles) and moderate maximum power densities ( $10 \text{mW}/\text{cm}^2$ ) [Dudney, 2005]. Furthermore, for crystalline electrodes, the discharge voltages are very flat, simplifying supply voltage regulation circuitry. In general, failure and electrode ageing may occur as a consequence of poor voltage regulation if overcharged, exposure to unsafe operating temperatures, and mechanical volume changes that might occur during electrochemical cycling, all of which can greatly affect the capacity and cycle life of the device [Dudney, 2005]. Typical anodes for thin-film lithium and lithium-ion batteries include lithium, silicon-tin oxynitrides,  $\text{Sn}_3\text{N}_4$ , and  $\text{Zn}_3\text{N}_2$ , to name a few, and cathodes such as  $\text{LiCoO}_2$ ,  $\text{LiMn}_2\text{O}_4$ , and  $\text{LiV}_2\text{O}_5$  have been thin film deposited. The thicknesses of thin film deposited cathodes and anodes are usually no greater than  $5 \mu\text{m}$ , and are limited by the inherent stress accumulated in the film due to processing, which results in difficulties adhering to substrates. For applications requiring high energy densities, the limited storage capacity of thin film microbatteries has been the greatest barrier to their widespread adoption as an integrated energy storage component.

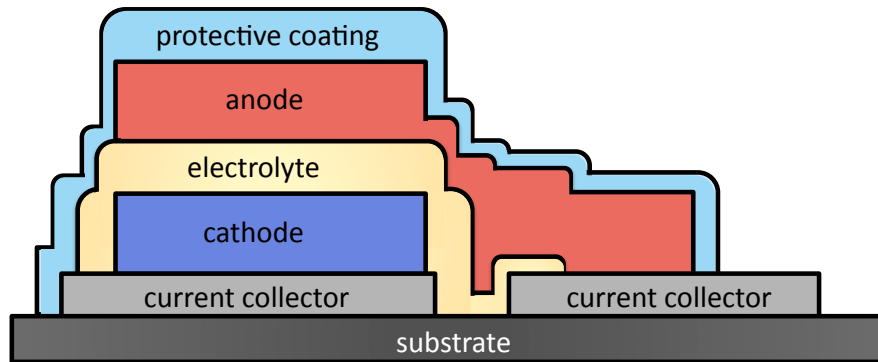


Figure 1.11. Thin film microbattery structure [Bates, *et al.*, 2000].

The difficulty in achieving higher energy densities is further compounded by inactive packaging and support components occupying a majority of the total device weight and volume, and this is further exacerbated as the microbattery size decreases. The greatest challenge in lithium-ion microbattery manufacture has been to find equally thin, cost-effective hermetic sealants that can protect the electrodes and electrolyte from exposure to moisture. For lithium-ion batteries, moisture levels must be kept below a few parts per million to avoid detrimental irreversible reactions and maintain prolonged operation [Aurbach, *et al.*, 1999]. For thin film microbatteries, finding a hermetic material that can be deposited conformably with the same fabrication tools used to deposit the active components of the microbattery would be ideal. Moisture permeability depends heavily on the encapsulating material used, its thickness, and its resilience to mechanical and chemical wear. Researchers have had varying degrees of success with depositing thin films of glass, polymers, and metals. At ORNL, a microbattery packaged with alternating layers of Parylene polymer and sputtered metal films was able to operate for a few months before failing due to moisture exposure [Dudney, 2005]. Other necessary improvements include the need for faster, more efficient manufacturing processes, higher

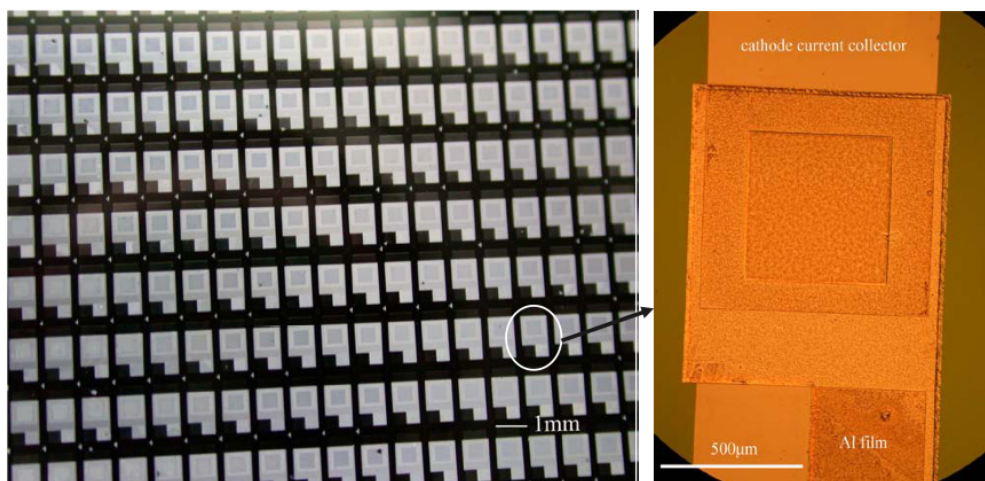


Figure 1.12. Array of thin film microfabricated microbatteries [Song, *et al.*, 2009].



device yield, and reduced materials and processing costs. Surprisingly, despite the achievements in thin film microbattery research and development, there has been a scarcity of reported attempts to integrate these microbatteries with energy harvesters, though feasibility and system architecture studies have been presented in literature.

### 1.3.2 Thick Film Microbatteries

Despite significant achievements in the development of thin film microbatteries, high processing costs and limitations in areal capacity motivated the development of alternative microbattery manufacturing strategies. In 1999, Birke, *et al.* proposed the development of miniaturized coin-cells of “monolithic” solid-state battery materials tailored in geometry so that, along with other integrated circuit components and microchips, the battery could be embedded into a substrate [Birke, *et al.*, 1999]. Their microbattery consisted of lithium titanate ( $\text{Li}_4\text{Ti}_5\text{O}_{12}$ ) and lithium manganese oxide ( $\text{LiMn}_2\text{O}_4$ ) electrodes and a ceramic lithium titanate phosphate based ( $\text{Li}_{1.3}\text{Al}_{0.3}\text{Ti}_{1.7}(\text{PO}_4)_3$ ) electrolyte. Two electrode pellets, each no more than a few millimeter thick, a 200  $\mu\text{m}$  thick electrolyte were stacked, cold pressed, sintered at  $750^\circ\text{C}$  for 12 hours. Then the electrodes were polished down to tens of micrometers and the entire structure was then cut into a desired shape so that the final monolithic microbattery could be incorporated into a substrate (see Figure 1.13). For a  $C/2$  discharge rate, a microbattery of  $1\text{ cm}^2$  diameter footprint area and 500  $\mu\text{m}$  in thickness had an approximate energy density of  $42.5\ \mu\text{Wh}/\text{cm}^2$  when cycled between 1.5 – 3.2 V. Though this assembly method would have been difficult to implement with smaller, more complex geometries, Birke seeded a few important concepts with regard to microbattery fabrication: (1) the need for a method to fabricate thicker electrodes from tens to hundreds of microns thick, and (2) the importance of developing a cost-effective method to tailor both the lateral and horizontal dimensions of all microbattery components. For example, balancing the maximum current density with the desired storage capacity performance for different device applications could change the optimal thicknesses of both microbattery electrodes by orders of magnitude, making methods that allow customization very compelling. Additionally, Birke acknowledged that the integration

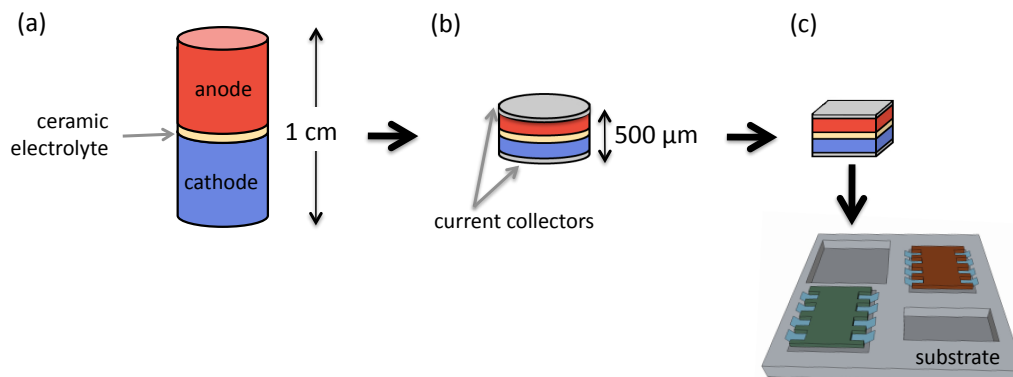


Figure 1.13. A monolithic solid-state battery formed by (a) cold pressing and sintering a stack of electrodes and ceramic electrolyte, (b) polishing the electrodes to the desired thickness and sputtering current collectors at each end, and (c) cutting the monolithic microbattery into a desired shape to be embedded into a substrate [Birke, *et al.*, 1999].

of a microbattery onto a substrate would create new temperature and stability limitations that might prompt alternative materials and processing choices that might be considered unconventional compared to macrobattery fabrication. These themes have continued to impel the microbattery research field, and many efforts concentrating on applying thick film, customizable fabrication processes have been explored.

Thick film microbatteries have electrode components with thicknesses that are at least an order of magnitude greater than thin film batteries, but still much thinner than button and coin cell macrobatteries. Therefore, like thin film microbatteries, thick film microbatteries can be embedded into or on substrates in an inconspicuous fashion. Though many thick film fabrication methods vary in actuation, they share a common advantage of being able to deposit thick and oftentimes porous electrodes, in the tens to hundreds of microns. As a consequence, significantly larger energy storage capacities can be achieved for a given footprint area. Generalizing the performance of thick film microbatteries can be quite difficult since the materials chemistries, cell configurations, and deposition capabilities are varied, but a few noteworthy efforts are discussed in the next sections.

### **Microfabricated Thick Film Microbatteries**

Microfabricated thick film microbatteries employ similar processing tools used to construct integrated circuits and MEMS devices. The microbatteries can be processed in parallel with other microfabricated components on a substrate, and many microbatteries can be made simultaneously with high throughput and yield. Humble *et al.* used standard microfabrication techniques to construct planar configurations of thin film nickel-zinc microbatteries on silicon wafer substrates [Humble, *et al.*, 2001]. Using a combination of electron-beam evaporation, electroplating, and photolithography, 15 to 75  $\mu\text{m}$  thick, porous zinc and NiOOH electrodes were patterned adjacent to each other with a total cell area of 2  $\text{mm}^2$  (see Figure 1.14). The electrodes were blanketed in a liquid alkaline electrolyte solution of potassium hydroxide and zinc oxide, and this electrolyte was retained by 100  $\mu\text{m}$  tall, spin-coated epoxy sidewalls. Manually applied polymer films were able to adequately seal the cell chambers to prevent evaporation and leakage of the corrosive electrolyte solution over short experimental times, but improved hermetic materials and encapsulation process will be needed for extended device lifetimes. The relative electrode geometries and their separation distances were modeled and optimized for specific power and energy density requirements [Humble, *et al.*, 2003]. The prototypes had operating voltages between 1.2 to 1.85 V, and for a C/1.2 discharge rate, demonstrated energy and power densities as high as 500  $\mu\text{Whr}/\text{cm}^2$  and 150  $\text{mW}/\text{cm}^2$ , respectively. To simulate the power demands of an autonomous microsensor, a commercial solar cell was used to charge the microbattery [Singh, *et al.*, 2006]. More than 2300 recurring pulse discharges were extracted from the microbattery without performance degradation. Additionally, this was one of the first reported implementations of a hybrid power supply combining an energy harvester with a microbattery.

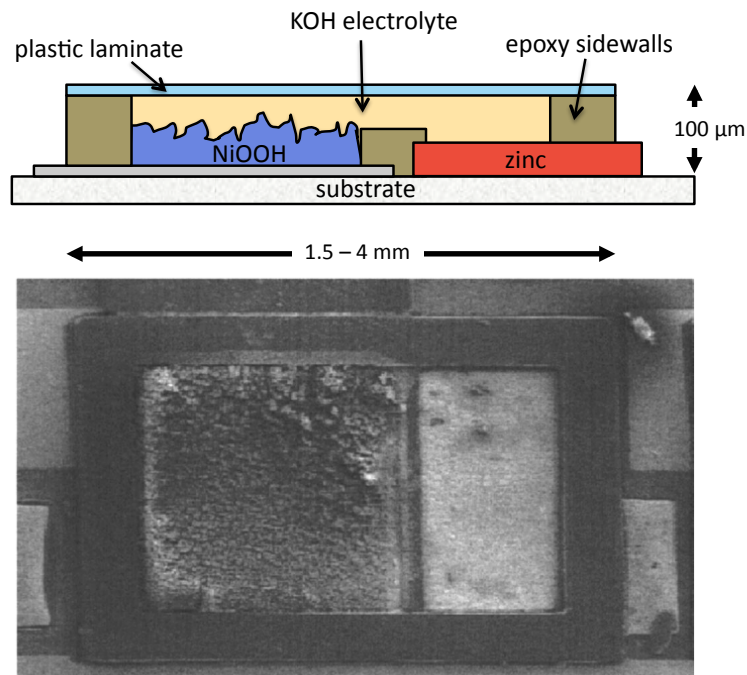


Figure 1.14. Microfabricated Zn-NiOOH planar microbattery with thick film electrodeposited electrodes [Humble, *et al.*, 2001].

### Solution Processed Microbatteries

The majority of thick film microbattery fabrication procedures are solution-based processes that can deposit porous electrodes with materials similar to those in commercial macrobatteries. The materials that can be deposited vary in content, including metals, ceramics, and polymers, and they can be deposited as suspensions, solutions, or slurries, all of which are referred to as “inks”. Most thick film electrodes are composites, containing active particles, conductive additives, a polymer binder, and a solvent that adjusts the rheology of the slurry and is eventually evaporated from the film after deposition. The active particles determine the electrochemical properties of the cells. While most conductive additives and polymer binders are electrochemically inactive, their functions are vital to the performance of the electrode, providing enhanced electronic conductivity and mechanical strength to the film, respectively. Adequate electronic conductivity in the electrodes is needed for the battery to provide high discharge rates, and this is achieved when a large enough population of conductive particles forms a contiguous network. Note that for most thick film methods, the electrochemical and materials properties of the deposited films are largely predetermined by the composition of the ink rather than its deposition and post-processing conditions. Consequently, most solution deposition processes deposit materials at room temperature and ambient conditions, are indiscriminate to the substrate they deposit on, and do not usually require post-processing steps such as doping or the application of extremely high

temperatures. Further understanding of the properties of a solution deposited film (such as film adhesion, deposited material quality, and interfacial morphology) and effective characterization methods are needed.

Viable solution processes for the fabrication of microbatteries include screen-printing and various direct write printing techniques. Though there has been a large amount of literature reporting electrode and electrolyte formulations compatible with screen-printing [Prosini, *et al.*, 2001], a fully screen printed microbattey has not yet been demonstrated; however, the successful screen printing of other microdevices suggests that microbatteries made with this process should be feasible. In the following sections, advanced demonstrations of microbatteries fabricated using direct write solutions processes will be discussed in detail.

### *Direct Write Fabricated Microbatteries*

Direct writing refers to a broad subset of patterning processes that are able to deposit functional materials onto specific locations of a substrate designated by computer controlled translational stages [Lewis, *et al.*, 2004]. With these processes, patterns and structures both simple and complex can be fabricated. Direct write processes can be classified according to their ink writing mechanisms: drop, flow, energy beam, and tip-based direct writing [Hon, *et al.*, 2008]. These categories of materials transfer techniques vary greatly in actuation, materials compatibility, fabrication capabilities, feature sizes, and writing speeds. Despite their variety, most direct write processes share a few general characteristics. Because materials are patterned additively and often at room temperature and ambient conditions, the amounts of wasted materials and energy expended are minimal, especially compared to production-scale microfabrication processes that depend on subtractive techniques like lithography and etching. Furthermore, the functionality and structure of the deposited materials are typically independent of the substrate material, its orientation, and its morphology. Because of the versatility of direct writing, there has been a growing interest in applying these manufacturing tools to a variety of fields. Common obstacles preventing the upwards scaling of these processes towards commercialization include necessary improvements in throughput, reliability, resolution, and cost.

The ability of direct write processes to precisely pattern multilayer structures both laterally and vertically in a repeatable and additive fashion is especially beneficial for the fabrication of energy storage devices, which rely on the precise geometry of their active layers as well as the quality of the interfaces between them to achieve good performance. For example, the geometry of a deposited electrode must be optimized to be thick enough to provide adequate energy storage capacity, but thin enough that charge carrier transport is not impeded. Additionally the electrode requires a high interfacial area with the electrolyte so that chemical reactions occur rapidly. The fabrication of microbattery components has been demonstrated using flow-based dispenser printing and energy-based laser direct writing, and these processes are discussed in the next few sections.

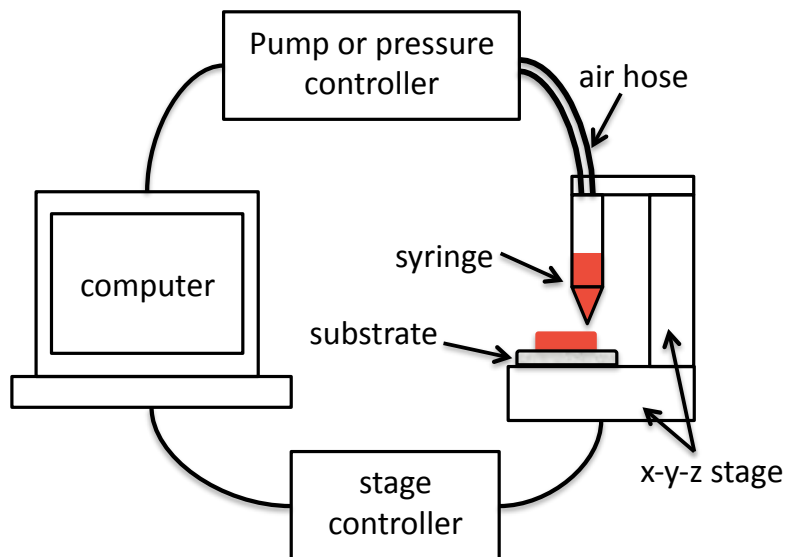


Figure 1.15. Schematic of flow-based direct write printing.

### Flow-based Direct Write Microbattery

Flow-based direct writing refers to a class of tools that, through a positive pressure, are able to dispense a flow of ink through a small orifice such as a syringe needle (Figure 1.15). This is an ambient, room temperature process that is capable of depositing small volumes (tens of picoliters) of inks ranging in viscosities from 10 to 1,000,000 cP. Linewidths and feature sizes depend heavily on the processing parameters employed and ink properties, but typically run between 10  $\mu\text{m}$  to 3 mm. Due to the flexibility of this tool to pattern a variety of materials, a few demonstrations of flow-based direct write microbatteries with different configurations and materials have been reported.

Dokko, *et al.* used a pneumatic-controlled micro-injector to pattern sol-gel materials

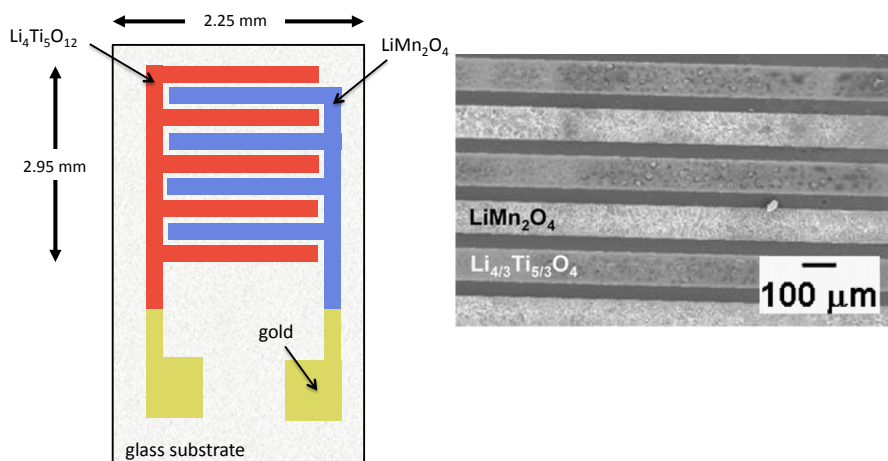


Figure 1.16. Flow-based printed interdigitated, planar lithium-ion electrode array [Dokko, *et al.*, 2007].

into planar micro-dot [Dokko, *et al.*, 2005] and interdigitated lithium manganese oxide ( $\text{LiMn}_2\text{O}_4$ ) and lithium titanate ( $\text{Li}_{4/3}\text{Ti}_{5/3}\text{O}_4$ ) electrode microarrays [Dokko, *et al.*, 2007]. As shown in Figure 1.16, the planar interdigitated electrodes were  $100\ \mu\text{m}$  in width and separated by  $50\ \mu\text{m}$  gaps. The resulting electrode thicknesses measured between of  $0.5\text{--}1\ \mu\text{m}$  after undergoing high temperature calcination ( $450^\circ\text{C}$ ) and anneal ( $700^\circ\text{C}$ ) processes. Polymer electrolyte films were manually applied, cast, or printed to cover the electrodes. The interdigitated planar array, occupying  $6.6\ \mu\text{m}^2$  and having an operating voltage of  $2.5\ \text{V}$ , displayed an areal energy density of  $11\ \mu\text{Wh}/\text{cm}^2$  for a 1C discharge rate. The authors suggested by increasing the thicknesses of the electrodes and decreasing the gaps between them, the performance could be improved.

Steingart, *et al.* developed a similar pneumatic dispenser printing process to fabricate stacked microbatteries with composite slurry electrodes and a gel electrolyte [Steingart, *et al.*, 2007 and Steingart, 2006]. Because this printing method is gentle (in comparison with other direct write processes, such as inkjet printing, which propels solution droplets or films towards a substrate with a large amount of kinetic energy), multiple conformal layers of different inks can be deposited without completely mixing and good interfacial adhesion is achieved [Wright, *et al.*, 2010]. As a result, the precise construction of interesting multilayer devices and structures is possible. Batteries of lithium-ion chemistry have been printed, however the printed battery's performance was hampered by residual moisture contamination.

#### *Laser Direct Write Printed Microbatteries*

Extensive research at the US Naval Research Laboratory on laser-induced forward transfer (LIFT) of electrochemical materials and laser micromachining has inspired the use of direct write technologies in a variety fields [Arnold, *et al.*, 2007 and Pique, *et al.*, 2003]. The variation of LIFT known as matrix-assisted pulsed laser evaporation (MAPLE) employs a laser beam which, when directed on ink ribbon mounted on the underside of a laser transparent support material, will propel the ink towards a substrate positioned in parallel to the ribbon (Figure 1.17). The ink is a composite of an active powder, solvent, and a matrix material, which upon interacting with the laser at the interface of the support material, evaporates to release the ink. The MAPLE process is capable of depositing thick films without altering or damaging their properties. This is especially advantageous in electrochemical systems that benefit from maintaining porous, high surface area electrode structures. Both planar and stacked microbattery configurations have been demonstrated using a combination of the MAPLE process along with laser micromachining [Arnold, *et al.*, 2004 and Pique, *et al.*, 2004]. For planar microbatteries, laser micromachining was used to create thin electronically isolated gaps between two adjacent electrodes. Typical micromachined line widths of  $10\ \text{to}\ 50\ \mu\text{m}$  have been shown. The added capability of laser micromachining allows for the high spatial utilization and intricate patterning of the electrodes with good accuracy and repeatability. Besides the printing of adjacent rectangular electrodes, some complex electrode configurations including interdigitated and concentric circle electrodes were also fabricated (Figure 1.18) [Arnold, *et al.*, 2007]. To activate the batteries, drops of alkaline electrolyte solutions were blanketed over the laser-transferred electrodes without any containment. For operation voltages of  $1.55\ \text{V}$ , the typical capacity and energy density

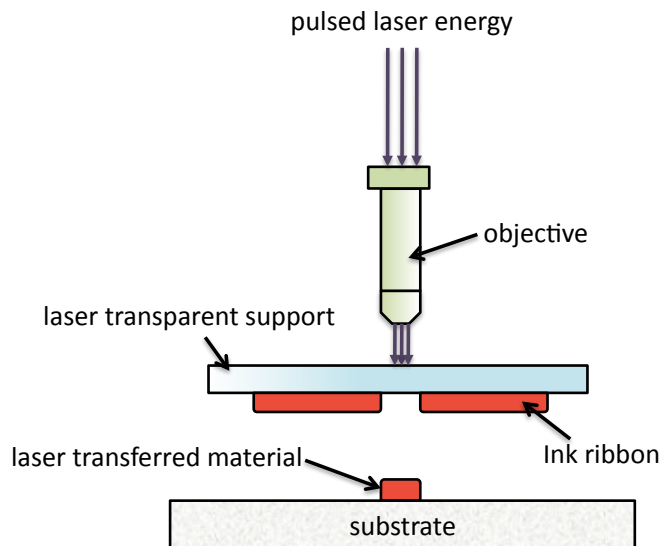


Figure 1.17. Schematic of matrix-assisted pulsed laser evaporation (MAPLE) direct write deposition [Pique, *et al.*, 2003].

measured were  $100 \mu\text{Ah}/\text{cm}^2$  and  $0.6 \text{ mWh}/\text{cm}^2$ , respectively. An approximate maximum power density of  $0.8 \text{ mW}/\text{cm}^2$  was reported.

Similarly, laser micromachining was also used in conjunction with the MAPLE process to fabricate stacked lithium-ion microbatteries embedded into a substrate. Sutto *et al.* micromachined a  $30 \mu\text{m}$  deep,  $3 \text{ mm}$  by  $3 \text{ mm}$  trench into polyimide backed with aluminum, which acts as the cathodic current collector [Sutto, *et al.*, 2006]. Laser-transferred inks of  $\text{LiMnO}_2$ , a ceramic-solid polymer ionic liquid (c-SPIL) nanocomposite electrolyte, and carbon electrode slurries were deposited sequentially into the trench, as shown in Figure 1.19. Platinum was sputtered onto the top of the trench, acting both as the anodic current collector as well as an encapsulant. When cycled at

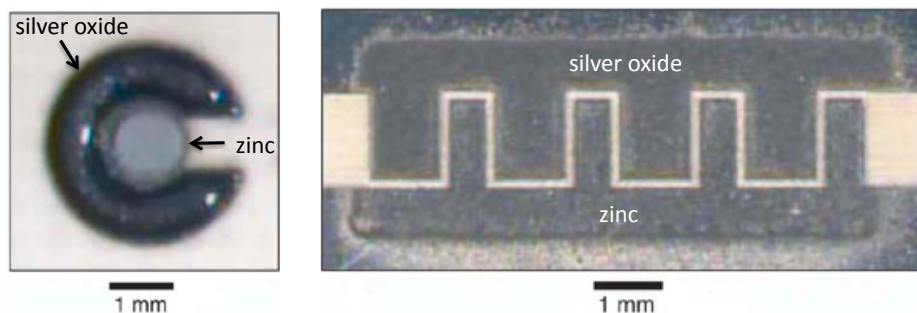


Figure 1.18. Planar (left) concentric circle and (right) interdigitated zinc-silver oxide alkaline microbatteries fabricated using laser direct write [Arnold, *et al.*, 2007].

a C/3 discharge rate between 3 to 4.65 V, the stacked microbattery exhibited a capacity and energy density of  $110 \mu\text{Ah}/\text{cm}^2$  and  $1.32 \text{ mWh}/\text{cm}^2$ , respectively. By designing the c-SPIIL to structurally retain separation between the electrodes during fabrication, Sutto et al. were able to successfully demonstrate the fabrication of a microbattery with a stacked configuration integrated and sealed into a substrate, doing so without any manual assembly. Because it is versatile and indiscriminate of materials and substrates, the laser forward transfer process could feasibly be applied to many other battery chemistry systems.

### 1.3.3 Concluding Remarks for 2D Microbatteries

The miniaturization of traditional, 2D, rechargeable macrobatteries in all three dimensions has proven to be a fairly challenging task because of the complexities in reconciling materials, geometrical, processing, and performance constraints into a small, integrated electrochemical device. Thin and thick film fabrication strategies have been explored and encouraging strides towards integrating these microbatteries into hybrid micropower supplies have been made. Table 1.3 summarizes 2D microbattery research discussed in this chapter.

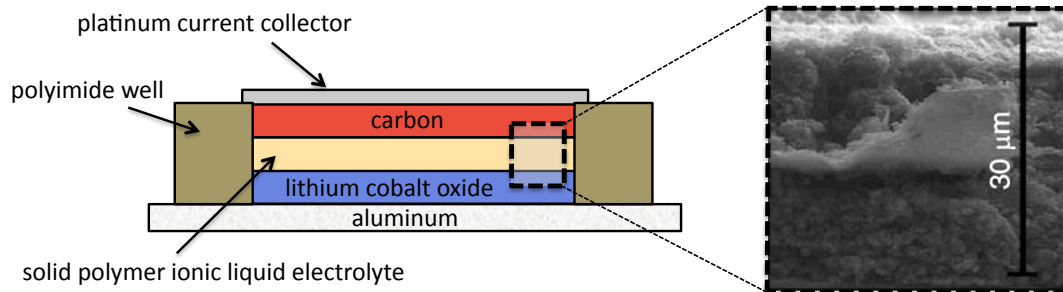


Figure 1.19. Stacked lithium-ion microbattery embedded in a substrate using laser direct write fabrication [Sutto, *et al.*, 2006].



Table 1.3. Two-dimensional microbatteries summary

<i>2D microbattery</i>	<i>Chemistry</i>	<i>Geometry*</i>	<i>Operating Voltage (V)</i>	<i>Areal Performance for 1 cm<sup>2</sup> footprint**</i>
Thin film				
Physical vapor deposition	Li-ion, glass electrolyte	(t) 10-15 $\mu\text{m}$ (f) 1 mm <sup>2</sup> – 25 cm <sup>2</sup> stacked	3 – 4.2	10 $\mu\text{Ah}$ – 1 mAh; 50 $\mu\text{Wh}$ – 5 mWh; 10mW
Thick film				
Electrode polishing	Li-ion, ceramic electrolyte	(t) 500 $\mu\text{m}$ (f) 1 cm <sup>2</sup> stacked monolith	1.5 – 3.2	15 $\mu\text{Ah}$ ; 42.5 $\mu\text{Wh}$
Microfabrication	Ni-Zn, liquid electrolyte	(t) 50 $\mu\text{m}$ (f) 2 mm <sup>2</sup> planar	1.2 – 1.85	305 $\mu\text{Ah}$ ; 500 $\mu\text{Wh}$ ; 150 mW
Dispenser printing	Li-ion, polymer electrolyte	(t) 0.5 – 1 $\mu\text{m}$ (f) 6.6 mm <sup>2</sup> planar, interdigitated electrodes	1.5 – 3	4.5 $\mu\text{Ah}$ ; 11 $\mu\text{Wh}$
Laser direct write printing	Zn-Ag <sub>2</sub> O, liquid electrolyte	(t) 10 – 20 $\mu\text{m}$ (f) 4.9 mm <sup>2</sup> planar, concentric electrodes	0.8 – 1.6	450 $\mu\text{Ah}$ ; 0.6 mWh; 0.8 mW
	Li-ion, gel electrolyte	(t) 30 $\mu\text{m}$ (f) 9 mm <sup>2</sup> stacked, embedded in substrate	2.9 – 4.2	110 $\mu\text{Ah}$ ; 1.32 mWh

\* (t) : thickness, (f): footprint area

\*\* areal capacity, energy density, and if provided power density are listed

## 1.4 Three-Dimensional Microbatteries

Designing a small footprint area two-dimensional microbatteries oftentimes leads to a fundamental conundrum: for a given electrochemical battery system, a trade-off exists between the amount of energy stored (determined by the electrode materials and their dimensions) and the rate at which this energy can be extracted (determined by the contact area between electrodes and electrolyte, their through thicknesses, and charge transport properties). For optimal performance in a 2D microbattery, this manifests as a practical limit to the relative electrode and electrolyte dimensions. As an alternative, non-traditional three-dimensional microbattery architectures have been explored, and initial implementations are discussed in the following section.

Three-dimensional microbatteries function identically to two-dimensional cells, but by increasing the amount of electrode and electrolyte interfaces while maintaining short ion

transport distances between electrodes, drastically enhanced electrochemical performance can be derived. This has been a burgeoning field of research with consistent developments in materials, processing, modeling, and characterization. Though configurations and approaches towards fabricating three-dimensional microbatteries may vary, a defining property is that at the microscopic scale, charge transport between the electrodes is essentially one-dimensional, while at the macroscopic level the electrodes exhibit non-planar geometries [Long, *et al.*, 2004]. As a consequence, large areal energy densities are achievable without sacrificing high rate power performance.

Various three-dimensional architectures are potentially suitable configurations for microbatteries. However, for classification purposes, the structures can be distinguished according to the continuity of their electrode and electrolyte phases. The most commonly examined architectures are cells with interdigitated cylinder or plate electrode arrays (Figure 1.20 a,b) or arrangements of concentric electrode and electrolyte units surrounded by a matrix of the opposing electrode (Figure 1.20 c). In both cases, at least one electrode component is discontinuous. Alternatively, microbatteries can also be constructed from 3D configurations in which all phases (both electrodes and the electrolyte) are continuous regardless of their arrangement, be it periodic or aperiodic. This can be as simple as using a 2D stacked battery motif and folding it into a 3D pattern (Figure 1.21 a), or creating two interpenetrating, uninterrupted electrode networks, either regular or irregular in morphologies, and separating them by a conformal and continuous electrolyte coating (Figure 1.21 b,c).

In the last two decades, there have been numerous feasibility studies on the fabrication and electrochemical properties of components that can be applied to 3D microbatteries. This section attempts to highlight those significant efforts. Note that as the fabrication technologies for 3D architectures are far from mature, the comparison of the performance of different 3D microbattery prototypes is difficult because most attempts use test structures that either do not fully exploit their 3D architecture or only successfully demonstrate some but not all necessary components.

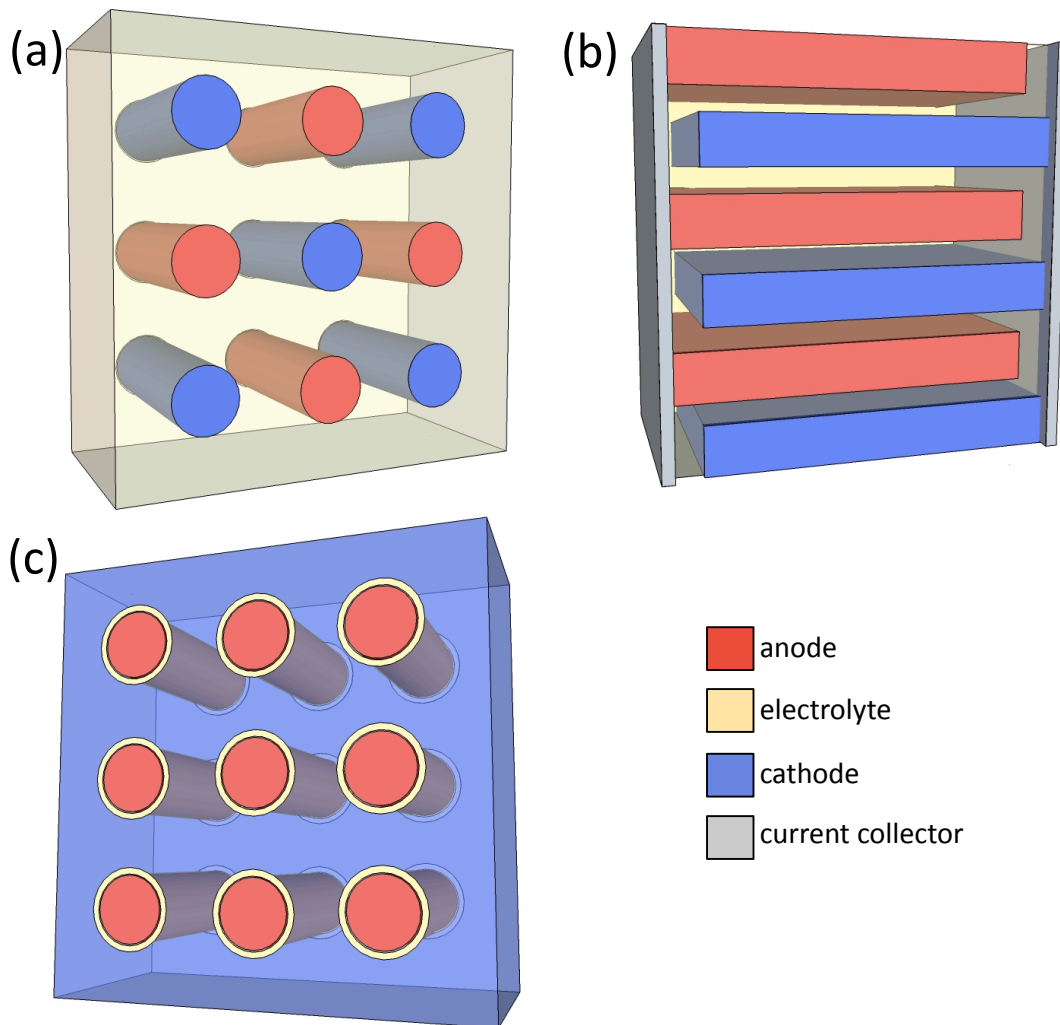


Figure 1.20. Three-dimensional microbattery architectures with at least one discontinuous component: (a) regular arrangements of interdigitated anode and cathode cylinders or (b) interdigitated electrode plate arrays distributed in an electrolyte; (c) electrolyte coated anode cylinders dispersed in a continuous phase of cathode material. Note (a) and (c) do not display current collectors [Long, *et al.*, 2004].

### 1.4.1 3D Microbattery Architectures With A Discontinuous Element

The microbattery architectures discussed in this section, summarized in Figure 1.20, are composed of at least one electrode phase that is made of discrete elements, usually arranged in an array. Each of the electrode components must be electronically connected using a current collector network. As an electrode arrangement becomes more elaborate, the current collector configuration will need to equally become as intricate. Most of the methods described involve constructing a 3D mold and then filling it with the active components by vapor deposition, electrodeposition, or colloidal methods, however alternate fabrication processes, for example direct-write printing, have also been used to construct three-dimensional geometries.

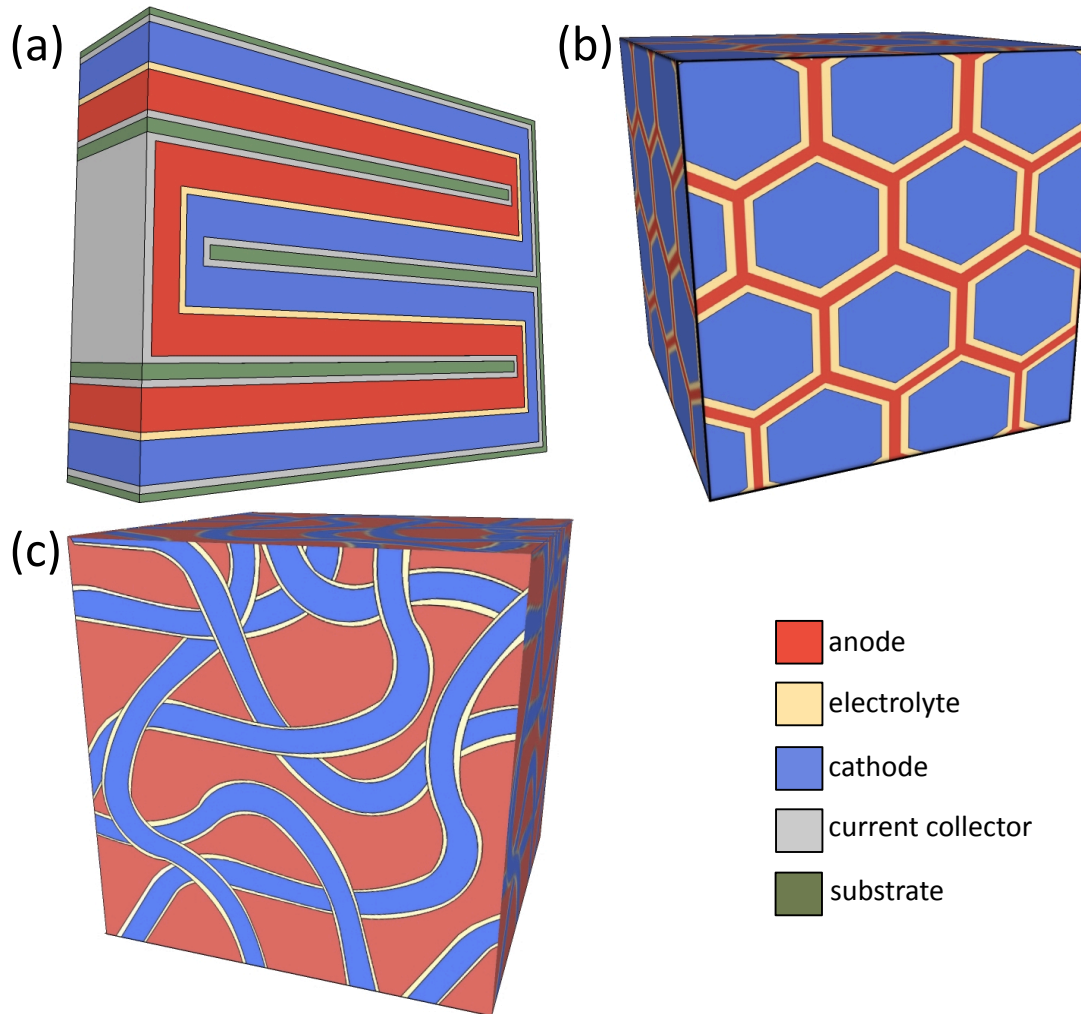


Figure 1.21. Three-dimensional microbattery architectures where the electrodes and electrolyte are each continuous phases: (a) a 2D stacked battery configuration that is folded into a 3D architecture; (b) a periodic and (c) an aperiodic scaffold (composed of cathode material conformably coated with a thin electrolyte) back-filled with anodic material occupying the free volume. Note that (b) and (c) do not display current collectors [Long, *et al.*, 2004].

### Interdigitated Electrode Array Microbattery

Interdigitated microbattery architectures incorporate regular arrangements of anode and cathode structures surrounded by a continuous electrolyte phase. Potential electrode shapes include plates, rods with triangular or square cross-sections, and most commonly, cylindrical rods. For this microbattery architecture, the relative locations and dimensions of the electrodes will determine current and potential distributions within the cell, therefore both precise spatial positioning and patterning capabilities are imperative. Chamran, *et al.* fabricated Ni-Zn and lithium-ion microbatteries with square and cylindrical electrode arrays by filling removable silicon molds with electrode materials via colloidal or electrodeposition methods [Chamran, *et al.*, 2006 and Chamran, *et al.*, 2007]. Electrodes with diameters ranging from tens to hundreds of micrometers and

aspect ratios between 10:1 to 50:1 (rod length:diameter) could be achieved by micromachining silicon substrates using a combination of photolithography with either deep reactive ion etching (DRIE) or photo-assisted anodic etching. Alternating rows of nickel hydroxide and zinc posts were fabricated on the same substrate within a 5 mm x 5 mm footprint (Figure 1.22), and when submerged in an alkaline electrolyte, demonstrated an areal capacity of  $2.5 \mu\text{Ah}/\text{cm}^2$  for operating potentials between 1.3 V – 1.75 V. The authors suggested that further capacity improvement could be achieved with higher density electrode arrays and alternative electrode arrangements, however the repeated cycling of the interdigitated Ni-Zn battery was severely impaired by the gradual removal of zinc electrode material by the electrolyte. This process is relatively indiscriminate to the electrode materials deposited; arrays of high-aspect ratio lithium-ion and zinc-air electrodes [Chamran, *et al.*, 2004] have also been demonstrated.

Similar to Dunn's work, Ripenbein, *et al.* used silicon substrates as molds for the patterning of electrode posts. Trenches were etched onto both sides of a silicon substrate using a deep reactive-ion etching (DRIE) process, and then the mold was made porous and electronically insulating through a metal-assisted etching and oxidation process [Ripenbein, *et al.*, 2009]. The resulting porous silicon partition serves multiple purposes, acting as a mold and physical separator between the anode and

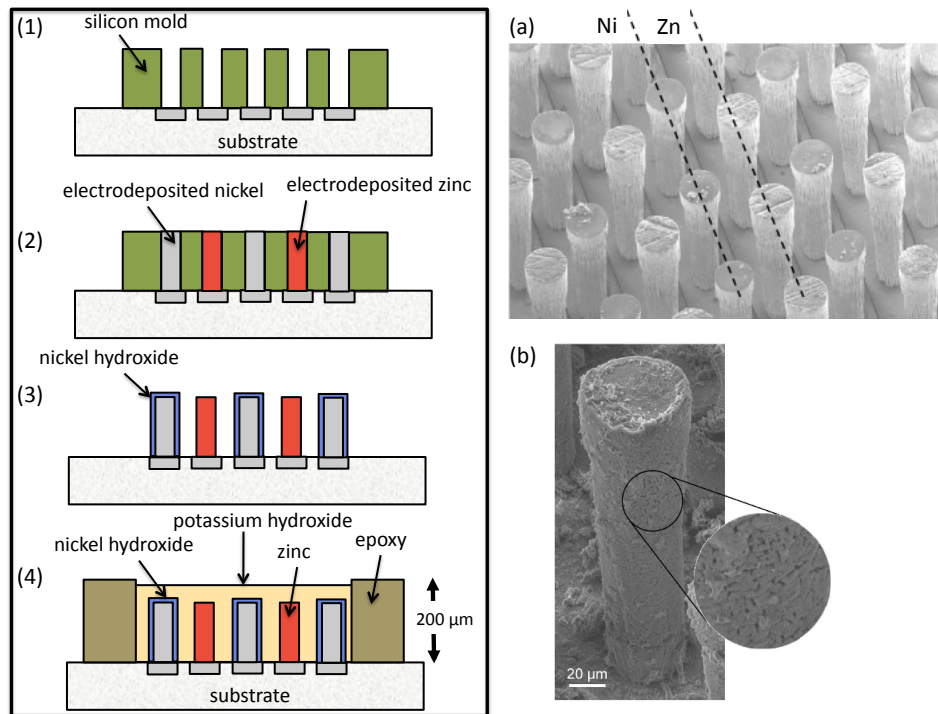


Figure 1.22. (left) Fabrication process of interdigitated Ni-Zn post electrode microbattery. (1) Silicon mold is micromachined with high aspect ratio trenches (2) nickel and zinc are selectively electrodeposited into the mold (3) silicon mold is removed and nickel hydroxide is conformally coated onto the nickel electrodes (4) microbattery is defined by epoxy walls and filled with aqueous alkaline electrolyte. (right) Micrographs of (a) the nickel and zinc electrodeposited posts and (b) a nickel post; (c) a nickel post coated with nickel hydroxide [Chamran, *et al.*, 2006].

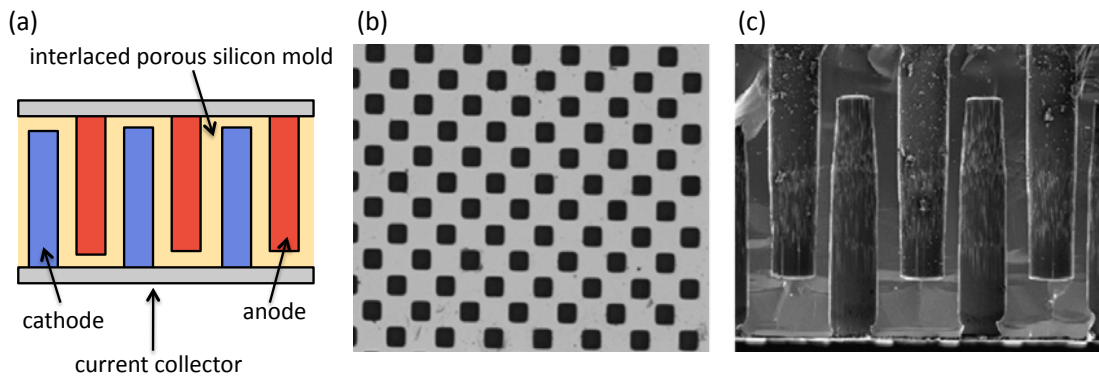


Figure 1.23. (a) Interlaced electrode rods separated by a porous silicon mold. (b-c) Top and cross-section views of the silicon mold [Rippenbein, *et al.*, 2009].

cathode structures, and also providing a porous network for a liquid or gel electrolyte (Figure 1.23). By etching trenches on both the top and bottom of the wafer, an interlaced geometry of electrode arrays was formed. By isolating the arrays, elaborate masking processes during electrode deposition can be avoided. The researchers developed a silicon porous partition with 8265 trenches/cm<sup>2</sup>, and plan to fill the trenches with MoO<sub>2</sub>, LiCoO<sub>2</sub>, or LiFePO<sub>4</sub> cathode materials and lithiated graphite anodes. Though full microbatteries have not yet been demonstrated, the researchers are optimizing the fabrication process to be compatible with more materials and to control properties such as pore morphology.

Interdigitated lithium-ion electrode arrays were also fabricated by Min *et al.* using carbon-microelectromechanical systems (C-MEMS) fabrication, a versatile process for patterning carbon structures and tailoring their materials properties [Min, *et al.*, 2008]. Photoresist is patterned using photolithography, then pyrolyzed under specific conditions [Taherabadi, *et al.*, 2004 and Wang, *et al.*, 2005]. Carbon posts of 65 μm height and aspect ratios ranging between 1 - 4 were fabricated into 120 by 120 arrays in a 1 cm<sup>2</sup> footprint area (Figure 1.24). Alternating rows of carbon posts became current collectors to electropolymerized coatings of polymer cathode material (dodecylbenzenesulfonate-doped polypyrrole or PPYDBS) while bare carbon posts were used as anodes, and when submerged in a liquid electrolyte, the interdigitated microbattery exhibited a capacity of 10.6 μAh/cm<sup>2</sup> when cycled between 0.7 – 3.5 V. Reported difficulties with the shorting between posts as well as high internal resistances measured in the carbon current collectors may have led to poor cycling behavior and reduced capacity.

By using a unique drop-on-demand ink jet printing system, Ho, *et al.* fabricated interdigitated zinc – silver oxide microelectrode arrays without the use of templates or surface patterning, eliminating the many fabrication steps typically associated with subtractive photolithography and etching processes [Ho, *et al.*, 2009]. The super ink jet (SIJ) printer used in this work is able to eject droplets of nanoparticle solutions three orders of magnitude smaller in volume than commercial ink jet printers, resulting in submicron printed feature sizes [Murata, *et al.*, 2005]. As a SIJ drop is ejected, its reduced volume facilitates rapid solvent evaporation so that when deposited, the droplet

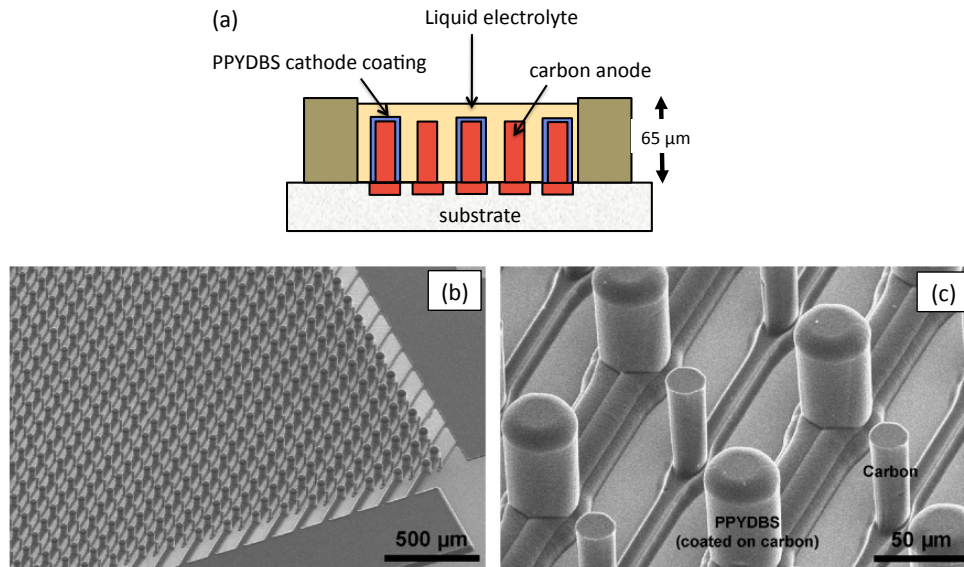


Figure 1.24. (a) Schematic of a C-MEMS fabricated interdigitated electrode post array of pyrolyzed carbon anodes and polymer cathode coatings of dodecylbenzenesulfonate- doped polypyrrole (PPYDBS). Micrographs (b-c) show an array of interdigitated carbon anodes and thick polymer coated cathodes [Min, *et al.*, 2008].

viscosity is so high that the printed ink is essentially dry, enabling the fabrication of 3D structures [Murata, 2007]. With the precise deposition of a succession of ink droplets, 10  $\mu\text{m}$  diameter – 40  $\mu\text{m}$  length pillars of silver were printed. Pairs of 3 mm by 3 mm electrode arrays, each with 722 pillars each were printed adjacent to each other and then submerged in an alkaline electrolyte solution with dissolved zinc oxide. Upon applying an electric field across the pair of silver electrode arrays, silver oxidizes on the positive electrode while the negative electrode acts as a current collector on which zinc electrodeposits from the electrolyte; essentially a zinc-silver oxide microbattery is assembled in its charge state (Figure 1.25). Though the configuration of the electrodes was not optimal, performance was enhanced significantly by the 3D structure. An areal capacity and energy density of 2.5  $\text{mAh}/\text{cm}^2$  and 3.95  $\text{mWh}/\text{cm}^2$  were measured, respectively, for operating potentials between 1.2 – 2 V. Implementing an interdigitated structure, increasing the density of pillars, and stabilizing the zinc electrode in the electrolyte solution can generate substantial improvements in performance.

Some of the most advanced 3D microbattery research efforts have utilized the interdigitated electrode architectures discussed in this section, and have been very convincing in demonstrating the inherent benefit of implementing non-planar microbattery configurations. Continued modeling and investigation are needed, including the consequences of the novel geometries on non-linear current and potential distributions, and an understanding of the materials stability and cycle life of the cells. Such efforts will ultimately be critical in demonstrating the viability of these new microbattery architectures.

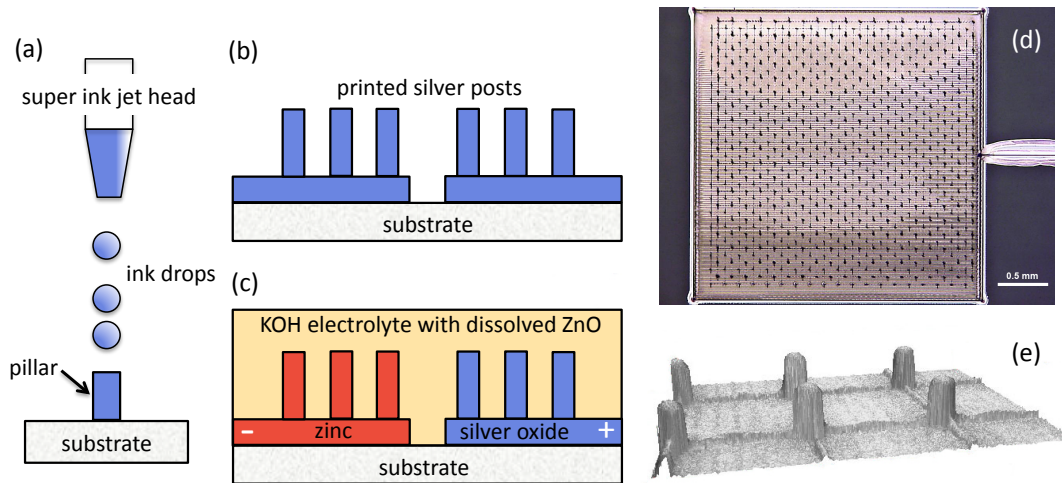


Figure 1.25. Super ink jet printed Zn-Ag<sub>2</sub>O post electrode arrays. (a-b) silver pillars are printed on a substrate. (c) When submerged in an alkaline electrolyte with dissolved zinc oxide, an applied electric field causes silver to oxidize at the positive electrode while zinc electrodeposits on the negative electrode, assembling a microbattery in its charged state. Micrographs of (d) an electrode array and (e) printed silver posts [Ho, *et al.*, 2009].

### Concentric Microbattery Array

Conformal-coated electrode arrays and interdigitated electrode architectures appear similar in configuration, however the former incorporate one electrode phase that is continuous through the structure. By implementing a concentric configuration of electrodes and electrolyte layers, simple 1D current and potential distributions are achieved through the individual concentric structures, and the electrochemical behavior can be assumed to resemble that of stacked 2D battery configurations. As a result, a 3D microbattery with this concentric architecture relies on the composite performance of many small concentric microbatteries. Though essentially simple in concept, the feasibility of fabricating such architectures has been difficult, and demonstration efforts remain in their infancy.

Nathan, *et al.* employed 2D microbattery techniques for deposition onto textured surfaces, sequentially depositing thin conformal films onto substrates modified with 3D features [Nathan, *et al.*, 2005]. By perforating silicon or glass substrates with micro-scale channels, the available surface area was enhanced an order of magnitude. 0.5 mm thick silicon substrates with 50  $\mu\text{m}$  diameter microchannels were conformally coated with thin films of a nickel current collector, MoS<sub>2</sub> cathode, and hybrid polymer electrolyte, and then back-filled with a graphite slurry (Figure 1.26). The cells displayed an operating voltage of 1.5 V and over more than a 200 cycles, capacities of 2 mAh/cm<sup>2</sup> were measured with high Faradaic efficiency, about 30 times greater than a 2D battery with the same chemistry and footprint area. Further improvements in conformal deposition techniques and materials properties have been explored [Golodnitsky, *et al.*, 2006]. Despite fabrication difficulties, this architecture offers a few advantages: though the discrete microbatteries were arranged in a periodic array in this work, the periodicity is not required since the individual concentric microbatteries presumably do not interact



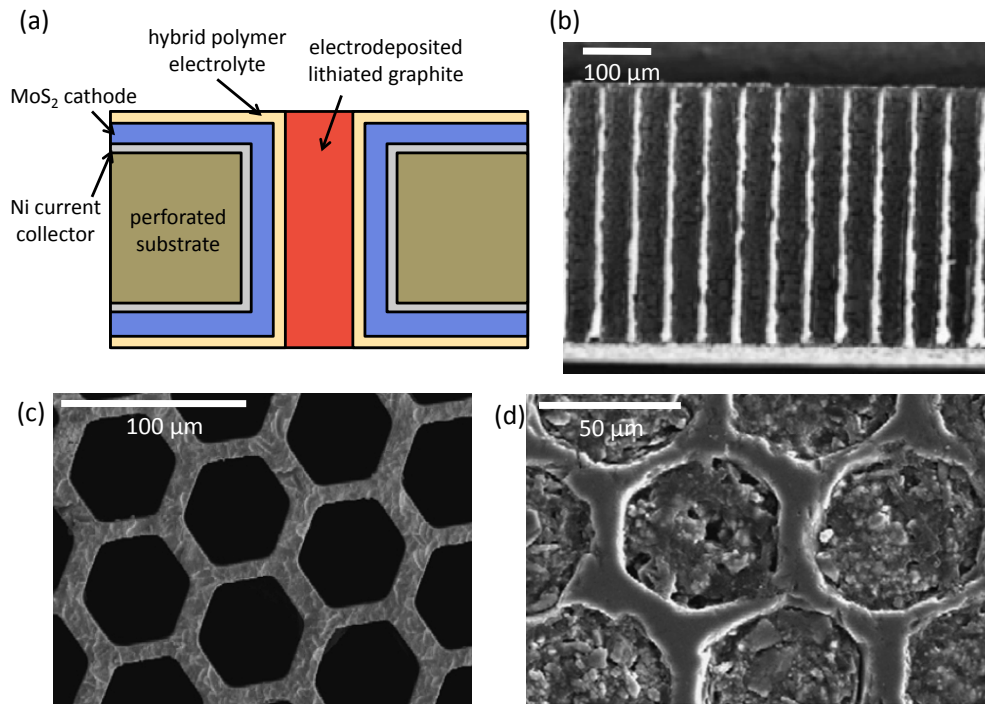


Figure 1.26. Concentric battery (a) schematic of the cross section of a perforated substrate with high aspect ratio holes that are conformably coated with continuous, thin films of current collector, cathode, and electrolyte layers. The anode is back-filled into the open volume. (b,c) Micrographs of the perforated substrate and (d) 3D enhanced microbattery with graphite filled microchannel volume [Nathan, *et al.*, 2005 and Golodnitsky, *et al.*, 2006].

with each other. Also, the energy density of the microbattery can be optimized by occupying the larger, continuous electrode phase with the electrode material of less theoretical volumetric capacity.

### 1.4.2 3D Microbattery Architectures With Continuous Elements

All microbattery configurations discussed in the next section have continuous electrode and electrolyte phases. These components may be arranged in regular patterns, examples of which are illustrated in Figure 1.21 a and b, or in aperiodic, undirected configurations, as shown in Figure 1.21 c. By having continuous electrodes, as long as they have sufficient electrical conductivity, applying current collectors to these structures may be less challenging since the electrodes need only be accessed at one point rather than throughout the whole structure.

#### 3D Enhanced Thin Film Microbatteries

The prospect of using silicon-compatible fabrication methods to concurrently integrate microbatteries with MEMS sensors or energy harvesting components onto the same substrate has encouraged researchers to extend the capabilities of thin film processes and develop complementary methods to fabricate 3D geometries. Niessen, *et al.* textured silicon substrates with high aspect ratio trenches and pores [Niessen, *et al.*, 2008 and Baggetto, *et al.*, 2009]. By successively depositing thin films of silicon, Lipon glass electrolyte, and  $\text{LiCoO}_2$  onto patterned silicon substrates with trenches 135  $\mu\text{m}$  deep and

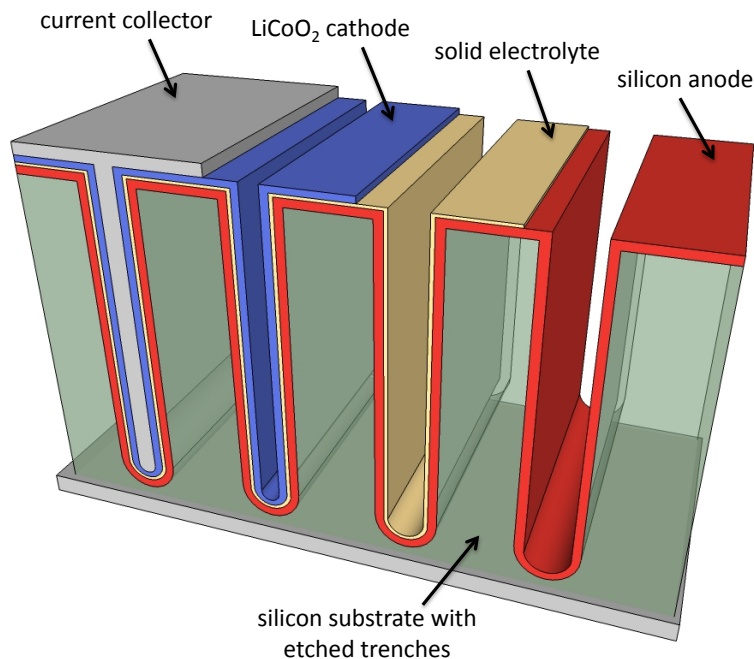


Figure 1.27. Schematic of textured silicon substrate conformably coated with a lithium-ion thin film battery layers [Niessen, et al., 2008].

5  $\mu\text{m}$  in width, a 3D microbattery with an operating voltage of 3.5 V and projected capacity and energy density of 1.5  $\text{mAh}/\mu\text{m}^2$  and 5  $\text{mWh}/\mu\text{m}^2$ , respectively, should be achievable (Figure 1.27). Efforts towards a working demonstration include fabrication and deposition improvements, an understanding of the silicon electrochemical behavior upon repeated cycling, and integration efforts to enable top and bottom substrate texturing to further increase the energy storage capacity. Since 3D silicon morphologies are of interest to a variety of other research fields such as thermoelectric and sensor devices [Paul, *et al.*, 2007], ongoing improvements in 3D micropatterning continue to increase the viability, cost-effectiveness, and appeal of fabricating 3D microbatteries using patterned substrates coupled with thin film deposition processes.

### Interpenetrating Microbatteries

The performance enhancements gained by incorporating nanostructured materials into electrochemical devices have been profound. Nanostructured materials have already been shown to significantly increase the electrochemical properties of 2D macrobatteries, and Ergang, *et al.* further exploited this phenomenon by patterning nanostructured electrochemical materials into 3D microbattery architectures [Ergang, *et al.*, 2007]. Patterned monoliths of carbon anode material were fabricated by dispersing colloidal poly(methyl methacrylate) (PMMA) spheres with 200 nm diameters in a precursor solution, which is then carbonized. The resulting three-dimensional ordered macroporous (3DOM) carbon electrode monolith served as a template for an interpenetrating microbattery. It was conformably coated by an electrodeposited pinhole-free poly(phenylene oxide) polymer electrolyte that was soaked in a liquid lithium salt solution, and then any free volume was infiltrated by vanadium pentoxide ( $\text{V}_2\text{O}_5$ )

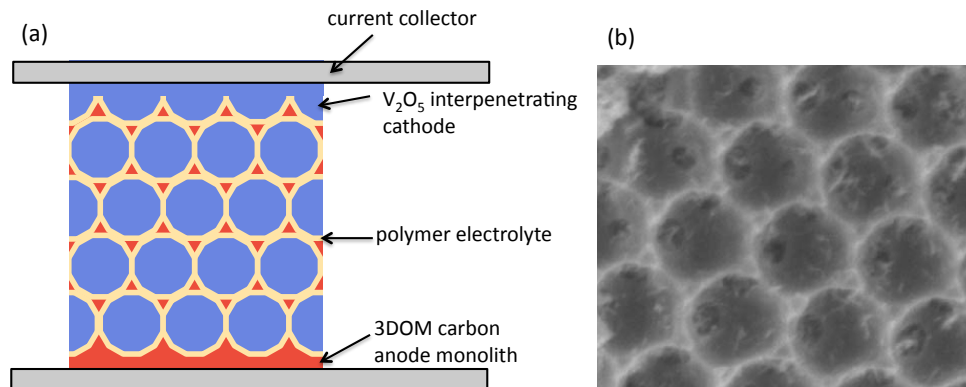


Figure 1.28. (a) Three-dimensional interpenetrating lithium-ion microbattery. A three-dimensional ordered macroporous (3DOM) carbon anode monolith is coated with a polymer electrolyte film, then (b) back-filled with a vanadium pentoxide ambigel cathode [Ergang, *et al.*, 2007].

ambigel cathode precursors. Subsequent careful ageing and removal of residual solvent was necessary to maintain the nanostructure of the vanadia ambigel. Finally, the interpenetrating 3D microbattery was manually sandwiched between two foil current collectors (Figure 1.28). For a microbattery occupying  $0.26 \text{ cm}^2$  footprint area and thickness of  $0.1343 \text{ cm}$ , when cycled between  $1.6 - 3.3 \text{ V}$ , a gravimetric capacity of  $350 \mu\text{Ah/g}$  was reported, resulting in an estimated areal capacity of  $25 \mu\text{Ah/cm}^2$ . Improved cathode and electrolyte materials properties may be achieved with processing improvements, however the largest difficulty has been increasing the electrical conductivity of the  $\text{V}_2\text{O}_5$  cathode.

Rolison, *et al.* have been developing a microbattery composed of networks of nano-scale interpenetrating electrodes and electrolyte structures engineered without periodicity constraints [Rolison, *et al.*, 2009 and Long, *et al.*, 2007]. The authors suggest that eliminating the periodic arrangement of battery components will reduce processing complications, especially since the self-assembly of nanodimensioned aperiodic sponge structures has been extensively demonstrated using simple solution processes such as sol-gel synthesis. A sponge structure, in this case an aerogel material, is used as one electrode that provides continuous scaffolding on which a thin electrolyte can be conformably deposited. The remaining open volume defined by the extensive network of pores throughout the electrolyte-covered electrode scaffolding is infiltrated with a continuous phase of the opposing electrode, forming a microbattery (Figure 1.29). So far aerogel electrodes of  $\text{MnO}_2$  covered in  $10 - 100 \text{ nm}$  electrodeposited poly(phenylene oxide) (PPO) polymer electrolyte were fabricated, and reversible lithium-ion intercalation and de-intercalation into and from  $\text{MnO}_2$  have been demonstrated through the thin electrolyte layer. Ruthenium oxide ( $\text{RuO}_2$ ) electrode colloids were back-filled into the pore volume of the structure using cryogenic methods, however difficulties ensuring good interfacial contact between the electrolyte and  $\text{RuO}_2$  electrode and electrically accessing this electrode have prevented full battery operation. Progress towards developing a full microbattery will only be possible with effective methods to evenly coat pin-hole free polymer films on 3D surfaces without occluding pores, enhanced electronic conductivity of the electrode materials, and successful infiltration of the final electrode within the open

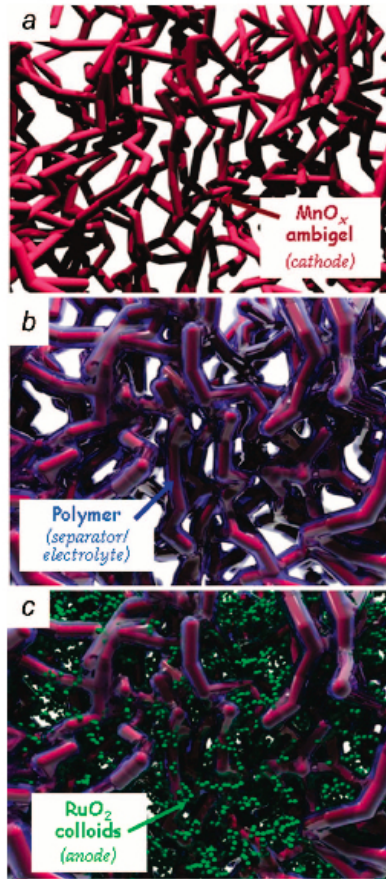


Figure 1.29. Aperiodic sponge microbattery assembled from (a) a manganese oxide cathode ambigel coated with a (b) continuous polymer electrolyte and back-filled with (c) ruthenium oxide anode material [Rolison, *et al.*, 2009].

volume of the sponge structure without damaging the scaffold. Architectures with interpenetrating “tricontinuous” components are promising structures for augmenting the areal storage capacity of microbatteries. New compelling concepts to implement percolating 3D battery structures are continually being proposed and demonstrated, such as the self-assembly of batteries from electrode colloids via their attractive and repulsive surface forces in a continuous electrolyte phase [Cho, *et al.*, 2007]. Complementary characterization techniques and device modeling for these structures will be needed for further maturation of the field.

### 1.4.3 Prospects for Three-Dimensional Microbattery Implementation

The ever-expanding field of three-dimensional microbattery research has provided extensive opportunities for truly architecting innovative battery structures, materials design, and new fabrication processes. Promising research efforts in the 3D microbattery field are summarized in Table 4. As was asserted throughout this section, deeper

understanding of the effects of these novel microbattery architectures on the current and potential distributions within the cell, interfacial reaction kinetics, modes of failure, and overall device performance will require new research including processing, characterization, and modeling capabilities. Though commercial viability is far from realization, important concerns that are often overlooked regarding packaging, environmental robustness and stability, as well as process scalability and cost should all be thoughtfully considered.

Table 1.4. Three-dimensional microbattery demonstrations and performance summary

	<i>Fabrication methods</i>	<i>Chemistry</i>	<i>Geometry*</i>	<i>Operating Voltage (V)</i>	<i>Areal Performance for 1 cm<sup>2</sup> footprint**</i>
<i>3D microbattery architectures with at least one discontinuous element</i>	<i>Interdigitated electrode array microbattery</i>				
	Removable silicon mold, electrodeposited rods	Ni-Zn, liquid electrolyte	(d) 50 $\mu\text{m}$ (l) 400 $\mu\text{m}$ (f) 0.25 $\text{cm}^2$	1.3 – 1.8	2.5 $\mu\text{Ah}$ ; 4 $\mu\text{Wh}$ (measured)
	Interlaced trenches in porous silicon mold	Li-ion, liquid electrolyte	(w) 50 $\mu\text{m}$ (l) 290 $\mu\text{m}$ (n) 8,265 (f) 1 $\text{cm}^2$	3 – 4	Cycling through porous silicon material demonstrated
	C-MEMS fabricated rods	Li-ion, liquid electrolyte	(d) 20 $\mu\text{m}$ (l) 65 $\mu\text{m}$ (n) 14,400 (f) 1 $\text{cm}^2$	0.7 – 3.5	10.6 $\mu\text{Ah}$ ; 31 $\mu\text{Wh}$ (measured)
	Super ink jet printed rods	Zn-Ag <sub>2</sub> O, liquid electrolyte	(d) 10 $\mu\text{m}$ (l) 40 $\mu\text{m}$ (n) 722 pillars (f) 0.9 $\text{cm}^2$	1.2 – 2	2.5 $\text{mAh}$ ; 3.95 $\text{mWh}$ (measured)
	<i>Concentric microbattery array</i>				
	Thin film-coated concentric rod array	Li-ion, hybrid polymer electrolyte	(d) 50 $\mu\text{m}$ (l) 0.5 $\text{mm}$ (f) 5.3 $\text{cm}^2$	1.3 – 2.2	2 $\text{mAh}$ ; 3 $\text{mWh}$ (measured)
<i>3D microbattery architectures with continuous elements</i>	<i>3D enhanced thin film microbatteries</i>				
	Thin film coated textured substrate	Li-ion, glass electrolyte	(w) 5 $\mu\text{m}$ (l) 130 $\mu\text{m}$ (f) 1 $\text{cm}^2$	3 – 4	1.5 $\text{mAh}$ ; 5 $\text{mWh}$ ; 50 $\text{mW}$ (predicted)
	<i>Interpenetrating microbattery structures</i>				
	Templated ordered scaffold	Li-ion, polymer electrolyte	(t) 0.1343 $\text{cm}$ (f) 0.26 $\text{cm}^2$	1.6 – 3.3	25 $\mu\text{Ah}$ ; 60 $\mu\text{Wh}$ (measured)
Aperiodic “sponge”	Li-ion, polymer electrolyte	10 $\text{nm}$ thin electrodeposited polymer	N/A	Inserted/removed Li ions from polymer-coated cathode at 2C rate	

\*d: element diameter, l: element length, w: element width, n: number of elements, t: thickness of device, f: footprint area of device

\*\* if provided, areal capacity, energy density and power density are listed

## 1.5 Electrochemical Microcapacitors

With ongoing improvements in materials performance and processing, electrochemical capacitors have also become viable energy storage buffers for autonomous wireless sensors. Alone, electrochemical capacitors are limited in energy density compared to batteries, but may be appropriate for scenarios requiring frequent, high power pulse operation such as in emergency response applications, which rely on rapid real-time information. Electrochemical capacitors can also be considered complementary technology when used with batteries for applications requiring larger energy storage capacity, and if used in conjunction, the capacitor can address high power surges demanded from the load, effectively mitigating detrimental battery operation and therefore increasing the battery's and consequently the device's lifetimes.

Largely overshadowed by microbattery research, microcapacitors have until recently been overlooked, except perhaps to vet fabrication processes developed primarily for microbatteries. This processing compatibility is possible due to their similar configurations and in some cases, identical materials. Like microbatteries, microcapacitors use materials similar to macrocapacitor devices, and implementation of these miniature devices has been explored for both two-dimensional and three-dimensional cell configurations.

### 1.5.1 Electrochemical Capacitor Materials

Electrochemical capacitor research efforts have largely concentrated on the discrete improvements of electrode and electrolyte materials. Typical materials used as electrochemical capacitor electrodes are listed in Table 1.5. Significantly higher capacitance can be achieved by using pseudocapacitive electrode materials. Unlike high surface area carbon electrodes, which derive their storage capacity from the electrostatic arrangement of electrolyte ions along their electrode-electrolyte interfaces, pseudocapacitive materials store energy through Faradaic reactions at these regions. In comparison to battery electrodes, which often undergo irreversible phase changes as a consequence of redox reactions, pseudocapacitive charge and discharge processes are almost reversible within reasonable voltage ranges. In general, pseudocapacitive electrodes provide higher capacitance in exchange for cycle life and power density [Conway, *et al.*, 2003].

To achieve higher cell voltages, complementary electrolytes stable within the operating potential range must be used. Traditionally, most electrochemical capacitors have utilized aqueous electrolytes, however water degrades at high voltages. Non-aqueous electrolytes such as carbonate-based organics and ionic liquids are able to achieve higher cell potentials between 2 to 5 V, but their ion conductivities are at least an order of magnitude less than aqueous solutions. Similar developments seen in microbatteries in solid-state and polymer electrolytes as well as nanostructured materials [Simon, *et al.*, 2008] have also been applied to microcapacitors as well.

Table 1.5. Electrochemical capacitor electrode materials

<i>Mode of energy storage</i>	<i>Capacitor material</i>	<i>Examples</i>	<i>Specific capacitance* (F/g)</i>	<i>Comments</i>
Purely electrostatic	Carbons	Activated carbon	150	Stable, long cycle life inexpensive
	High surface area carbon nanomaterial	Carbon aerogels, fibers, and nanotubes	300	Moderately expensive
Pseudocapacitive	Conductive Polymers	Polyaniline, thiophene-based polymers	300	Inexpensive, unpredictable cycle behavior and stability
	Metal oxides	Hydrous ruthenium oxide	1358	High electrical conductivity, fast charge transport, expensive
		Manganese dioxide, nickel oxide	800	Inexpensive, environmentally friendly, poor electrical conductivity

\* Reported values are maximum reported specific capacitances found in literature (Simon, *et al.*, 2008 and Naoi, *et al.*, 2008]

### 1.5.2 Microcapacitor Prototypes

In the last decade there have been limited demonstrations of capacitors with diminutive geometries ( $< 1 \text{ cm}^2$  footprint area), however working prototypes utilizing thin film microfabrication and direct-write fabrication methods have been reported. Configurations described in the microbattery section, including 2D adjacent pads or interdigitated electrodes, stacked cells, and 3D interdispersed cells have been applied to microcapacitor structures as well. For comparison areal capacitances ( $\text{mF}/\text{cm}^2$ ) with respect to footprint area occupied will be reported.

#### Thin Film Microcapacitors

Thin film supercapacitor (TFSC) research has largely benefited from the advancements of thin film battery research, so trends in electrode and solid-state electrolyte battery materials have largely translated into the TFSC field. Kim, *et al.* [Kim, *et al.*, 2003] demonstrated some of the first TFSCs by incorporating  $5 \mu\text{m}$  stacked configurations (as illustrated in Figure 1.30) of amorphous Lipon ( $\text{Li}_x\text{PO}_y\text{N}_z$ ) solid-state electrolytes with pairs of ruthenium oxide ( $\text{RuO}_x$ ) electrodes, and later with less costly sputtered cobalt oxide ( $\text{Co}_3\text{O}_4$ ) electrodes [Kim, *et al.*, 2001]. Capacitances of  $28.5 \text{ mF}/\text{cm}^2$  and  $13.2 \text{ mF}/\text{cm}^2$ , respectively, were reported. Both TFSC chemistries experienced problematic capacity fade due to structural changes in the thin film electrodes with extensive cycling.

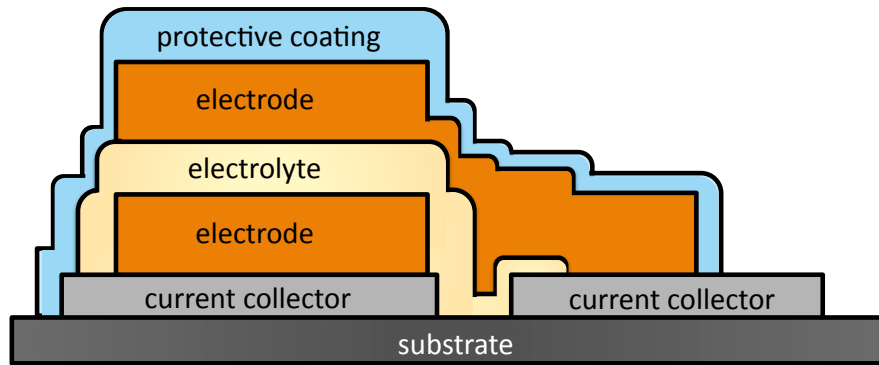


Figure 1.30. Schematic of thin film electrochemical capacitor.

### Origami Microcapacitors

The Nanostructured Origami™ process reported by In, *et al.* [In, *et al.*, 2006] applies 2D planar microfabrication techniques to fabricate structures that are “automatically folded” via strain and Lorentz force actuation into 3D structures (see Figure 1.31). Carbon slurry electrodes and a droplet of liquid electrolyte were manually deposited onto the microfabricated features and folded into stacked capacitor structures. With an aqueous liquid electrolyte, the microcapacitor showed a capacitance of  $0.4 \text{ mF/cm}^2$  when cycled between 0 – 0.6 V. Using this method, a high-density array of capacitors with micro-dimensions could be fabricated, however the feasibility of scaling the folding process to large substrate areas will need to be addressed.

### Direct Write Fabricated Microcapacitors

Because of the versatility and reduced processing complexity required to pattern materials, a few direct write methods have been used to demonstrate both planar and stacked configurations of microcapacitors. Pech, *et al.* [Pech, *et al.*, 2009] used microfabrication methods to pattern interdigitated gold or platinum current collectors on which carbon slurries were ink jet printed (Figure 1.32). Each interdigitated finger was  $40 \mu\text{m}$  and  $400 \mu\text{m}$  width and length, respectively, and spaced  $40 \mu\text{m}$  from each other. The total device occupied a  $2 \text{ mm}^2$  footprint area. In an organic electrolyte the cell was cycled to 2.5 V and achieved  $2.1 \text{ mF/cm}^2$ .

Arnold, *et al.* fabricated microcapacitors with planar configurations utilizing both square and interdigitated electrodes [Arnold, *et al.*, 2003]. Laser direct writing was used to deposit thick film pseudocapacitive ruthenium oxide capacitor electrode slurries using planar configurations. A laser-deposited capacitor film was bisected with a 10 to  $20 \mu\text{m}$  microchannel defined using laser micromachining. With an aqueous liquid electrolyte, the capacitors were cycled up to 1 V and displayed a high areal capacitance of  $320 \text{ mF/cm}^2$ . Capacitors in series and parallel configurations were also demonstrated to exhibit the ability to achieve higher voltages and currents.

Stacked carbon microcapacitors were fabricated by Ho *et al.* using direct write dispenser printing [Ho, *et al.*, 2006]. Layers of activated carbon slurry electrodes and an ionic



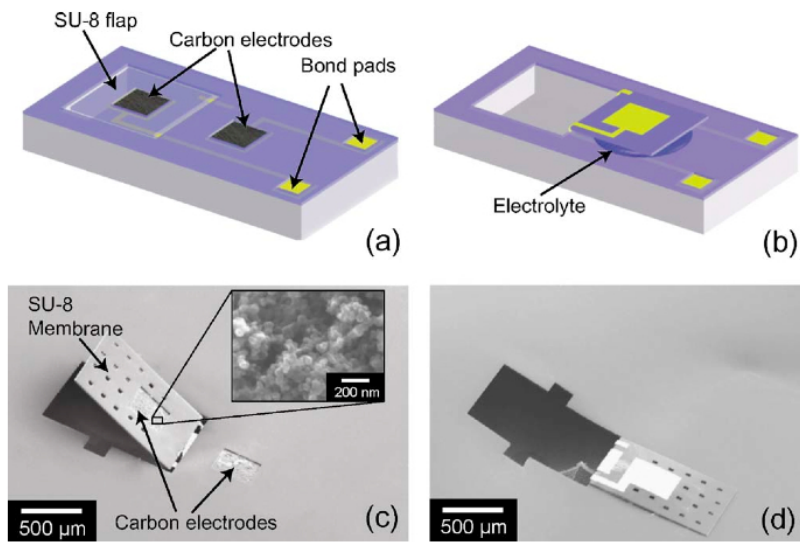


Figure 1.31. Schematics (a-b) and micrographs (c-d) of origami folded supercapacitors [In, *et al.*, 2006].

liquid gel electrolyte were deposited in succession within a 1 cm<sup>2</sup> footprint area and 100-150 μm thickness, as shown in Figure 1.33. The gel electrolyte developed was able to provide physical separation between the electrodes even under significant compression, yet maintain good ion transport. The resulting structure was shown to cycle over 120,000 times up to 2 V and average capacitances ranged from 40-100 mF/cm<sup>2</sup>. This corresponded to a maximum areal energy and power density of 10 μWh/cm<sup>2</sup> and 575 mWh/cm<sup>2</sup>, respectively [Miller, *et al.*, 2009]. Microcapacitors fabricated using simple direct write processes were able to demonstrate some of the highest capacitance performances, largely due to the ability to pattern thick porous electrodes.

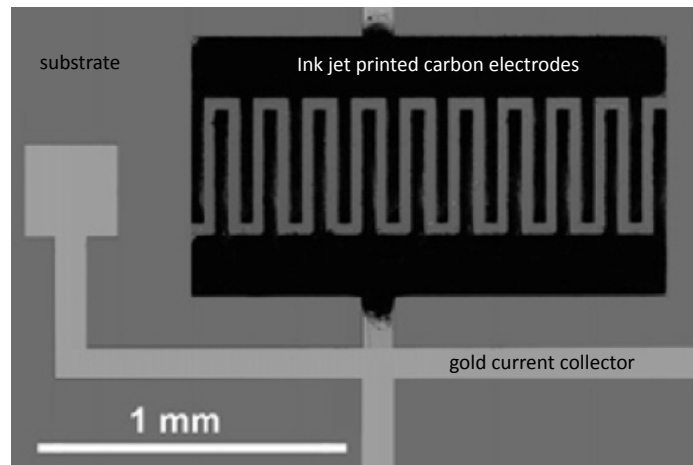


Figure 1.32. Ink-jet printed carbon supercapacitor electrodes on gold, interdigitated current collectors [Pech, *et al.*, 2009].

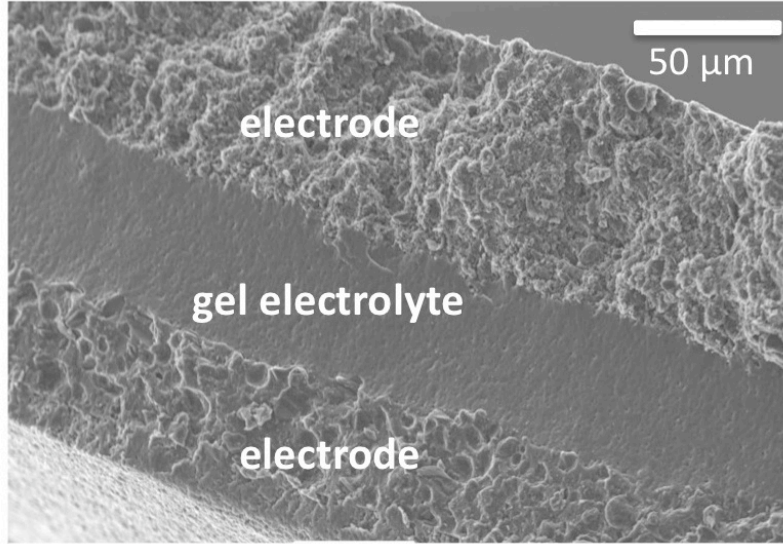


Figure 1.33. Cross section micrograph of a dispenser printed stacked, carbon electrochemical capacitor [Ho, *et al.*, 2006].

### Interpenetrating Microcapacitors

The concept of a sponge-like, 3D, interpenetrating energy storage device developed by Rolison, *et al.* has also been applied to asymmetric hybrid electrochemical capacitors [Rolison, *et al.*, 2009]. Pairing a nanostructured carbon foam anode with an interpenetrating  $\text{MnO}_2$  cathode, electrochemical measurements in an aqueous electrolyte resulted in energy densities of 20 Wh/kg with rapid charge and discharge times of less than 10 seconds (areal capacitance was not reported). Because of the high overpotential of hydrogen evolution achieved at the carbon electrode, the cells were cycled to 2 V, well above the typical water breakdown potential.

### 1.5.3 Conclusions and Prospects for Microcapacitors

The implementations of microcapacitors have for the most part resembled the progress of microbatteries. Continued materials improvements have diminished the gap between achievable battery and electrochemical capacitor energy densities, and fabrication advancements have resulted in the preliminary demonstrations of microcapacitors for integrated micropower supplies, which are summarized in Table 1.6.

Besides the prospects described in this chapter, there are opportunities for even large performance improvements, specifically through accessing higher cell voltages by using two dissimilar electrode materials of either battery or capacitor character. These asymmetric capacitor configurations are known as hybrid electrochemical capacitors [Amatucci, *et al.*, 2001]. By combining a battery cathode with a pseudocapacitive anode, the hybrid electrochemical devices in theory offers the “best of both worlds,” providing high energy density from its battery electrode, yet maintaining high power density

Table 1.6. Electrochemical microcapacitor demonstrations and performance

<i>Fabrication methods</i>	<i>Chemistry</i>	<i>Geometry*</i>	<i>Operating Voltage (V)</i>	<i>Performance</i>
Thin film	RuO <sub>x</sub> , glass electrolyte	(t) 5 μm, stacked	0 – 2	28.5 mF/cm <sup>2</sup>
	Co <sub>3</sub> O <sub>4</sub> , glass electrolyte	(t) 5 μm, stacked	0 – 2	13.2 mF/cm <sup>2</sup>
Origami	Carbon, liquid electrolyte	(f) 0.12 mm <sup>2</sup> , stacked	0 – 0.6	0.4 mF/cm <sup>2</sup>
Ink jet printing	Carbon	(l) 400 μm (w) 40 μm (f) 2 mm <sup>2</sup> planar interdigitated	0 – 2.5	2.1 mF/cm <sup>2</sup>
Laser direct writing	RuO <sub>x</sub> , liquid electrolyte	(t) 15 μm (f) 2 mm <sup>2</sup> planar	0 – 1	320 mF/cm <sup>2</sup>
Dispenser printing	Carbon, gel electrolyte	(t) 100 μm (f) 1 cm <sup>2</sup> , stacked	0 – 2	100 mF/cm <sup>2</sup>
Interpenetrating sponge	MnO <sub>2</sub> , carbon, liquid electrolyte	N/A	0 – 2	350 F/g

\*l: element length, w: element width, t: thickness of device, f: footprint area of full device

through its pseudocapacitive electrode. Achievable energy densities are usually an order of magnitude greater than carbon electrochemical capacitors without significant power density reduction (~1 kW/kg). Future work investigating the operating principles and longevity of this device is necessary, but it seems that the eventual miniaturization of this device could be straightforward.

## 1.6 Conclusion

The need for miniature electrochemical energy storage devices for secondary storage with microenergy harvesting devices has prompted new paradigms in materials, geometry, and processing. As a result, a surge of new research concepts and demonstrations has emerged, especially in the last decade. Both microbatteries and microcapacitors, have been fabricated with a variety of two-dimensional and three-dimensional configurations, and depending on the processing methods developed, a wide-range of materials chemistries has been implemented. Perhaps the numerous endeavors summarized in this chapter indicate that there will not be a single energy storage solution, but rather many appropriate strategies for a diverse number of applications.

## 1.7 References

- Amatucci, G, F Badway, A Du Pasquier, and T Zheng. "An Asymmetric Hybrid Nonaqueous Energy Storage Cell." *Journal of The Electrochemical Society* 148, no. 8 (Jan 2001): A930-A939.
- Arico, Antonino Salvatore, Peter Bruce, Bruno Scrosati, Jean-Marie Tarascon, and Walter Van Schalkwijk. "Nanostructured materials for advanced energy conversion and storage devices." *Nature Materials* 4 (Apr 2005): 366-377.
- Armand, M, and J Tarascon. "Building Better Batteries." *Nature* 451, no. 7 (January 2008): 652-657.
- Arnold, C, P Serra, and A Piqué. "Laser Direct-Write Techniques for Printing of Complex Materials." *MRS BULLETIN* 32 (Jan 2007): 23-31.
- Arnold, C, R Wartena, K Swider-Lyons, and A Pique. "Direct-Write Planar Microultracapacitors by Laser Engineering." *Journal of The Electrochemical Society* 150, no. 5 (Jan 2003): A571-A575.
- Arnold, CB, H Kim, and A Pique. "Laser direct write of planar alkaline microbatteries." *Applied Physics A* 79 (May 2004): 417-420.
- Aurbach, D, I Weissman, A Zaban, and P Danb. "On the role of water contamination in rechargeable Li batteries." *Electrochimica Acta* 45 (Nov 1999): 1135-1140.
- Baggetto, L, et al. "On the electrochemistry of an anode stack for all-solid-state 3D-integrated batteries." *Journal of Power Sources* (Elsevier B.V.) 189 (Jan 2009): 402-410.
- Bates, JB, NJ Dudney, B Neudecker, A Ueda, and CD Evans. "Thin-film lithium and lithium-ion batteries ." *Solid State Ionics* 135 (Nov 2000): 33-45.
- Birke, P, F Salam, S Doring, and W Weppner. "A first approach to a monolithic all solid state inorganic lithium battery." *Solid State Ionics* 118 (Jan 1999): 149-157.
- Chamran, F, H Min, B Dunn, and C Kim. "Three-Dimensional Nickel-Zinc Microbatteries." *Micro Electro Mechanical Systems, 2006. MEMS 2006 Istanbul. 19th IEEE International Conference*, Jan 2006: 950-953.
- Chamran, F, Y Yeh, B Dunn, and Chang-Jin Kim. "3-Dimensional Electrodes for Microbatteries." *Proc. ASME Int. Mechanical Eng. Congress*, 2004: 1-4.
- Chamran, F, Y Yeh, H Min, B Dunn, and C Kim. "Fabrication of High-Aspect-Ratio Electrode Arrays for Three-Dimensional Microbatteries." *Journal of Microelectromechanical Systems* 16, no. 4 (Jan 2007): 844-852.
- Chee, Y.H., et al. "PicoCube: A 1cm<sup>3</sup> Sensor Node Powered by Harvested Energy." *The 45th Annual Design Automation Conference*. 2008. 114-119.

Cho, Young Kyu, Ryan Wartena, Steven M Tobias, and Yet-Ming Chiang. "Self-Assembling Colloidal-Scale Devices: Selecting and Using Short-Range Surface Forces Between Conductive Solids." *Advanced Functional Materials* 17 (Jan 2007): 379-389.

Conway, BE, and WG Pell. "Double-layer and pseudocapacitance types of electrochemical capacitors and their applications to the development of hybrid devices." *J Solid State Electrochem* 7 (Sep 2003): 637-644.

Creus, R, J Sarradin, R Astier, A Pradel, and M Ribes. "The Use of Ionic and Mixed Conductive Glasses in Microbatteries." *Materials Science and Engineering B3* (Oct 1989): 109-112.

Cymbet. <http://www.cymbet.com>.

Dokko, K, J Sugaya, H Munakata, and Kiyoshi Kanamura. "Preparation of micro-dot electrodes of LiCoO<sub>2</sub> and LiTiO<sub>4</sub> for lithium micro-batteries ." *Electrochimica Acta* 51 (Oct 2005): 966-971.

Dokko, K, J Sugaya, H Nakano, T Yasukawa, T Matsue, and K Kanamura. "Sol-gel fabrication of lithium-ion microarray battery." *Electrochemistry Communication* 9 (Apr 2007): 857-862.

Duclot, Michel, and Jean-Louis Souquet. "Glassy materials for lithium batteries: electrochemical properties and devices performances." *Journal of Power Sources* (Elsevier B.V.) 97-98 (Jun 2001): 610-615.

Dudney, N. "Solid-state thin-film rechargeable batteries." *Materials Science and Engineering B* 116 (Jan 2005): 245-249.

Dunn, B., J.W. Long, and D. Rolison. "Rethinking Multifunction in Three Dimensions for Miniaturizing Electrical Energy Storage." *The Electrochemical Society Interface*, no. Fall (2008): 49-53.

Ergang, Nicholas S, MA Fierke, Z Wang, William H Smyrl, and Andreas Stein. "Fabrication of a Fully Infiltrated Three-Dimensional Solid-State Interpenetrating Electrochemical Cell." *Journal of The Electrochemical Society* 154, no. 12 (Oct 2007): A1135-A1139.

Fuller, Joan, Amy C Breda, and Richard T Carlin. "Ionic liquid-polymer gel electrolytes from hydrophilic and hydrophobic ionic liquids." *Journal of Electroanalytical Chemistry* 459 (Jan 1998): 29-34.

Galiński, M, A Lewandowski, and I Stepniak. "Ionic Liquids as Electrolytes." *Electrochimica Acta* 51 (Jan 2006): 5567-5580.

Golodnitsky, D, et al. "Advanced materials for the 3D microbattery." *Journal of Power Sources* (Elsevier B.V.) 153 (Jan 2006): 281-287.

Golodnitsky, D, et al. "Progress in three-dimensional (3D) Li-ion microbatteries." *Solid State Ionics* 177 (Jan 2006): 2811-2819.

Ho, C.C., et al. "Dispenser Printed Electrochemical Capacitors for Power Management of Millimeter Scale Lithium Ion Polymer Microbatteries for Wireless Sensors." *Sixth International Workshop on Micro and Nanotechnology for Power Generation and Energy Conversion Applications*. 2006. 219-222.

Ho, CC, et al. "Technologies for an Autonomous Wireless Home Healthcare System." *Body Sensor Networks*. Berkeley, 2009. 29-34.

Ho, Christine C, K Murata, Daniel A Steingart, James W Evans, and Paul K Wright. "A super ink jet printed zinc-silver 3D microbattery." *Journal of Micromechanics and Microengineering* 19 (Aug 2009): 094013 (5pp).

Hon, K, L Li, and I Hutchings. "Direct writing technology—Advances and developments." *CIRP Annals-Manufacturing Technology* 57 (Jan 2008): 601-620.

Humble, Paul H, and John N Harb. "Optimization of Nickel-Zinc Microbatteries for Hybrid Powered Microsensor Systems ." *Journal of The Electrochemical Society* 150, no. 9 (Jul 2003): A1182-A1187.

Humble, Paul H, John N Harb, and R LaFollette. "Microscopic Nickel-Zinc Batteries for Use in Autonomous Microsystems ." *Journal of The Electrochemical Society* 148, no. 12 (Nov 2001): A1357-A1361.

In, Hyun Jin, Sundeep Kumar, Yang Shao-Horn, and George Barbastathis. "Origami fabrication of nanostructured, three-dimensional devices: Electrochemical capacitors with carbon electrodes." *Applied Physics Letters* 88, no. 8 (Jan 2006): 083104 (pp. 3).

*Infinite Power Solutions*. <http://www.infinitepowersolutions.com/>.

Kötz, R, and M Carlen. "Principles and applications of electrochemical capacitors." *Electrochimica Acta* 45 (Jan 2000): 2483-2409.

Kennedy, John H. "THIN FILM SOLID ELECTROLYTE SYSTEMS." *Thin Solid Films* 43 (May 1977): 41-92.

Kim, Han-Ki, Suk-Ho Cho, Young-Woo Ok, Tae-Yeon Seong, and Young Soo Yoon. "All solid-state rechargeable thin-film microsupercapacitor fabricated with tungsten cosputtered ruthenium oxide electrodes." *J. Vac. Sci. Technol. B* 21, no. 3 (Apr 2003): 949-952.

Kim, Han-Ki, T Seong, J Lim, WI Cho, and Young Soo Yoon. "Electrochemical and structural properties of radio frequency sputtered cobalt oxide electrodes for thin-film supercapacitors." *Journal of Power Sources* (Elsevier B.V.) 102 (Nov 2001): 167-171.

Kushida, K, K Kuriyama, and T Nozaki. "Hundred-micron-sized all-solid-state Li secondary battery arrays embedded in a Si substrate ." *Applied Physics Letters* 81, no. 26 (Dec 2002): 5066-5068.

Lai, W, et al. "Ultrahigh-Energy Density Microbatteries Enabled by New Electrode Architecture and Micropackaging Design." *Advanced Materials* 22 (2010): E1-E6.

- Lewis, Jennifer A, and GM Gratson. "Direct writing in three dimensions." *Materials Today* 7, no. 7-8 (Aug 2004): 32-39.
- Linden, H.D. *Handbook of Batteries*. 2nd Edition. New York: McGraw-Hill, 1995.
- Long, J, B Dunn, D Rolison, and H White. "Three-Dimensional Battery Architectures." *Chem. Rev* 104 (Jan 2004): 4463-4492.
- Long, Jeffrey W, and Debra R Rolison. "Architectural Design, Interior Decoration, and Three-Dimensional Plumbing en Route to Multifunctional Nanoarchitectures." *Acc. Chem. Res.* 40 (Sep 2007): 854-862.
- Meyer, Wolfgang H. "Polymer Electrolytes for Lithium-Ion Batteries." *Advanced materials* 10, no. 6 (Dec 1998): 439-448.
- Miller, Lindsay M, Christine C Ho, Padraic C Shafer, Paul K Wright, James W Evans, and R Ramesh. "Integration of a Low Frequency, Tunable MEMS Piezoelectric Energy Harvester and a Thick Film Micro Capacitor as a Power Supply System for Wireless Sensor Nodes." *Proceedings from IEEE-ECCE*, Jul 2009: 2627-2634.
- Min, H, et al. "Fabrication and properties of a carbon/polypyrrole three-dimensional microbattery." *Journal of Power Sources* (Elsevier B.V.) 178 (Jan 2008): 795-800.
- Murata, K. "Direct Fabrication of Super-Fine Wiring and Bumping by Using Inkjet Process." *Polymers and Adhesives in Microelectronics and Photonic*, Jan 2007: 293-296.
- Murata, Kazuhiro, Junichi Matsumoto, Akira Tezuka, Yorishige Matsuba, and Hiroshi Yokoyama. "Super-fine ink-jet printing: toward the minimal manufacturing system." *Microsystem Technologies* 12, no. 1-2 (Dec 2005): 2-7.
- Nam, K, D Kim, P Yoo, C Chiang, and N Meethong. "Virus-Enabled Synthesis and Assembly of Nanowires for Lithium Ion Battery Electrodes." *Science* 312 (Jan 2006): 885-888.
- Nam, K, et al. "Stamped microbattery electrodes based on self-assembled M13 viruses ." *PNAS* 105, no. 45 (Nov 2008): 17227-17231.
- Naoui, K, and P Simon. "New Materials and New Configurations for Advanced Electrochemical Capacitors." *The Electrochemical Society Interface*, no. Spring (2008): 34-37.
- Nathan, M, et al. "Three-dimensional thin-film Li-ion microbatteries for autonomous MEMS." *Journal of Microelectromechanical Systems* 14, no. 5 (Jan 2005): 879-885.
- Niessen, R, F Roozeboom, and P Notten. "High Energy Density All-Solid-State Batteries: A Challenging Concept Towards 3D ..." *Advanced Functional Materials* 18 (Jan 2008): 1057-1066.
- Ota, Nathan, Spencer Ahrens, Andrew Redfern, Paul Wright, and Xin Yang. "An Application-Driven Architecture for Residential Energy Management with Wireless

Sensor Networks." *Mobile Adhoc and Sensor Systems (MASS), 2006 IEEE International Conference*, Nov 2006: 639-644.

Otis, B, et al. "Modelling and Simulation Techniques for Highly Integrated, Low-Power Wireless Sensor Networks." *IET Computer Digital Technology* 1, no. 5 (2007): 528-536.

Paek, Jeongyeup, Krishna Chintalapudi, Ramesh Govindan, John Caffrey, and Sami Masri. "A Wireless Sensor Network for Structural Health Monitoring: Performance and Experience." *Embedded Networked Sensors, 2005. EmNetS-II. The Second IEEE Workshop*, Nov 2005: 1-10.

Paul, O, J Gaspar, and P Ruther. "Advanced Silicon Microstructures, Sensors, and Systems." *Transactions on Electrical and Electronic Engineering* 2 (April 2007): 199-215.

Pech, David, et al. "Elaboration of a microstructured inkjet-printed carbon electrochemical capacitor." *Journal of Power Sources* (Elsevier B.V.), Sep 2009: 1-4.

Pique, A, C Arnold, H Kim, M Ollinger, and T Sutto. "Rapid prototyping of micropower sources by laser direct-write." *Applied Physics A: Materials Science & Processing* 79 (Jan 2004): 783-786.

Pique, A, et al. "Laser direct-write of miniature sensor and microbattery systems ." *RIKEN Review* 50 (Jan 2003): 57-62.

Prosini, Pier Paolo, Rita Mancini, Lorenzo Petrucci, Vittoria Contini, and Paola Villano. "Li<sub>4</sub>Ti<sub>5</sub>O<sub>12</sub> as anode in all-solid-state, plastic, lithium-ion batteries for low-power applications." *Solid State Ionics* 144 (Sep 2001): 185-192.

Ripenbein, T, D Golodnitsky, M Nathan, and E Peled. "Novel porous-silicon structures for 3D-interlaced microbatteries." *Electrochimica Acta*, Jan 2009.

Rolison, D, et al. "Multifunctional 3D nanoarchitectures for energy storage and conversion." *Chemical Society Reviews* 38 (Jan 2009): 226-252.

Roundy, Shad, Dan Steingart, Luc Frechette, Paul Wright, and Jan Rabaey. "Power Sources for Wireless Sensor Networks." *Proceedings of EWSN 2004, Berlin, Germany*, Nov 2003: 1-17.

Sequeria, C.A.C, and A. Hooper. *Solid State Batteries*. Dordrecht: Martinus Nijhof Publishers, 1985.

Simon, P, and Y Gogotsi. "Materials for electrochemical capacitors." *Nature Materials* 7 (Oct 2008): 845-854.

Singh, P, et al. "Prototype Silicon Micropower Supply for Sensors." *IEEE Sensors Journal* 6, no. 1 (February 2006): 211-222.

Snijders, F. "Ambient Intelligence Technology. An Overview." In *Ambient Intelligence*, 255-270. Berlin Heidelberg: Springer, 2005.



Song, J.Y, Y.Y Wang, and C.C.Wan. "Review of gel-type polymer electrolytes for lithium-ion batteries." *Journal of Power Sources* (Elsevier B.V.) 77 (Feb 1999): 183-197.

Song, Jie, et al. "Solid-state microscale lithium batteries prepared with microfabrication processes." *Journal of Micromechanics and Microengineering* 19 (Mar 2009): 045004 (6pp).

Soo, Philip P, Biying Huang, Young-II Jang, Yet-Ming Chiang, Donald R Sadoway, and Anne M Mayes. "Rubbery Block Copolymer Electrolytes for Solid-State Rechargeable Lithium Batteries." *Journal of The Electrochemical Society* 146, no. 1 (Oct 1999): 32-37.

Steingart, D, C Ho, J Salminen, J Evans, and PK Wright. "Dispenser Printing of Solid Polymer-Ionic Liquid Electrolytes for Lithium Ion Cells." *Polymers and Adhesives in Microelectronics and Photonics, 2007. Polytronic 2007. 6th International Conference, Jan 2007*: 261-264.

Steingart, Daniel A. "Printed On-Chip Electrochemical Storage." PhD Dissertation, Materials Science and Engineering, University of California, Berkeley, 2006.

Sutto, Thomas E, Michael Ollinger, H Kim, CB Arnold, and A Pique. "Laser Transferable Polymer-Ionic Liquid Separator/Electrolytes for Solid-State Rechargeable Lithium-Ion Microbatteries." *Electrochemical and Solid-State Letters* 9, no. 2 (Feb 2006): A69-A71.

Taherabadi, L, G Jia, M Madou, and Y Yeh. "C-MEMS for the manufacture of 3D microbatteries." *Electrochemical and Solid-State Letters* 7, no. 11 (Jan 2004): A435-A438.

Wang, C, G Jia, L Taherabadi, and M Madou. "A novel method for the fabrication of high-aspect ratio C-MEMS structures." *Journal of Microelectromechanical Systems* 14, no. 2 (Jan 2005): 348-358.

Warneke, Brett, Matt Last, Brian Liebowitz, and Kristofer S.J Pister. "Smart Dust: Communicating with a Cubic-Millimeter Computer." *Computer* 44, no. 1 (Sep 2001): 44-51.

West, W C, J F Whitacre, V White, and B V Ratnakumar. "Fabrication and testing of all solid-state microscale lithium batteries for microspacecraft applications." *Journal of Micromechanics and Microengineering* 12 (Dec 2002): 58-62.

Wilson, J, V Bhargava, A Redfern, and P Wright. "A Wireless Sensor Network and Incident Command Interface for Urban Firefighting." *Mobile and Ubiquitous Systems: Networking & Services, 2007. MobiQuitous 2007. Fourth Annual International Conference, Nov 2007*: 1-7.

Winter, M, and RJ Brodd. "What Are Batteries, Fuel Cells, and Supercapacitors? ." *Chem. Rev.* 104, no. 10 (Jun 2004): 4245-4269.

Wright, Paul K, David A Dornfeld, Alic Chen, Christine C Ho, and James W Evans.  
"Dispenser Printing for Prototyping Microscope Devices." *Transactions of NAMRI/SME*.  
2010. 555-561.

# Chapter 2

## Direct write dispenser printing

The need for energy dense microbatteries with miniature dimensions has prompted the development of unconventional materials, cell geometries, and processing methods. As discussed in the previous chapter, a host of new fabrication strategies have been proposed for miniaturizing batteries of footprint areas smaller than 1 cm<sup>2</sup>. For microbatteries requiring substantial energy storage capacities, processing methods capable of depositing thick films of electrode materials within small footprint areas are advantageous. In this work, a direct write dispenser printer is used to fabricate thick film microbatteries. This fabrication tool can precisely pattern multilayer structures and devices onto many substrate materials and configurations. In this work, processing considerations revolving around direct write dispenser printing are bound by the materials and device design constraints. This chapter discusses this printing method and fabrication equipment in detail. Materials properties, especially solution rheologies that are compatible with the dispenser printing process are characterized. Typical materials handling and post-processing procedures implemented are also highlighted. Finally, the dispenser printer's fabrication capabilities are demonstrated.

### 2.1 Printing Process and Equipment

Direct write dispenser printing is a simple and versatile method for additively depositing a variety of materials, including slurries, solutions, and suspensions, generally referred to as "inks." This is a flow-based method of direct write patterning with the ability to deposit inks at room temperature and ambient conditions, all the while generating negligible materials waste and requiring minimal environmental overhead. In comparison to conventional microfabrication techniques, which utilize subtractive processes such as lithography and etching, the number of process steps, energy demanded, and waste generated is significantly less, as illustrated in Figure 2.1. Dispenser printing has been demonstrated to be a flexible prototyping tool with the ability to pattern many materials into diverse two and three-dimensional shapes and devices [Hon, *et al.*, 2008 and Lewis, *et al.*, 2004]. Because of the simplicity of the process, it lends itself to scaling towards mass manufacture.

To pattern a material using the dispenser printer, an ink is loaded into a syringe, extruded through a hollow needle of predetermined dimensions, and written onto a substrate via a

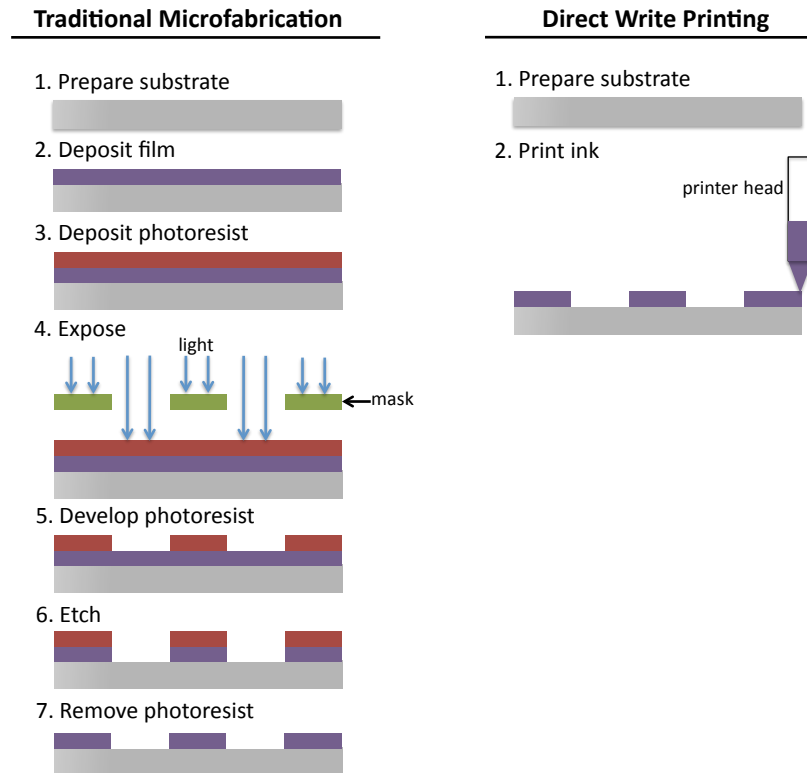


Figure 2.1. A comparison of the processing steps involved in subtractive microfabrication (left) and additive direct write printing (right).

succession of drops, or “shots” as illustrated in Figure 2.2. The drop size is determined by the needle’s dimensions, ink rheology, and applied pressure. The resulting printed film morphology depends on the dimensions of the extruded drops as well as the traversing distance, speed, and time between shots. The motion of the three-axis stage on which the syringe and substrate are mounted along with the pressure applied from a pneumatic controller generates the dimensions and shapes of the deposited films. According to the manufacturer’s specifications, the Newmark Systems NLS4 series stages have  $0.3\ \mu\text{m}$  resolution and  $5\ \mu\text{m}$  repeatability, while the Newmark Systems MSC-M 4-axis stage controller has  $1\ \mu\text{m}$  resolution [Newmark Systems]. Maximum traversing speeds of  $40\ \text{mm/s}$  can be achieved with the automated stages. Pneumatic pressure is applied using a Musashi ML-808FX controller that is capable of  $2 - 50\ \text{kPa}$  output [Musashi Engineering]. Cheap, disposable syringe needles of  $16 - 30\ \text{Ga}$  ( $0.15$  to  $1.35\ \text{mm}$  inner diameter) are used to print the inks; tips with inner diameters as small as  $0.05\ \text{mm}$  can be fabricated by pulling capillary glass tubes using a glass pipette puller. A variety of tips and their needle sizes are photographed in Figure 2.3. With the assortment of needle sizes and wide span of pneumatic pressures that can be applied, the dispenser printer is able to process a variety of inks into a range of printed feature sizes. All the equipment is controlled and automated through custom Java software implemented on a personal computer. A schematic and photograph of the custom dispenser printer is included in Figure 2.4.

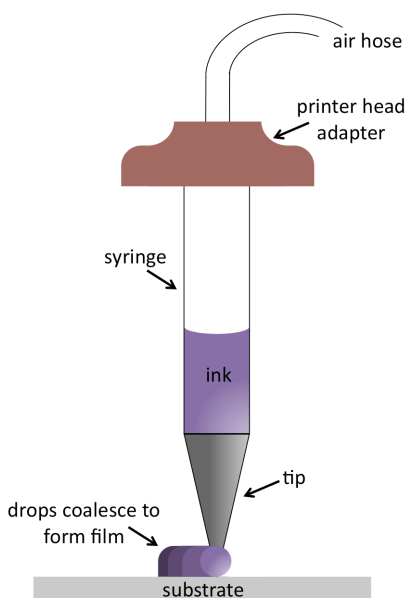


Figure 2.2. Schematic of direct write dispenser printing.

## 2.2 Compatible Materials

Typical inks utilized in this work's printed energy storage devices are either polymer solutions or composite slurries, the former for electrolyte and separator layers while the latter are for electrode and current collector films. The inks are synthesized, mixed thoroughly to form flowing solutions, and then printed, as illustrated in Figure 2.5.

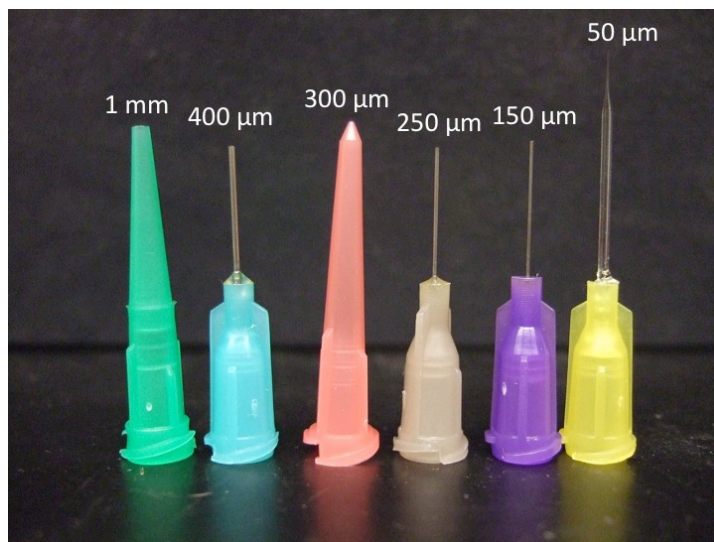


Figure 2.3. Examples of syringe tips and corresponding inner diameter dimensions compatible with dispenser printing.

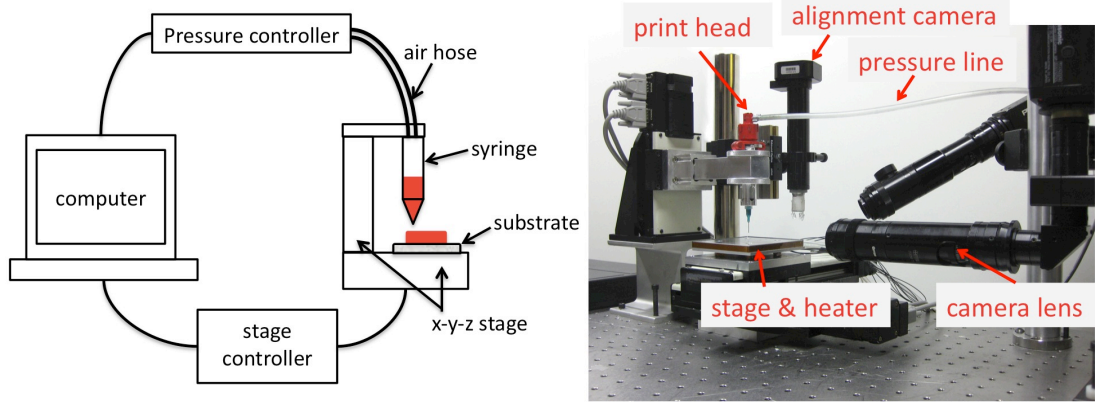


Figure 2.4. (left) Dispenser printer schematic and (right) image of laboratory setup.

Usually a solvent or “vehicle”, which later can be evaporated from the film, is used to tailor the viscosity of the ink. Slurries are typically composed of a polymer, active particles, and if necessary, additives. Efforts to achieve well-mixed inks are often necessary, and rigorous control of powder size distributions and mixing sequences has been implemented. As a general rule, the smallest diameter needle that a slurry can be consistently printed through must be at least an order of magnitude larger than its largest particles. Depending on the ink, preparation may include a combination of ball milling the particles, physical mixing (magnetic stirrers, paint shakers, vibrating surfaces) and ultrasonic mixing (with a water bath or wand).

### 2.2.1 Characterizing Ink Viscosity

The viscosity of a typical slurry and polymer solution are recorded as a response to shear rates applied to the inks in Figure 2.6. The slurry measured for this experiment is a representative formula for a battery electrode, and the polymer solution is composed of a prototypical formula for the gel electrolyte; their recipes are shown in Table 2.1. The viscosities of the inks were measured with respect to varying shear rates applied by a

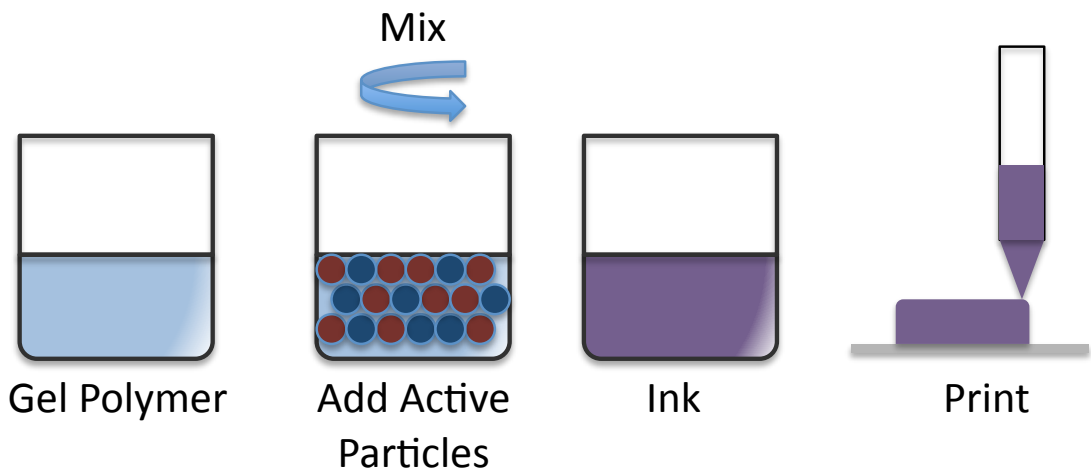


Figure 2.5. Schematic of ink synthesis for dispenser printing.

Table 2.1. Recipes of composite slurry and polymer solution inks used for viscosity studies.

<i>Ink</i>	<i>Components *</i>	<i>Weight Percent (%)</i>
Composite slurry	Mesocarbon microbead (MCMB)	96
	PVDF-HFP polymer binder	4
Polymer solution	Ionic Liquid	50
	PVDF-HFP polymer binder	50

\* Note that the n-methyl-2-pyrrolidone (NMP) was used the “vehicle” solvent, and was added in a 1:10 polymer binder:solvent weight ratio.

Rheometric ARES rheometer [TA Instruments]. The polymer solution displays a relatively constant viscosity for the shear rates applied, demonstrating Newtonian behavior [Poirier, *et al.*, 1994]. For shear rates greater than 0.2 1/s, the composite slurry ink viscosity decreases linearly with increasing shear rate on a log-log plot; this shear thinning behavior is common to the slurries investigated in this work. The minimum and maximum shear rates applied to the ink by the printer are determined and then related to the corresponding dimensions of the printed feature. This was calculated by measuring the flow rate of ink through the smallest and largest syringe tips as a function of applied pressure. The flow rate ( $\text{m}^3/\text{s}$ ) of an ink through a needle is approximated by measuring the volume of ink ( $\text{m}^3$ ) extruded from the syringe for a shot time (s) using the following formula:

$$\text{flow rate} = \frac{\text{ink volume}}{\text{shot time}} \quad (\text{Equation 2.1})$$

The maximum shear rate (1/s) experienced by the ink is then determined by Equation 2.2. A thorough derivation of this expression from the flow through a needle can be found in Section 9.3.1.

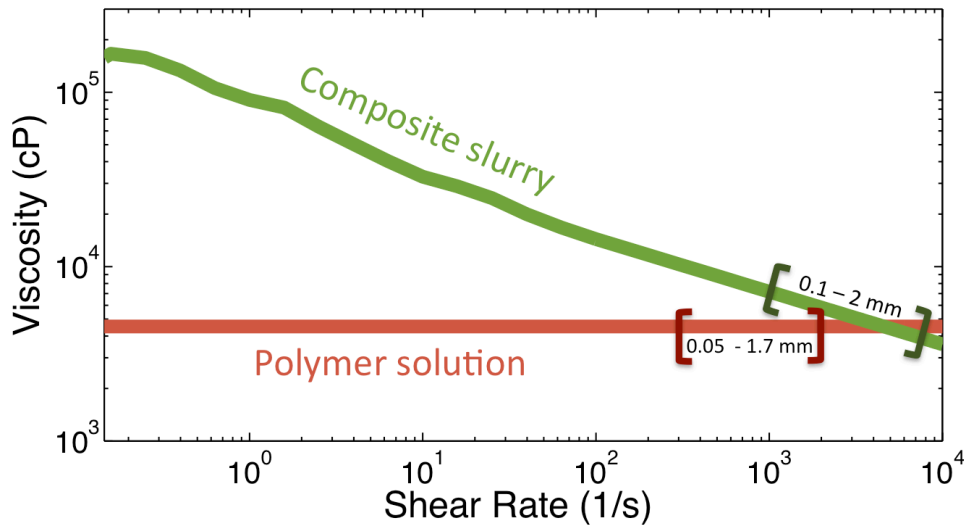


Figure 2.6. Viscosity with respect to applied shear rate for composite slurry and polymer solution inks. The ranges of shear rates and corresponding printed feature sizes applied by the dispenser printer are bracketed for both inks.

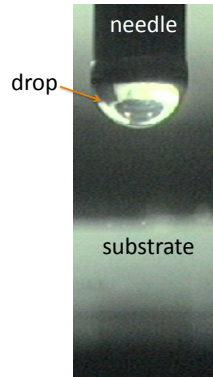


Figure 2.7. Image of drop extruded from dispenser printer needle hovering above substrate.

$$\text{maximum shear} = \frac{4 \cdot \text{flow rate}}{\pi R^3} \quad (\text{Equation 2.2})$$

where R (m) is the inner radius of the cylindrical needle that the ink flows through. For example, for a dispenser shot time of 10 ms and the smallest pneumatic pressure of 20 kPa, the polymer electrolyte solution extruded from a 16 gauge needle was visually recorded with an orthogonally mounted camera, as shown in Figure 2.7, and then the drop volume was determined using image analysis software. The volume of ink was approximated as 1.18 mm<sup>3</sup>, and according to Equation 2.2, the shear rate experienced by the ink under these conditions was 491.9 1/s, resulting in a dot pitch of 150 μm. This experiment was repeated for the smallest and largest gauge disposable needles available that could extrude the ink (between 16 – 30 gauge, respectively), and with the lowest and highest pneumatic pressures applied by the controller. The printing of inks through needles with inner diameters < 150 μm was not studied in this experiment since such small feature sizes were deemed unnecessary for the applications of interest.

A summary of the shear rates calculated for both inks is shown in Table 2.2. From this information, the span of shear rates that can be applied by the dispenser printer was determined and this range is bracketed in Figure 2.6 for both inks, as well as the range of feature sizes the dispenser printer is capable of depositing. Note that Equations 2.1 and 2.2 are only valid for Newtonian fluids, however the calculation serves as an approximation for the printing behavior of the composite slurry ink.

Table 2.2. Shear rates (1/s) applied by the printer for a gel polymer ink extruded through varying needle diameters calculated as a function of the pneumatic controller applied pressure.

<i>Applied pressure (kPa)</i>	<i>Shear rates (1/s) applied by the printer on ink</i>		
	<i>As a function of gauge (needle inner diameter, mm)</i>		
	<i>16 (1.3462)</i>	<i>25 (0.3048)</i>	<i>30 (0.1524)</i>
20	491.91 1/s	916.20 1/s	1710.40 1/s
400	983.81 1/s	1518.90 1/s	1784.20 1/s



## 2.3 Post-processing

A printed film's morphology and ability to adhere to a substrate strongly depend on the drying and post-processing procedures applied to it. Different drying rates between the edges and center of the film can have the adverse affect of causing an uneven distribution of stress and convection across the film while drying, causing particles to disperse irregularly. This phenomenon has been studied previously for dispenser printed films [Ho, *et al.*, 2007]. As a result, an uneven stress distribution may occur through the film, causing it to delaminate from the substrate. To avoid this, meticulous drying procedures are required, and such routines can vary with the ink and the substrate used. Typically printed films are dried at room temperature for 15 minutes, and then 60-90°C for at least 30 minutes, however in some instances, controlled drying is only achieved for films that are dried under vacuum (with and without applied temperature).

## 2.4 Architecting Structures

Compared to other direct write processes which employ kinetic methods of ink deposition such as ink jetting and laser forward transfer, dispenser printing is a gentle contact fabrication method, and with it multiple films can be deposited conformably without mixing between the films. This is an important attribute, especially for patterning multilayer devices such as capacitors and batteries. An illustration of the multilayer printing process for a printed capacitor is shown in Figure 2.8 (a-c). Note that a printed battery utilizes a very similar configuration to capacitors and would be processed similarly. Figure 2.8 (a) shows a porous electrode film formed after drying a printed slurry ink. In Figure 2.8 (b), a gel electrolyte is printed and dried on top of the electrode film. The gel electrolyte film also exhibits a porous structure, but can be differentiated from the electrode film because of its visibly large “grains”: these are polymer pockets swelled with an ionic liquid electrolyte. The interface between the electrode and electrolyte film is indicated on the micrograph. The cross section of a stacked multilayer

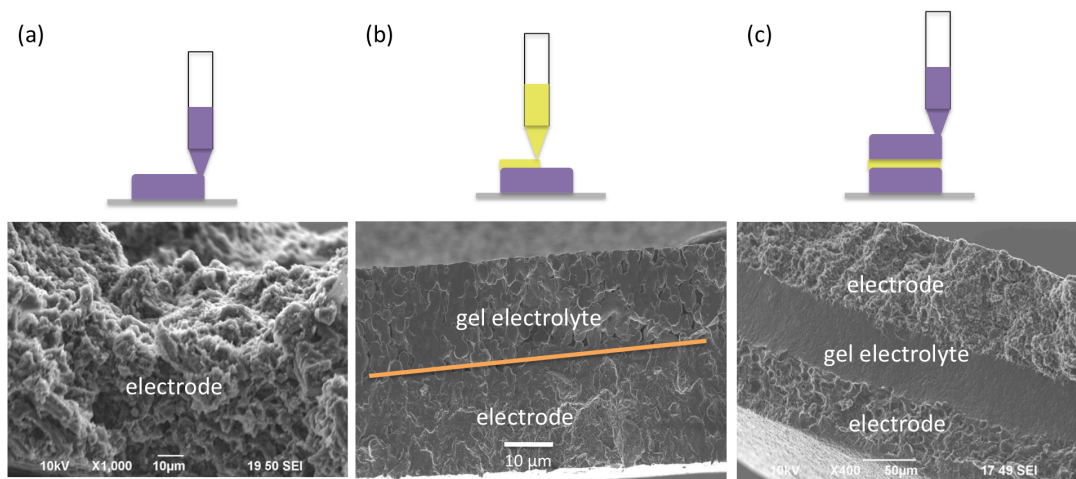


Figure 2.8. (a-c) Dispenser printing procedure for the fabrication of a multilayer device.

structure is displayed in Figure 2.8 (c), with the addition of a top electrode film. In this micrograph, the two interfaces between the electrolyte and electrode films are both visible. It is interesting to compare the porous morphology of the gel electrolyte in Figure 2.8 (b) to that of Figure 2.8 (c); with the addition of the top printed electrode, the gel electrolyte in Figure 2.8 (c) appears dense and relatively smooth. This suggests that with the printing of a subsequent film, the properties of all films underneath may be altered; for example, the gel electrolyte may have become compact or compressed due to the propagation of stresses accumulated in the electrode film while drying. The morphological alterations observed during multilayer printing suggest that the other film properties may also change, including electrical resistivity in the electrode layer and the ion conductivity through the gel electrolyte. The adjustment of these properties can lead to significant performance differences; hence careful studies are needed to understand these changes during the printing process. Besides multilayer structures, the dispenser printer is capable of patterning a diverse number of architectures, as featured in Figure 2.9. As a result it has become a versatile prototyping tool for a variety of devices, including thermoelectric energy harvesters [Chen, *et al.*, 2009] and current sensing MEMS structures [Leland, *et al.*, 2009].

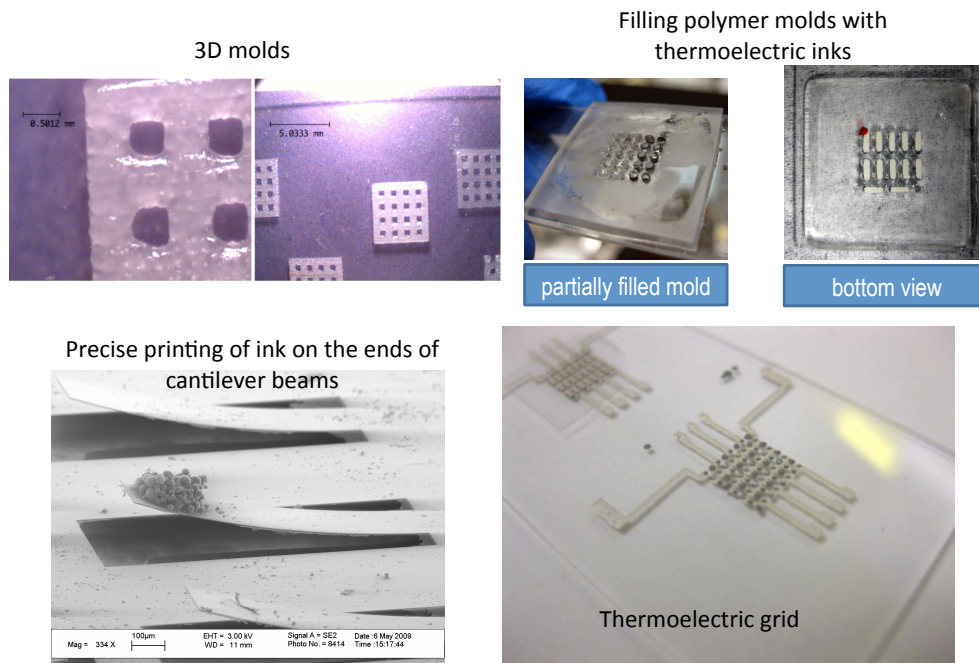


Figure 2.9. (a-d) Other capabilities using dispenser printing including (a) 3D polymer molds, (b) back-filling the molds, (c) precise deposition of magnetic ink on the ends of MEMS cantilever beams [Leland, *et al.*, 2009] and (d) the fabrication of thermoelectric grid devices [Chen, *et al.*, 2009].

## 2.5 Concluding Remarks on Direct Write Dispenser Printing

In this work, a simple solution-based process is leveraged to fabricate highly functional energy storage structures. The printing process is especially conducive to forming multilayer, thick film structures. Because dispenser printing is able to handle such a wide range of materials and is versatile in its functionality, it ultimately is an extremely useful fabrication tool for patterning thick film micro-energy storage systems. Achieving compatibility with this process will inform all future materials and device design considerations.

## 2.6 References

- Chen, A., Madan, D., Koplow, M., Wright, P. K., & Evans, J. W. (2009). Dispenser Printed Thermoelectric Energy Generators. *PowerMEMS*, (pp. 277-280). Washington, D.C.
- Ho, C. C. (2007). *Pneumatic Dispenser Printed Electrochemical Capacitors*. Masters Thesis, University of California, Berkeley, Materials Science and Engineering.
- Hon, K., Li, L., & Hutchings, I. (2008). Direct writing technology—Advances and developments. *CIRP Annals-Manufacturing Technology*, 57, 601-620.
- Leland, E. S., Wright, P. K., & White, R. W. (2009). A MEMS AC current sensor for residential and commercial electricity end-use monitoring. *Journal of Micromechanics and Microengineering*, 19, 094018 (6pp).
- Lewis, J., & Gratson, G. (2004). Direct writing in three dimensions. *Materials Today*, 7 (7-8), 32-39.
- McMaster Carr. (n.d.). From <http://www.mcmaster.com/>: <http://www.mcmaster.com/>
- Musashi Engineering. (n.d.). From <http://www.musashi-engineering.co.jp/>: <http://www.musashi-engineering.co.jp/>
- Newmark Systems. (n.d.). From <http://www.newmarksystems.com/>: <http://www.newmarksystems.com/>
- Poirier, D., & Geiger, G. (1994). *Transport Phenomena in Materials Processing*. Warrendale, Pennsylvania: The Minerals, Metals & Materials Society.
- TA Instruments. (n.d.). From [www.tainstruments.com](http://www.tainstruments.com)

# Chapter 3

## Gel Electrolyte Design and Characterization

For autonomous wireless sensor systems, a printable, thick film microbattery with performance outputs outlined in Chapter 1 is desired. A novel zinc-based battery chemistry that is compatible with dispenser printing has been identified as a potential candidate. To qualify this new battery chemistry, each component must be extensively designed and characterized; then the constituents must demonstrate compatibility with each other. Typical microbatteries contain at least five different materials (two electrodes, current collector(s), electrolyte, and packaging), of which the properties of the electrolyte material can oftentimes be considered most critical to the performance of the system. Along with its transport and mechanical properties, its electrochemical interactions with the electrodes determine a battery's capacity and power. In addition, its materials compatibilities with all other components it is in contact with, including current collectors, substrate, and packaging, are vital to the health of the battery. In this next section, the design and characterization of a printable gel electrolyte material are investigated. The relevant properties of the gel electrolyte constituents, comprising of an ionic liquid electrolyte and polymer binder, are initially optimized, then combined to form a gel electrolyte so that its composite performance can be examined. Its compatibilities with both anode and cathode materials as well as various current collectors are also examined.

### 3.1 Ionic Liquid Electrolytes – an Introduction

In the last decade there has been a renaissance in the use of zinc battery chemistries, which has been motivated by its high volumetric energy and power densities, inherent safety and low toxicity, relative ease in handling, and low cost [Karpinski, *et al.*, 1999]. Alkaline nickel-zinc [Humble, *et al.*, 2001], zinc-silver oxide [Ho, *et al.*, 2009], and zinc-metal oxide [Arnold, *et al.*, 2007] microbatteries have all been demonstrated with varying degrees of implementation and a number of device configurations, including planar, stacked, and 3D interdigitated architectures. The challenges hampering these efforts largely stem from difficulties in achieving repeated recharge predominantly due to unwanted shape changes in the zinc electrode, dendrite formation, and the solubility of reaction products within the alkaline electrolyte [McLarnon, *et al.*, 1991]. Furthermore,

alkaline liquid electrolytes are difficult to handle especially at the microscale because of its corrosive nature and volatility. In this work, an alternative electrolyte chemistry is proposed to avoid these complications.

In the more heavily researched lithium battery field, alternative electrolytes are being explored, with emphasis on solid-like materials for microbattery systems. There has been a surge of interest surrounding novel room temperature ionic liquids, which can potentially be used as the liquid component in a gel electrolyte system. Room temperature ionic liquids are aprotic molten salts at room temperatures with interesting properties such as high ionic conductivity, large electrochemical and temperature stabilities, and negligible vapor pressure [Forsyth, *et al.*, 2004]. Because of these characteristics, room temperature ionic liquids have piqued the interest of many researchers for use in widespread electrochemical applications, including electrodeposition and battery electrolytes [Endres 2002] and [Galiński, *et al.*, 2006]. They can be incorporated into polymers to form gel electrolytes, and in lithium-ion systems they have demonstrated ion transport properties a few orders of magnitude greater than other polymeric or solid-state electrolyte materials. Furthermore gel electrolytes can be designed to be structurally robust so that physical separation between electrodes is maintained even under compression. In the next section, an ionic liquid electrolyte designed to conduct zinc ions is discussed, and its relevant electrochemical properties are explored. This exploration is highly inspired by lithium-based ionic liquid electrolyte research, so when possible any comparisons of any zinc electrolyte properties with that of lithium will be accentuated.

## **3.2 Design of a Zinc Ion Conducting Ionic Liquid Electrolyte**

The electrochemical and transport properties of an ionic liquid electrolyte and its compatibility with a zinc ion conducting battery were investigated. For this work, the 1-butyl-3-methylimidazolium trifluoromethanesulfonate (BMIM<sup>+</sup>Tf<sup>-</sup>) ionic liquid was investigated because of its availability, affordability, and its compatible anion with a zinc salt (zinc trifluoromethanesulfonate), however future research exploring the compatibility of other ionic liquids and salt pairs for this electrochemical system would be extremely valuable; for example, ionic liquids with reduced viscosities and more stable anions could demonstrate significant improvements in performance. The electrochemical properties of the BMIM<sup>+</sup>Tf<sup>-</sup> ionic liquid with zinc salt concentrations varying between 0 – 0.75 M were compared. Note that beyond 0.75 M, the zinc salt was no longer completely soluble in the ionic liquid. In an analogous lithium electrolyte solution, the lithium salt lithium trifluoromethanesulfonate was soluble to approximately 1.4 M concentration in the same ionic liquid.

### **3.2.1 Electrochemical Potential Stability**

An electrolyte is only effective if it is stable within the operating electrochemical potential range of a device. Linear sweep voltammetry (LSV) experiments were performed on each of the ionic liquid electrolytes to determine its electrochemical potential range of stability with respect to a zinc anode. Details of this characterization

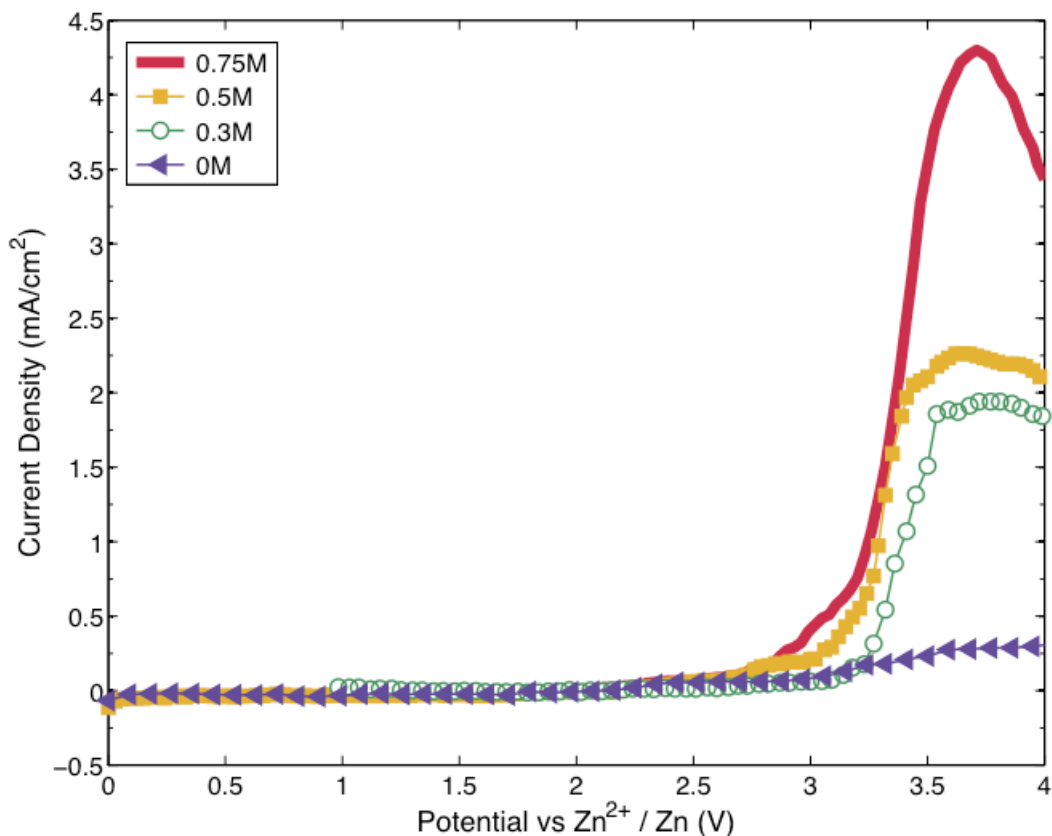


Figure 3.1. Electrochemical potential stability ionic liquid electrolytes with 0 to 0.75 M zinc salt concentrations. The occurrence of a large magnitude current density corresponds to electrolyte decomposition. Scan rate of 5mV/s used with positive polarization direction.

method can be found in Section 9.2.1. By applying a sweeping voltage at a rate of 5 mV/s to a cell containing the ionic liquid electrolyte between zinc and a stainless steel blocking electrode, the electrochemical stability of the electrolyte was determined by monitoring the resulting cell current density (Figure 3.1). The LSV measurement detects the electrochemical breakdown of the ionic electrolyte at the stainless steel blocking electrode with respect to a zinc electrode; the relative electrochemical potential and current density of the electrolyte breakdown are characterized with respect to different electrolyte concentrations. With respect to the zinc electrode, all concentrations showed negligible current densities between 0 and 2.7 V, and therefore all electrolytes can provide the requisite electrochemical stability for a battery operating between the device voltages of 1 – 2 V. The measured current densities of the cells above 2.7 V rose accordingly with the increased zinc salt concentrations of the electrolyte; for the ionic liquids incorporating zinc salt, the current densities exceeded 1 mA/cm<sup>2</sup>.

### 3.2.2 Ionic Electrolyte Transport Properties

#### Ionic Conductivity and Viscosity

Comparisons of the ionic conductivities and viscosities of ionic liquid electrolytes with zinc salt concentrations varying between 0 – 0.75 M are shown in Figure 3.2. The

viscosities of the ionic liquids were measured with a Brookfield DV-III+ with a small sample, small volume adapter [Brookfield]. Ionic conductivity properties were extracted via electrochemical impedance spectroscopy (EIS) measurements of symmetric cells containing the liquid electrolyte sandwiched by two blocking stainless steel electrodes. The neat  $\text{BMIM}^+\text{Tf}^-$  ionic liquid exhibited an ionic conductivity of 3.15 mS/cm. With increased addition of zinc salt to the ionic liquid, a decrease in ionic conductivity was measured. Conversely, the added zinc salt concentration in the  $\text{BMIM}^+\text{Tf}^-$  ionic liquid reduces overall ion mobility in the system, as could be detected with a significant viscosity increase; hence an inverse relationship between the two properties is detected and illustrated in Figure 3.2.

### Zinc Ion Diffusion

Similarly, the electrolytes' zinc ion diffusion coefficients measured using restricted diffusion methods (Ma, Doyle, Fuller, Doeff, Jonghe, & Newman, 1995) showed a diminishing trend with increased zinc salt concentration, as shown in Figure 3.3. This trend can also be attributed to the escalation of electrolyte viscosity with added solute to the system. A comparison of these transport property trends with an analog lithium ion – ionic liquid system can provide additional empirical observations on how the divalent nature and relative size of the zinc ion may affect its behavior in an ionic liquid electrolyte. Note that the lithium electrolyte is solely composed of lithium ions ( $\text{Li}^+$ ), imidazolium-based cations ( $\text{BMIM}^+$ ), and trifluoromethanesulfonate anions ( $\text{Tf}^-$ ); the zinc electrolyte constituents are zinc ions ( $\text{Zn}^{2+}$ ),  $\text{BMIM}^+$  cations, and  $\text{Tf}^-$  anions. The ionic conductivities of the  $\text{BMIM}^+\text{Tf}^-$  ionic liquid with varying concentrations of lithium trifluoromethanesulfonate salt were measured in the same manner described with the zinc

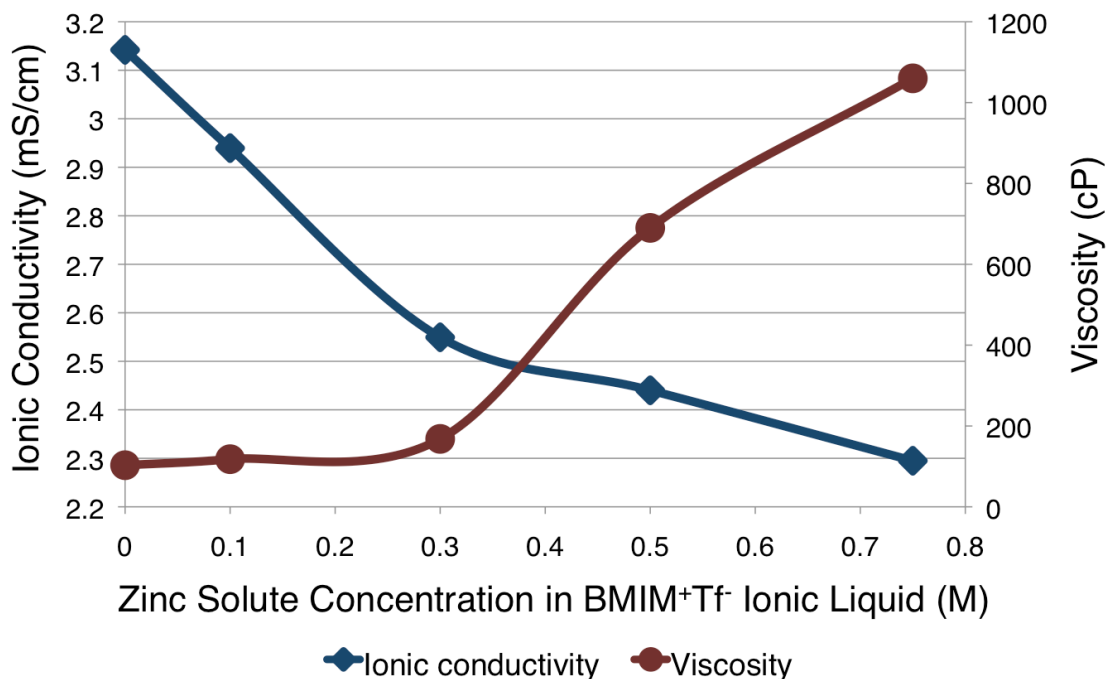


Figure 3.2. The ionic conductivity and viscosity of  $\text{BMIM}^+\text{Tf}^-$  ionic liquid electrolytes as a function of zinc solute concentrations.

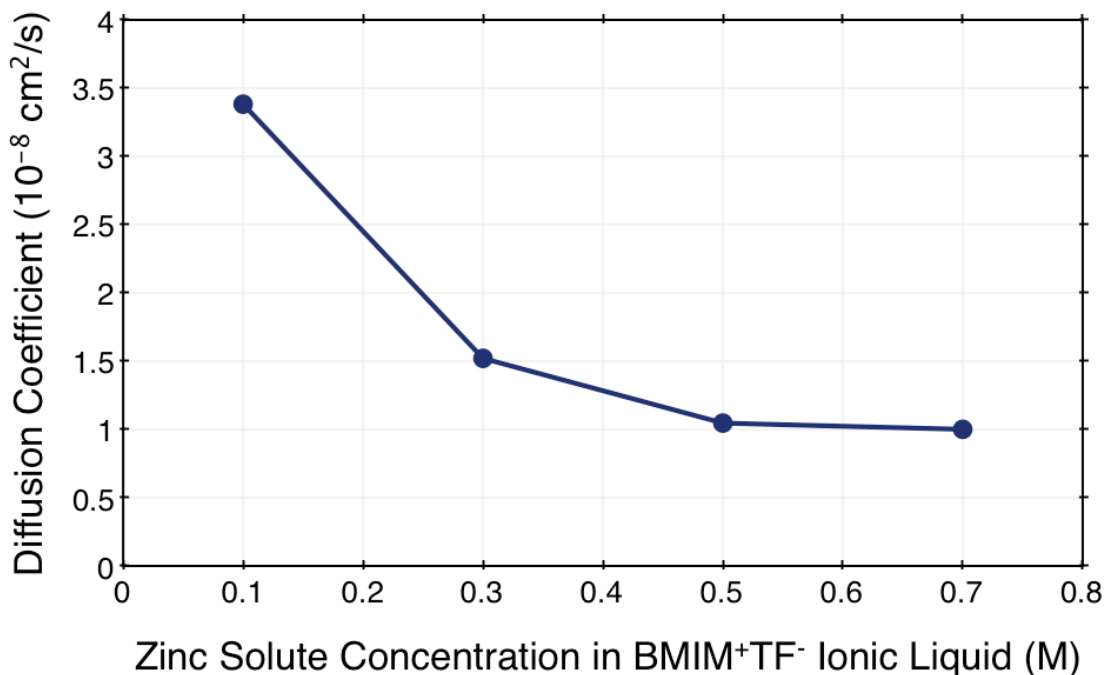


Figure 3.3. The diffusion coefficients of zinc ions in BMIM<sup>+</sup>Tf<sup>-</sup> ionic liquid electrolytes as a function of zinc solute concentrations.

system and plotted in Figure 3.4. At solute concentrations below 0.3M, both systems showed similar ionic conductivities, but as more solute was added to the electrolytes, their behaviors diverged. In both electrolytes, the ionic conductivity decreased with increasing solute concentration, but the conductivity of the lithium ionic liquid electrolyte system diminished at a more rapid rate. In comparing the two electrolyte systems, the cations of the solutes differ in size and valence (lithium ions have an ionic radii of 0.68 Å and valence of 1 while a zinc ions have an ionic radii of 0.74 Å and valence of 2) [Dean, 1992], however since the Tf anions are relatively much larger than the cations (Tf cations have approximate ionic radii of 3Å), the relative sizes of the cations is less consequential to the overall properties of the system. The differences in ionic conductivity behaviors with respect to solute concentration for the lithium and zinc ionic liquid electrolyte systems depend heavily on the population of trifluoromethanesulfonate ions in the electrolyte. The lithium-based ionic liquid electrolyte differs from the zinc-based ionic liquid electrolyte due to the different valences of the solute cations. For every mole of zinc salt, Zn<sup>+</sup>(Tf)<sub>2</sub>, to a given volume, the volume will contain two moles less of BMIM<sup>+</sup>Tf. For one mole of lithium salt, Li<sup>+</sup>Tf, to the same volume, there will be only one mole less of BMIM<sup>+</sup>Tf. These statements are possible assuming that the cationic volumes in the electrolyte are equal. As a result, the zinc-based ionic liquid electrolyte demonstrates higher ionic conductivities and lower viscosity than the lithium-based ionic liquid electrolyte.

A comparison of the diffusion coefficients of zinc and lithium cations with respect to solute concentration in the ionic liquid electrolyte was conducted, and its results support the observations seen in the ionic conductivity experiments. From the data exhibited in



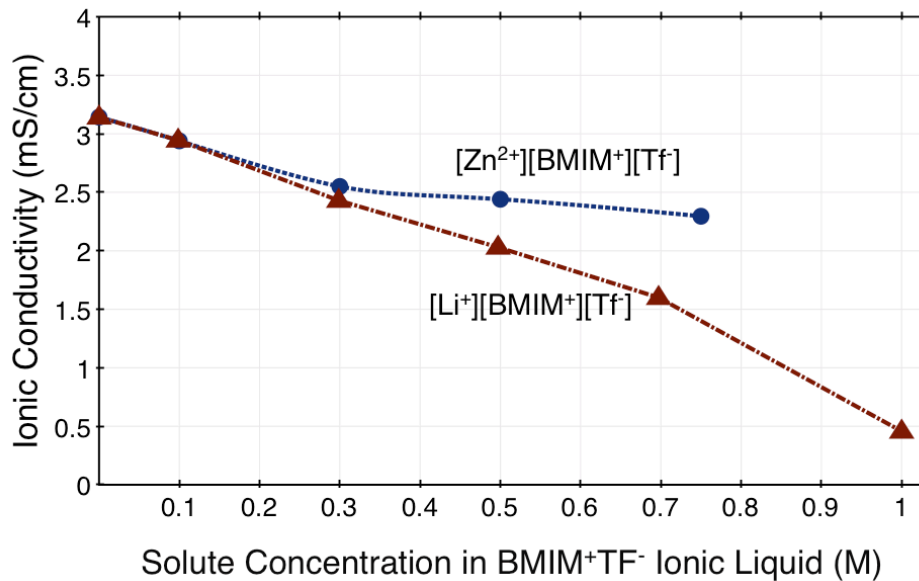


Figure 3.4. Comparison of the ionic conductivities of zinc and lithium ion – ionic liquid electrolytes as a function of solute concentration in the BMIM<sup>+</sup>Tf<sup>-</sup> ionic liquid.

Figure 3.5 taken using the restricted diffusion measurement method, lithium ions are seen to have greater diffusion coefficients than zinc ions in the ionic liquid electrolyte for all salt concentrations. This suggests that though the [Zn<sup>2+</sup>][BMIM<sup>+</sup>][Tf<sup>-</sup>] electrolyte exhibits an overall higher ionic conductivity than [Li<sup>+</sup>][BMIM<sup>+</sup>][Tf<sup>-</sup>], the zinc ions are not as mobile as the lithium ions. With a divalent charge, a zinc cation may interact more strongly with neighboring Tf<sup>-</sup> anions, creating ion complexes tethering pairs, trios, and

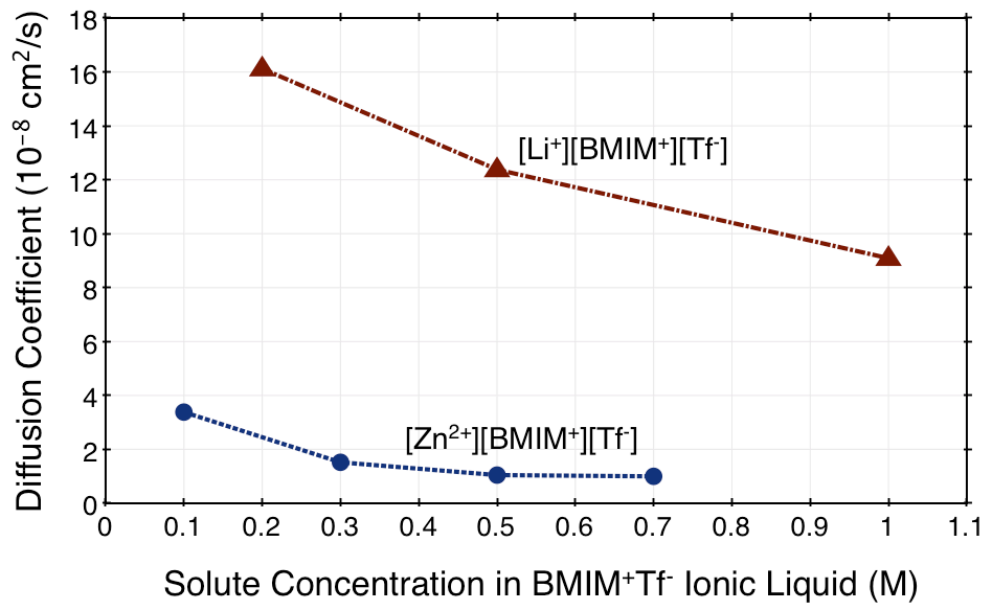


Figure 3.5. Comparison of diffusion coefficient of zinc and lithium ions in ionic liquid electrolytes as a function of solute concentration in the BMIM<sup>+</sup>Tf<sup>-</sup> ionic liquid.

plausibly more anions. As a result, the zinc ion transport is greatly hindered compared to the lithium ion. These ion complexes however, may be freeing the large [BMIM<sup>+</sup>] cations in the [Zn<sup>2+</sup>][BMIM<sup>+</sup>][Tf] electrolyte, allowing their rapid transport within the electrolyte, and as a consequence, contributing to higher overall ionic conductivities. Further confirmation of these observed trends with alternative characterization methods can strengthen the proposed hypotheses, and a complete characterization of the transport properties, including measurements of active ion transference numbers, would contribute to greater understanding of these new ionic liquid materials.

### 3.2.3 Zinc Electrodeposition and Dissolution

The reversibility of the zinc dissolution ( $\text{Zn} \rightarrow \text{Zn}^{2+} + 2\text{e}^-$ ) and converse deposition reactions across a zinc electrode and electrolyte interface as a function of electrolyte concentration were determined by comparing their respective current densities measured using cyclic voltammetry of symmetric cells sandwiching the electrolyte between two zinc electrodes. A scan rate of 10 mV/s was used. For example, a cyclic voltammogram of the first cycle of a cell with 0.75 M zinc salt in BMIM<sup>+</sup>Tf ionic liquid electrolyte is shown in Figure 3.6. The largest magnitudes of the anodic (positive) and cathodic (negative) current densities occur at 0.73 V and -0.69 V, and correspond to the maximum rate of dissolution and deposition occurring at the working electrode, respectively; the magnitude of the current density peaks are 2.21 mA/cm<sup>2</sup> and -2.63 mA/cm<sup>2</sup>. The reversibility of the reaction, calculated by comparing the ratio of the anodic and cathodic current densities, is 84%. The voltammogram illustrates that zinc ions are able to transport through the ionic liquid electrolyte and then plate and strip onto or away from a zinc electrode. Therefore the ionic liquid is a candidate electrolyte for a zinc ion battery.

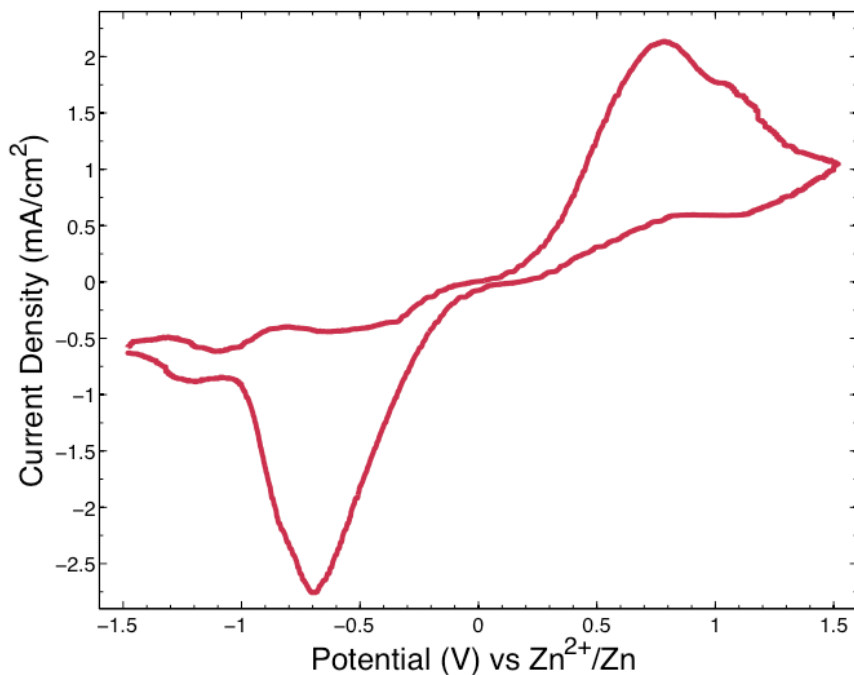


Figure 3.6. Zinc deposition (negative potentials) and dissolution (positive potentials) from an ionic liquid electrolyte with 0.75 M zinc salt. Scan rate of 10 mV/s. The initial polarization direction was towards more positive potentials.

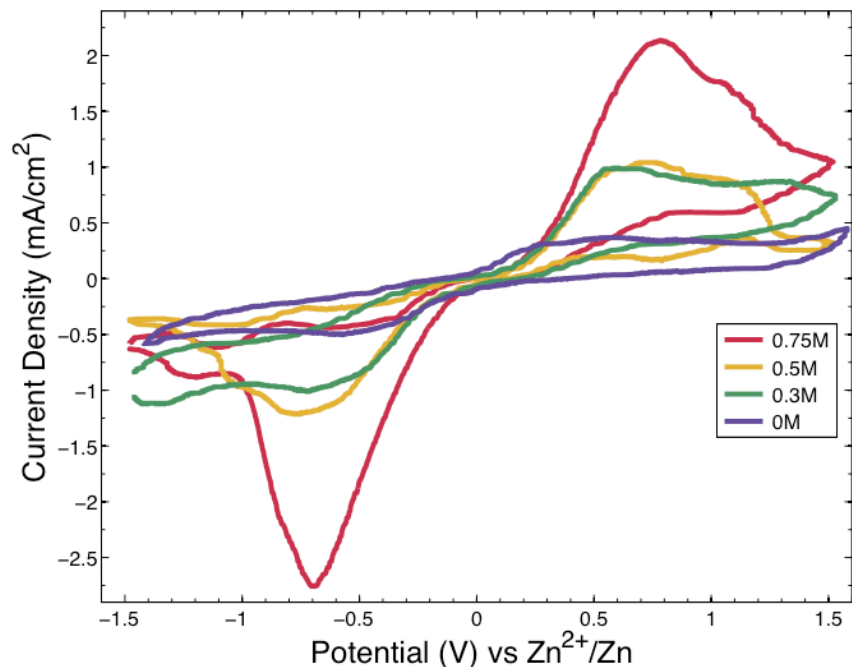


Figure 3.7. Voltammograms of ionic liquid electrolytes with zinc salt concentrations ranging from 0 to 0.75 M. Scan rate of 10 mV/s. The initial polarization direction was towards more positive potentials.

The first cycle voltammograms of ionic liquid electrolyte with zinc solute concentrations ranging from 0 to 0.75 M are displayed in Figure 3.7. With added zinc salt, the maximum anodic and cathodic current densities showed an increasing trend. Upon cycling, the electrochemical behavior of the cells varies depending on the electrolyte concentration. The magnitudes of the anodic peak current densities for the ionic liquid electrolytes with varying zinc salt concentrations are shown as a function of cycle in Figure 3.8. There is a general increasing trend in anodic peak current density for increasing zinc solute in BMIM<sup>+</sup>Tf ionic liquid electrolyte, however 0.3 M and 0.5 M zinc solute-ionic liquid electrolytes showed very similar current density magnitudes. When comparing the maximum current densities of the cyclic voltammograms with respect to cycle number, the electrolytes with zinc concentrations between 0.1 – 0.5 M showed stable current densities that maintained with cycle number; for 0.75 M zinc salt concentration, the electrolyte was unable to demonstrate steady cycling behavior, and a decrease of approximately 70% in the peak anodic current density occurred within the first seven cycles. For electrolytes at and above 0.75 M zinc solute concentration, irreversible behavior occurs due to the diminished transport properties observed in the previous experiments; over many cycles, the poor ionic conductivity and diffusion of the zinc ions hinders any zinc ions from successfully approaching the electrode-electrolyte interface and electrochemically reacting while reacted complexes and also inhibits the opposite mechanism from occurring when the cell polarization is reversed. The same trends were also observed in the cathodic sweep, though the relative magnitudes of the maximum current densities differed. From these studies, it was empirically determined that a 0.5 M zinc salt concentration in BMIM<sup>+</sup>Tf exhibited desirable electrochemical and physical properties and was used as the ionic liquid electrolyte in all future experiments. However,

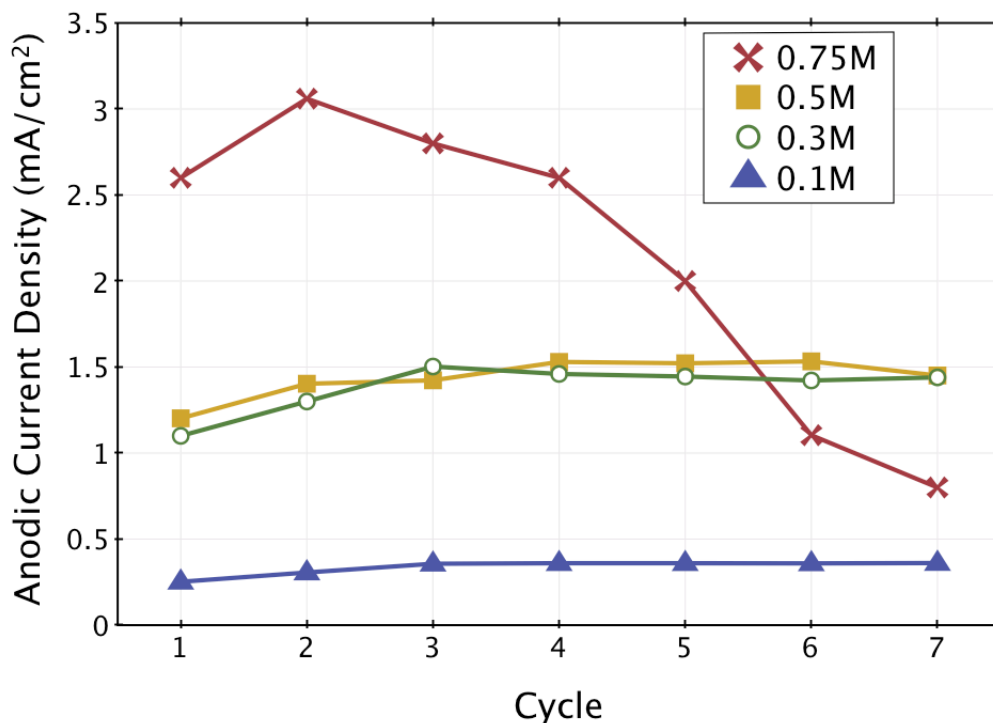


Figure 3.8. Cyclic behavior of the peak zinc dissolution current densities measured from ionic liquid electrolytes with zinc salt concentrations of 0 to 0.75 M. The anodic current density values were extracted from repeated cyclic voltammogram tests using the experimental parameters described in Figure 3.7.

as has become increasingly apparent in subsequent device testing and failure analysis, further optimization and more detailed understanding of the physical processes occurring in the electrolyte will become paramount.

### 3.3 Design of a Zinc Ion Conducting Ionic Liquid Gel Electrolyte

The ionic liquid electrolyte developed in the previous section was swelled into a polymer to form a gel that will act as both the battery separator as well as an ion-conducting medium. Poly(vinylidene fluoride-co-hexafluoropropene) (PVDF-HFP) co-polymer material is commonly used in electrochemical systems because of its ability to remain structurally robust while absorbing large volumes of liquid. Crystalline junctions that provide the gel with mechanical strength are dispersed throughout amorphous regions; these amorphous regions are able to swell with a liquid phase, forming a continuous liquid network through the film.

#### 3.3.1 Gel Electrolyte Morphology

As seen in Figure 3.9 (a-c), “grains” in the gel are observed to enlarge significantly in volume with the increased incorporation of a liquid (from 25 to 60 wt.% ionic liquid electrolyte). The gels of these compositions essentially act like flexible yet mechanically strong films, and can be compressed substantially without damage to the structure or

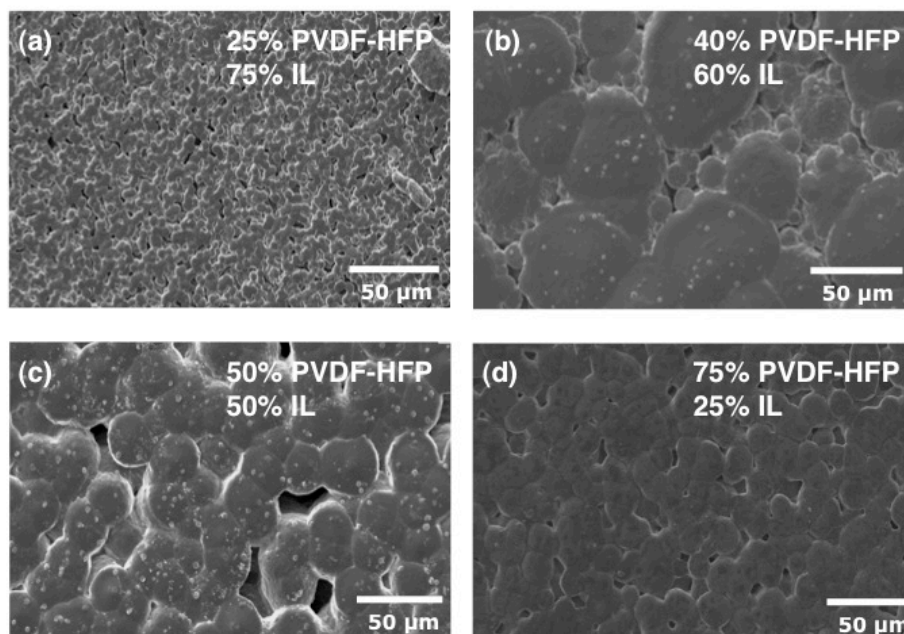


Figure 3.9. (a-d) Micrographs of ionic liquid gel electrolytes showing the morphological changes in the film with decreasing ionic liquid electrolyte swelled into the polymer.

oozing of the liquid phase. No visible “sweating” of the ionic liquid from the gel could be discerned even after extended use or shelf life. Exceeding 75 wt.% ionic liquid, the polymer is unable to accommodate the liquid; a significant diminishment in the film’s grain sizes seen in Figure 3.9 (d) is accompanied by an observed film wetness and fragility. The average grain size for a gel with increasing ionic liquid concentration was measured using image analysis software and is shown in Figure 3.10. X-ray

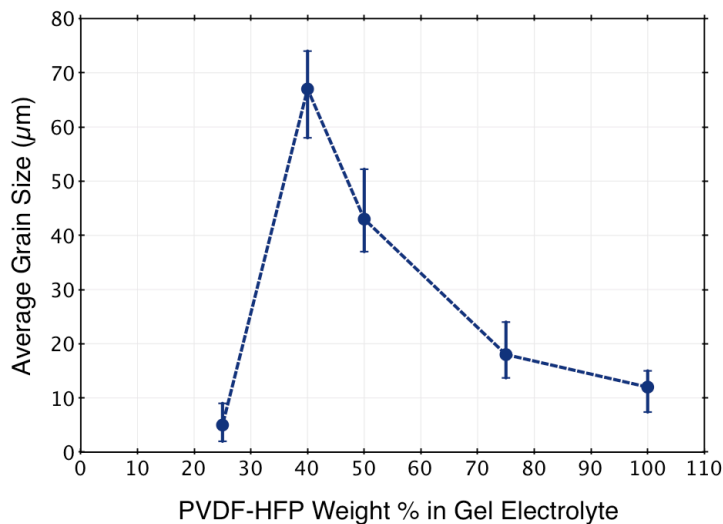


Figure 3.10. Average gel grain sizes with varying concentrations of PVDF-HFP in the ionic liquid gel electrolyte.

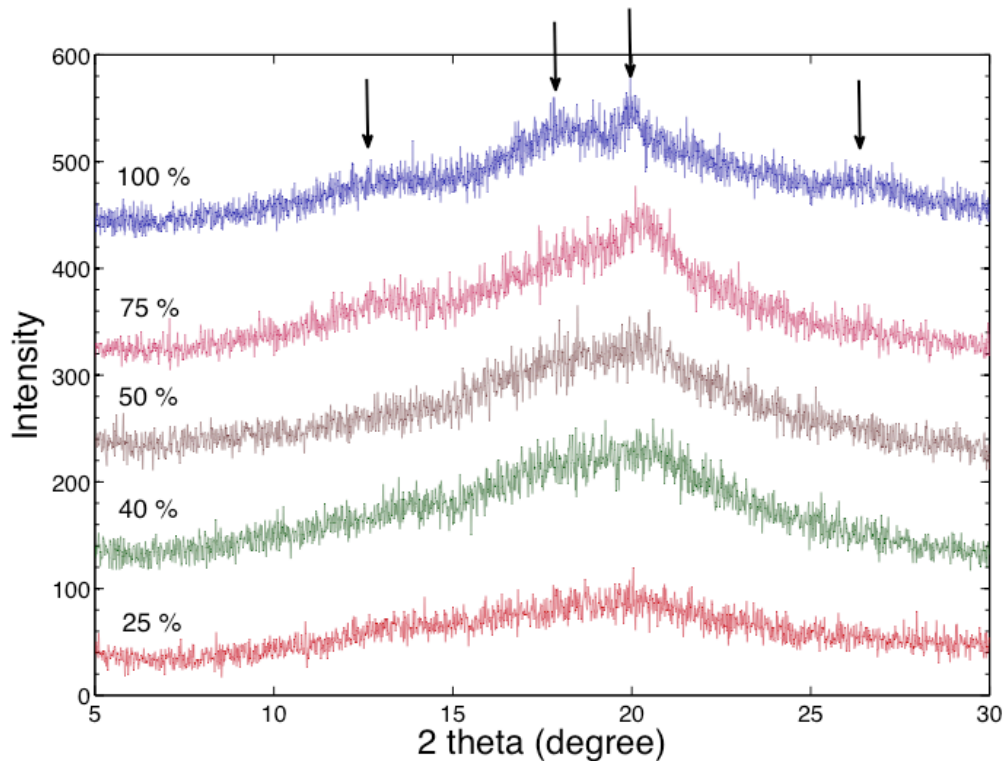


Figure 3.11. X-ray diffraction scans for ionic liquid gel films with increasing polymer concentration (from 25 to 100 %). Arrows direct the eye along peak features that evolve over the varying gel compositions, corresponding to the crystalline nature of the film.

diffraction of the gel electrolyte films also confirmed the reduced population of crystalline regions as amorphous regions inflate with increased ionic liquid concentration (Figure 3.11). Four peaks corresponding to the dispersed crystalline phase can be distinguished from the diffraction scan of a PVDF-HFP film (without ionic liquid) at approximately  $12.9^\circ$ ,  $15.6^\circ$ ,  $19.9^\circ$ , and  $25.7^\circ$ . The strongest peak at  $19.9^\circ$  broadens as more ionic liquid electrolyte is incorporated into the gel, while the remaining peaks gradually disappear.

### 3.3.2 Gel Electrolyte Transport Properties

#### Ionic Conductivity

The bulk transport properties of the ionic liquid gels were analyzed to determine an optimal gel electrolyte composition. The ionic conductivities of the gels were measured with EIS on symmetric cells formed by casting the gels between two blocking stainless steel electrodes. The gel film thicknesses were measured subsequently with digital calipers and verified using microscopy. The room temperature ionic conductivities of the gels (Figure 3.12) were found to increase with higher ionic liquid electrolyte concentration.

A gel composition of 1:1 ionic liquid electrolyte to PVDF-HFP weight ratio was determined to have optimal mechanical integrity and transport properties, and has been

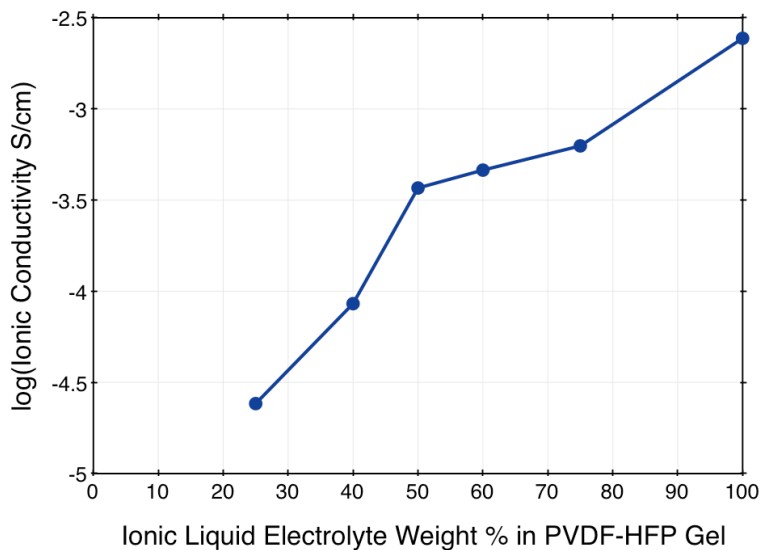


Figure 3.12. Room temperature ionic conductivities of gels with varying ionic liquid concentrations in PVDF-HFP.

employed as the gel electrolyte for all future experiments. At this composition, the room temperature gel ionic conductivity (0.37 mS/cm) is reduced an order of magnitude lower than the neat ionic liquid (2.4 mS/cm), however the gel is considered fairly conductive compared to dry polymer (0.01 mS/cm) and glassy (< 10  $\mu$ S/cm) electrolyte alternatives [Meyer, 1998] and [Dudney, 2005].

### Viscosity

The viscosities of the constituents for the gel electrolyte are displayed in Figure 3.13. The addition of the zinc salt to the ionic liquid increased the viscosity of the solution an

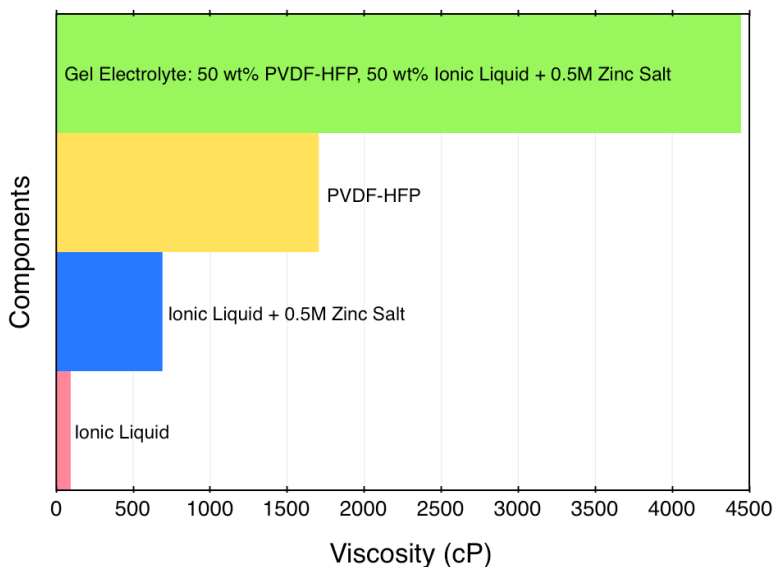


Figure 3.13. Viscosities of the gel electrolyte constituents

order of magnitude, while the gel electrolyte has a viscosity 2.5 times greater than the polymer alone. The average measured viscosity of the gel electrolyte was 4,446 cP.

### 3.4 Concluding Remarks on Gel Electrolyte Design and Characterization

Zinc ions were demonstrated to be able to travel through an ionic liquid electrolyte, with an optimal formula that maximized its transport, viscosity, and electrochemical properties. The zinc salt and ionic liquid solution was swelled into a polymer binder to form a gel electrolyte. The printable gel retains liquid-like ion transport properties, but acts like a solid film that can be flexed and compressed without damage. Furthermore, because of its negligible volatility, the ionic liquid does not “sweat” from the gel. With successful implementation of a printable gel electrolyte, design of a compatible electrode pair which can electrochemically react with zinc ions will be examined in the next section.

### 3.5 References

Arnold, C., Serra, P., & Piqué, A. (2007). Laser Direct-Write Techniques for Printing of Complex Materials. *MRS BULLETIN*, 32, 23-31.

Brookfield . (n.d.). From [www.brookfieldengineering.com](http://www.brookfieldengineering.com)

Dean, J. (1992). *Lange's Handbook of Chemistry*. New York: McGraw Hill.

Dudney, N. (2005). Solid-state thin-film rechargeable batteries. *Materials Science and Engineering B*, 116, 245-249.

Endres, F. (2002). Ionic Liquids: Solvents for the Electrodeposition of Metals and Semiconductors. *ChemPhysChem*, 3, 144-154.

Forsyth, S. A., Pringle, J. M., & MacFarlane, D. R. (2004). Ionic Liquids - An overview. *Australian Journal of Chemistry*, 57, 113-119.

Galiński, M., Lewandowski, A., & Stepniak, I. (2006). Ionic Liquids as Electrolytes. *Electrochimica Acta*, 51, 5567-5580.

Ho, C., Murata, K., Steingart, D., Evans, J., & Wright, P. (2009). A super ink jet printed zinc-silver 3D microbattery. *Journal of Micromechanics and Microengineering*, 19, 094013 (5pp).

Humble, P., Harb, J., & LaFollette, R. (2001). Microscopic Nickel-Zinc Batteries for Use in Autonomous Microsystems . *Journal of The Electrochemical Society*, 148 (12), A1357-A1361.

Karpinski, A. P., Makovetski, B., Russel, S., Serenyi, J. R., & Williams, D. (1999). Silver-Zinc: Status of Technology and Applications. *Journal of Power Sources*, 80, 53-60.



Ma, Y., Doyle, M., Fuller, T., Doeff, M. M., Jonghe, L. D., & Newman, J. (1995). The Measurement of a Complete Set of Transport Properties for a Concentrated Solid Polymer Electrolyte Solution. *Journal of The Electrochemical Society* , 142 (6), 1859-1868.

McLarnon, F. R., & Cairns, E. J. (1991). The Secondary Alkaline Zinc Electrode. *Journal of the Electrochemical Society* , 138, 645-656.

Meyer, W. (1998). Polymer Electrolytes for Lithium-Ion Batteries. *Advanced materials* , 10 (6), 439-448.

Prentice, G. (1991). *Electrochemical Engineering Principles*. Englewood Cliffs, New Jersey: Prentice Hall.

# Chapter 4

## Gel Electrolyte Compatibility With the Anode

Depending on how a printed battery is constructed, it is likely that the electrolyte will come into physical contact with all other components in the device because of its dual role as an ion conductor as well as electronic insulator. In some cases where the electrolyte is a solid material, it may even be used as a structural component. Therefore an electrolyte's compatibility with the other material constituents in the battery is critical to its performance. In the next three sections, the compatibilities of different battery components with the gel electrolyte developed in this work are investigated; interactions between the gel electrolyte with various components of the battery are determined systematically before a full device is tested. This chapter focuses on the design of a printable zinc anode that is compatible with the gel electrolyte as well as the fabrication constraints set by the dispenser printing process.

### 4.1 Gel Electrolyte Compatibility with a Zinc Anode

Thus far, an ionic liquid electrolyte has been demonstrated to successfully allow the transport of zinc ions as well as allow the reversible electrodeposition and dissolution of zinc from zinc foil electrodes. Similarly, a gel electrolyte incorporating this ionic liquid electrolyte also exhibited zinc ion transport properties and electrochemical behavior with zinc electrodes. The interfacial behavior and stability of the gel electrolyte with zinc will be presented in this section. A comparison of the electrodeposition and dissolution behavior of the gel electrolyte and ionic liquid will also be explored.

#### 4.1.1 The Zinc and Gel Electrolyte Interface

Understanding the interfacial activity between a rechargeable battery's electrodes and electrolyte is paramount especially in a reversible system. In electrochemical systems, the contribution of an interfacial product to a battery's performance can be two-fold. In some systems, the formation of interfacial side products may be so vigorous that the interfacial activity becomes detrimental, continually consuming reactants until they become depleted and ineffective. In other systems, after the initial formation of the interfacial side products, the interface becomes a protective barrier, preventing further depletion of the reactants and effectively protecting the electrodes. The latter phenomenon has been

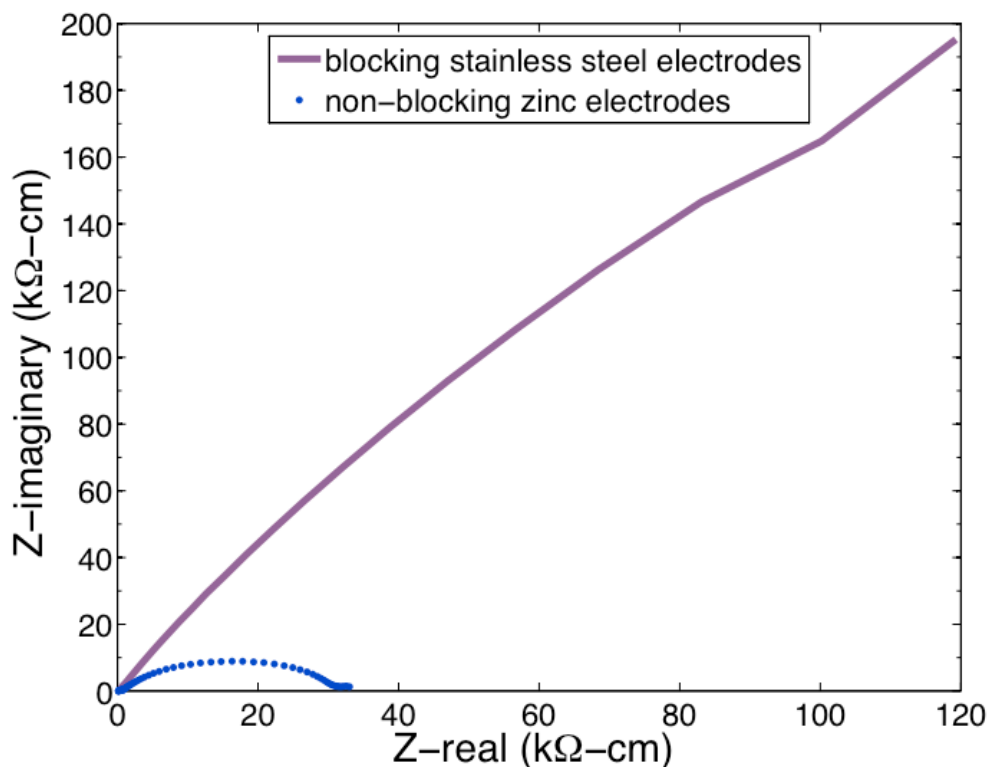


Figure 4.1. The electrochemical impedance spectra for gel electrolyte films sandwiched between two blocking stainless steel electrodes in comparison with two non-blocking zinc electrodes. Cells were swept with a  $V_{AC}$  of 10 mV from 1 MHz to 1 Hz with 0V DC bias.

identified in lithium-ion batteries, some of which have carbon electrodes that form solid-electrolyte interface (SEI) layers with the organic electrolytes when initially assembled and charged [Aurbach, 2000]. With the formation of the SEI, active lithium ions are initially consumed, causing a significant decrease in achievable capacity, however the reaction becomes self-limiting; after a thickness and density is achieved, the SEI protects from further consumption of the electrolyte and electrode at the interface, thereby protecting any residual and unreacted lithium ions from further irreversible consumption at the SEI. Furthermore, the SEI is able to conduct lithium ions through it, allowing the reversible electrochemical reactions between lithium ions and the electrode. This in turn allows the remaining lithium ions to reversibly react electrochemically with the carbon electrode during subsequent charge and discharge cycles as long as the SEI remains intact.

The formation and composition of an interfacial layer is quite complex, and the following studies intend to provide some initial investigations of its properties. The reactivity of the ionic liquid gel electrolyte with various electrode materials is relatively unknown. As a comparison, the Nyquist impedance spectra measured using electrochemical impedance spectra (EIS) methods of the gel electrolyte sandwiched between two stainless steel electrodes is compared to that of a cell with zinc electrodes in Figure 4.1. As would be

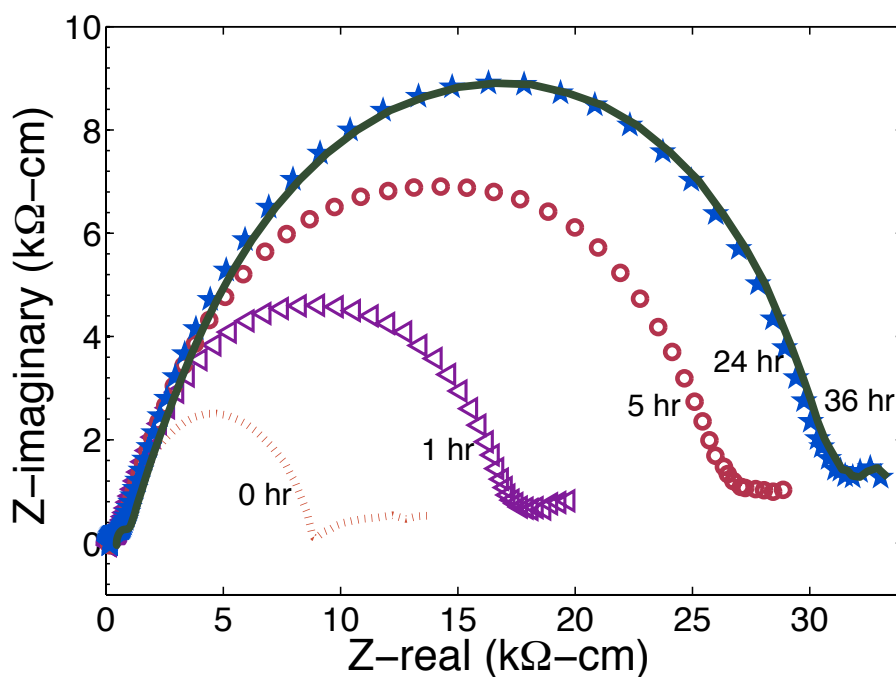


Figure 4.2. Electrochemical impedance spectra of a cell monitored through the course of 36 hours. The cell contained a gel electrolyte film sandwiched between two zinc foil electrodes. The change in morphology of the spectra can be attributed to the increased interfacial impedance over time. Cells were swept with a  $V_{AC}$  of 10 mV from 1 MHz to 1 Hz with 0V DC bias.

expected for blocking electrodes like stainless steel, the gel is seen to be non-reactive with the stainless steel electrodes: the impedance spectrum appears as a sloped line with an increasing trajectory at lower frequencies. In comparison, the zinc electrodes form a semicircular impedance spectrum, which is indicative of electrodes that are non-blocking in nature and reactive with the gel electrolyte [Newman, *et al.*, 2004]. The evolution of an interfacial product between the zinc electrode and ionic liquid gel electrolyte was tracked over 36 hours after assembly using interfacial impedance measurements; these experiments were conducted on a symmetric cell containing a gel electrolyte sandwiched between two zinc electrodes. Nyquist plots of the impedance measurements detected from high to low frequencies exhibited a semi-circle followed by a sloped line. If modeled with an equivalent circuit, the left intercept with the horizontal axis corresponds to the bulk resistance of the cell, the right intercept with the horizontal axis corresponds to the interfacial resistance between the electrode and gel, and the tail-end of the semicircle gives some indication of the diffusion behavior of the system. By comparing the impedance spectra of the cell over the course of 36 hours after assembly (Figure 4.2), the widening of the impedance spectra semi-circles with increased shelf-time is evidence of a development of an interfacial product between the electrodes and gel film. The interfacial resistance detected increases rapidly within the first hours after assembly, and stabilized within 24 hours. In this cell the measured interfacial impedance increased to four times its initial assembled value over 24 hours.

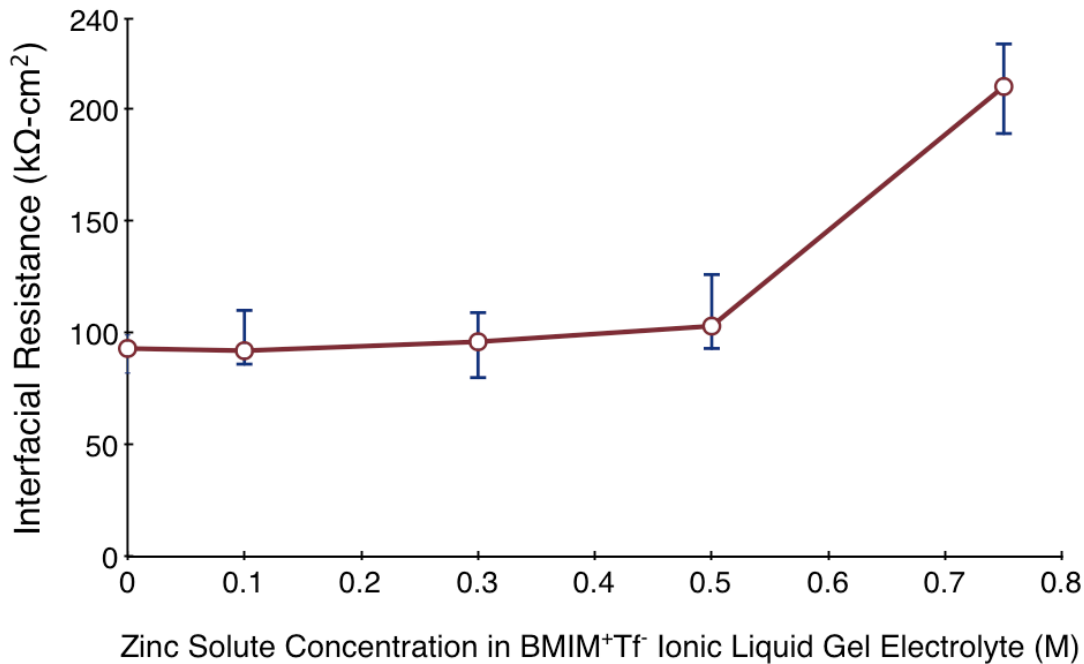


Figure 4.3. Interfacial impedances of BMIM<sup>+</sup>Tf<sup>-</sup> gel films with varying zinc solute concentrations. Interfacial impedance measurements were derived from electrochemical impedance spectra (EIS) tests. Cells were allowed to stabilize for 24 hours after assembly and then were swept with a  $V_{AC}$  of 10 mV from 1 MHz to 1 Hz with 0V DC bias.

The affect of adjusting the zinc salt concentration in the ionic liquid gel electrolyte on the interfacial reactivity with a zinc electrode was explored using the same EIS methods described in the previous experiment. The gel electrolytes were synthesized to have the same proportion of liquid and polymer components (1:1 weight ratio), while the zinc salt concentration in the BMIM<sup>+</sup>TF<sup>-</sup> ionic liquid was varied between 0 and 0.75 M. The cells were allowed to stabilize for 24 hours before impedance measurements were collected. As displayed in Figure 4.3, the interfacial impedance was observed to generally increase with added zinc salt concentration. From 0 to 0.5 M, the resistances of the interfacial products between the gels and electrode ranged from 93 – 103 kΩ/cm<sup>2</sup>. The impedance of the 0.75 M gel electrolyte was twice that of the 0.5 M electrolyte. The sharp increase in impedance indicated greater reactivity at the interface between the electrolyte and electrode in the 0.75 M electrolyte in comparison to that of 0.5 M. This observation also correlates to the experiment discussed in the previous chapter on cyclic zinc deposition and dissolution current densities of the ionic liquid electrolytes measured by cyclic voltammetry (refer back to Figure 3.8). Beyond 0.5 M zinc salt concentration, an escalation in reactivity between the electrolyte and electrode results in greater interfacial reactivity inferred from the high interfacial impedance established after cell assembly and large anodic and cathodic current densities during the first cyclic voltammogram cycle. After the interfacial film is established, which is detected through the stabilization of the cell's interfacial resistance after 24 hours, electrochemical kinetics decreases significantly; this was detected through the diminishment in the cell's anodic and cathodic current densities over any subsequent cycles. Future studies

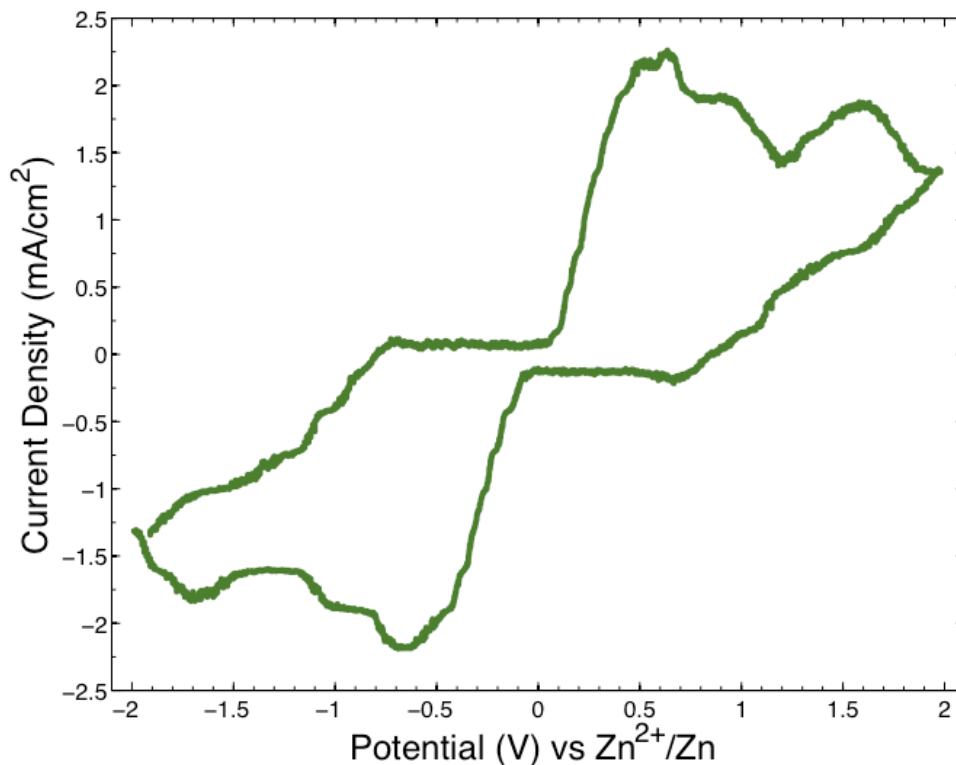


Figure 4.4. Zinc deposition (negative potentials) and dissolution (positive potentials) from an ionic liquid gel electrolyte with 0.5 M zinc solute concentration. Scan rate of 10 mV/s. The initial polarization direction was towards more positive potentials.

on the nature of this interfacial layer and its evolution over the lifetime of the battery will be of profound importance to the rechargability of the system. Other influential factors that may change the mechanism of formation and morphology of the interfacial layer that should be examined in the future are temperature and shelf-time.

#### 4.1.2 Zinc Electrodeposition and Dissolution

To determine if the passivation layer between the gel electrolyte and zinc electrode inhibits or allows for the reversible dissolution and deposition of zinc for gel electrolytes, cyclic voltammery measurements were conducted on the cell after the interfacial film experiments. An example of one voltammogram cycle taken at a 10 mV/s scan rate is shown in Figure 4.4. The cell's zinc ion concentration was 0.5 M. The current peaks at -0.69 and 0.59 V correspond to the deposition and dissolution of zinc, respectively, and over many cycles these reactions occur reversibly with similar current densities. The anodic and cathodic current densities were 2.25 and  $-2.2 \text{ mA/cm}^2$ , respectively. Figure 4.5 displays the gel electrolyte voltammogram overlaid with that of the ionic liquid electrolyte; a comparison of the two plots indicates that the relative peak positions are relatively consistent: the anodic peak of the gel electrolyte shifted - 0.14 V while the cathodic peaks align. The cell was cycled ten times using the same cyclic voltammery parameters and demonstrated the same voltammogram output as the first cycle displayed in Figure 4.4.

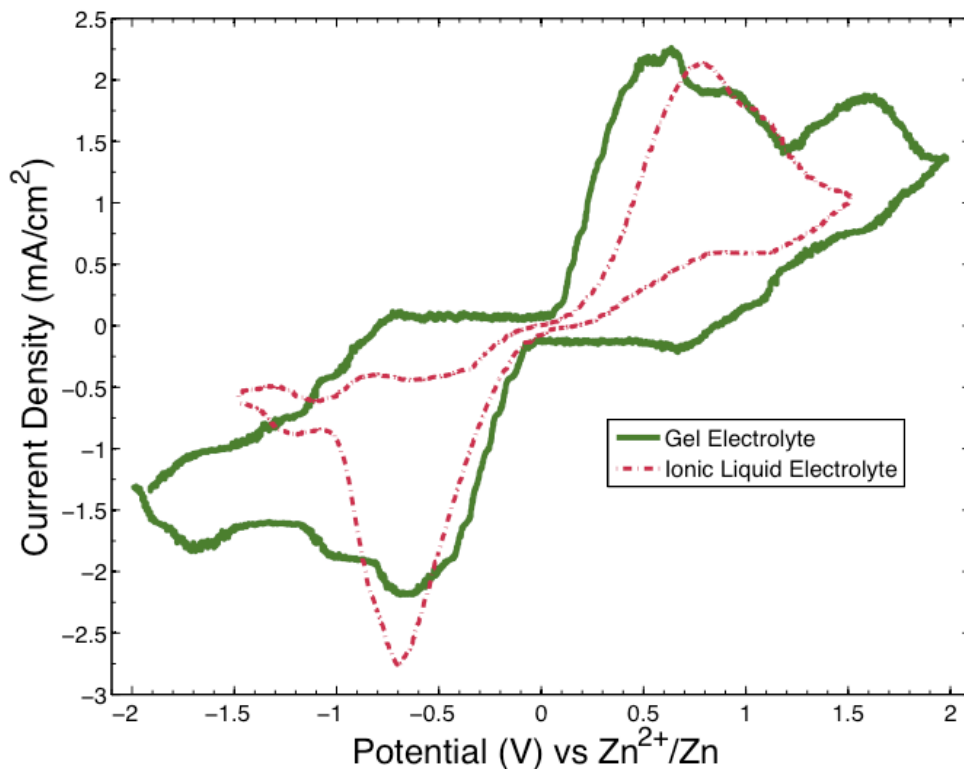


Figure 4.5. Voltammograms comparing the zinc deposition and dissolution behaviors from an ionic liquid or gel electrolyte. Both the ionic liquid and gel electrolyte had a zinc solute concentration of 0.5 M. Scan rate of 10 mV/s. The initial polarization direction was towards more positive potentials.

### 4.1.3 Electrodeposit Morphology

In alkaline battery systems, zinc electrodes are notorious for having poor cycle performance, dendrite propagation, and problematic shape changes during the course of the battery's lifetime. This in large part has prevented many alkaline zinc-based battery chemistries from providing extended cycle-life, and for the most part, zinc-based batteries are used as primary energy storage sources. The following studies examine the morphology of zinc electrodeposition through the ionic liquid and ionic liquid gel electrolytes. Figure 4.6 displays a cyclic galvanostatic experiment that was designed to induce zinc dendrites through rapid cycling between zinc foils and the ionic liquid electrolyte. A schematic of the test cell is illustrated in the Chapter 9 in Figure 9.6. As seen in Figure 4.7 (a), two zinc foils with a gap of 2 mm were submerged in the liquid electrolyte, and after being cycled with alternating applications of positive and negative current densities with magnitudes of  $1.67 \text{ mA/cm}^2$ , dendrites were visible near the interface of the electrodes and electrolyte in Figure 4.7 (b-d). Each pulse lasted five minutes. Within the first 24 cycles, the magnitudes of the maximum cell potential established upon galvanostatic charge or discharge diminished significantly (as much as 70% from 1.8 V to 0.5 V for the anodic pulses); for the remaining duration of the experiment, the peak cell potential of each cycle ranged between 0.48 – 0.51 V for the next 72 cycles. Micrographs of the cells (displayed in insets Figure 4.7 (b-d) showed moss-like growth within the ionic liquid gap

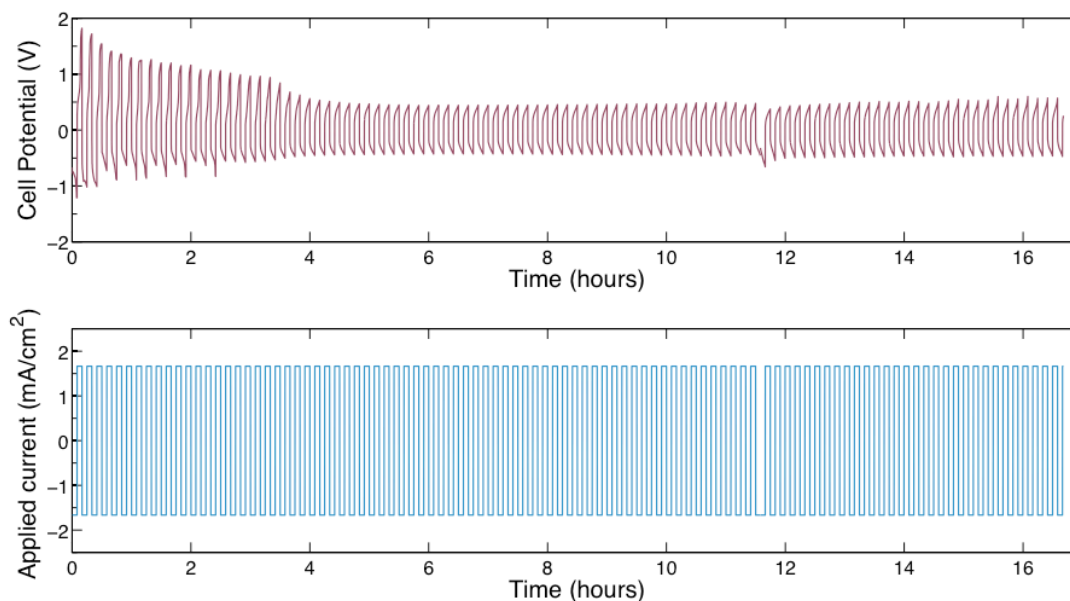


Figure 4.6. A dendrite study induced by galvanostatic cycling of a cell containing 0.5 M zinc solute in BMIM<sup>+</sup>Tf<sup>-</sup> ionic liquid electrolyte sandwiched by two zinc foil electrodes. An applied current density of 1.67 mA/cm<sup>2</sup> is applied for 5 minutes in both the positive and negative direction, and the resulting cell potential is measured. Note that the experiment was interrupted at t=11.5 hr and resumed within 15 minutes.

between the two zinc electrode edges. After 96 galvanostatic cycles, the diminishment of the peak voltage was caused by the zinc dendrite growth, which effectively reduced the gap distance between the zinc electrodes and increased the electrode surface areas; this led to a resistance decrease across the electrodes, and therefore reduced the measured cell potential. Within 96 cycles, there was no indication of a short circuit pathway between the two zinc electrode terminals due to dendrite propagation. This experiment establishes that indeed like many other metals, despite using a non-alkaline electrolyte, the electrodeposition of zinc through an ionic liquid electrolyte is not uniform, but rather mossy. The propagation of the electrodeposited zinc within the through-thickness of the electrolyte presents a problematic conundrum especially for long-term operation and cycling applications.

The same accelerated galvanostatic cycling test was conducted for the ionic liquid gel electrolyte. By behaving as a physical barrier, a gel electrolyte may be proficient in preventing dendrite propagation through the film. The mechanical properties of the film may also alter the electrodeposit morphology. After repeated cycling, micrographs of zinc electrodeposits on a zinc foil electrode from the gel electrolyte are shown in Figure 4.8. The electrodeposits were examined after 15 cyclic voltammetry cycles. On the surface of the smooth zinc foil, regions of zinc electrodeposited from the gel electrolyte are visible: as irregular bulbous electrodeposits that create a bumpy surface morphology on the zinc foil, with rounded protrusions as large as 30  $\mu\text{m}$  in diameter. Comparing the micrograph of the electrodeposited zinc (Figure 4.8b) to that of the gel electrolyte (Figure 4.8a), the rotund, non-uniform electrodeposits mimic the morphology and sizes of the grains in the gel electrolyte. Also, the shape of the zinc electrodeposited from the gel



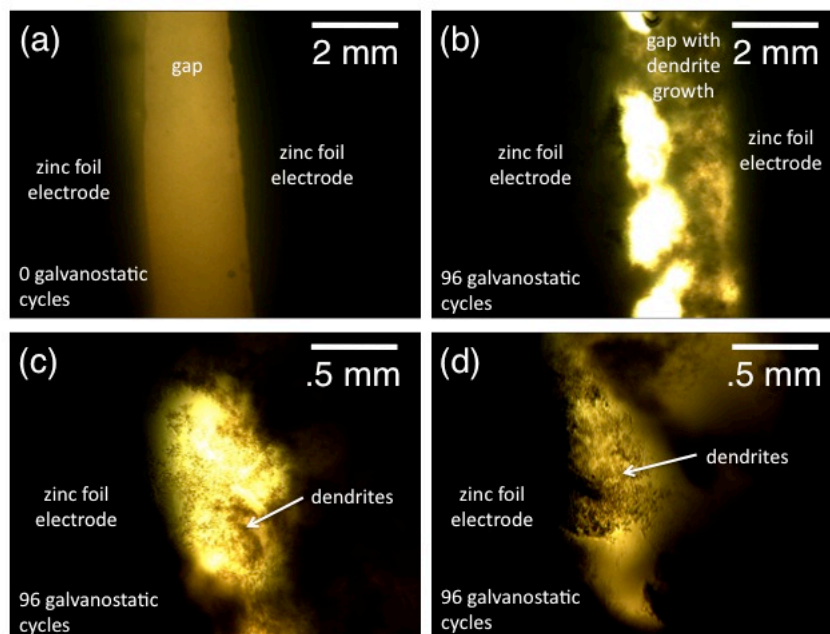


Figure 4.7. Zinc foil dendrite study in ionic liquid electrolyte. (a) Two foil electrodes are separated by a 2mm gap and covered with ionic liquid electrolyte. After rapid galvanostatic cycling, (b-d) mossy growth is visible especially at the interfaces between the electrolyte and zinc foils.

electrolyte lacks the dendritic appearance found at the liquid electrolyte and electrode interface of the previous experiment. It is imperative to more clearly understand the conditions and mechanisms which may constitute these varying zinc electrodeposited morphologies and whether a system using a gel electrolyte can truly withstand repeatable cycling (for example more than 3,000 deep discharge cycles) without risk of dendrite propagation, capacity loss, or cell shorting.

## 4.2 Gel Electrolyte Compatibility with Printed Zinc Anodes

To achieve a fully printable battery, a printable zinc electrode was fabricated. Its electrochemical properties and compatibility with the gel electrolyte were determined. These properties were compared to that of the zinc foil electrode discussed in the previous section. Any variations in properties due to the printed nature of the zinc electrode are highlighted in the following sections.

### 4.2.1 Printed Zinc Electrode Fabrication

Printable zinc electrodes were fabricated from zinc slurry inks. The slurries were synthesized by mixing zinc powder with poly(vinylidene fluoride-co-hexafluoropropene) (PVDF-HFP) polymer binder. In some instances a conductive additive such as acetylene black (AB) was also added to the slurry. Zinc powders of varying morphology and sizes can be purchased, and for printability purposes, spherical powder with particle sizes < 10

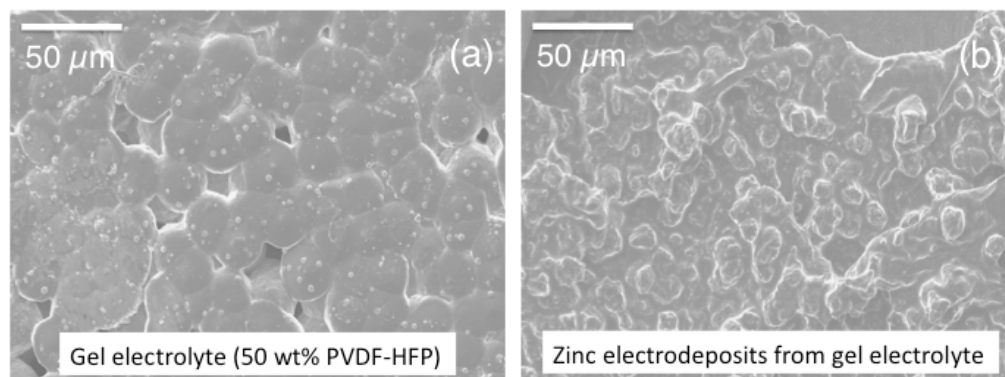


Figure 4.8. (a-b) Micrographs comparing the morphologies of (a) a gel electrolyte film and (b) zinc electrodeposits from a gel electrolyte onto a zinc foil

$\mu\text{m}$  were chosen. The ranges of compositions of the various constituents of the slurry varied: 85-95 wt.% zinc powder, 0-12 wt.% conductive additive, and 3-15 wt.% PVDF-HFP. N-methyl-2-pyrrolidone (NMP) solvent was used to tailor the viscosity of the ink. A micrograph of a printed zinc electrode film formed from slurry ink is displayed in Figure 4.9.

#### 4.2.2 Measuring Printed Zinc Film Electrical Resistance

The electrical resistances of a few printed zinc films with varying compositions are displayed in Figure 4.10. For each composition, ten samples were fabricated and tested. Film electrical resistance was determined using a handheld multimeter and confirmed with a 4-point probe. For 89.5 wt.% zinc powder, the measured electrical resistances of films with this composition varied substantially, depending on the probe position and pressure applied on the film; for a number of samples with compositions below 89.5 wt.%, electrical resistances could not be measured using multimeter or 4-point probe methods. Below 89.5 wt.%, the film was unable to establish a consistent electrical resistance because the network of zinc powder was below its percolation threshold

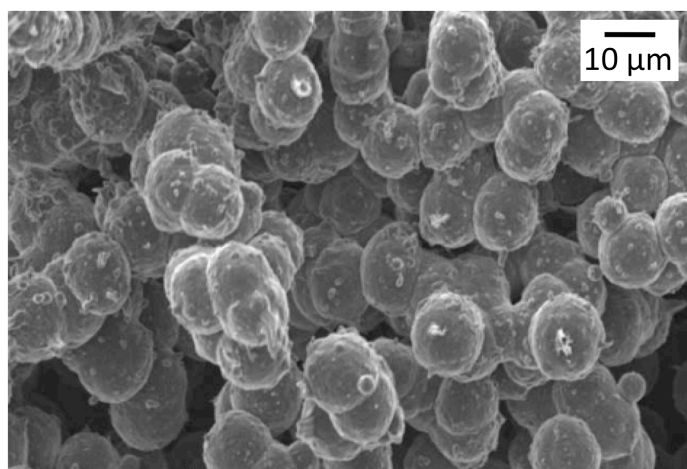


Figure 4.9. Micrograph of a printed film containing 10  $\mu\text{m}$  zinc particles held together with PVDF-HFP polymer binder.

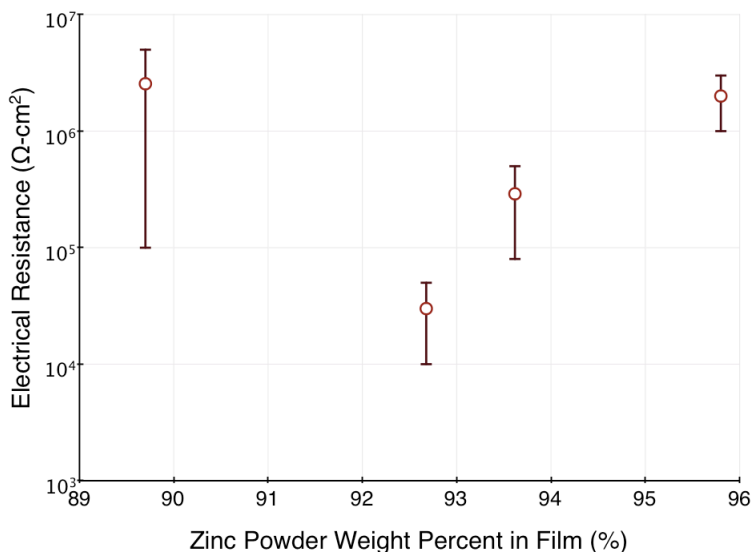


Figure 4.10. Electrical resistances of printed films with varying weight percents of zinc powder in PVDF-HFP polymer binder.

within the polymer binder. Above 92.7 wt. % the electrical resistance of the films increase with increasing zinc powder composition. This is a common phenomenon in composite slurry systems and can be attributed to an increased contribution of the interfacial resistances between particles as increased powder composition. Conductive acetylene black powder was added to the slurry with an original composition of 92.7 wt.% zinc powder and 7.3 wt.% PVDF-HFP, and the electrical resistances of the resulting printed films decreased at least an order of magnitude from the original formula

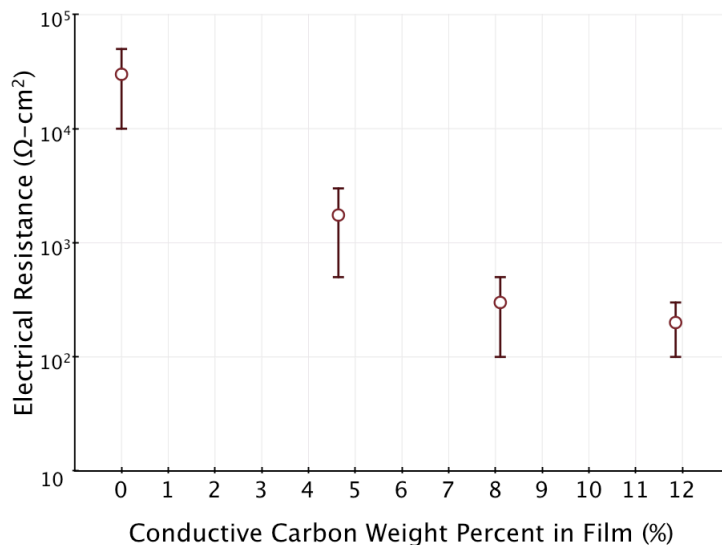


Figure 4.11. Electrical resistances of printed films with varying weight percents of acetylene black conductive carbon powder mixed into a slurry of zinc powder in a PVDF-HFP polymer binder (original composition of slurry before addition of acetylene black was 92.7 wt.% zinc powder and 7.3 wt.% PVDF-HFP).

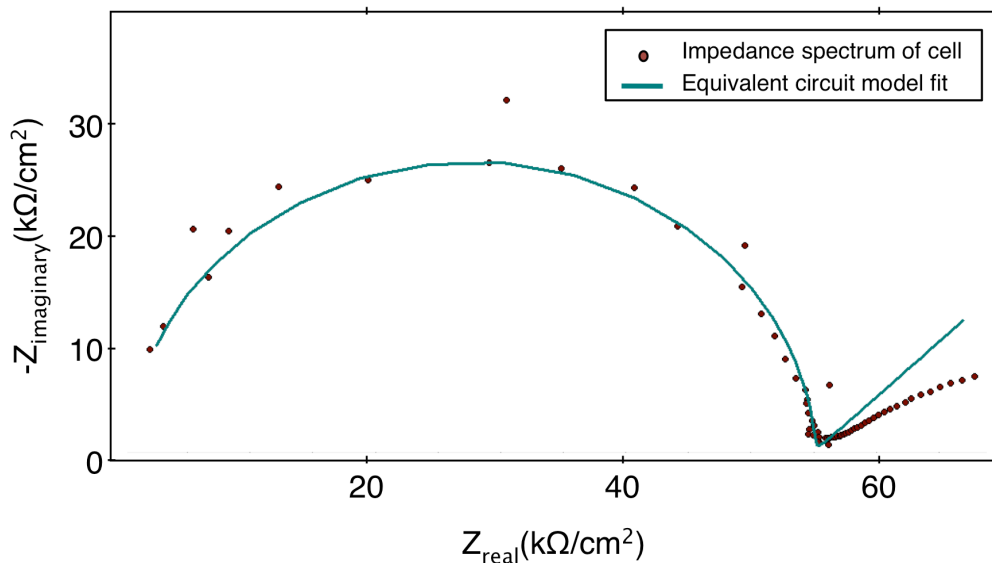


Figure 4.12. Electrochemical impedance spectrum and equivalent circuit model fit of planar pair of printed zinc-carbon electrodes covered in a printed gel electrolyte. From the equivalent circuit fit, the cell's solution resistance  $R_{\text{solution}}=55.4 \Omega$ , surface film resistance  $R_{\text{surface}}=54.4 \text{ k}\Omega$ , surface film constant phase element  $Q=24.7 \text{ S}\cdot\text{s}$ , and Warburg diffusion element  $W= 4.4 \text{ kS}\cdot\text{s}^{1/2}$ .

with additions of acetylene black greater than 4 wt.% (Figure 4.11). Further testing should be conducted to understand at which compositions are the printed electrode film's electrical resistance and electrochemical capacity optimized.

### 4.2.3 Measuring Printed Zinc Electrode Electrochemical Impedance

The impedance behavior of the printed zinc electrode was investigated using electrochemical impedance spectroscopy (EIS). A planar test structure was constructed by printing two adjacent zinc electrodes onto a glass substrate. Gel electrolyte was printed on the pair of electrode pads, covering all but the electrode ends, which were left uncovered to provide electrical access to the electrodes. For each of the electrodes,  $0.5 \text{ cm}^2$  of the electrode surface was covered in printed gel electrolyte while the rest of the electrode was left uncovered to be accessed by the potentiostat probes. The test structure, illustrated in Chapter 9 in Figure 9.6, was allowed to stabilize over 24 hours after assembly, and afterwards, an EIS test was conducted on the cell; from the test, the cell exhibited the impedance spectrum shown in Figure 4.12. Due to the poor electrical conductivity of the zinc-carbon electrodes, the output impedance spectrum exhibited noise and some incongruous data points. The equivalent circuit which best models this system is illustrated in Figure 4.13. The system can be expressed as an equivalent circuit containing a solution resistor in series with a constant phase element that is in parallel with a surface film resistor and Warburg diffusion element. The constant phase element correlates to a dispersed double layer capacitance signal due to the porous and inhomogeneous nature of the electrodes. The fit determined by the equivalent circuit model is also included in Figure 4.12. The impedance spectra of test structures containing printed zinc electrodes compared to zinc foil electrodes (using the same gel electrolyte

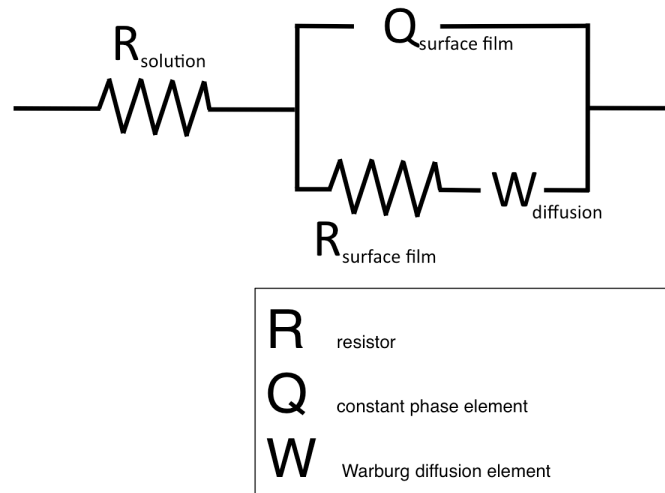


Figure 4.13. Equivalent circuit model for a test structure containing two printed composite zinc-carbon electrodes covered in a gel electrolyte.

formula) are shown in Figure 4.14. The drastic affect on the impedance due to the composite nature of the printed zinc electrodes is apparent with the increase in semi-oval diameter (greater than twice that of the foil electrode). From the equivalent circuit model, the interfacial resistance of the printed system was  $56.7 \text{ k}\Omega/\text{cm}^2$ , nearly three times larger than the zinc foil electrodes. This was expected because for a given electrode area, the printed composite electrodes contain substantially more interfacial area than the foil electrodes.

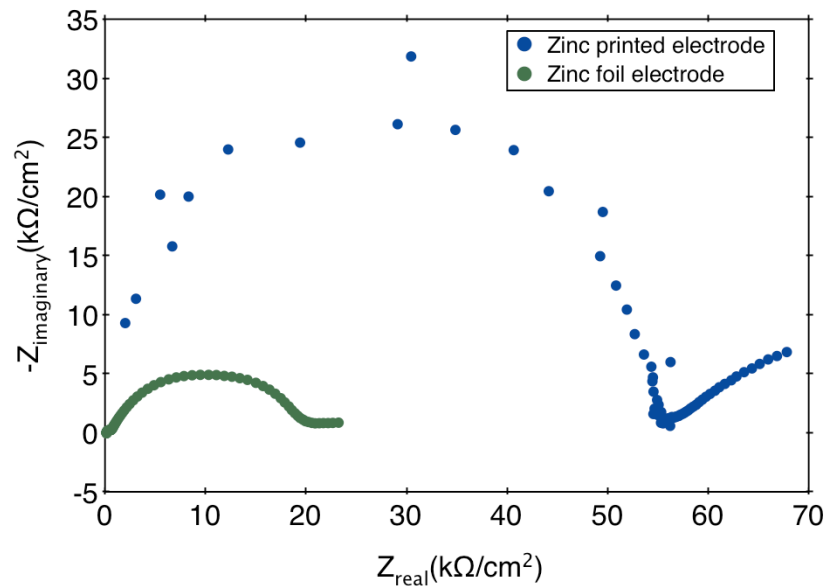


Figure 4.14. The impedance spectra of two test structures containing zinc electrodes in foil or printed form. Both test structures were symmetric and planar cells covered by gel electrolyte.

#### 4.2.4 Zinc Electrodeposition and Dissolution from Printed Electrodes

The planar test structure containing two printed zinc electrodes covered by gel electrolyte was cycled using CV, and an example of a voltammogram is shown in Figure 4.15. Anodic and cathodic current peaks corresponding to cell potentials of 0.54 and -0.53 V, respectively, display a ratio of nearly 95%. In Figure 4.16 the printed cell's voltammogram is compared to that of a cell containing zinc foil electrodes, which was first discussed in Figure 4.4. Both cells used the same gel electrolyte formula. The shapes of both voltammograms are similar, with relatively similar anodic and cathodic peak positions along the cell voltage axis. The additional peaks beyond the -1 and 1 V electrochemical window seen in the zinc foil cell are also visible in the printed cell voltammogram. As would be expected, the voltammogram envelope of the printed cell appears broader than the foil electrode cell, indicating greater internal resistance in the system. Ultimately, these studies have demonstrated that the gel electrolyte is electrochemically compatible with a printed zinc system. Difficulties in achieving a highly conductive printed zinc material may be due to the inherent oxide formed on the surface of the zinc particles. Though in this work a composite electrode of zinc and carbon particles was used, future studies on alternate zinc powder morphologies or zinc nanoparticle dispersions may be beneficial to achieve higher electrical conductivities and electrochemical output. Further studies on the printed zinc electrode's cyclability, electrodeposit morphology, and shape change with the gel electrolyte are crucial for demonstrating long-term performance.

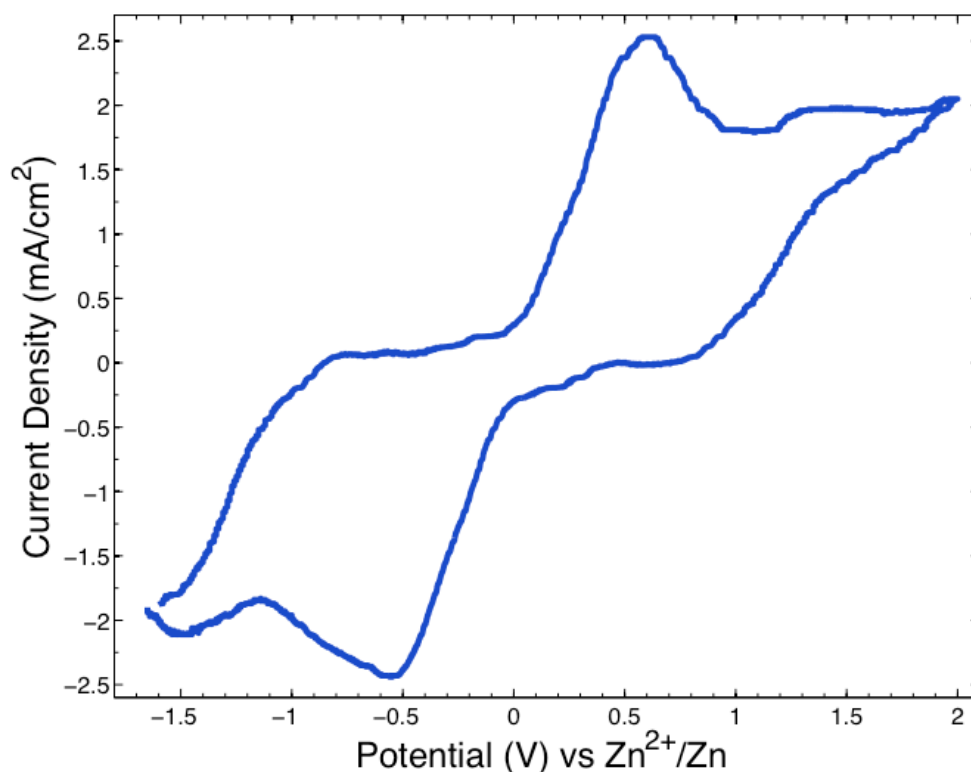


Figure 4.15. Zinc deposition (negative potentials) and dissolution (positive potentials) from an ionic liquid gel electrolyte with printed zinc-carbon composite electrodes. Scan rate of 10 mV/s. The initial polarization direction was towards more positive potentials.

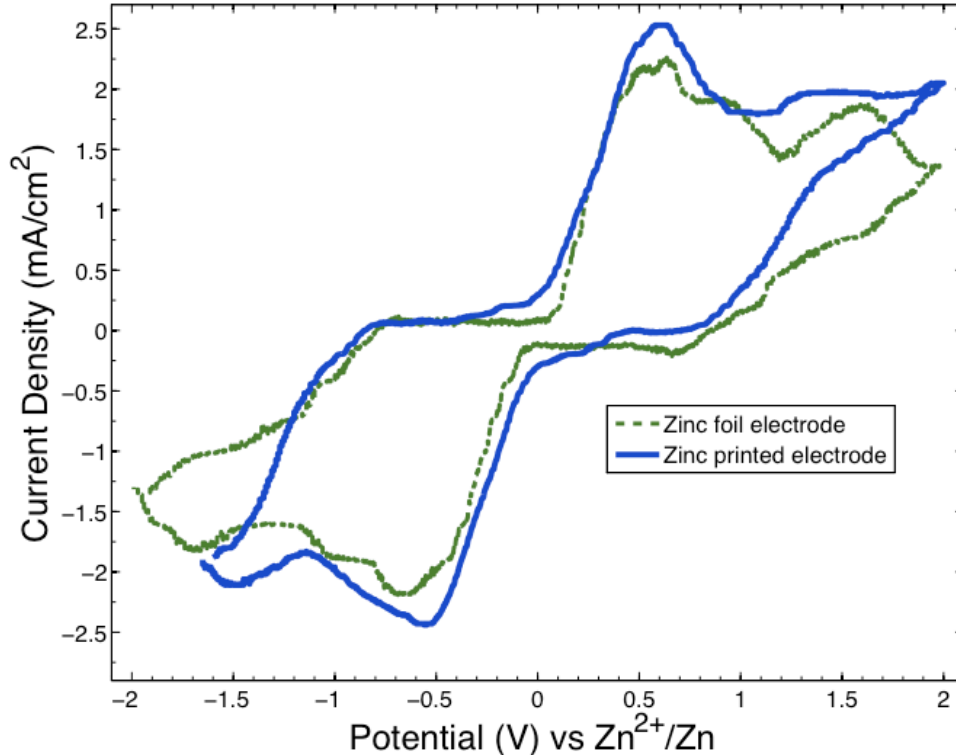


Figure 4.16. Voltammograms comparing the zinc deposition and dissolution behaviors from an ionic liquid gel electrolyte with foil and printed electrodes. Scan rate of 10 mV/s. The initial polarization direction was towards more positive potentials.

### 4.3 Concluding Remarks about the Gel Electrolyte Compatibility With the Anode

A printable zinc electrode was fabricated and determined to be electrochemically compatible with the gel electrolyte developed in the previous section. Its interfacial behavior and electrochemical impedance was compared to that of a zinc foil electrode. A substantial increase in interfacial resistance due to the high surface area of the printable electrode may lead to impedance barriers especially during high power pulsing. The reversible cycling of the zinc electrode will depend on the morphology of the electrodeposits along its interface with the gel electrolyte. In the ionic liquid, mossy electrodeposits formed after accelerated cycling. A similar study conducted with the gel electrolyte suggests that the electrodeposit morphology is substantially different, and may in fact impede dendrite formation or propagation. More extensive studies on this topic are critical for the long-term cycle life of this device.

## 4.4 References

Aurbach, D. (2000). Review of Selected Electrode-Solution Interactions Which Determine the Performance of Li and Li ion Batteries. *Journal of Power Sources* , 89, 206-218.

Newman, J., & Thomas-Alyea, K. E. (2004). *Electrochemical Systems* (3rd Edition ed.). Hoboken, New Jersey: Wiley-Interscience.



## Chapter 5

# Gel Electrolyte Compatibility with Transition Metal Oxide Cathodes

With the development of a printable gel electrolyte capable of transporting zinc ions as well as a printable zinc electrode with which those ions can react, the remaining active component that must be designed for a printable battery is the printable cathode. By modeling this system after lithium ion intercalation batteries, the search for a cathode material centered on battery materials with the ability of inserting and electrochemically reacting with zinc ions. Battery insertion host materials are capable of withstanding the reversible electrochemical insertion and extraction of electroactive species and electrons without the destruction of their fundamental structure [Chippindale, *et al.*, 1991]. In the last three decades, the increased understanding of these materials as battery electrodes has contributed to performance enhancements for a variety of battery chemistries, including lithium-ion, nickel-metal hydride and zinc-based systems. Transition metal oxides are a common class of insertion host materials, largely because of their capacity for accommodating a large population of electroactive species within their core crystal structure; the transition metal oxide parent structure is able to remain stable even as the composition of foreign species in the host structure varies with insertion. Common cations for transition metal oxides include vanadium, manganese, and cobalt, all of which demonstrate multiple oxidation states and have a propensity for redox reactions. The anions of an insertion host material are usually much greater in size than the cations, and (despite the oversimplification) in most cases their size and arrangement determine the crystal structure upon which the host material cations organize within [Ohzuku, *et al.*, 1994]. This ultimately creates an ionic matrix that can accommodate foreign ions. Oxygen is a very common insertion host material anion because of its high volumetric capacity for inserting small cations within the crystal structure of oxide materials; the ionic radius of oxygen ions is large (1.40 Å) compared to that of an insertion cation; for example, the zinc ionic radius is 0.74 Å while a lithium ionic radius is 0.68 Å [Dean, 1992]. Typical transition metal oxides used as battery electrodes include vanadium pentoxide, manganese dioxide, lithium cobalt oxide and lithium titanate, to name a few. In this chapter, two potential cathode materials are examined, and their electrochemical behaviors with a zinc conducting gel electrolyte are characterized.

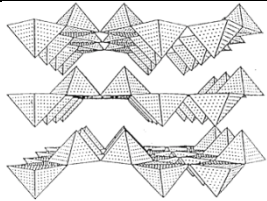

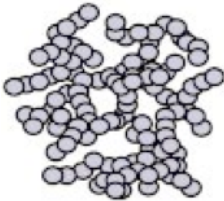
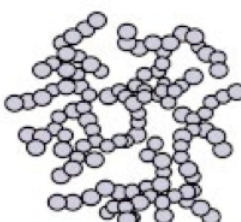
## 5.1 Gel Electrolyte Compatibility with Printed Vanadium Pentoxide Cathodes

Drawing from lithium battery research, there have been extensive studies dedicated to understanding materials that can intercalate and electrochemically react with lithium ions. In contrast, less is known about the electrochemical insertion of polyvalent ions such as  $\text{Zn}^{2+}$ . Preliminary work, motivated by the desire to explore new materials systems for energy storage and sensors, has been conducted to understand the mechanisms of ion insertion of lithium ion alternatives into host materials.

### 5.1.1 A Review of Multivalent Ion Insertion into Vanadium Pentoxide Materials

Le *et al.* reported the first known successful chemical insertion of polyvalent ions into a vanadium pentoxide ( $\text{V}_2\text{O}_5$ ) aerogel host in 1998 [Le *et al.*, 1998]. Polyvalent ions such as  $\text{Mg}^{2+}$ ,  $\text{Al}^{3+}$  and  $\text{Zn}^{2+}$  were demonstrated to react with and incorporate into the host structure of the  $\text{V}_2\text{O}_5$  aerogel after soaking the aerogel in a salt solution (typically the solutions are in an alkane, for example dimethyl zinc in heptane) for one week, and the reported capacities for intercalation were encouraging. Meticulous studies have showed the electrochemical reversibility of the insertion and de-insertion of zinc ions into  $\text{V}_2\text{O}_5$  aerogels [Giorgetti *et al.*, 1999], and confirmed that  $\text{V}_2\text{O}_5$  aerogels served as excellent host structures for polyvalent ions. Other studies confirmed that aerogels are capable of dramatically greater capacity for polyvalent ions than any other forms of  $\text{V}_2\text{O}_5$  because of their unique materials properties, including their very porous structure and high surface area to volume ratio, as well as increased interlayer spacing [Giorgetti, *et al.*, 1999, Tang, *et al.* 2004, and Amatucci, *et al.*, 2001]. By having increased porosity and surface area, the diffusion distances that a polyvalent cation must travel within the bulk material is greatly reduced, for example typical diffusion distances are on the order of 10-50 nm in  $\text{V}_2\text{O}_5$  aerogels while in crystalline  $\text{V}_2\text{O}_5$  the diffusion distances are defined by its average particle sizes, and are oftentimes greater than 10  $\mu\text{m}$  [Le, *et al.*, 1998]. The high density of accessible surfaces on which ions can react leads to dramatically greater pseudocapacitive charge storage. Similarly, the increased layer spacing in aerogels compared to crystalline materials expedites cation insertion into the host material. Table 5.1 summarizes the approximate interlayer spacing for common forms of insertion host materials. It also has been reported that the greater interlayer spacing alters the thermodynamic energy of the host material, which in some cases can lead to greater cation insertion capacity [Tang, *et al.* 2004]. Because the polyvalent ions are less limited by kinetic bulk diffusion barriers in non-crystalline material structures (xerogels, ambigels, and aerogels), they show dramatically higher storage capacities.

Table 5.1. Interlayer spacing of common forms of electrochemical insertion host materials [Braithwaite, *et al.*, 1999 and Rolison, *et al.*, 2001]. The images are illustrations of the host material structures and are not displayed to scale.

<i>Host material structure</i>	<i>Schematic</i>	<i>Interlayer spacing (Å)</i>	<i>Specific surface area (m<sup>2</sup>/g)</i>
Crystalline		4.4	1-10
Xerogel		8.8	10
Ambigel		10.1	40
Aerogel		12.5	150-450

## 5.1.2 Synthesis of a Vanadium Pentoxide Printable Electrode

### Synthesis of Vanadium Pentoxide Ambigel Powder

Dong, *et al.* have described the synthesis of aerogels using sol-gel methods in great detail [Dong, *et al.*, 2003]. The beginning precursor is vanadium tri-isopropoxide, a liquid, that is dissolved in water and acetone. Upon combining the precursor with water and acetone, hydrolysis and condensation reactions occur, creating a network of colloidal particles in a gel, known as a sol-gel. Depending on the concentration of precursor in the solution, the competing rates of hydrolysis and condensation can be controlled to tailor the resulting sol-gel's morphology [Rolison, *et al.*, 2001]. Monolithic gels were formed by combining 1 part vanadium tri-isopropoxide : 3 parts water : 6 parts acetone (stated in weight ratios). Solvent trapped within the porous solid network must be carefully removed to preserve its delicate structure; quick ambient air evaporation of the solvent results in a xerogel, slow ambient air drying derives an ambigel, and supercritical drying preserves the colloidal sol network, creating an aerogel. The synthesis of aerogel material in large quantities is difficult and expensive due to the supercritical drying step. Supercritical

Supercritical drying allows the precise removal of liquid from a structure by infiltrating it with a fluid (like CO<sub>2</sub>), which can be taken from its liquid to gas phase without crossing its phase boundary. Instead it is brought to its supercritical state where the densities of the liquid and gas phases are equal. By doing so, the process avoids the manifestation of surface tension that might damage the aerogel structure while being dried. This usually requires a large volume of CO<sub>2</sub> (or any other suitable fluid) and a chamber able to achieve the supercritical temperatures and pressures of the fluid (for CO<sub>2</sub>: T<sub>supercritical</sub> = 304.25 K, P<sub>supercritical</sub> = 7.39 MPa), and must be done in small batches. To avoid these limitations, large quantities of V<sub>2</sub>O<sub>5</sub> ambigels were synthesized instead. Despite having a diminished storage capacity in comparison to aerogels, the synthesis of V<sub>2</sub>O<sub>5</sub> ambigel host material proved to be more cost and time-effective. To synthesize V<sub>2</sub>O<sub>5</sub> ambigels, the sol-gel recipe described above was used to form a gel which was allowed to age for six days. The gel was then flushed for three days with acetone, and then flushed with hexane for one day. Hexane was then slowly evaporated to prevent substantial pore collapse.

### Synthesis of a Printed Vanadium Pentoxide Ambigel Electrode

The dried monoliths of vanadium pentoxide ambigel were crushed manually using a mortar and pestle into a fine powder and mixed with acetylene black (a fine conductive carbon powder), PVDF-HFP, and NMP to form a printable slurry. The slurry composition is included in Table 5.2.

Table 5.2. V<sub>2</sub>O<sub>5</sub> ambigel composite slurry ink formula

	<i>Components</i>	<i>Weight Percent (%)</i>
V <sub>2</sub> O <sub>5</sub> composite slurry	V <sub>2</sub> O <sub>5</sub> ambigel powder	92
	Acetylene black	4
	PVDF-HFP polymer binder	4

### 5.1.3 Detecting Zinc Ion Electrochemical Insertion

To test the electrochemical insertion of zinc into the V<sub>2</sub>O<sub>5</sub> ambigel, a test structure was constructed by printing a 1 cm<sup>2</sup> V<sub>2</sub>O<sub>5</sub> ambigel film and subsequently a 1.21 cm<sup>2</sup> gel electrolyte film on top of the V<sub>2</sub>O<sub>5</sub> film. A nickel foil was used as the current collector and substrate for the printed MnO<sub>2</sub> film while zinc foil acted both as the electrode and its own current collector. A cross section of the interface between the printed films, the gel and V<sub>2</sub>O<sub>5</sub> ambigel films, is shown in Figure 5.1. To investigate the electrochemical

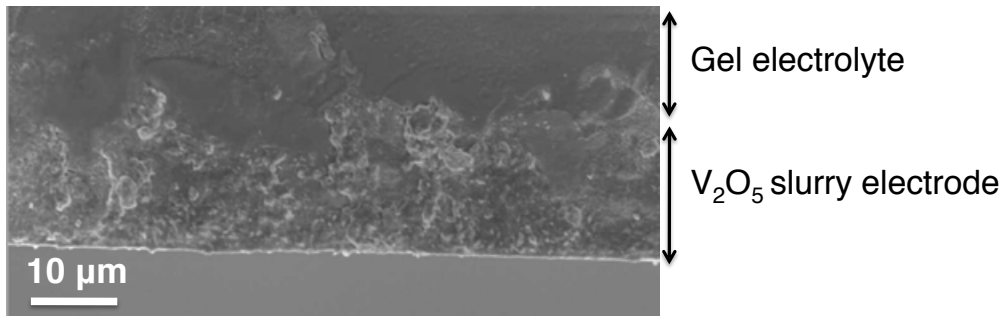


Figure 5.1. Micrograph of the cross-section of a printed V<sub>2</sub>O<sub>5</sub> ambigel film and gel electrolyte.

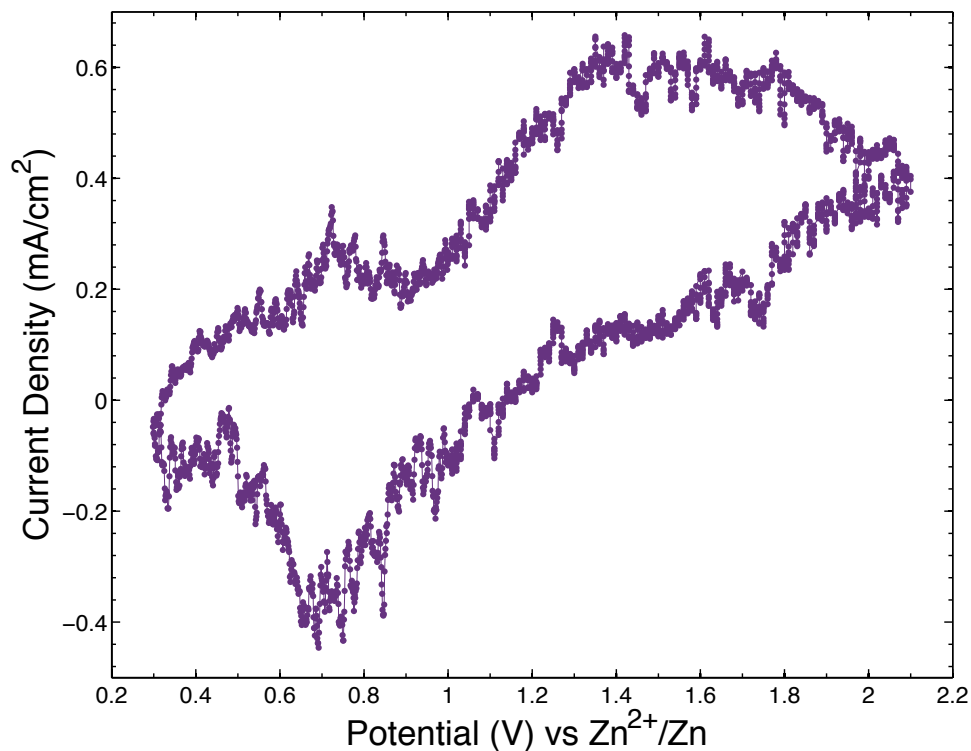


Figure 5.2. Voltammogram for a printed  $V_2O_5$  ambigel electrode, printed gel electrolyte, and zinc foil electrode cell on a nickel substrate. Upon a decreasing voltage sweep, zinc ions insert into the  $V_2O_5$  material, while with increasing voltage, zinc ions extract from the electrode structure. Scan rate of 1 mV/s. The initial polarization direction was towards more positive potentials.

behavior between zinc ions and the  $V_2O_5$  ambigel, cyclic voltammetry of the structure was conducted, and the resulting voltammogram for a 1 mV/s scan rate is shown in Figure 5.2. The broad anodic and cathodic current density peaks detected between 0.25 to 2 V vs.  $Zn^{2+}/Zn$  demonstrate the movement of charge with indications that the reversible electrochemical insertion and extraction of  $Zn^{2+}$  to and from the  $V_2O_5$  ambigel film occurred. Further electrochemical behavior was detected using galvanostatic methods.

#### 5.1.4 Measuring Galvanostatic Cyclability

The same  $V_2O_5$  test structure was probed galvanostatically. The cell potential output between 0.3 and 1.8 V for a constant current discharge using a C/3 rate is displayed in Figure 5.3. The discharge curve exhibits a decreasing cell potential between 1.8 to 0.3V, with slight inflections at approximately 0.9 V and 0.5 V. The discharge potential decreases with increasing depth of discharge; the sloping nature of this decline suggests the mechanism of charge storage is predominantly pseudocapacitive. Galvanostatic cycling of the cell was conducted at the C/3 charge and discharge rate, and the resulting charge (increasing potential with time) and discharge (decreasing potential with time) potential cycles of the cell are displayed in Figure 5.4. The corresponding discharge capacity evolution with cycle was recorded in Figure 5.5. In Figure 5.4, the charge curves (where potential increases from 0.3 to 1.8 V) show a rapid increase between 0.3 to 1.1 V until an inflection, and then increases gradually to 1.8 V. In comparison to the charge cycles, the discharge cycles (where potential decreases from 1.8 V to 0.3 V) displayed

different behavior: the potential decreased without the inflection detected when charging the cell. The difference in charge and discharge behaviors of the cell may stem from the low electronic conductivity of the  $V_2O_5$  ambigel film and low gel electrolyte ionic conductivity, resulting in cumulatively large ohmic losses in the system; this may be remedied by increasing the concentration of electronic conductive additives in the slurry formula to increase the film electronic conductivity (but potentially at the expense of its electrochemical capacity). The coulombic efficiency of the cell at this rate ranged between 85 to 95 %, and its energy efficiency averaged between 40 to 55 %. In Figure 5.5 the cell showed an initial discharge capacity of  $0.36 \text{ mAh/cm}^2$ , and after 14 cycles the capacity diminished about 17%.

### 5.1.5 Tailoring the Electrode Capacity using Dispenser Printing

To demonstrate the printer's ability to tailor the  $V_2O_5$  electrode storage capacity, three test structures were constructed with varying  $V_2O_5$  film thicknesses: 15, 30 and 45  $\mu\text{m}$ . Each of cells was printed on a nickel foil substrate and then coated with a printed gel electrolyte film and a zinc foil electrode. The cells were cycled using the same  $0.1 \text{ mA/cm}^2$  current density, and the discharge potentials of each were recorded between 1.8 and 0.3 V. The discharge cell potentials of the three electrodes are compared in Figure 5.6, and the intersections of their potential curves with the horizontal axis indicate their relative discharge capacities. The thinnest electrode demonstrated  $0.29 \text{ mAh/cm}^2$  storage capacity. The 30  $\mu\text{m}$  electrode (twice as thick as the thinnest electrode) output  $0.58 \text{ mAh/cm}^2$ , twice the capacity of the 15  $\mu\text{m}$  electrode, and the 45  $\mu\text{m}$  electrode (three times as thick as the thinnest electrode) demonstrated a storage of  $0.89 \text{ mAh/cm}^2$ . As illustrated in this exercise, the dispenser printer's ability to pattern with precision in both the lateral and horizontal dimensions is an important asset, and a microbattery's output energy storage capacity can be tailored using this deposition system.

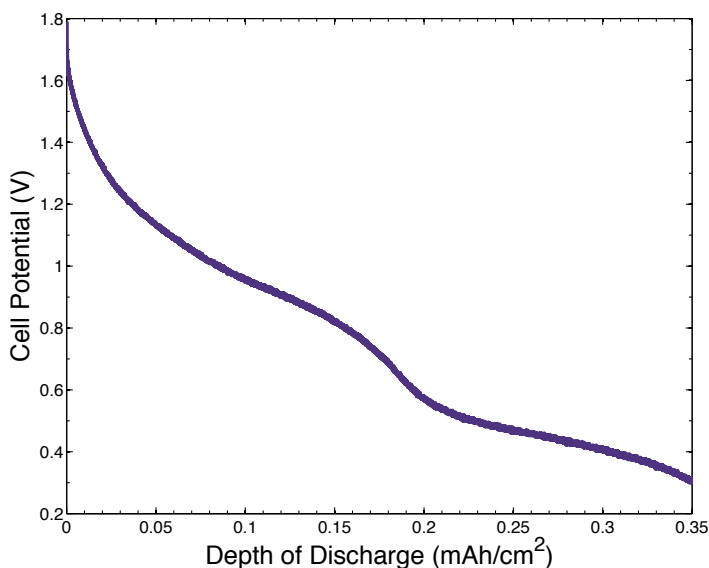


Figure 5.3. Discharge cell potential of a  $V_2O_5$  ambigel electrode, gel electrolyte, and zinc foil electrode on a nickel substrate. Cell was discharged at a C/3 rate.

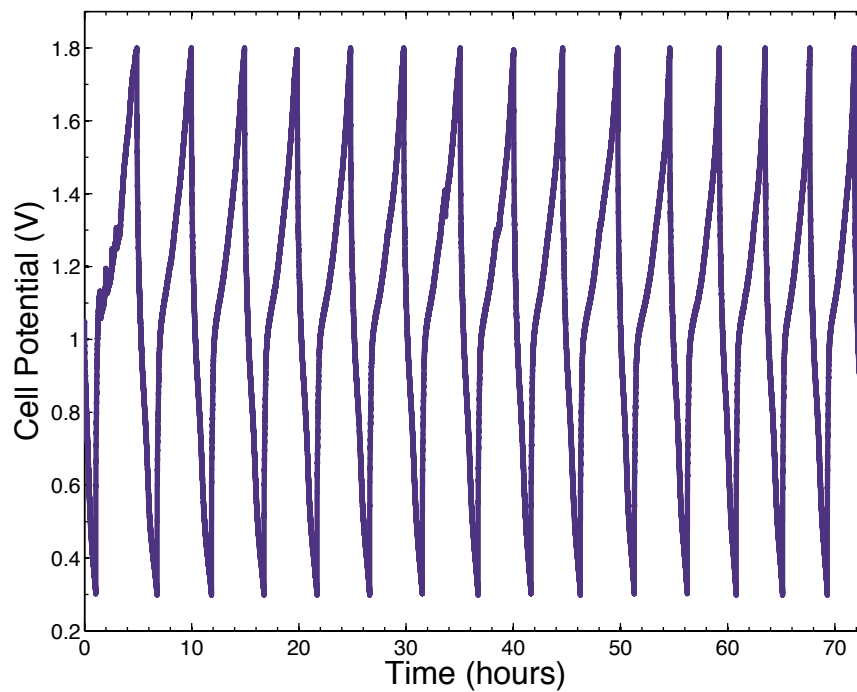


Figure 5.4. The cell potential of a cell containing a  $V_2O_5$  ambigel electrode, gel electrolyte, and zinc foil electrode on a nickel foil substrate due to galvanostatic cycling. Approximately  $C/3$  charge and discharge rates were used.

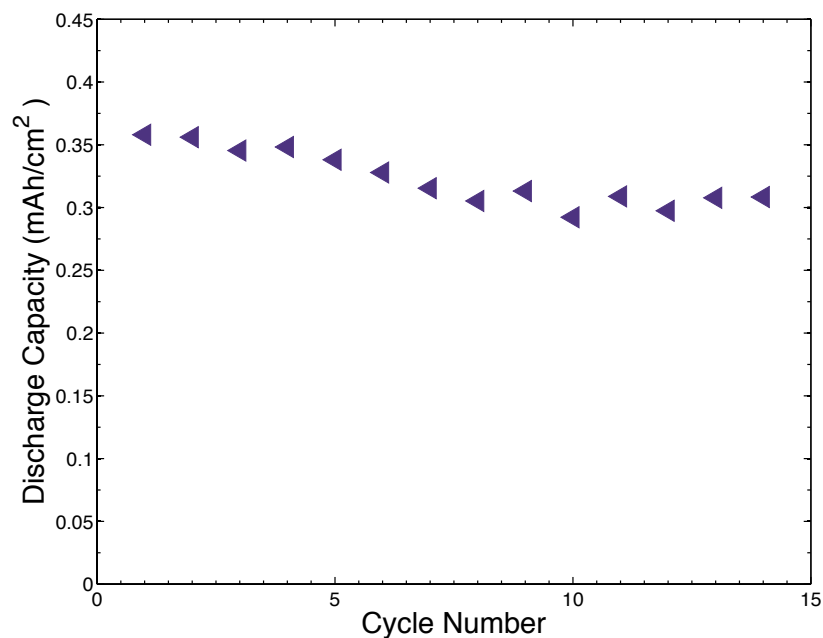


Figure 5.5. The cyclic progression of the discharge capacity of a cell containing a  $V_2O_5$  ambigel electrode, gel electrolyte, and zinc foil electrode on nickel substrate due to galvanostatic cycling. A  $C/3$  discharge rate was used.

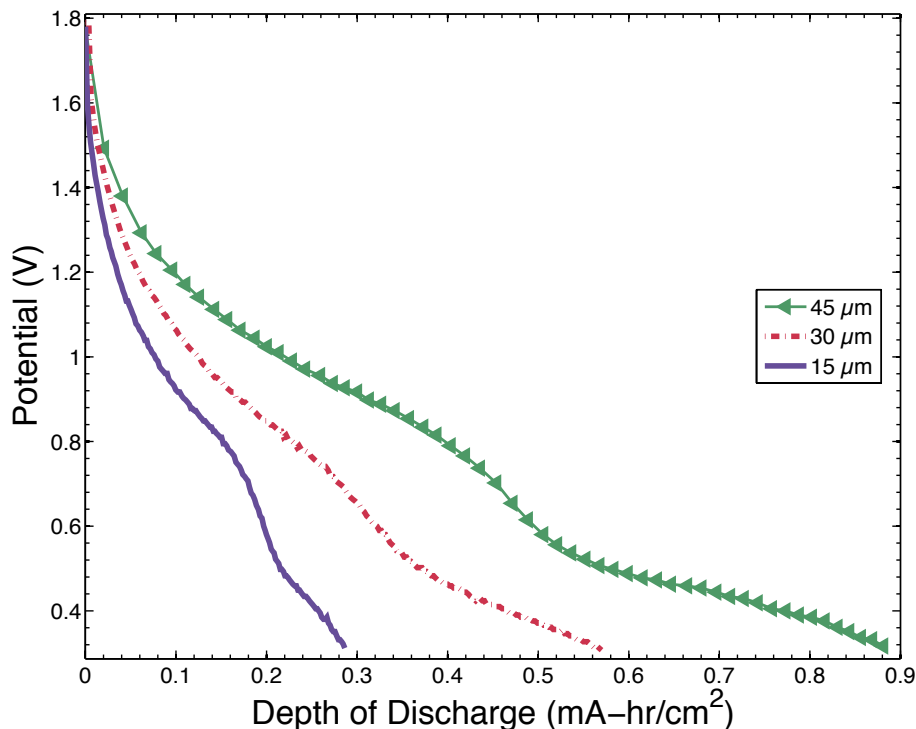


Figure 5.6. The discharge cell potentials of three test cells with 15, 30, and 45  $\mu\text{m}$  thick  $\text{V}_2\text{O}_5$  ambigel dispenser printed electrodes. A  $0.1 \text{ mA/cm}^2$  discharge current density was applied to all cells. The corresponding discharge capacities are 0.29, 0.58, and  $0.89 \text{ mAh/cm}^2$ .

### 5.1.6 Comparing the Electrochemical Capacity of $\text{V}_2\text{O}_5$ Ambigel and Crystalline Powders

The electrochemical performance of the  $\text{V}_2\text{O}_5$  ambigel electrode was compared to that of commercially purchased crystalline  $\text{V}_2\text{O}_5$  material [Sigma Aldrich]. Using the same slurry composition, a printed crystalline  $\text{V}_2\text{O}_5$  electrode assembled in a similar test structure described in section 5.1.4 was cycled galvanostatically, outputting a slightly lower storage capacity of  $0.22 \text{ mAh/cm}^2$ . In comparison to the crystalline material, the  $\text{V}_2\text{O}_5$  ambigel delivered only slight better storage capacity (its measured discharge capacity was  $0.36 \text{ mAh/cm}^2$ ) despite its expected improved properties such as surface area; this may be attributable to processing variability when synthesizing the ambigel, especially during the long-term drying regimen and when crushing the ambigel into a powder. Furthermore, the inconsistency in powder morphology introduced by the synthesis process may have resulted in uneven ambigel particle distribution through the printed films, possibly leading to inhomogeneous performance and therefore a diminished realization of its maximum storage capacity. Regardless, this study of zinc ion insertion in these vanadium pentoxide materials served as an educational feasibility study, and the difficulties with synthesizing the material motivated the search for commercially available electrode powders with better controlled shape, morphology, size distributions, and electrochemical performance.



## 5.2 Compatibility with Printed Manganese Dioxide Cathodes

An alternative insertion electrode material common amongst a few battery chemistries is manganese dioxide ( $\text{MnO}_2$ ). Similar to vanadium pentoxide's properties described in the previous section,  $\text{MnO}_2$  is a transition metal oxide where certain phases have been demonstrated to withstand the reversible electrochemical insertion and extraction of certain ions, such as lithium, and electrons. Compared to other intercalation compounds, it is considered inexpensive, and has an open layered structure amenable to the insertion of ions such as lithium in lithium batteries and water in some alkaline systems.

### 5.2.1 Synthesis of a Printed Manganese Dioxide Electrode

A  $\text{MnO}_2$  and carbon composite electrode ink was synthesized with the formula outlined in Table 5.3. The  $\text{MnO}_2$  ink was printed using the dispenser printer, and Figure 5.7 displays a micrograph of the film's cross section. The  $\text{MnO}_2$  powder size distribution ranges from  $< 1$  to  $20 \mu\text{m}$ , and the particles vary in shape from round spheres to oblong particles.

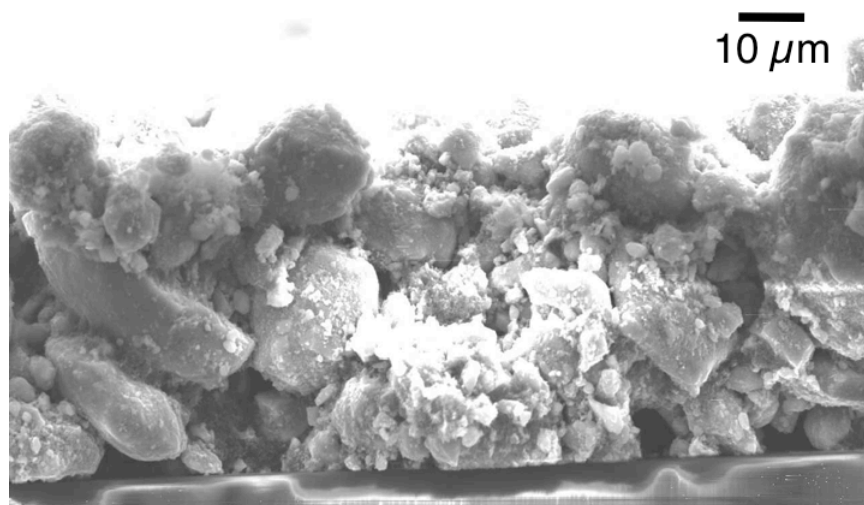


Figure 5.7. Commercial  $\text{MnO}_2$  powder incorporated into a printed film.

Table 5.3.  $\text{MnO}_2$  composite slurry ink composition

	<i>Components</i>	<i>Weight Percent (%)</i>
MnO <sub>2</sub> composite slurry	MnO <sub>2</sub> powder	92
	Acetylene black	4
	PVDF-HFP polymer binder	4

## 5.2.2 Detecting Zinc Ion Electrochemical Insertion in the Printed Manganese Dioxide Electrode

### Cyclic Voltammetry

The electrochemical behavior of the printed  $\text{MnO}_2$  film was characterized using CV. The resulting voltammogram for a 1 mV/s scan rate is displayed in Figure 5.8. Note that nickel foil was used as the current collector and substrate for the printed  $\text{MnO}_2$  film while zinc foil acted both as the electrode and its own current collector. The voltammogram for the  $\text{MnO}_2$  electrode is compared to that of the  $\text{V}_2\text{O}_5$  ambipol film in Figure 5.9. Within the range of 0.3 to 2 V, the voltammogram envelopes for both electrode materials match each other in shape and current density magnitudes. The  $\text{MnO}_2$  cell was probed for a wider electrochemical potential window (from 0 to 2.5 V) but no additional features were discerned.

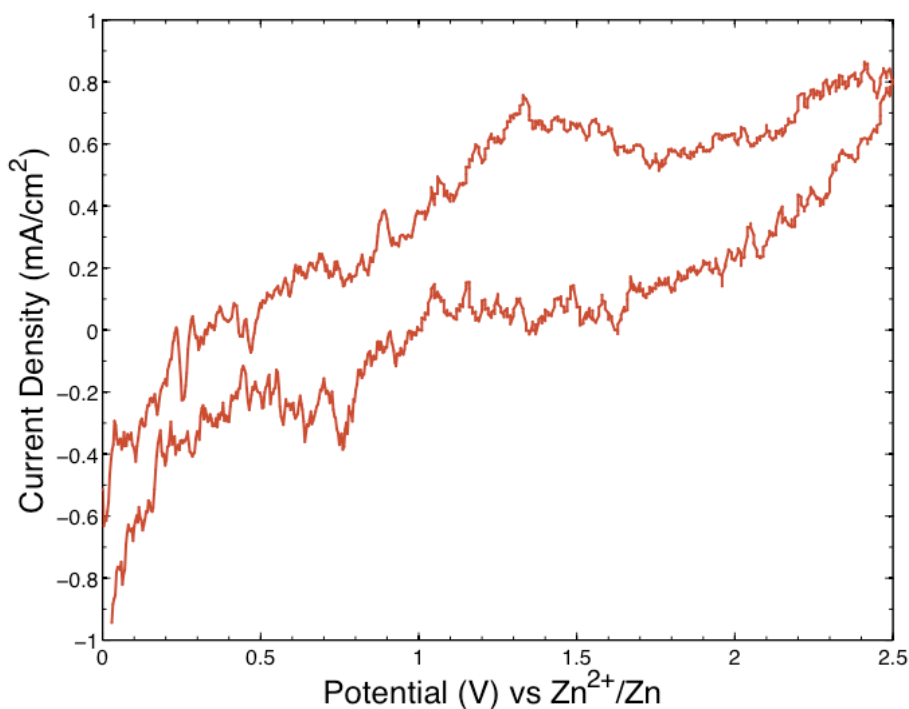


Figure 5.8. Voltammogram for a printed  $\text{MnO}_2$  electrode, printed gel electrolyte, and zinc foil electrode cell. Upon a decreasing voltage sweep, zinc ions insert into the  $\text{MnO}_2$  material, while with increasing voltage, zinc ions extract from the electrode structure. Scan rate of 1 mV/s. The initial polarization direction was towards more positive potentials.

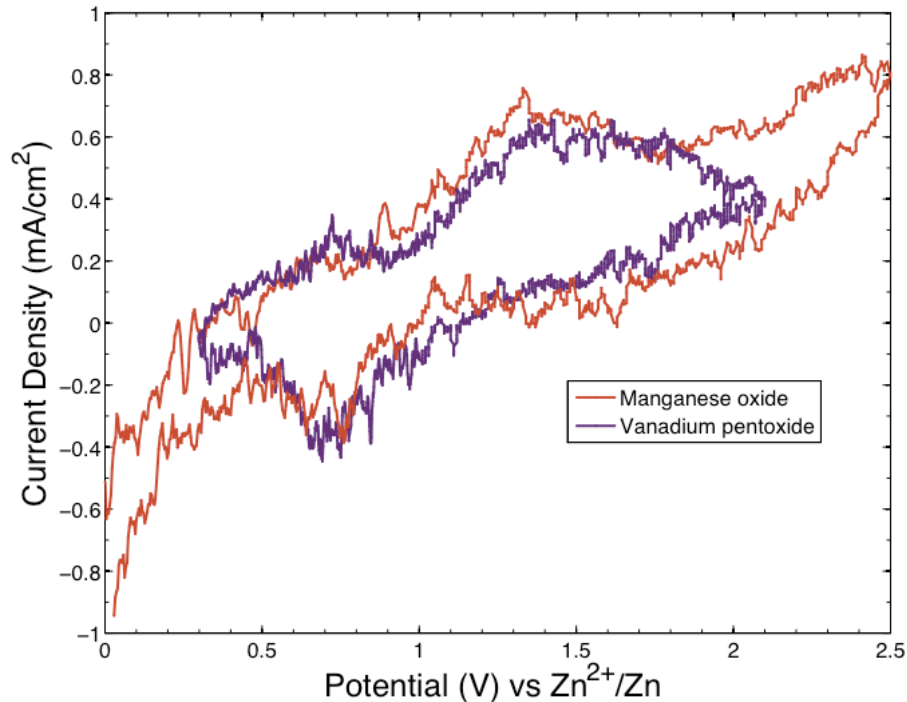


Figure 5.9. Comparison of the voltammograms for test cells with a printed MnO<sub>2</sub> electrode and printed V<sub>2</sub>O<sub>5</sub> electrode, For both voltammograms the scan rate of 1 mV/s was used. The initial polarization direction was towards more positive potentials.

### Electron Dispersive X-Ray Spectroscopy

To confirm that zinc ions had successfully inserted into the cathode material, a cycled MnO<sub>2</sub> composite electrode was compared to fresh MnO<sub>2</sub> films using electron dispersive x-ray spectroscopy (EDS) for elemental analysis. The EDS spectrum of a fresh printed MnO<sub>2</sub> composite film is shown in Figure 5.10 (a), confirming the presence of manganese, oxygen, carbon (both from the conductive carbon additives as well as the polymer), and fluorine atoms from the fluorinated polymer binder (the constituents of PVDF-HFP are  $[-(C_2H_2F_2)_n-]$  and  $[C_3F_6]$ ). To improve the film robustness for characterization purposes, both cycled and fresh films were cast on gel electrolyte film backings. The EDS spectrum of the fresh MnO<sub>2</sub> film on the gel backing in Figure 5.10 (b) showed an additional presence of sulfur and an enhanced fluorine peak, both due to the additional contributions of the zinc salt triflate anion  $[CF_3SO_3^-]$  in the gel electrolyte. The cycled film, which was cycled 20 times using cyclic voltammetry and then held at 1.0 V with respect to a zinc electrode for 5 hours, exhibited the EDS spectrum shown in Figure 5.10 (c). Note that the electron beam was positioned on the exposed side of the MnO<sub>2</sub> film, which when electrochemically cycled would have been in contact with the nickel current collector and farthest away from the gel electrolyte interface as well as the zinc electrode. In this film, two zinc peaks are clearly visible, indicating the presence of zinc within the cycled electrode film. Though the EDS experiments confirm an increased zinc concentration in the cycled cathode film, they do not distinguish between zinc atoms that may have adsorbed onto the surface of the MnO<sub>2</sub> particles versus those that may have inserted into the host structure. Further studies differentiating the pseudocapacitive from intercalated zinc within the MnO<sub>2</sub> material are needed.

### 5.2.3 Galvanostatic Characterization of the Printed Manganese Dioxide Electrode

#### Cathode Activation

The MnO<sub>2</sub> composite electrode test structure was also galvanostatically cycled against a zinc foil electrode. For many cells that were tested, it was observed that with a moderately slow charge and discharge rate ( $< C/2$ ), an activation process occurred within the initial cycles. This usually manifested in a significant capacity increase within the first 25 galvanostatic cycles. As seen in Figure 5.11, the printed battery's discharge capacity increased more than two-fold between cycles 7 and 9, and maintains this storage capacity with further cycling. A comparison of the charge and discharge curves for cycle 3 and cycle 11 is shown in Figure 5.12. Note that when comparing the two cycles, not only do cycle 11's charge and discharge potential curves lengthen two-fold with depth of discharge, the shape of the curve is also altered: a sharp knee is visible upon charging at 1.52 V, and a steeper vertical decline occurs when switching between charge and discharge. The former feature suggests that the manganese dioxide electrode undergoes an activation process induced by the insertion of zinc ions, which may be causing the crystalline material to increase in volume or undergo a phase change. There have been reports suggesting that the manganese dioxide material is prone to change from its crystalline to amorphous phase when electrochemically cycled [Ohzuku, *et al.*, 1991]. This phase change is accompanied by an enhanced accessibility to interfacial sites upon which zinc ions may react, and therefore an increase in storage capacity. In addition to a capacity increase, the cell demonstrates an increased ohmic drop when switching current directions. This increase in ohmic resistance in the cell after initial cycling may have occurred due to the amorphous phase of manganese dioxide being more electronically resistive than the crystalline phase, or a morphology change may have occurred, causing a disruption in electronic pathways through the electrode film. Further characterization of this activation mechanism, for example with x-ray diffraction, is recommended.

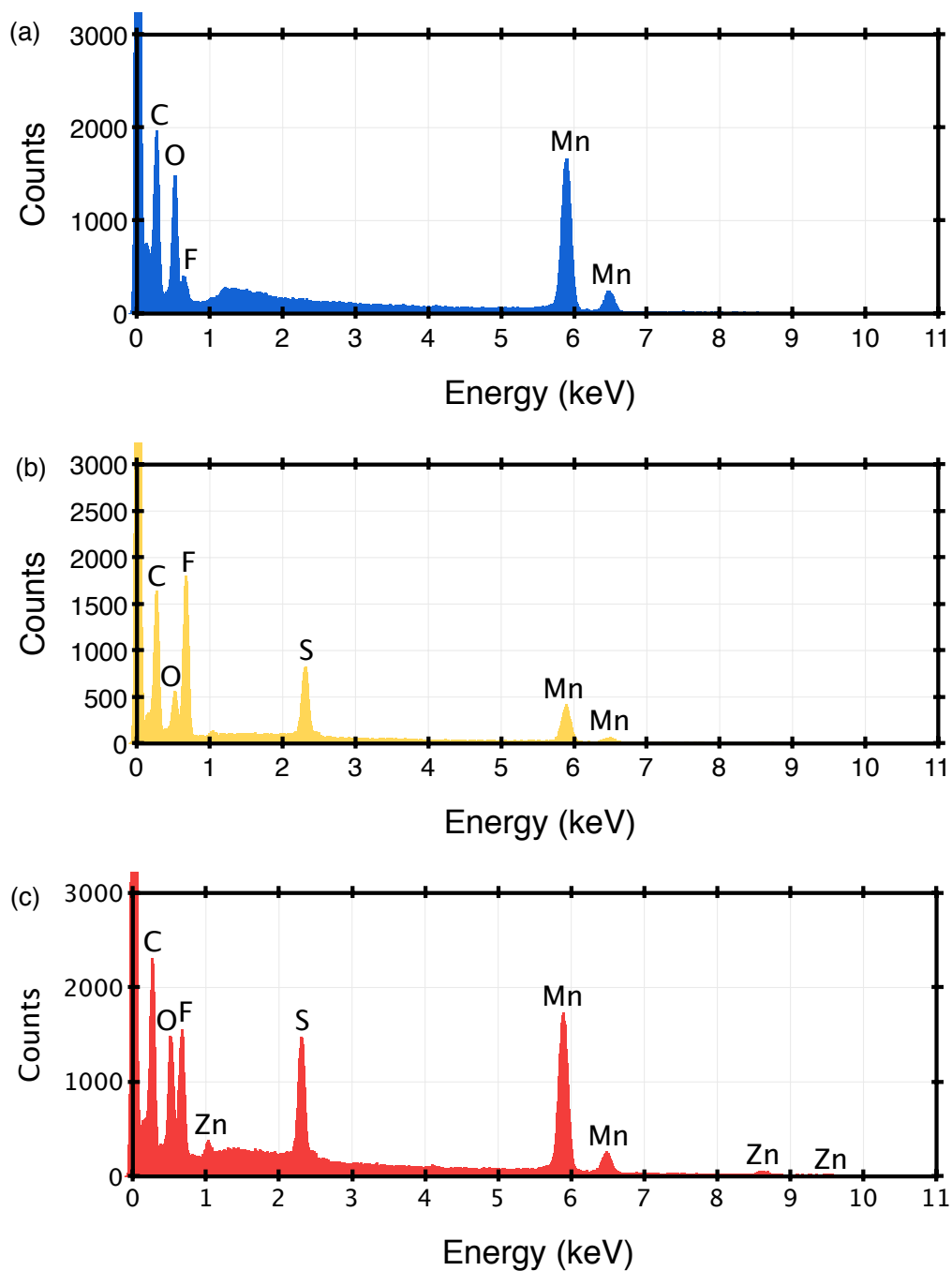


Figure 5.10. (a-c) Energy dispersive x-ray spectroscopy (EDS) scans for (a) a freshly printed MnO<sub>2</sub> film, (b) a freshly printed MnO<sub>2</sub> film on a gel electrolyte backing, and (c) a MnO<sub>2</sub> film on a gel electrolyte backing after 20 galvanostatic cycles against a zinc foil electrode (zinc foil was removed from the cell during the EDS experiment).

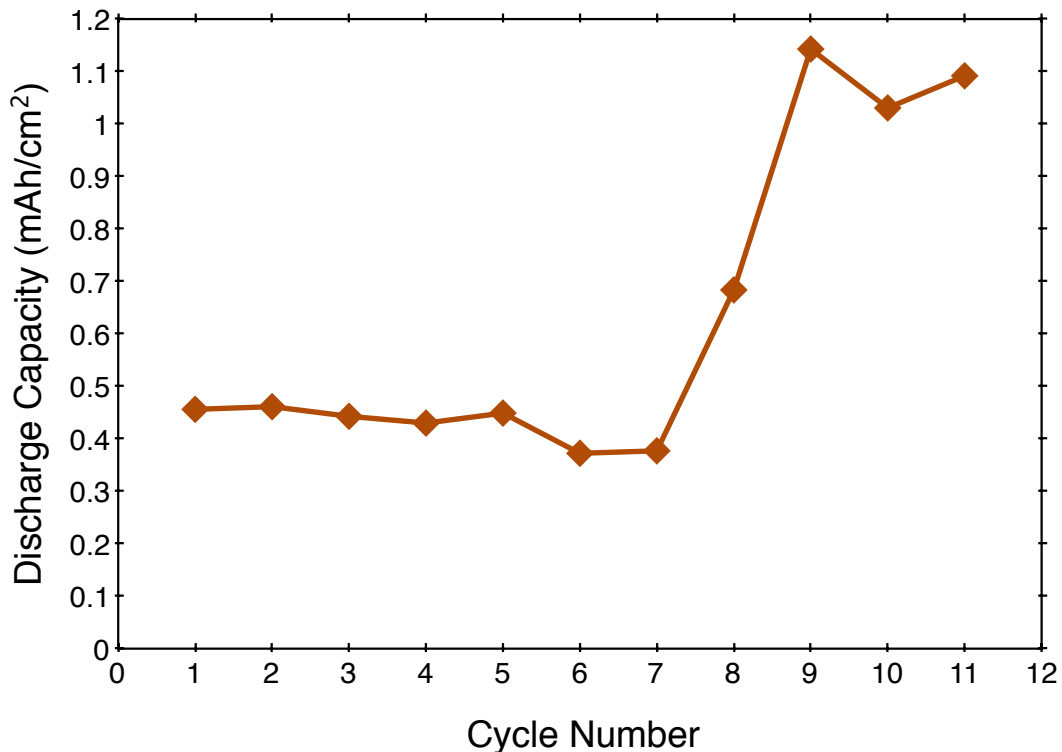


Figure 5.11. The first eleven galvanostatic cycles of a cell containing a printed MnO<sub>2</sub> composite electrode, gel electrolyte, and zinc foil electrode. A C/5 discharge rate was used. Between cycle 7 and cycle 9 a significant discharge capacity increase is observed.

### Galvanostatic Intermittent Titration Technique

A supplementary study on the galvanostatic behavior of the cell was conducted using the galvanostatic intermittent titration technique (GITT). GITT utilizes a series of transient and steady state measurements to determine the kinetic properties of zinc ion transport within the MnO<sub>2</sub> host material. A more detailed description of this electrochemical technique and derivation for determining the chemical diffusion coefficient in the solid conducting structure are available in Section 9.4.3.

A cell containing an MnO<sub>2</sub> composite electrode, gel electrolyte, and zinc foil electrode was tested. An example of one GITT cycle involved a 10  $\mu$ A (40  $\mu$ A/cm<sup>2</sup>) discharge current held for 30 minutes followed by five hours of rest at open circuit. The cell potential's response is shown in Figure 5.13. The steady state potential ( $E_{\text{steady state}}$ ) that the cell evolves to after five hours of equilibration is tracked for each current pulse, which can be correlated to the stoichiometric addition of zinc to the MnO<sub>2</sub> electrode. For a discharge GITT routine, the steady state potential of the cell with increased depth of discharge is displayed in Figure 5.14. The equilibrium potentials are shown to decrease from 1.56 to 1.25 V, and the cell exhibited a capacity of 258  $\mu$ Ah/cm<sup>2</sup>. The stoichiometric addition of zinc ions inserted in the MnO<sub>2</sub> composite electrode ( $\Delta\delta$ ) can be

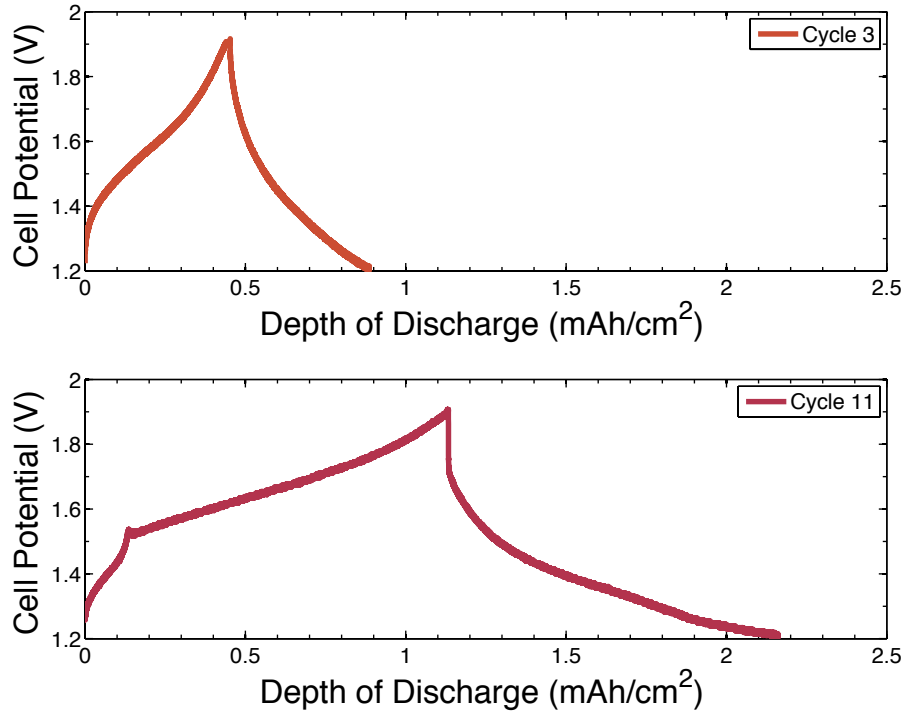


Figure 5.12. A comparison of the potential of a printed MnO<sub>2</sub> electrode, gel electrolyte, and zinc foil electrode cell. The galvanostatic charge (increasing cell potential) and discharge (decreasing cell potential) potentials of the third and eleventh cycle are compared.

quantified using the following expression:

$$\Delta\delta = \frac{I\tau M_{\text{host}}}{z_{\text{ion}} m_{\text{host}} F} \quad (\text{Equation 5.1})$$

In this expression,  $I$  is the current applied over a defined amount of time ( $\tau$ ),  $M_{\text{host}}$  is the atomic weight of the host material,  $z_{\text{ion}}$  is the valence of the electroactive ion,  $m_{\text{host}}$  is the mass of the host material, and  $F$  is Faraday's constant. From the exhibited capacity,  $\Delta\delta = 0.58$ , which represents the amount of zinc ion insertion into Zn<sub>δ</sub>MnO<sub>2</sub>. The cell was not discharged to lower potentials because of its large internal resistance, as observed in the ohmic drop in Figure 5.14. By evaluating the steady state potentials as well as the transient cell voltage behavior over time, the chemical diffusion coefficient ( $\tilde{D}$ ) in Zn<sub>δ</sub>MnO<sub>2</sub> can be expressed as:

$$\tilde{D} = \frac{4}{\pi} \left( \frac{m_{\text{host}} V_M}{M_{\text{host}} S} \right)^2 \left( \frac{\Delta E_{\text{steady state}}}{\tau \left( \frac{dE}{d\sqrt{t}} \right)} \right) \quad \text{for } \tau \ll \frac{L^2}{\tilde{D}} \quad (\text{Equation 5.2})$$

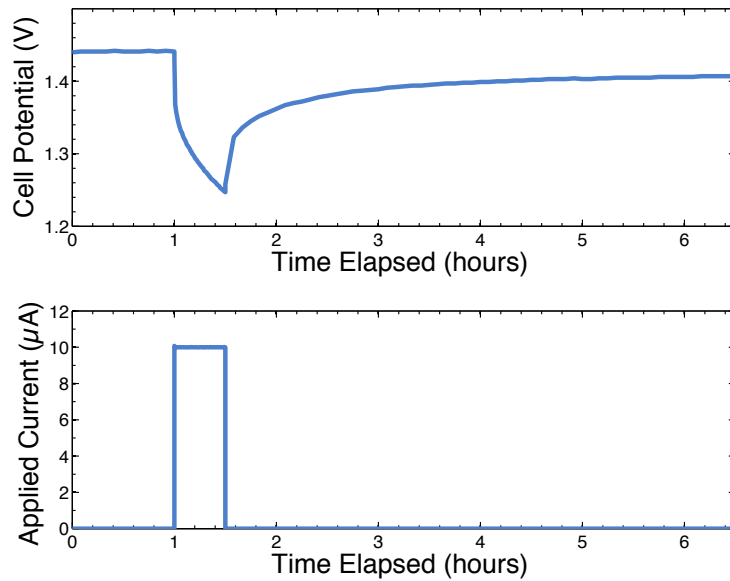


Figure 5.13. Galvanostatic intermittent titration technique (GITT) procedure: current is applied for 30 minutes to a cell, then held at open circuit for 5 hours while the cell potential is monitored.

where  $V_M$  is the molar volume of the sample,  $S$  is the interfacial area between the electrode and electrolyte,  $(\Delta E_{\text{steady state}})$  is the change in steady state potential,  $\left(\frac{dE}{d\sqrt{t}}\right)$  is the slope of the transient cell potential with respect to the square root foot of time

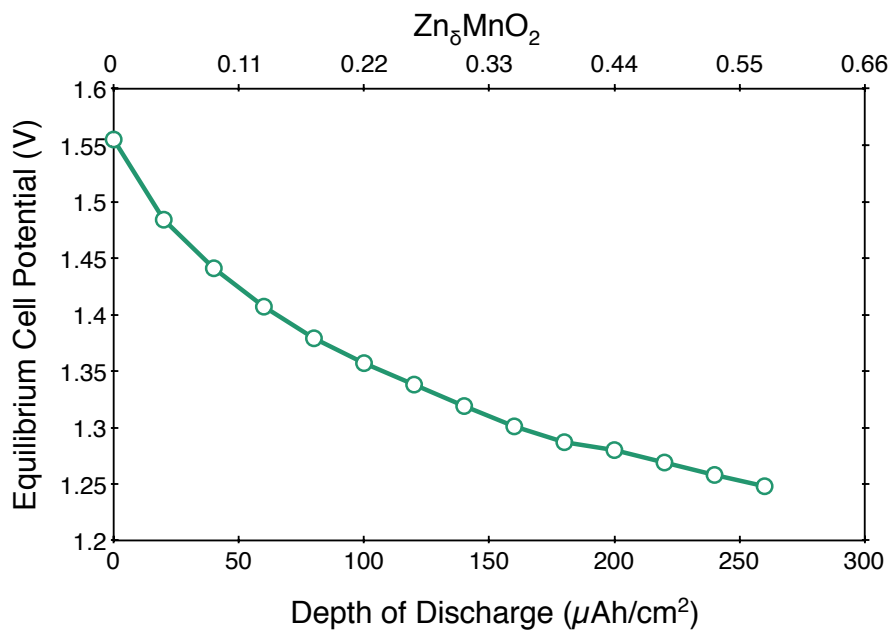


Figure 5.14. The equilibrium potential as a function of depth of discharge and stoichiometry for a cell comprised of a printed  $\text{MnO}_2$  electrode, gel electrolyte, and zinc foil electrode from GITT measurements.



elapsed, and L is the mid length of the electrolyte layer. This is the measure of solid-state diffusion within the electrode host material. From this expression, the average chemical diffusion coefficient of  $Zn_8MnO_2$  over the measured cell potentials was  $1.8 \cdot 10^{-14}$  cm<sup>2</sup>/s. The zinc ion component diffusion in manganese dioxide was calculated from the following equation:

$$D_{\text{component}} = -\frac{4kTm_{\text{host}}V_M I_o}{\pi c_{\text{ion}} z_{\text{ion}}^2 q^2 M_{\text{host}} S^2 \tau} \frac{\Delta E_{\text{steady state}}}{\left(\frac{dE}{d\sqrt{t}}\right)^2} \quad \text{for } \tau \ll \frac{L^2}{\tilde{D}} \quad (\text{Equation 5.3})$$

where k is Boltzmann's constant, T is the absolute temperature, and  $c_{\text{ion}}$  is the concentration of the electroactive ion. From the above calculation, the average component diffusion coefficient of zinc in  $Zn_8MnO_2$  was  $3.1 \cdot 10^{-17}$  cm<sup>2</sup>/s. Sources of comparison to this value include the proton diffusion coefficient in electrolytic manganese dioxide ( $10^{-15}$  to  $10^{-16}$  cm<sup>2</sup>/s) [Qu, 2004], the diffusion coefficient of lithium ions in manganese oxides (from  $10^{-9}$  to  $10^{-12}$  cm<sup>2</sup>/s, variability due to difference processing methods of the manganese oxides) [Chen, *et al.*, 1995], the lithium ion diffusion coefficient in crystalline vanadium pentoxide ( $10^{-11}$  to  $10^{-12}$  cm<sup>2</sup>/s), and the diffusion coefficient of polyvalent yttrium in vanadium pentoxide ( $10^{-14}$  to  $10^{-15}$  cm<sup>2</sup>/s) [Amatucci, *et al.*, 2001]. In this system, zinc ions exhibit transport a few orders of magnitude slower than the diffusion of the other species reported. Better control of the electrode properties including the enhancement of its electronic conductivity as well as the reduction of its ion diffusion pathways by using nanostructured materials could drastically improve the zinc ion transport within manganese dioxide.

The GITT routine's current pulse direction was reversed, and the steady state charge potentials were recorded, as illustrated in Figure 5.15. The steady state potentials generally increase with charge extraction, however the shape of the curve shows various horizontal and decreasing regions. These features may correspond to changes in the electrode volume or phase changes due to zinc ions extracting out of the host material. From 1.26 to 1.63 V, the cell exhibits a capacity of 1210  $\mu\text{Ah}/\text{cm}^2$ . With a 24 % coulombic efficiency, the large discrepancy in discharge and charge capacities demonstrated the irreversible nature of the zinc insertion and extraction mechanisms in the electrode, however with further cycling, the GITT discharge showed substantial capacity increase; for example the second discharge cycle exhibited a 40% increase from the first cycle, achieving nearly 400  $\mu\text{Ah}/\text{cm}^2$ , and an improved coulombic efficiency of 38 % (Figure 5.16).

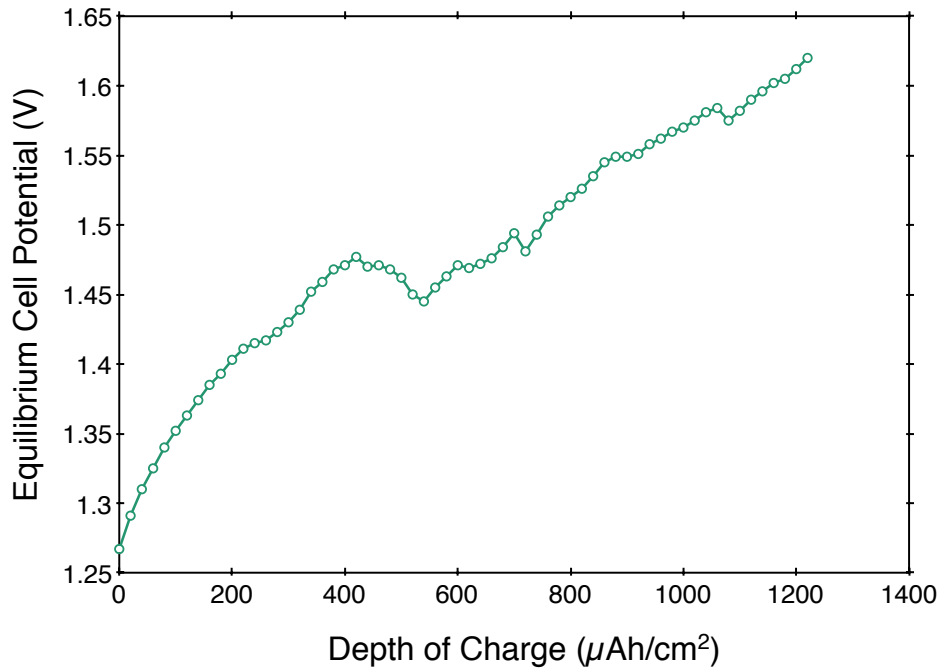


Figure 5.15. The equilibrium potential as a function of depth of charge for a cell comprised of a printed MnO<sub>2</sub> electrode, gel electrolyte, and zinc foil electrode from GITT measurements.

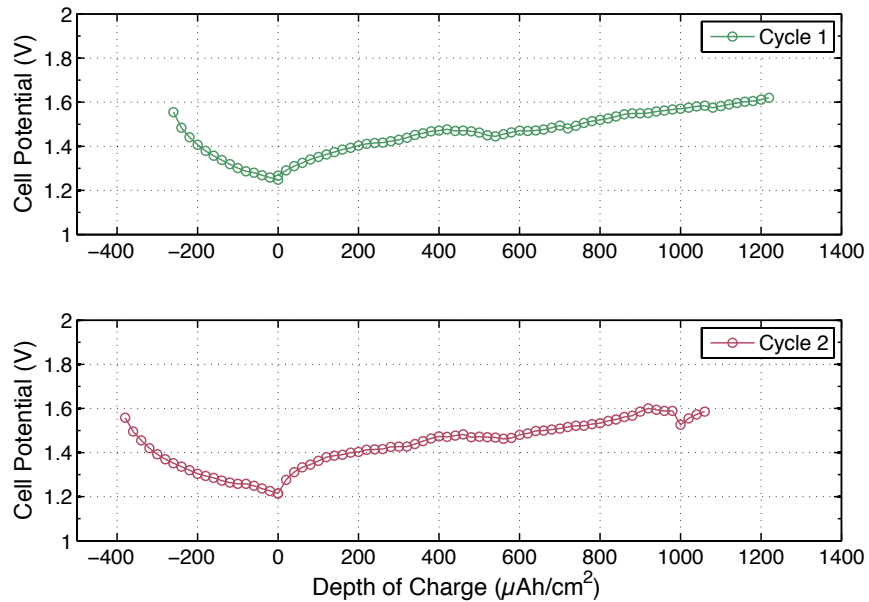


Figure 5.16. The equilibrium potentials as a function of depth of charge (for a cell comprised of a printed MnO<sub>2</sub> electrode, gel electrolyte, and zinc foil electrode from GITT measurements). The equilibrium cell potentials with respect to the discharge capacity (negative depth of charge) and charge capacity (positive depth of charge) are plotted for the first two cycles.

## 5.2.4 Electrochemical Impedance Spectroscopy

The influence of the cell potential on the electrochemical behavior of zinc ions in the manganese dioxide composite electrode was also investigated using electrochemical impedance spectroscopy (EIS). The EIS experiments were done in tandem with the GITT measurements so that the impedance spectra of the cell could be recorded within the range of equilibrium cell potentials that were tested. With the application of small AC signals to an electrochemical cell, any impedances to these signals can be detected; by varying the frequencies of the input signals, different types of impedances can be differentiated due to their frequency response. As a result, some transport properties can be extrapolated from these measurements.

For a small AC input amplitude of 5 mV and a frequency sweep between 0.01 to  $10^6$  Hz, the impedance spectra of a cell containing a  $\text{MnO}_2$  composite electrode, gel electrolyte, and zinc foil were recorded along one discharge and charge GITT cycle at each steady state potential without the application of a DC bias. An example of an impedance spectrum of a cell taken at 1.555 V is shown in Figure 5.17. The spectrum maps the low to high frequency responses of the cell from the right to left of the plot. The impedance output for the cell appears as an envelope combining one quarter circle at high frequencies (corresponding to  $Z_{\text{real}} = 1\text{-}7 \text{ k}\Omega/\text{cm}^2$ ) and a large semi-oval encompassing most of the mid to low frequency range (corresponding to  $Z_{\text{real}} = 7\text{-}63 \text{ k}\Omega/\text{cm}^2$ ), followed by a short upturn (corresponding to  $Z_{\text{real}} = 63\text{-}68 \text{ k}\Omega/\text{cm}^2$ ). This spectrum suggests four phenomena contributing to the cell's overall polarization: the solution resistance at very high frequencies, the resistance due to the presence of surface films, the charge transfer resistance at the electrode and electrolyte interface, and diffusion effects at low frequencies. The quarter circle (the part of the spectrum corresponding to  $Z_{\text{real}} = 1\text{-}7 \text{ k}\Omega/\text{cm}^2$ ) results from the surface film and solution

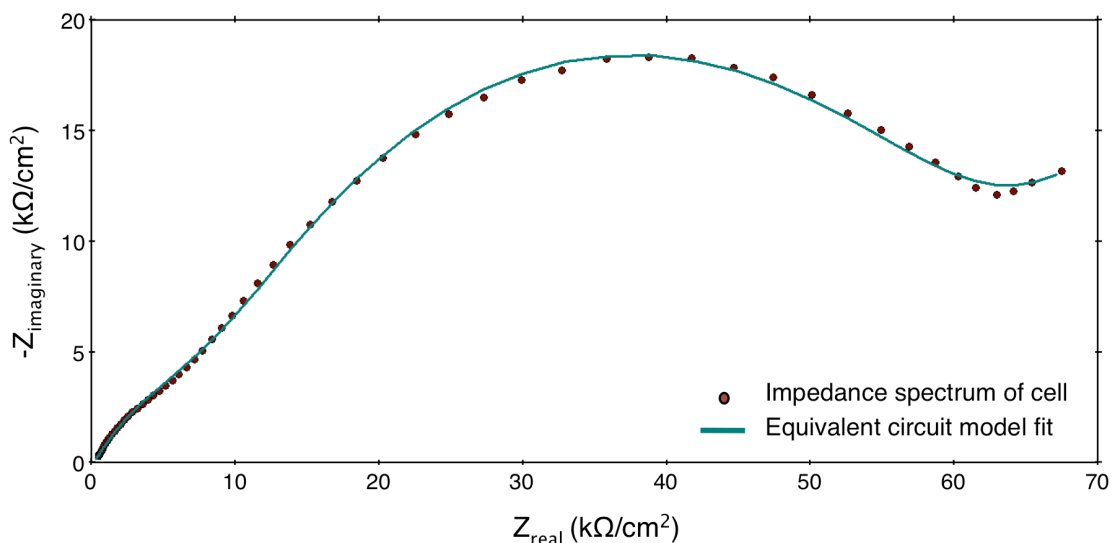


Figure 5.17. Electrochemical impedance spectrum of a printed  $\text{MnO}_2$  electrode, gel electrolyte, and zinc foil cell at 1.555 V with equivalent circuit model fit. The EIS scans were recorded at the equilibrium potential of the cell with an AC input amplitude of 5 mV and a frequency sweep between 0.01 to  $10^6$  Hz. From the equivalent circuit model fit,  $R_{\text{solution}}=239.6 \text{ }\Omega$ ,  $R_{\text{surface}}=9.86 \text{ k}\Omega$ ,  $R_{\text{charge transfer}}=49.5 \text{ k}\Omega$ . All fit parameters are listed in Chapter 9, Table 9.2.

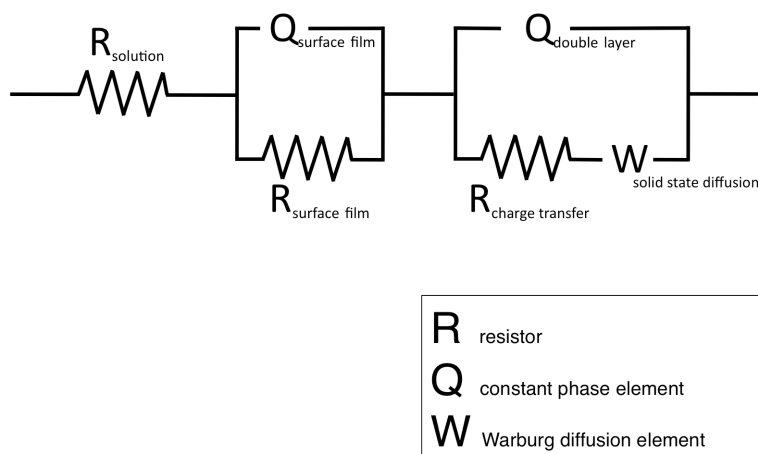


Figure 5.18. Equivalent circuit model for a printed  $\text{MnO}_2$  electrode, gel electrolyte, and zinc foil cell.

impedance, while the larger semi-oval and upturn (corresponding to  $Z_{\text{real}} = 7\text{-}68 \text{ k}\Omega/\text{cm}^2$ ) are due to the mixed contributions of charge transfer and diffusion. The combination of these four mechanisms of impedance can be summarized with the equivalent circuit illustrated in Figure 5.18. Details on the equivalent circuit elements and EIS experimental principles are discussed in the Section 9.3. Note that constant phase elements were used in place of capacitors to better represent their non-ideal behavior, especially in systems in which the capacitive signals are distributed due to interfacial inhomogeneity and surface roughness. Furthermore, a Warburg diffusion element was included in the circuit to represent the solid-state diffusion of zinc within the  $\text{MnO}_2$  composite electrode. The electrical characteristics of the constant phase elements and Warburg diffusion element are discussed in detail in the Section 9.3.1. For each equilibrium cell potential, its corresponding impedance spectrum was fitted with the equivalent circuit model. Figure 5.17 includes the best fit of the impedance spectrum data taken for the cell at 1.555 V, and that the model and data align demonstrates the efficacy of the equivalent circuit model selected for this system.

The cell's impedance spectra from the discharge routine were recorded from 1.555 to 1.248 V, and the first and last measurements are displayed in Figure 5.19. The spectrum taken for the cell at 1.248 V replicates the high frequency behavior of the 1.555 V scan but deviates in the charge transfer region; its charge transfer semi-circle appears more compressed. Of the phenomena contributing to the cell impedances, the mixed contributions of the charge transfer kinetics and diffusion appear to be most profoundly affected by the cell's steady state voltage. This is supported by the EIS spectra of the charge scans compared in Figure 5.20. With increasing cell potential from 1.267 to 1.620 V, the charge transfer and diffusion semi-circles elongate and expand with the same trend as the discharge scan. The kinetics of a charge transfer reaction can be expressed using the Butler-Volmer equation:

$$i = i_o \left( e^{\frac{\alpha n F \eta}{RT}} - e^{-\frac{(1-\alpha) n F \eta}{RT}} \right) \quad (\text{Equation 5.4})$$

where the reaction current ( $i$ ) depends on the exchange current density ( $i_o$ ), the overpotential ( $\eta=E-E_o$ ), and the transfer coefficient ( $\alpha$ ), the number of electrons passed ( $n$ ), the cell temperature ( $T$ ), and the gas constant ( $R$ ). The expression above is valid when the concentrations of oxidants and reactants in the bulk are the same as at the surface of the electrode, and when a system is solely charge transfer limited [Orazem, *et al.*, 2006]. The Butler-Volmer equation can be simplified further to estimate the exchange current density, which indicates the inherent rate of electron transfer for an electrochemical reaction, from the charge transfer resistance ( $R_{\text{charge transfer}}$ ) measured using EIS. For small alternating current (AC) perturbations and a system at equilibrium (where no direct current (DC) bias is applied), the exchange current density can be expressed as:

$$i_o = \frac{RT}{2FR_{\text{charge transfer}}} \quad (\text{Equation 5.5})$$

The relationship between the charge transfer resistance measured for different steady state voltages from the MnO<sub>2</sub> composite electrode, gel electrolyte, and zinc foil cell and its estimated exchange current density is summarized in Figure 5.21. All data are represented in terms of the amount of charge passed into or out of the MnO<sub>2</sub> electrode. The average charge resistance and exchange current density for the cell are 65.2 kΩ and 0.21 μA/cm<sup>2</sup>, respectively. Upon discharge, the charge transfer resistance of the cell shows a generally increasing but non-monotonic trend with decreasing cell potential, resulting in the opposite trend for the exchange current density. Interestingly, the charge transfer resistance does not show a hysteresis when charging the cell; instead the charge transfer resistance increases with increasing cell potential upon charge, resulting in a gradual decrease in exchange current density. Repeating this experiment over a few discharge and charge cycles may be insightful in understanding the evolution of these charge transfer properties with cycle life. A table describing all the parameters calculated using the equivalent circuit model is included in Table 9.1, and the equivalent circuit fit for the EIS data for the microbatteries can be compared for the range of equilibrium cell potentials measured for charge and discharge sweeps by examining the fit variables in Tables 9.2 and 9.3.

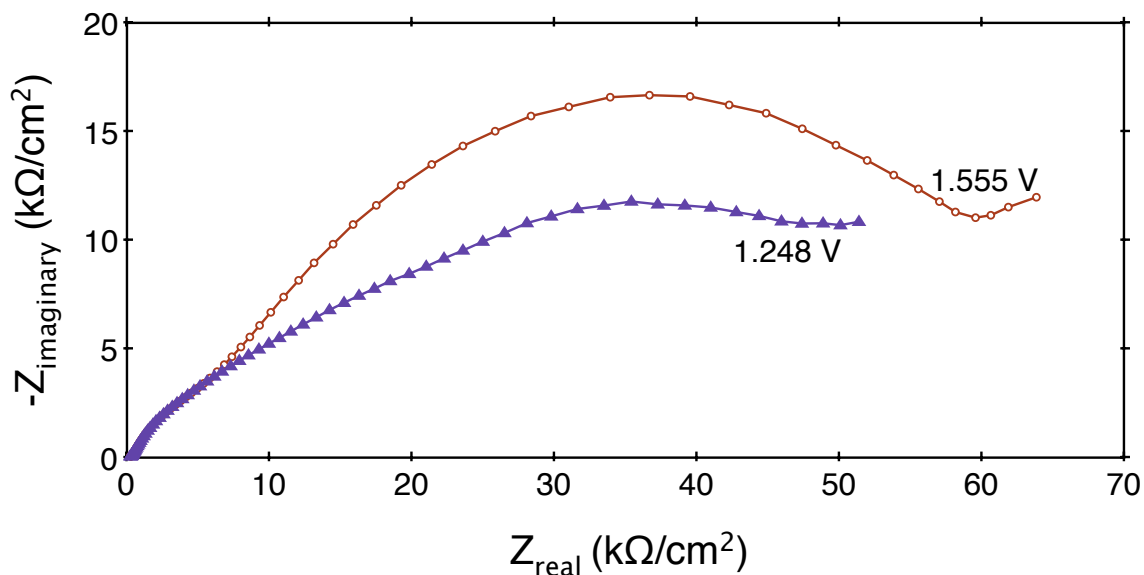


Figure 5.19. The first and last discharge impedance spectra corresponding to equilibrium cell potentials of 1.555 V and 1.248 V. The cell that was probed contained a printed MnO<sub>2</sub> electrode, gel electrolyte, and zinc foil electrode. The EIS scans were recorded at the equilibrium potential of the cell with an AC input amplitude of 5 mV and a frequency sweep between 0.01 to 10<sup>6</sup> Hz.

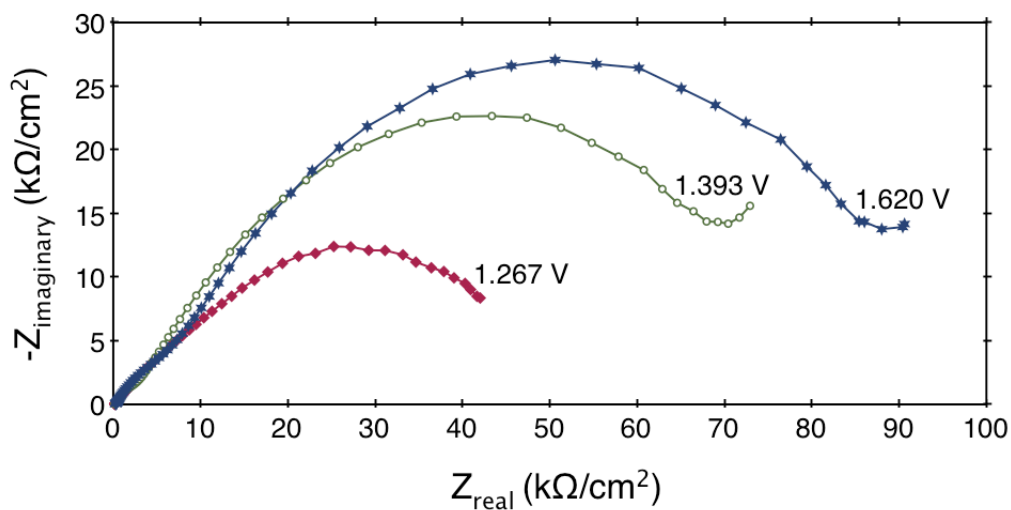


Figure 5.20. A comparison of the charge impedance spectra corresponding to equilibrium cell potentials of 1.267, 1.393, and 1.620 V. The cell that was probed contained a printed MnO<sub>2</sub> electrode, gel electrolyte, and zinc foil electrode. The EIS scans were recorded at the equilibrium potential of the cell with an AC input amplitude of 5 mV and a frequency sweep between 0.01 to 10<sup>6</sup> Hz.

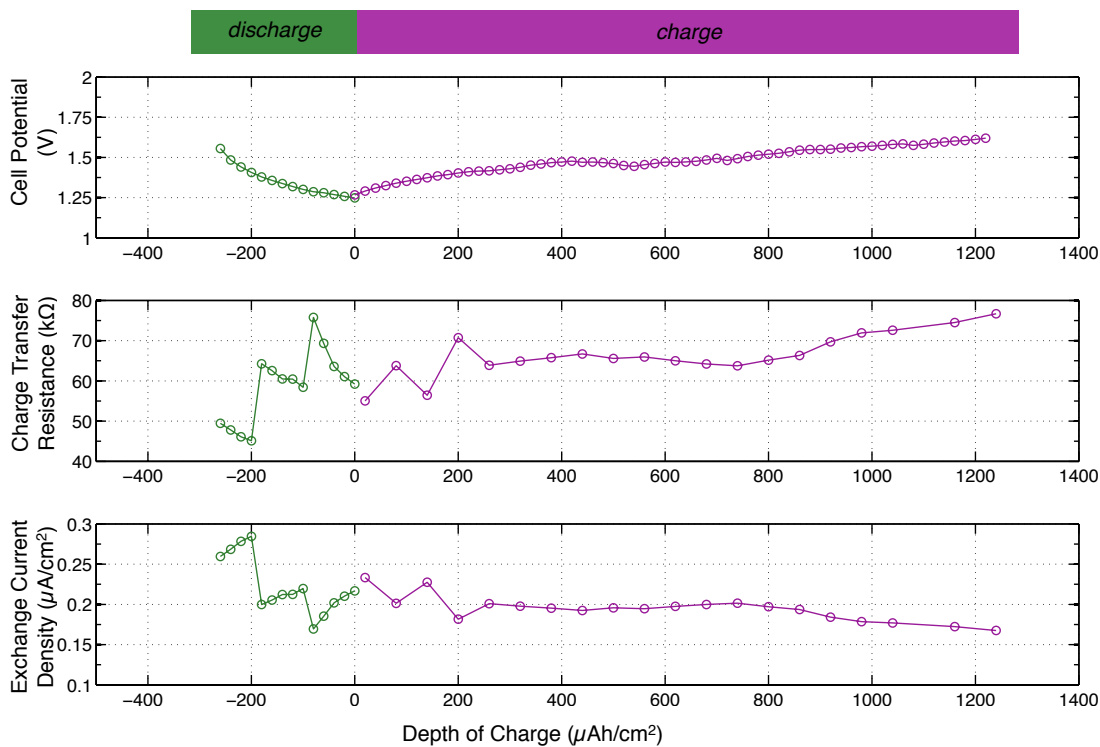


Figure 5.21. Equilibrium cell voltage, charge transfer resistance, and exchange current density of a cell containing a printed MnO<sub>2</sub> electrode, gel electrolyte, and zinc foil electrode. The charge transfer resistances and exchange current densities were calculated from equivalent circuit models used to fit electrochemical impedance spectra (EIS) measurements. The EIS scans were recorded at the equilibrium potential of the cell with an AC input amplitude of 5 mV and a frequency sweep between 0.01 to 10<sup>6</sup> Hz.

### 5.3 Concluding Remarks on the Gel Electrolyte Compatibility with Transition Metal Oxide Cathodes

From the experiments described in this section, manganese dioxide appears to be a suitable insertion host for zinc ions, and will serve as a cathode material in a zinc-metal oxide electrochemical battery. The charge transfer and transport behavior of zinc in manganese dioxide appears complex, and further characterization of these properties are important to the development and optimization of this battery chemistry.

### 5.4 References

Amatucci, G. G., Badway, F., Singhal, A., Beaudoin, B., Skandan, G., Bowmer, T., et al. (2001). Investigation of Yttrium and Polyvalent Ion Intercalation into Nanocrystalline Vanadium Oxide. *Journal of the Electrochemical Society*, 148 (8), A940-A950.

Braithwaite, J. S., Catlow, C. R., Gale, J. D., & Harding, J. H. (1999). Lithium Intercalation into Vanadium Pentoxide: a Theoretical Study. *Chemistry of Materials*, 11 (8), 1990-1998.

- Chen, L., Huang, X., Kelder, E., & Schoonman, J. (1995). Diffusion Enhancement in  $\text{Li}_x\text{Mn}_2\text{O}_4$ . *Solid State Ionics* , 76, 91-96.
- Chippindale, A. M., Dickens, P. G., & Powell, A. (1991). Insertion Compounds Of Transition-Metal And Uranium Oxides. *Progress in Solid State Chemistry* , 21, 133-198.
- Dean, J. (1992). *Lange's Handbook of Chemistry*. New York: McGraw Hill.
- Dong, W., Sakamoto, J., & Dunn, B. (2003). Electrochemical Properties of Vanadium Oxide Aerogels and Aerogel Nanocomposites . *Journal of Sol-Gel Science and Technology* , 26, 641-644.
- Giogetti, M., Passerini, S., Berrettoni, M., & Smyrl, W. (1999). XAS investigation on polyvalent cation intercalation in  $\text{V}_2\text{O}_5$  aerogels. *Journal of Synchrotron Radiation* , 6, 743-745.
- Giorgetti, M., Passerini, S., & Smyrl, W. H. (1999). Identification of an Unconventional Zinc Coordination Site in Anhydrous  $\text{Zn}_x\text{V}_2\text{O}_5$  Aerogels from X-ray Absorption Spectroscopy . *Chemistry of Materials* , 11 (8), 2257-2264.
- Le, D. B., Passerini, S., Coustier, F., Guo, J., Soderstrom, T., Owens, B. B., et al. (1998). Intercalation of Polyvalent Cations into  $\text{V}_2\text{O}_5$  Aerogels. *Chemistry of Materials* , 10 (3), 682-684.
- Ohzuku, T., & Ueda, A. (1994). Why Transition Metal (di) Oxides are the Most Attractive Materials for Batteries. *Solid State Ionics* , 69, 201-211.
- Ohzuku, T., Kato, J., Sawai, K., & Hirai, T. (1991). Electrochemistry of Manganese Dioxide in Lithium Nonaqueous Cells. *Journal of the Electrochemical Society* , 138 (9), 2556-2560.
- Orazem, M., & Tribollet, B. (2006). *Electrochemical Impedance Spectroscopy*. New York: Wiley-Interscience.
- Qu, D. (2004). The Study of the Proton Diffusion Process in the Porous  $\text{MnO}_2$  Electrode . *Electrochimica Acta* , 49 (4), 657-665.
- Rolison, D. R., & Dunn, B. (2001). Electrically Conductive Oxide Aerogels: New Materials in Electrochemistry. *Journal of Materials Chemistry* , 11 (4), 963-980.
- Sigma Aldrich*. (n.d.). From [www.sigmaaldrich.com](http://www.sigmaaldrich.com)
- Tang, P. E., Sakamoto, J. S., Baudrin, E., & Dunn, B. (2004).  $\text{V}_2\text{O}_5$  Aerogel as a Versatile Host for Metal Ions . *Journal of Non-crystalline Solids* , 350, 67-72.



# Chapter 6

## Current Collectors and Other Microbattery Constituents

In the last two chapters, electrode materials were chosen according to their electrochemical compatibility with the gel electrolyte. Conversely, the gel electrolyte must be relatively inert towards all other components within a microbattery to ensure extensive device lifetimes and prevent premature failure. These microbattery constituents include the current collectors, substrate, and any packaging. The material compatibilities of the inactive microbattery components with the gel electrolyte are determined by investigating the electrochemical stability of the material within the operating potentials of the battery, its interfacial activity, and processing compatibility. From these findings, informed materials choices can be generated. This work focuses on the development of a printable current collector, however the design process could be repeated when formulating all other inactive components such as packaging or structural materials.

### 6.1 Current Collector Requirements and Potential Materials

Current collector materials are often used in a battery to guide and quickly direct charges to the active components of the battery. Current collectors for batteries are typically electrochemically inactive with the battery electrolyte and are usually highly electrically conductive materials applied as thin films, meshes or coatings to the device electrodes. Two oppositely charged current collectors are able to apply an electric field across a battery cell, and depending on its configuration, current density paths through the battery can be directed. The criteria for a current collector compatible with an electrochemical system include cost, electrical conductivity, stability with other chemical constituents, processing compatibility, as well as stability with cycling, temperature, and the electrochemical environment. Common current collector materials used in conventional batteries are listed in Table 6.1 [Whitehead, *et al.*, 2005]. Their electrical conductivities are reported with respect to volume occupied, mass, as well as unit cost as estimated from bulk prices in 2005, all normalized to copper.

Table 6.1. Relative conductivity normalized for volume, mass and cost of candidate current collector materials with respect to copper at room temperature.

<b>Material</b>	<i>Relative conductivity per unit volume</i>	<i>Relative conductivity per unit mass</i>	<i>Relative conductivity per unit cost*</i>
<b>Ag</b>	1.05	0.9	0.01
<b>Cu</b>	1	1	1
<b>Au</b>	0.7	0.33	0.0008
<b>Al</b>	0.4	1.3	2
<b>Zn</b>	0.28	0.36	0.8
<b>Ni</b>	0.24	0.25	0.05
<b>C black</b>	0.00001	0.00004	0.00002

\* All materials costs were extracted from bulk prices (in US dollars) in 2005.

A printable current collector is needed for the manganese dioxide composite electrode because of its inherently poor electrical conductivity. A zinc electrode, if conductive enough, may be able to serve both as an electroactive film and its own current collector. The electrochemical stability of current collector materials with the ionic liquid gel electrolytes will be the most critical parameter in choosing a compatible current collector.

## 6.2 Printable Silver Current Collector

In previous studies, copper was shown to be electrochemically unstable with the ionic liquid electrolyte, showing visible corrosion behavior [Ho, 2007]. Silver was investigated as a potential current collector because of its high electronic conductivity. Many printable silver inks are readily available commercially [ESL ElectroScience]. To test its electrochemical behavior with the gel electrolyte, a test cell was fabricated with adjacent silver current collector electrodes printed onto a glass substrate. The ionic liquid gel electrolyte was printed on top of the two silver electrodes, and the cell was subjected to cyclic voltammetry measurements. Using a 10 mV/s scan rate within the range of -3 to 3 V with respect to a silver electrode, the silver current collectors showed a significant passage of current in Figure 6.1, and visible dendrite formation at the interfaces between the printed silver and gel electrolyte was observed with optical microscopy (Figure 6.2). From this study, silver proved to be an unsuitable current collector material for the battery chemistry developed in this work.

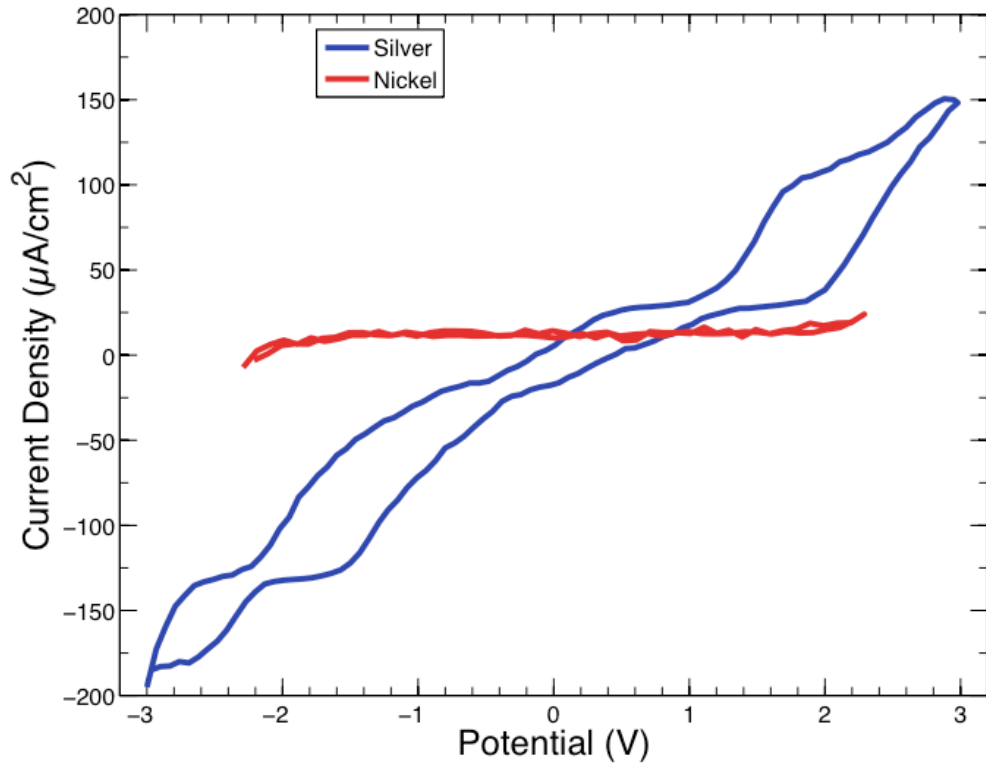


Figure 6.1. Voltammograms of symmetric cells containing two adjacently printed current collector films covered in a printed gel electrolyte. The electrochemical instabilities of silver and nickel in the gel electrolyte correspond with the magnitude of current density detected for a given potential. Scan rate of 10 mV/s. The initial polarization direction was towards more positive potentials.

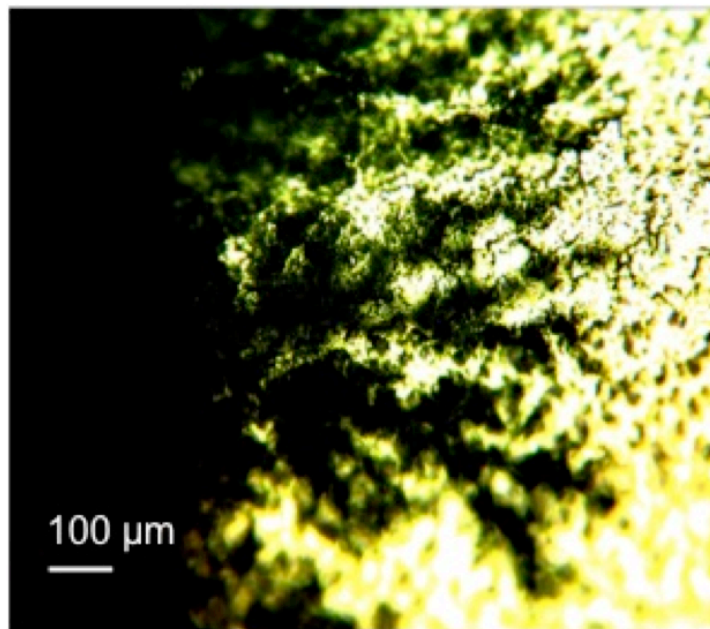


Figure 6.2. Micrograph showing silver dendrite formation along the interface between the printed silver (black) and the gel electrolyte (yellow).

## 6.3 Printable Nickel Current Collector

### 6.3.1 Electrochemical Stability

Nickel was also tested as a printable current collector. Both commercially available nickel ink as well as in-lab synthesized nickel inks were tested. Using a planar test cell, an ink composed of 93 wt. % spherical nickel powder [E-Fill, Sulzer Metco Canada] and 7 wt. % PVDF-HFP was subjected to a 10 mV/s CV scan between -2 to 2 V. The nickel exhibited fairly stable behavior with the gel electrolyte, with negligible current densities and no morphology changes detected at the current collector interfaces over 25 cycles. The voltammogram of the printed nickel is compared to that of printed silver in Figure 6.1, which shows that within the voltage range investigated, negligible current densities are measured from the nickel test structure, therefore demonstrating its electrochemical stability with the gel electrolyte. Future testing should involve long-term cycling of the current collectors with various environmental conditions such as temperature or humidity. Though the printed nickel films appear to be an electrochemically stable current collector for the battery chemistry of interest, their electrical conductivity has proven to be too low for this purpose; average conductivities of 0.01 to 1 mS/cm<sup>2</sup> have been measured. Along with the nickel spherical powder, other nickel particle morphologies have been investigated including flakes and fibers, all of which were incorporated into inks, printed, and imaged as films in the micrographs of Figure 6.3 (a-c). The latter two inks showed substantial improvement in electrical conductivity, ranging from 0.1 to 10 S/cm<sup>2</sup>. The current collector ink incorporating nickel fiber was very conductive (1 to 10 S/cm<sup>2</sup>) even with low mass loadings < 50 wt.%. As visible in the micrograph of the film incorporating nickel fiber (Figure 6.3 c), the film was extremely porous due to the poor packing of the fibers, and homogenous inks were difficult to achieve with mass loadings greater than 50 wt.%.

### 6.3.2 Printed Current Collector Processing Considerations

By utilizing nickel fiber particles in the current collector films, some processing issues were observed. Stratifications of fiber powder and polymer regions resulted in inhomogeneous properties through the thickness of the film. For example, a nickel fiber current collector film was printed on a substrate and then subsequently covered with a printed polymer film. As seen in Figure 6.4, because the composite film was fairly porous, during the printing process the polymer ink seeped through the porous composite film, displacing it from the substrate. Inhomogenous current collector films could lead to uneven distributions in electrical conductivity through the film and uneven interfacial resistances between the current collector and any adjacent films. Ultimately inhomogeneity of the current collector film will reduce the electrochemical performance of the active components in the battery. In a battery, if any insulating polymer ink seeps through its structure, this would prevent electrical connection or create an interfacial barrier between its layers. As a result, this could lead to huge impedances at the interfaces of a stacked structure. This has proven to be problematic when processing highly porous films as current collectors. Some suggestions to improve the current collector films include incorporating other conductive additives within the film to create denser particle

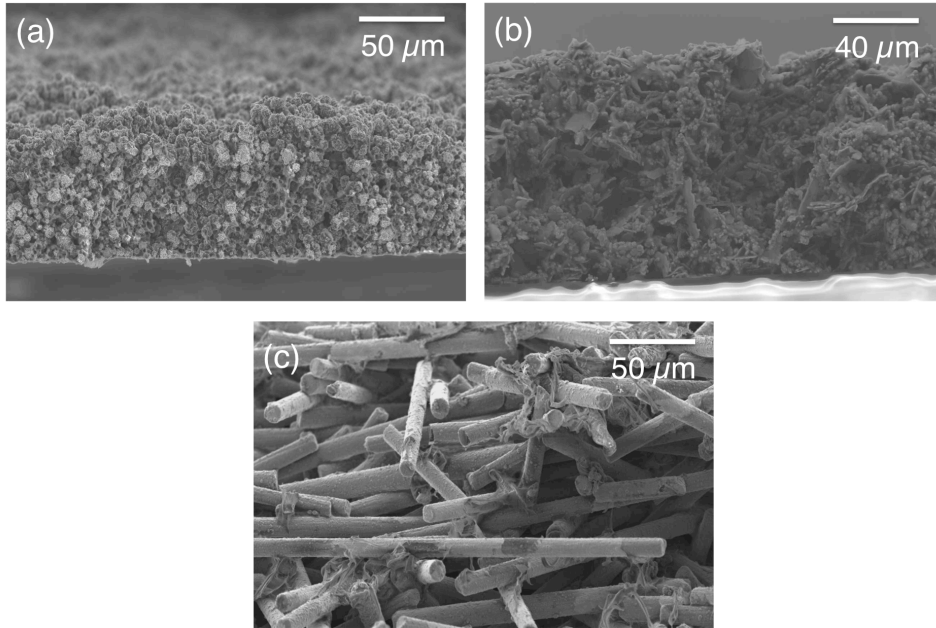


Figure 6.3. (a-c) Nickel films containing spherical, flake, and fiber particles dispersed in a polymer binder.

packing as well as using dense conductive coatings to electrically join electrode and current collector layers.

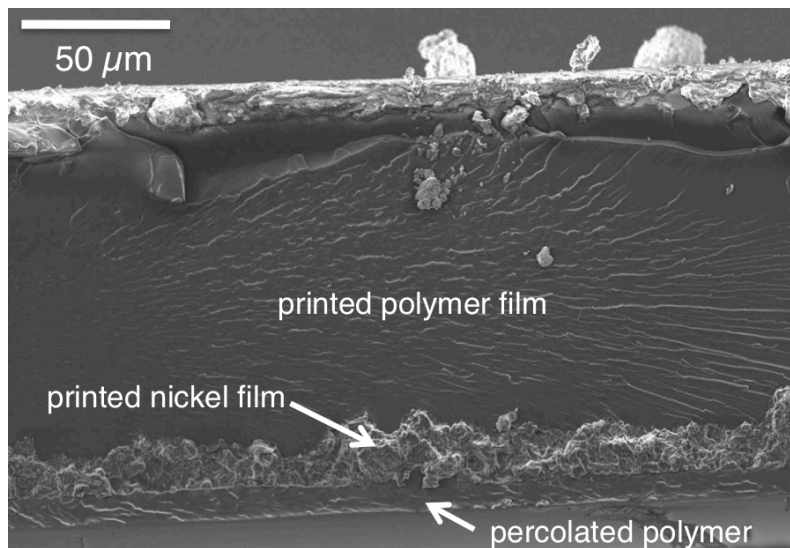


Figure 6.4. Cross section of a printed test structure comprising of polymer printed on top of a printed nickel fiber film. The polymer ink percolated through the printed nickel film, forming a uniform layer of polymer underneath it and displacing it from the substrate the nickel film was printed on (glass substrate was removed to image the printed films).

## 6.4 Other Microbattery Constituents

When designing a microbattery, additional considerations concerning the stability of other microbattery components such as the substrate and packaging are also critical to the device performance. These issues are oftentimes treated as afterthoughts in the microbattery design process, but can prove to be critical to the health of a battery. For example, if the active materials in a battery are sensitive to moisture from the ambient environment, any permeation of water through its packaging and substrate will cause premature failure to the battery. Furthermore, if an active material such as the gel electrolyte undergoes parasitic side reactions with any of the inactive materials, the battery could suffer from permanent capacity loss.

### 6.4.1 Substrate Materials

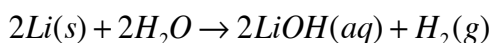
Potential material systems for substrates have only been empirically studied. For example, most rigid surfaces such as silicon, printed circuit boards, and glass are suitable. Some highly chemically and thermally resistant substrates such as polyimide are also suitable. More extensive studies on this subject are needed.

### 6.4.2 Packaging Materials

Packaging strategies compatible with dispenser printing are currently being explored in this lab. A study of the moisture tolerances of various electronics devices was conducted. Devices which have minimal to moderate moisture tolerances can be packaged with as little as a single layer barrier such as polyimide, glass, or a metal oxide film. For devices incorporating organic materials that are environmentally sensitive such as organic light emitting diodes (OLEDs) and organic transistors, the moisture tolerances, measured by the water vapor transmission rate (WVTR), of these devices are very low ( $< 10^{-3}$  g/m<sup>2</sup>/day) (Lewis, 2006). These devices require much more sophisticated barriers such as multilayer structures alternating with organic and inorganic materials. According to a simple back-of-the-envelope estimation, a lithium battery can tolerate a WVTR no greater than  $1.96 \cdot 10^{-4}$  g/m<sup>2</sup>/day and this value is verified by Aurbach, et al. (Aurbach, Weissman, Zaban, & Danb, 1999). The estimation stems from the following calculation:

$$\text{Rate of degradation} = \frac{\text{thickness of sensitive component in battery} \cdot \text{its density}}{\text{desired lifetime}} \quad (\text{Equation 6.1})$$

For a lithium battery where a 3.5 $\mu$ m thick lithium electrode (with a density of 530 kg/m<sup>3</sup>) is the most moisture sensitive component and the battery must last 10 years of 3650 days, the maximum tolerable rate of degradation of the lithium electrode is  $5.08 \cdot 10^{-4}$  g/m<sup>2</sup>/day. Lithium metal reacts with water according to the following expression:



According to this expression, for each molecule of water, a molecule of lithium is converted to LiOH. The atomic weight of lithium is 6.93 g/mol and 18 g/mol for water. If it can be assumed that the maximum tolerable rate of degradation of the lithium electrode can be related to the maximum water vapor transmission rate (WVTR) of an encapsulant film, the WVTR can be approximated as:

$$\text{WVTR} = \text{Rate of lithium degradation} \cdot \frac{6.93 \text{ g Li}}{\text{mol}} \cdot \frac{\text{mol}}{18 \text{ g H}_2\text{O}} = 1.96 \cdot 10^{-4} \text{ g/m}^2/\text{day}$$

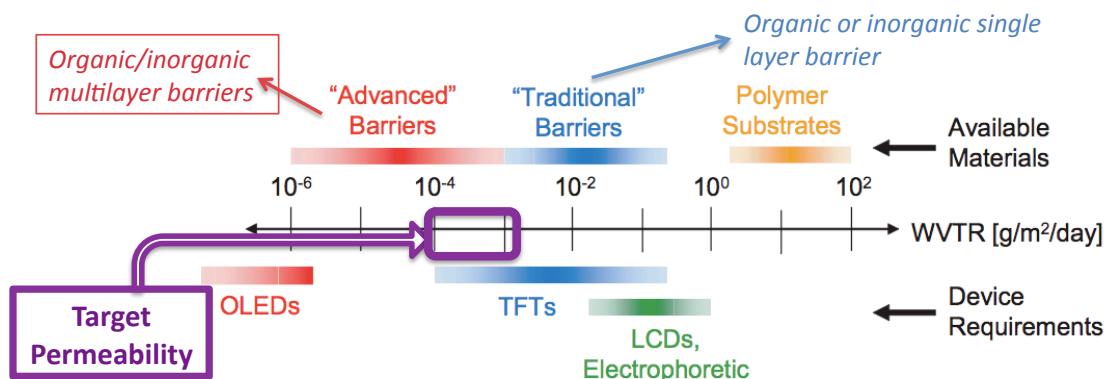


Figure 6.5. Barrier material permeabilities quantified by water vapor transmission rates (WVTR – g/m<sup>2</sup>/day). Available barrier materials and corresponding device moisture exposure tolerances are listed. For the printed microbattery developed in this work, we hypothesize that the minimum permeability requirement is approximately 10<sup>-3</sup> g/m<sup>2</sup>/day (adapted from [Lewis, 2006]).

In comparison to lithium batteries, we hypothesize that the zinc microbatteries are less moisture sensitive because elementary zinc does not react with water molecules (all processing and tests have been conducted in the ambient air with little indication of moisture sensitivity). However, the environmental sensitivity of this zinc battery has yet to be determined. A conservative estimate is to design a barrier layer with a moisture permeability no greater than  $5 \cdot 10^{-4}$ , slightly more tolerable to water vapor transmission in comparison to a lithium battery. Currently, various printable multilayer barrier strategies and materials are being explored. After identifying functional barrier materials, their electrochemical and processing compatibilities will also need to be defined using the measurements described in the previous sections.

## 6.5 Concluding Remarks about Current Collectors and Other Battery Constituents

Any inactive components in a microbattery must be unreactive towards the active films in the device. In most cases, the gel electrolyte must be relatively electrochemically inert with any other component, and this prerequisite should inform the materials decisions of the current collectors, substrate, and packaging constituents. Current collector materials compatible with the gel electrolyte were studied, and nickel was demonstrated as a suitable choice. Difficulties in using a printable, porous current collector revolve around its propensity for inhomogenous distribution of particles and polymer through the film. In addition, percolation of subsequently printed inks through a porous current collector film is problematic. Further research should focus on the development of printable yet dense and electronically conductive current collector films.

Although the substrate material choice and packaging strategies are typically afterthoughts in the design process, their properties can be paramount to the battery device health. So far inorganic and some organic and flexible substrates have been initially explored. For the printed zinc, gel electrolyte, and manganese dioxide batteries, a barrier which can prevent the permeation of moisture by reducing the water vapor transmission rate to  $< 10^{-3}$  g/m<sup>2</sup>/day has been proposed as the minimum protection needed. Characterization of these properties and potential functional materials that are compatible with the microbattery components are needed. Since further exploration of packaging materials is needed, all tests conducted in this work do not incorporate any packaging materials, but instead were implemented exposed to the ambient air.

## 6.6 References

Aurbach, D., Weissman, I., Zaban, A., & Danb, P. (1999). On the role of water contamination in rechargeable Li batteries. *Electrochimica Acta* , 45, 1135-1140.

*E-Fill, Sulzer Metco Canada.* (n.d.). From <http://www.conductivefillers.com/>

*ESL ElectroScience.* (n.d.). From <http://www.electroscience.com/>

Ho, C. C. (2007). *Pneumatic Dispenser Printed Electrochemical Capacitors*. Masters Thesis, University of California, Berkeley, Materials Science and Engineering.

Lewis, J. (2006). Material Challenge for Flexible Organic Devices. *Materials Today* , 9 (4), 38-45.

Whitehead, A., & Schreiber, M. (2005). Current Collectors for Positive Electrodes of Lithium-Based Batteries. *Journal of The Electrochemical Society* , 152, A2105-A2113.



# Chapter 7

## Printed Microbatteries: Device Fabrication and Testing

The investigation of the material properties of various electrode, electrolyte and current collector constituents and their compatibilities with each other were pertinent in successfully designing an electrochemical system. In this next section, the combination of these materials to form a dispenser printed microbattery is described. How this device is characterized to identify relevant properties indicating its potential as a rechargeable energy storage component for small, autonomous wireless sensor platforms will be discussed.

### 7.1 Microbattery Fabrication

Batteries were printed with the stacked configuration illustrated in Figure 7.1. Each film was printed and then dried at 60°C for 15 to 30 minutes depending on the film properties. Square test cells were printed within 0.25 cm<sup>2</sup> footprint areas and had total thicknesses between 80 and 120 μm. A micrograph of the cross section of a printed microbattery is shown in Figure 7.2. For this configuration, the zinc film serves both as the electrode and its own current collector. Nickel foil was used as the current collector of the manganese dioxide electrode as well as the substrate upon which the battery was printed. Though it was intended to utilize a printed nickel current collector to achieve a fully printed battery, the current microbattery configuration emulates the likely circumstance in which the microbattery will be printed onto a patterned substrate such as a printed circuit board (PCB) board in which the bottom current collector is already fabricated through previous processes such as vapor deposition.

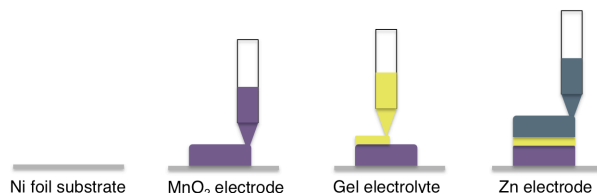


Figure 7.1. Dispenser printing procedure for stacked zinc, gel electrolyte, and manganese dioxide microbattery on a nickel foil substrate.

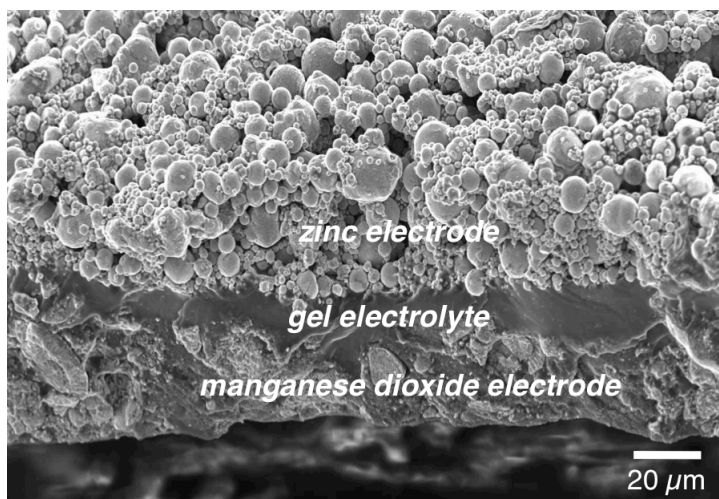


Figure 7.2. Micrograph of the cross section of a zinc, gel electrolyte, and manganese dioxide printed microbattery. The nickel foil substrate was removed so that the printed structure could be imaged.

## 7.2 Microbattery Device Characterization

### 7.2.1 Galvanostatic Characterization

#### Measuring Capacity and Cycle Life

After printing the stacked battery structures described in the previous section, the devices were allowed to equilibrate over 24 hours before characterization. The typical cell potential evolution of the printed battery as a function of depth of discharge for a galvanostatic discharge rate of  $C/3$  is shown in Figure 7.3. The working range of this battery lies between 1 and 2 V. The cells were cycled galvanostatically at discharge rates of  $C/5$ , and as seen in Figure 7.4, over 70 cycles were achieved without sign of performance degradation. This printed battery also showed similar activation behavior of its manganese dioxide electrode within the first 15 cycles, as discussed in section 5.2.3. Test cells achieved an average of  $1 \text{ mAh/cm}^2$  in capacity and  $1.2 \text{ mWh/cm}^2$  in areal energy density.

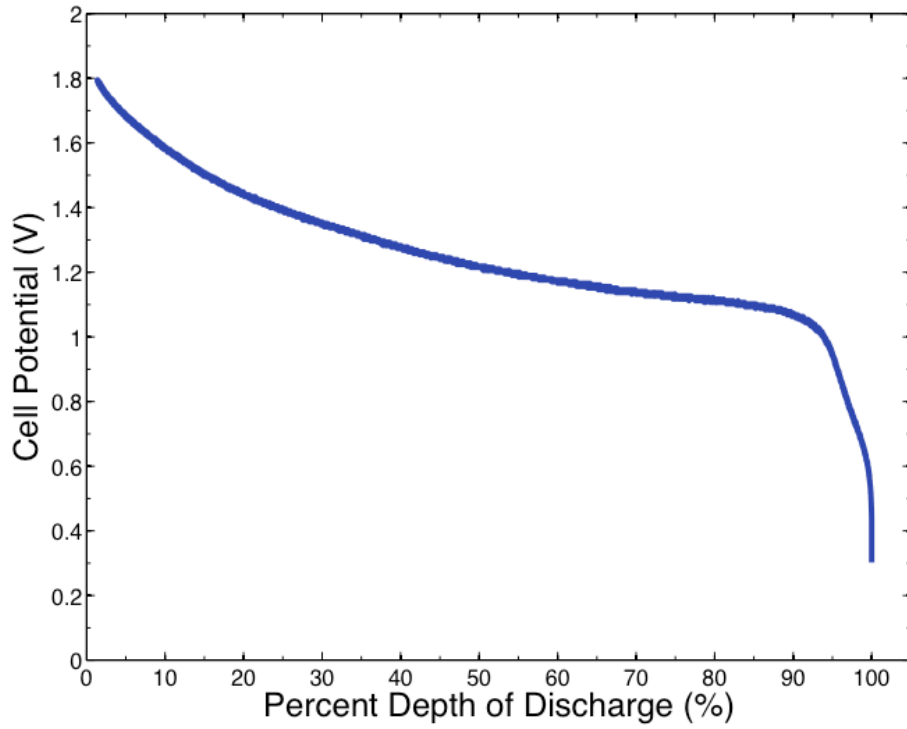


Figure 7.3. Cell potential of a printed zinc, gel electrolyte, and MnO<sub>2</sub> microbattery as a function of percent depth of galvanostatic discharge. The discharge rate was  $C/3$ .

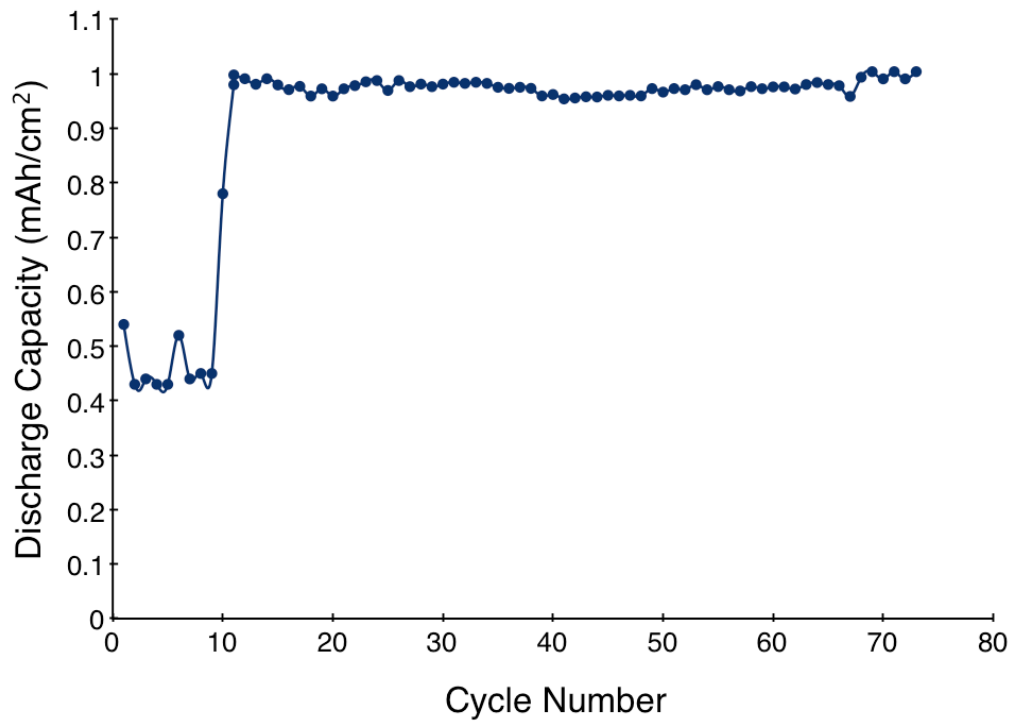


Figure 7.4. The galvanostatic cycling of a printed zinc, gel electrolyte, and MnO<sub>2</sub> microbattery at a  $C/5$  rate. Activation of the battery occurred within the first 15 cycles. After more than 70 cycles no signs of performance degradation is visible.

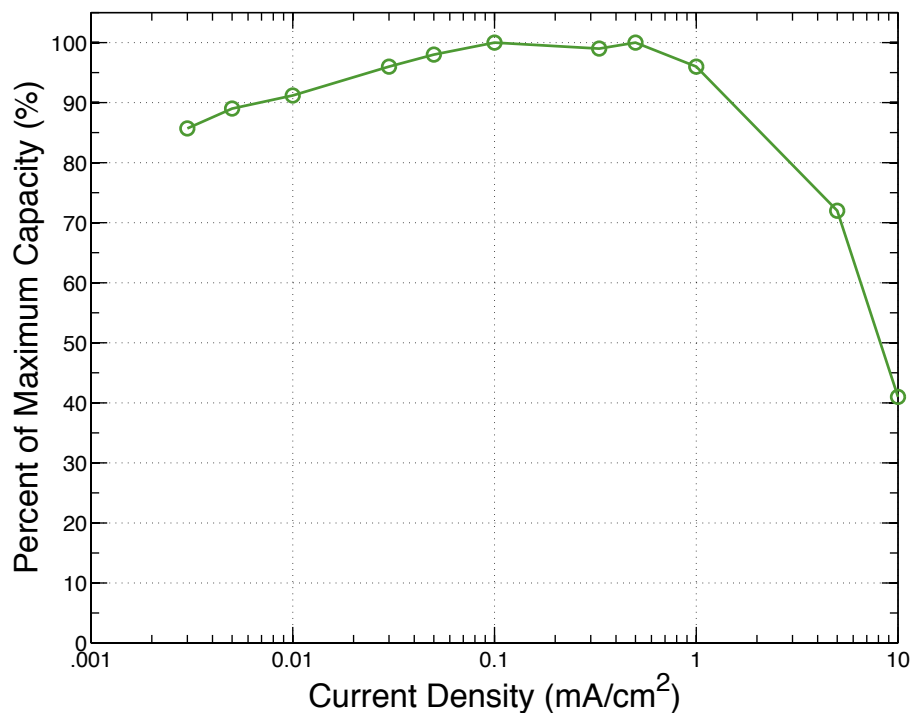


Figure 7.5. Percent of maximum discharge capacity extracted from the printed microbattery as a function of discharge current density.

### Measuring Rate Performance

Initial studies on the rate performance of the printed battery are shown in Figure 7.5. Deep galvanostatic discharge capacities were measured for varying discharge current densities, and normalized with respect to the maximum capacity measured (approximately 1 mAh/cm<sup>2</sup>). The cells were charged using the same protocol: a constant current charge of 0.1 mAh/cm<sup>2</sup> followed by holding the cell at a constant voltage of 1.8 V for 3 hours. Cells were discharged between 1.8 to 0.3 V. The maximum achievable storage capacity was attained for discharge current densities ranging between 0.1 and 1 mA/cm<sup>2</sup>, which corresponds to approximately C/2 – C/7 rates. For current densities higher and lower than this range, the extractable discharge capacity diminished due to the high cell impedance for the former, while self-discharge and leakage mechanisms dominated the latter. For microdevice applications, it's unlikely that the microbattery will be discharged at a rate lower than C/10, even if used in conjunction with an energy harvesting device. On the other hand, high rates of discharge are likely, and the rapid decrease in usable capacity for any rates above 1C prevents this device from suitably addressing the exacting high power pulses typically demanded from microdevices such as wireless sensors. A load leveling capacitor may alleviate such high power density demands, and protect the battery from detrimental pulsing. Load leveling is discussed extensively in a few publications [Ho, 2007 and Otis, *et al.*, 2007].

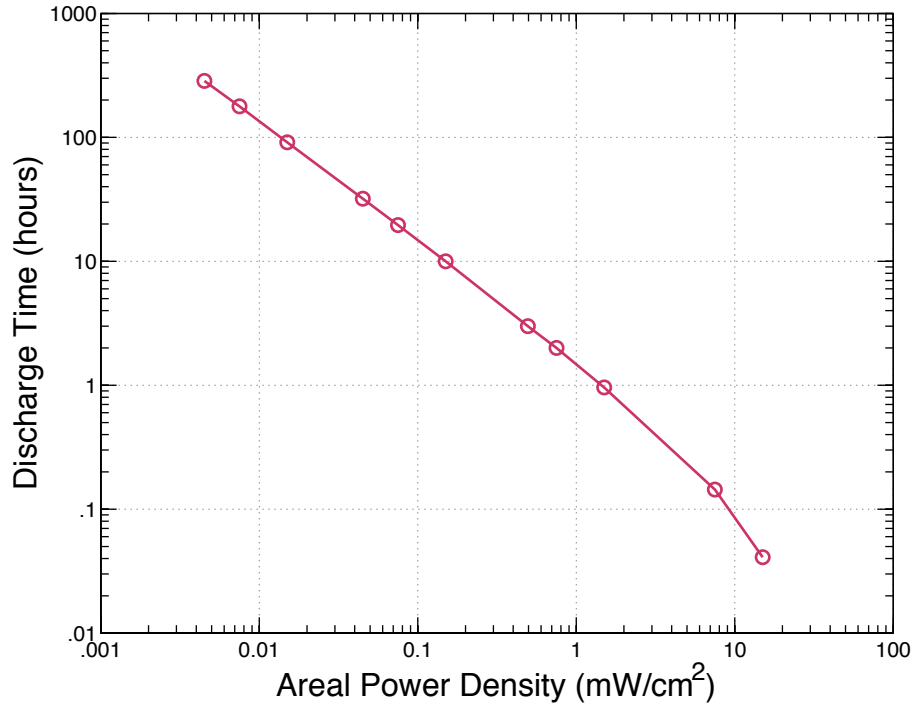


Figure 7.6. Printed microbattery discharge times as a function of discharge power density.

From this same study, the effect of the power densities drawn from the printed microbattery on its discharge times for a full discharge was calculated and plotted in Figure 7.6. As has been reported for other electrochemical systems, when plotted on logarithmic axes, the discharge time decreases linearly with greater applied power density. With a 15 mW/cm<sup>2</sup> pulse, the battery fully discharged in approximately 150 seconds. With alternative characterization equipment, higher power pulsing properties should be investigated in future work. The dependence of the energy density from the printed microbattery on the power drawn is summarized in a Ragone plot Figure 7.7. A maximum energy density of 1.49 mW/cm<sup>2</sup> was measured for moderate power densities between 0.05 – 1 mW/cm<sup>2</sup>, and beyond this window, the energy density diminishes. From this plot a maximum power density can be approximated as the value at which 75% of the battery's energy density is drawn; the corresponding maximum power density is 2 mW/cm<sup>2</sup>.

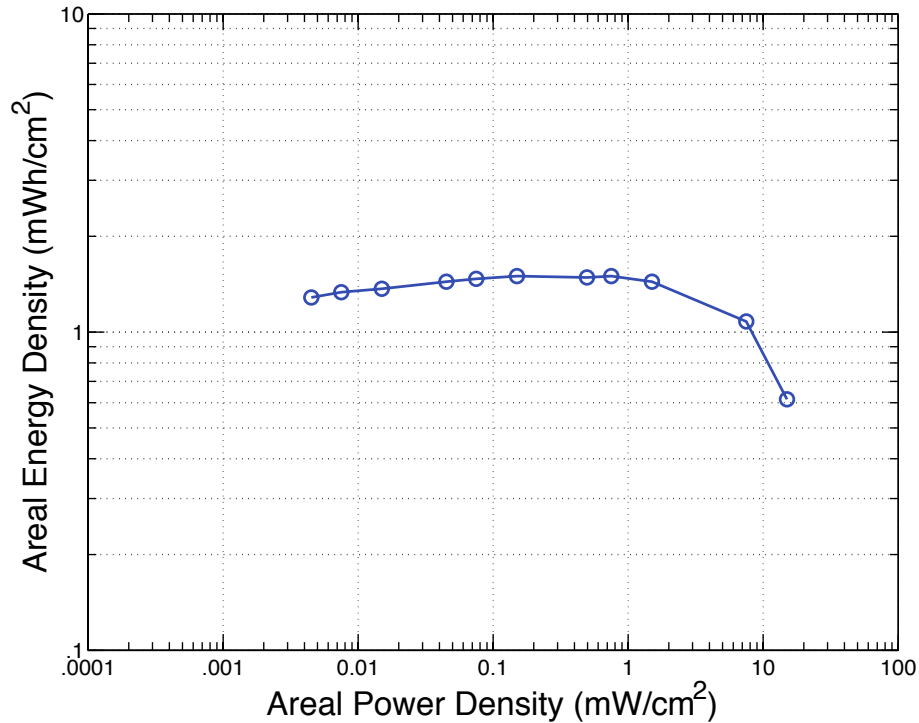


Figure 7.7. Ragone plot illustrating the affect of the discharge power density on the achievable energy density of a printed microbattery for deep discharges.

## 7.2.2 Self-Discharge Characterization

### Measuring Open Circuit Decay

For applications in which the recharge of the battery occurs infrequently or with unknown intermittency, the battery's self-discharge behavior (also known as leakage) is a critical property to investigate. By definition self-discharge in a battery is the progressive time dependent loss of charge typically due to coupled Faradaic processes occurring at the anode and cathode. The main culprits are usually parasitic interfacial charge transfer processes [Niu, *et al.*, 2004]. The rates and mechanisms of self-discharge in a battery can vary greatly with cell potential. To determine the mechanism of self-discharge, the most common method is to monitor a cell's potential decay after polarizing it for a short time. For this experiment, there is no external circuit connected to the battery for charge to pass; therefore the rate of decreasing state of charge must primarily depend on the self-discharge processes within the cell. As proposed by Niu, *et al.*, the potential decay behavior can be used to distinguish between three types of self-discharge mechanisms: (1) self-discharge due to coupled faradaic processes at the anode and cathode (2) diffusion controlled self-discharge of electroactive impurities, or (3) short circuit leakage between the electrodes. For the first process where self-discharge is attributable to faradaic reactions, for example due to the continued solution decomposition in a cell after being overcharged, the leakage current ( $i_{\text{self-discharge}}$ ) measured at a cell potential (V) is approximated as:

$$i_{\text{self-discharge}} = -C \frac{dV}{dt} = i_o \exp\left[\frac{V}{A}\right] \quad (\text{Equation 7.1})$$

$$A = \frac{RT}{\alpha F} \quad (\text{Equation 7.2})$$

where C is the electrode double layer capacitance,  $i_o$  is the exchange current density, and A is the Tafel slope given by the gas constant R, the absolute temperature T, the transfer coefficient  $\alpha$  and F is Faraday's constant. By integrating this expression and solving for the voltage, the time-dependence of the open circuit potential ( $V_t$ ) can be expressed as:

$$V_t = -A \ln\left(\frac{i_o}{bC}\right) - A \ln(t + \theta) \quad (\text{Equation 7.3})$$

$$i_{V_{\text{initial}}} = i_o \exp\left(\frac{V_{\text{initial}}}{A}\right) \quad (\text{Equation 7.4})$$

$$V_t = V_{\text{initial}} - A \ln(t + \theta) \quad (\text{Equation 7.5})$$

where  $\theta$  is the integration constant and the double layer capacitance C is approximated to remain unchanged as the cell potential varies. This approximation is typically valid for long self-discharge processes (greater than 2 hours). Therefore for faradaic self-discharge processes, the open circuit potential should exhibit a logarithmic decay with time.

The second mechanism may occur in a cell when electroactive impurities participate in faradaic reactions, causing the depolarization of an electrode. Since the relative concentration of impurities is low, the phenomenon relies on the transport of the redox species to the electrode surface in order to react, and is therefore diffusion controlled. The equation for the cell potential ( $V_t$ ) that is dominated by this mechanism is expressed as follows:

$$V_t = V_{\text{initial}} - \frac{2zFAD^{1/2}\pi^{1/2}c_o}{C} t^{1/2} \quad (\text{Equation 7.6})$$

where z is the charge of the redox species, D is its diffusion coefficient,  $c_o$  is its initial concentration, and A is the interfacial area where the redox reactions occur. The equation can be simplified to reflect the cell potential's square-root relationship with the time for a diffusion controlled self-discharge mechanism:

$$B = \frac{2zFAD^{1/2}\pi^{1/2}c_o}{C} \quad (\text{Equation 7.7})$$

$$V_t = V_{\text{initial}} - B\sqrt{t} \quad (\text{Equation 7.1})$$

In the event that a short circuit occurs within the cell due to poor construction or mechanical failure, the third self-discharge mechanism can be easily distinguished from the first two. Internal ohmic self-discharge will depend on the resistance provided by the leakage pathway ( $R_{leakage}$ ) due to the ohmic contact formed between the electrodes, and the cell potential is defined as:

$$\ln V_t = \ln V_{initial} - \frac{t}{R_{leakage} C} \quad (\text{Equation 7.9})$$

By plotting the open circuit potential decay of a cell and discerning its relationship with respect to time, the mechanism of self-discharge can be easily determined. For this study, it is assumed that the printed batteries were fabricated without short circuit defects so that no ohmic leakage occurs. Therefore, only the first two mechanisms were considered potential contributors to any self-discharge phenomena.

A printed battery test cell was subjected to the same transient and steady state routine as the GITT experiments described in section 5.2.3; a  $10 \mu\text{A}$  ( $40 \mu\text{A}/\text{cm}^2$ ) constant current was applied for 30 minutes, then followed by five hours of rest at open circuit. The potential decay of the battery after being exposed to charge pulses (with a positive current) is recorded in Figure 7.8. The cell potential the cell was polarized to after each pulse is determined by the intercept of the self-discharge curves with the y-axis at time  $t = 0$ . For each pulse, the cell is shown to relax and equilibrate to a lower potential after 5 hours or 18,000 seconds. Over sixty charge pulses were applied to the battery leading to a gradual increase in cell potential from 1.5 to 2.2 V. The plots of the cell's potential decay showed a gradual trend marching upwards due to the increased addition of charge to the

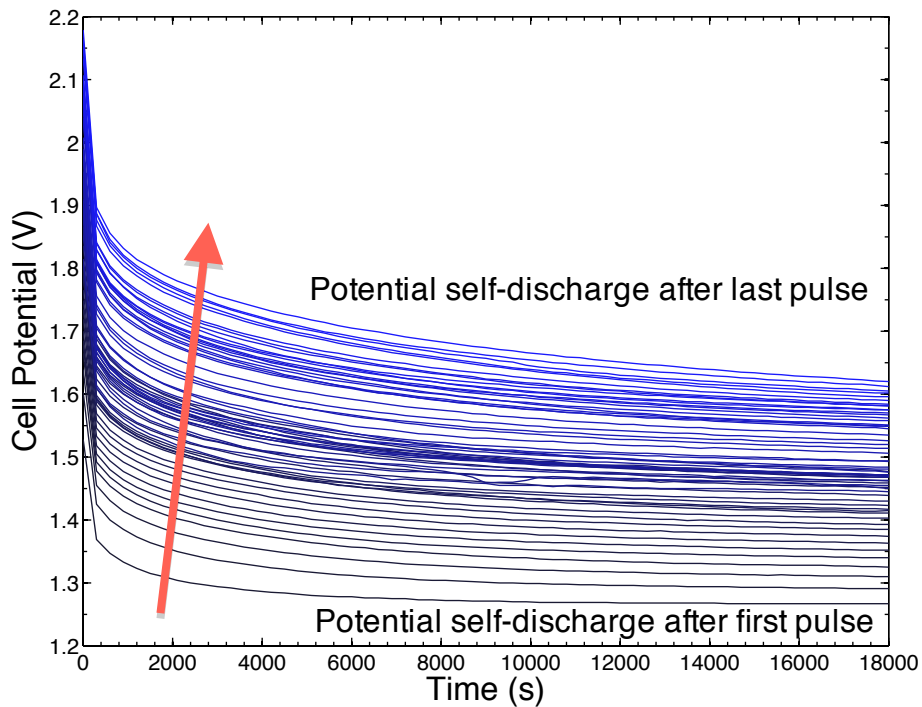


Figure 7.8. A series of self-discharge routines of the printed microbattery after charging. Potential decay at open circuit is plotted with respect to time.



system. To determine the mechanism of self-discharge, the cell potential was plotted in Figure 7.9 and Figure 7.10 with respect to the logarithm and square root of time, corresponding to faradaic and diffusion controlled leakage mechanisms, respectively. In Figure 7.9, the cell potential self-discharge curves were plotted with respect to the logarithm of time for all times after the cell's initial 500 seconds of open circuit potential. For times less than 500 seconds, other phenomena such as a drop in cell potential due to ohmic resistance would cause erroneous behavior plotted on the logarithmic diagram, and therefore was omitted. Comparing figures 7.9 and 7.10, it is apparent the cell potential decays approximately linearly with  $\log(t)$ , suggesting that the mechanism of self-discharge in the printed battery is of faradaic origin due to coupled reactions at the anode and cathode rather than due to the diffusion of redox active impurities. In Figure 7.11, the slopes of these linear sweeps ( $dE/d[\log(t)]$ ) are graphed with respect to the initial cell potential the battery was polarized to; the negative slopes correspond to the rate of potential decay in the battery, and a trend of increased self-discharge rate (or greater magnitude of  $dE/d[\log(t)]$ ) with higher polarization cell potential is apparent. The contrast in rates of self-discharge for cell potentials between 1.5 to 2.2 V indicates that the relative parasitic redox reactions occurring at the anode and cathode vary substantially with the cell's state of charge. Studies utilizing a reference electrode may elucidate the magnitudes of leakage contributions and mechanisms of self-discharge at each electrode.

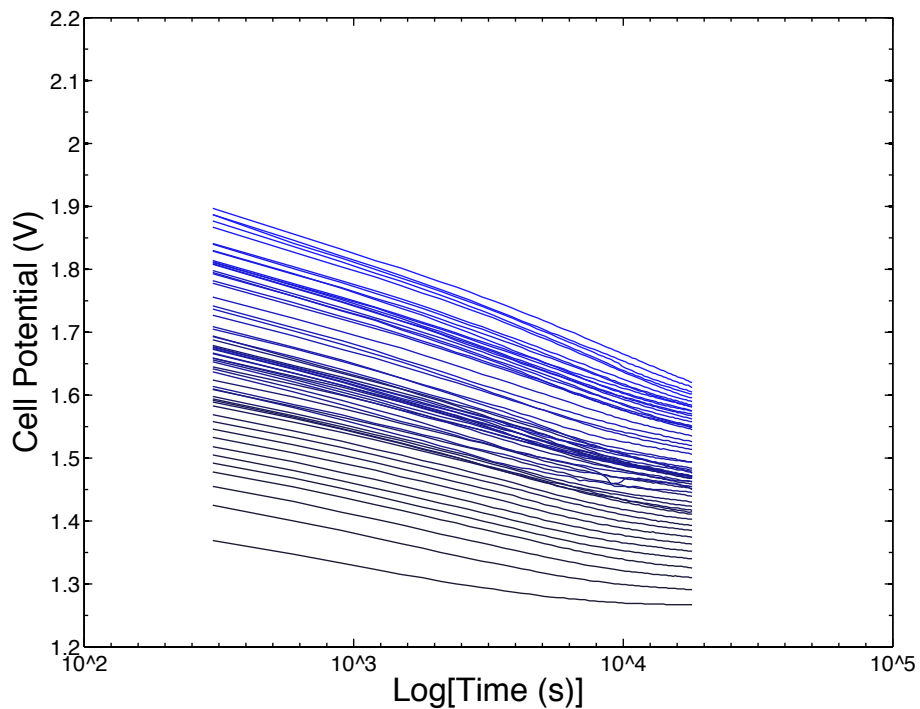


Figure 7.9. A series of self-discharge routines of the printed microbattery after charging. Potential decay at open circuit is plotted with respect to the logarithm of time.

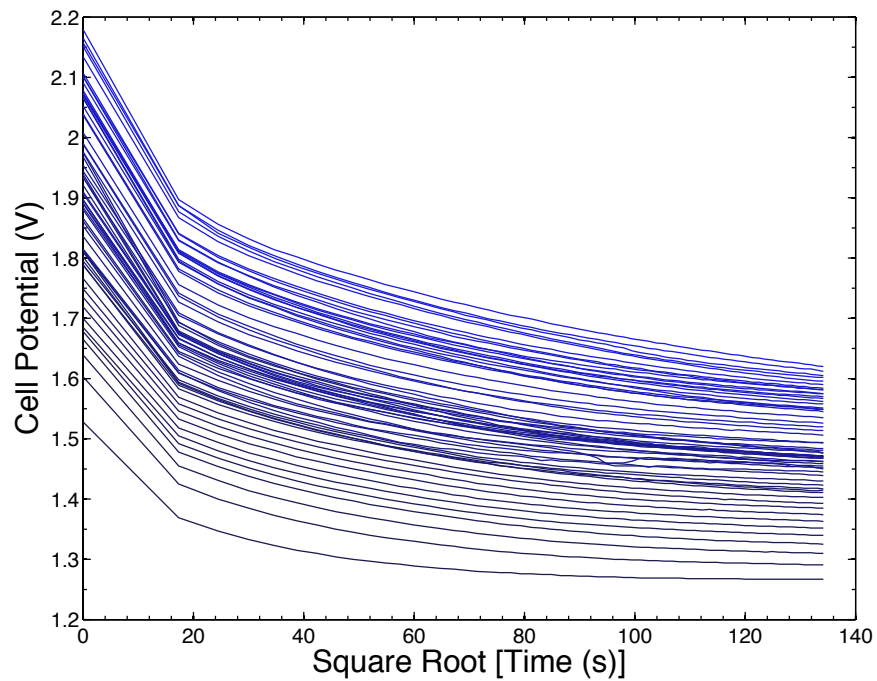


Figure 7.10. A series of self-discharge routines of the printed microbattery after charging. Potential decay at open circuit is plotted with respect to the square root of time.

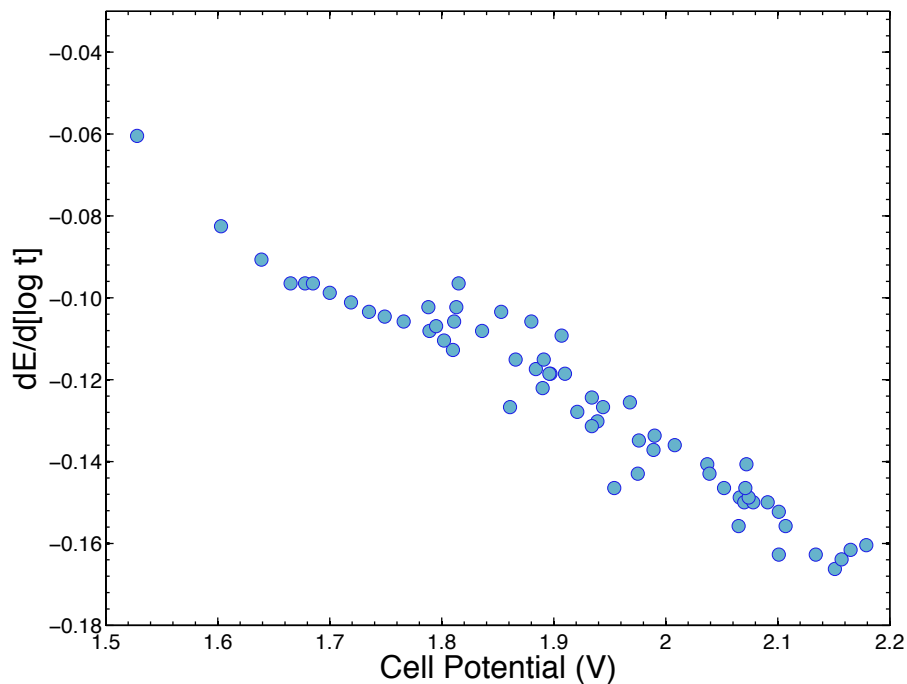


Figure 7.11. Magnitudes of self-discharge of the printed microbattery due to charging. The slope of the potential decay at open circuit is plotted with respect to the logarithm of time as a function of cell potential.

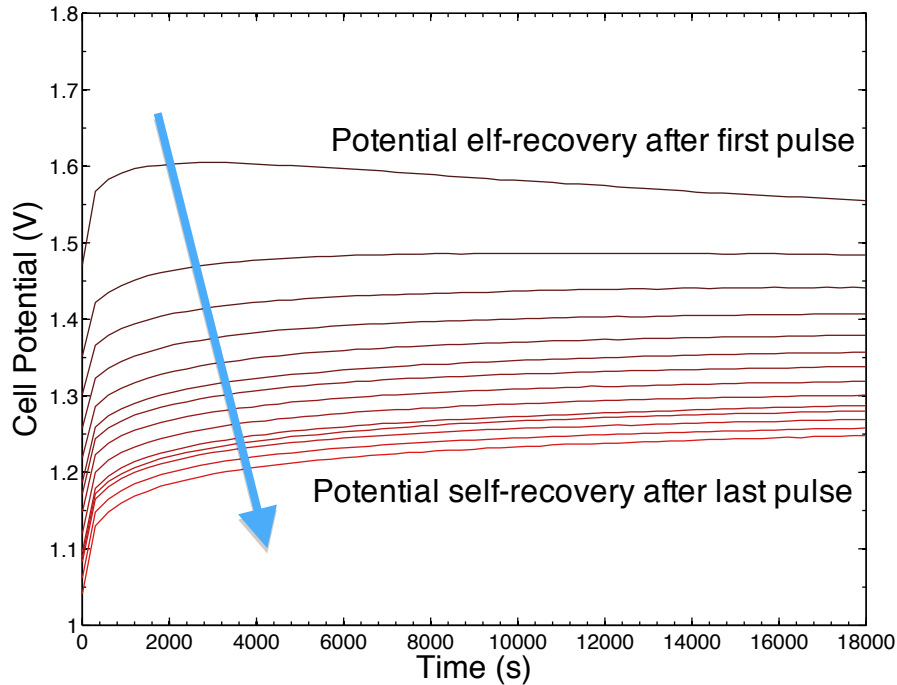


Figure 7.12. A series of self-recovery routines of the printed microbattery after discharging. Potential recovery at open circuit is plotted with respect to time.

By subjecting the cell to a discharge pulse of opposite polarity but of the same magnitude and length of time as the potential decay study above (a  $10 \mu\text{A}$  ( $40 \mu\text{A}/\text{cm}^2$ ) constant discharge current was applied for 30 minutes, then followed by five hours of rest at open circuit), the battery demonstrated potential “recovery” behavior where the cell potential increased at open circuit after each discharge pulse. What was observed in Figure 7.12 was a gradual increase in the cell’s potential when it was allowed to rest at open circuit after a discharge pulse. As was applied in the self-discharge study, the relationship between cell potential and time was used to distinguish the mechanism of self-recovery. In Figure 7.13, the cell potential self-discharge curves were plotted with respect to the logarithm of time for all times after the cell’s initial 500 seconds of open circuit potential. For times less than 500 seconds, other phenomena such as a drop in cell potential due to ohmic resistance would cause erroneous behavior plotted on the logarithmic diagram, and therefore was omitted. By plotting the cell potential data as a function of the logarithm (Figure 7.13) and the square root of time (Figure 7.14), the linear behavior visible in Figure 7.13 suggests that the recovery mechanism is not diffusion controlled, but rather dependent on the faradaic reactions of species at the anode and cathode; the mechanism of self-recovery is consistent with the self-discharge study. Note that the self-discharge potential of the cell after the last pulse showed non-linear logarithmic behavior. (It was suspected that a failure in the cell occurred: afterwards, the cell was unable to store charge and did not respond characteristically to galvanostatic pulses.) Future studies to identify the processes contributing to the potential recovery in this printed battery are needed. By comparing the slope of the cell potentials with respect to the logarithm of time for each initial cell voltage in Figure 7.15, the rate of potential recovery is greater for polarizations occurring at lower cell potentials. As seen in the charge case, the rate of this recovery phenomenon varies with cell’s state of charge. Future studies on the

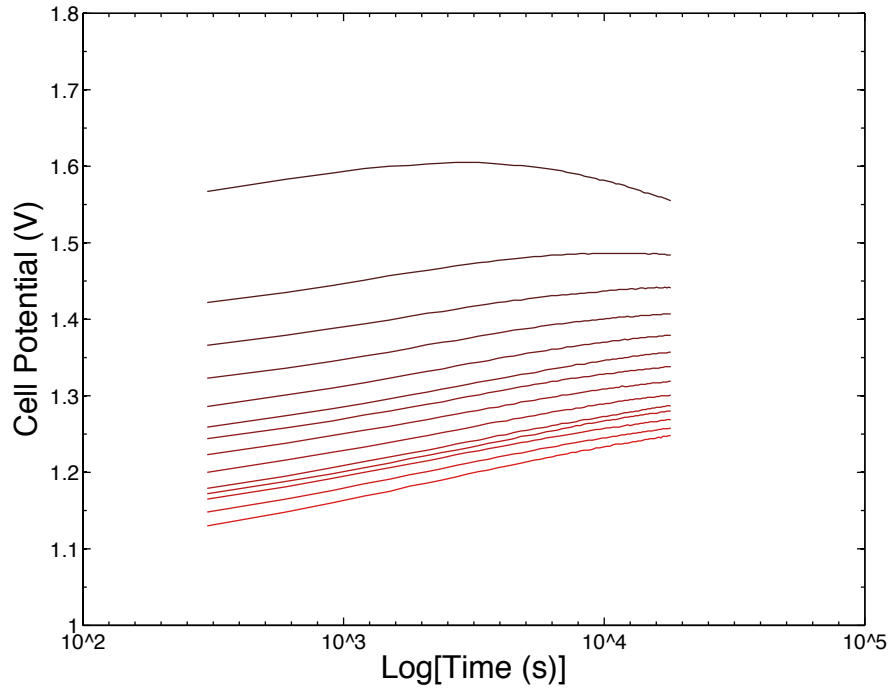


Figure 7.13. A series of self-recovery routines of the printed microbattery after discharging. The potential recovery of the battery at open circuit is plotted with respect to the logarithm of time.

influence of the magnitude and duration of applied current pulses on the self-recovery mechanism would be beneficial.

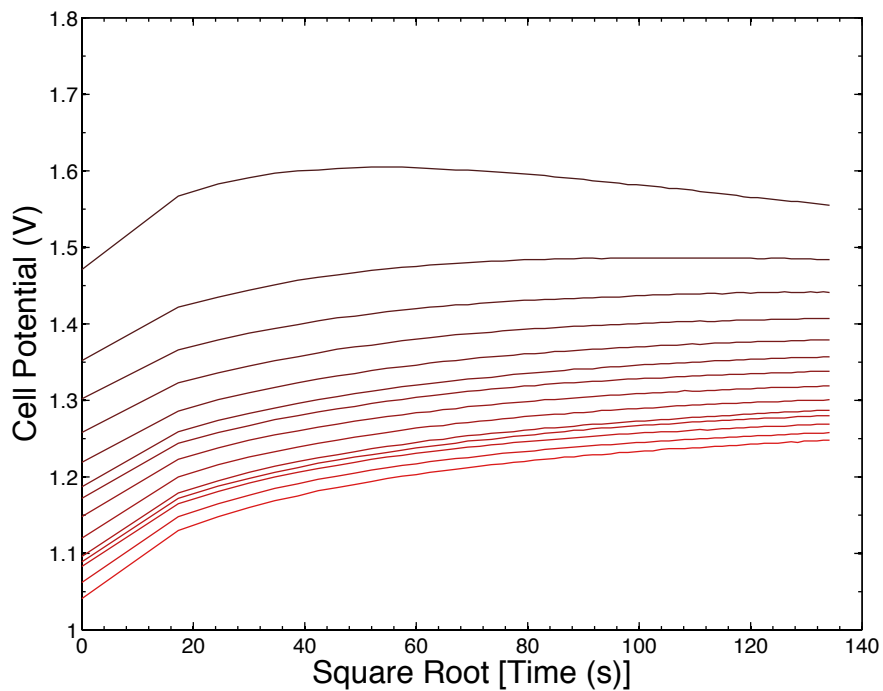


Figure 7.14. A series of self-recovery routines of the printed microbattery after discharging. Potential recovery at open circuit is plotted with respect to the square root of time.

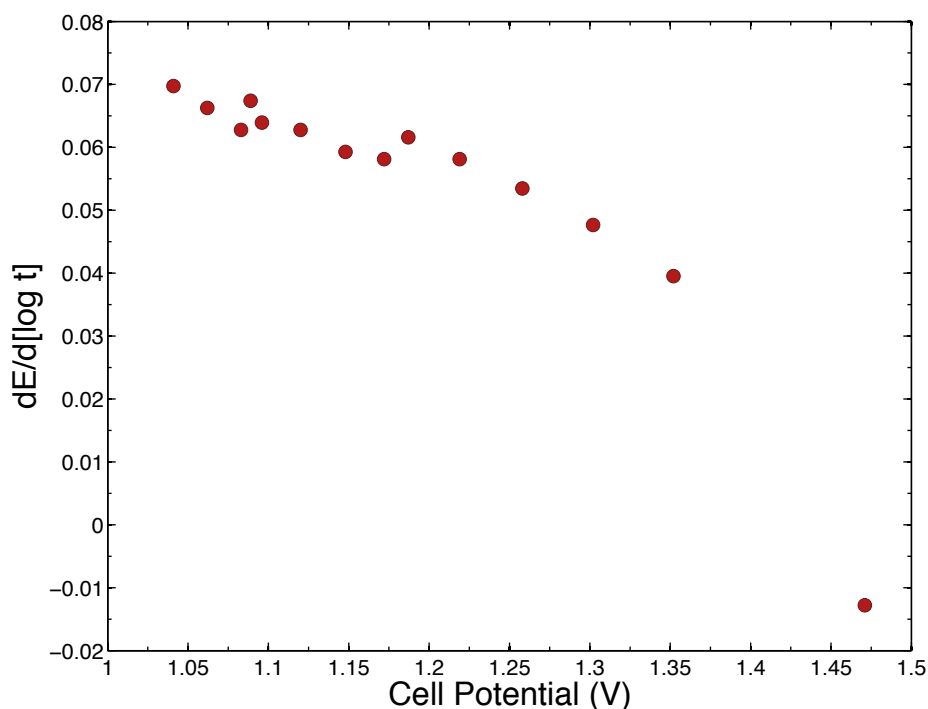


Figure 7.15. Magnitudes of self-recovery of the printed microbattery due to discharging. The slope of the potential recovery at open circuit is plotted with respect to the logarithm of time as a function of cell potential.

### Measuring Float Current as a Function of State of Charge

A complementary study to determine the voltage dependence of the leakage behavior in an electrochemical system is the float current technique. The float current is the current needed to maintain the electrodes at a cell potential. The float current matches the magnitude of the spontaneous self-discharge current flowing in the cell and therefore prevents the parasitic currents from diminishing the cell's state of charge. To determine the voltage dependence of the printed battery's leakage, the cell's potential was held for eight hours and its current response was measured. At the onset of holding the cell at a certain voltage, the resulting current response exhibits its maximum value and then gradually decays over time until it reaches steady state. An example of the current measured in a printed battery held at 1.65 V is shown in Figure 7.16. The float current is estimated as the current measured after eight hours of holding the cell at a given potential, and assumed to be equal in magnitude to the leakage currents occurring spontaneously in the cell. The amount of charge passed due to these parasitic mechanisms is determined by integrating the area under the current response curves, and from this a leakage power can be calculated.

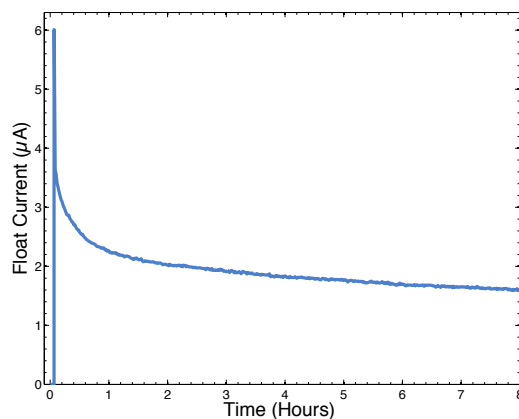


Figure 7.16. The current response to potentiostatic control of a printed battery. The float current is assumed to be the steady state current achieved after holding the cell at a certain potential for extended times.

For the printed battery, the study was conducted over two charge and discharge cycles. In Figure 7.17, the charge cycle float currents recorded for cell potentials between 1.1 and 2 V showed an increasing trend with increasing state of charge. Both first and second charge cycles exhibited similar leakage currents as well as increasing float currents with escalating applied cell potential. A considerable spike in float current between 1.62 and 1.84 V was detected in both cycles, possibly indicating a repeatable leakage mechanism dependent on the state of charge (such as the electrochemical breakdown of an electrolyte constituent). In Figure 7.18, the

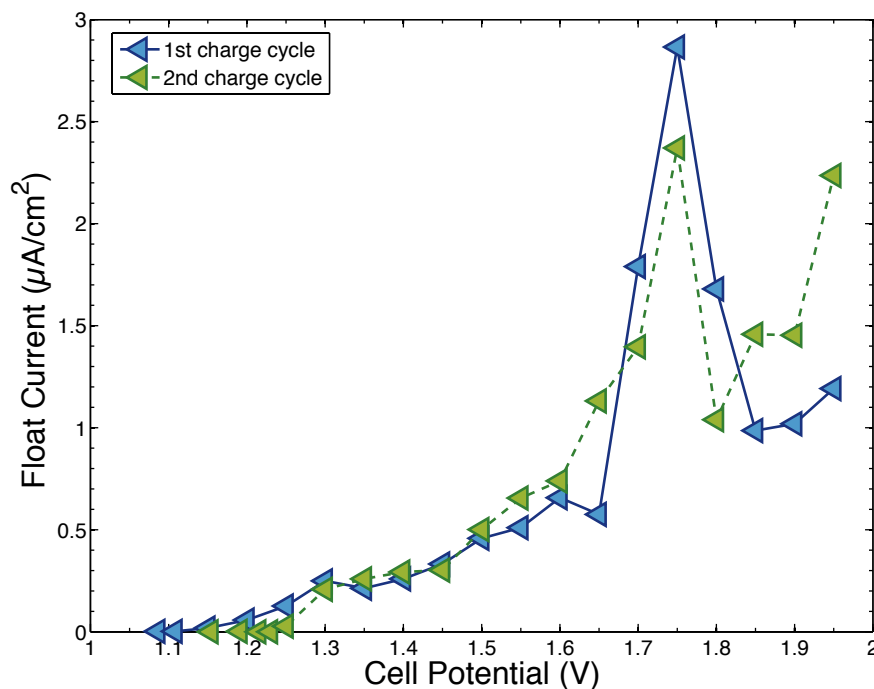


Figure 7.17. The float currents for two charge cycles as a function of cell potential.

float current of the printed battery is observed to increase with decreasing cell potential for both discharge cycles, and again similar magnitudes of leakage currents were measured. Both trends seen in Figures 7.17 and 7.18 agree with the observations discussed in the potential decay measurements. From the float current measurements of the printed batteries, the charge passed potentiostatically (Figures 7.19 and 7.20) and the power due to leakage (Figures 7.21 and 7.22) were also plotted. The trends for the measured charge and power passed during the charge and discharge cycles matched that of the float current with cell potential, and in general the measured properties of the first and second cycle exhibited similar values. The leakage power upon charge varied between 0 to  $6.4 \mu\text{W}/\text{cm}^2$ , while upon discharge, the maximum leakage power measured was  $2.5 \mu\text{W}/\text{cm}^2$ . The average leakage power measured in the printed battery was  $1.38 \mu\text{W}/\text{cm}^2$ . A wider window of potentials is currently being explored especially for the discharge cycles where high internal resistance prevented measurements for high states of charge, and further characterization of the physical phenomena on each of the electrodes contributing to the self-discharge should be investigated. Methods to reduce the magnitude of leakage are desired, especially since many recent research efforts have demonstrated the fabrication of wireless node prototypes with average low power draws on the same order as the leakage power reported for this printed battery.

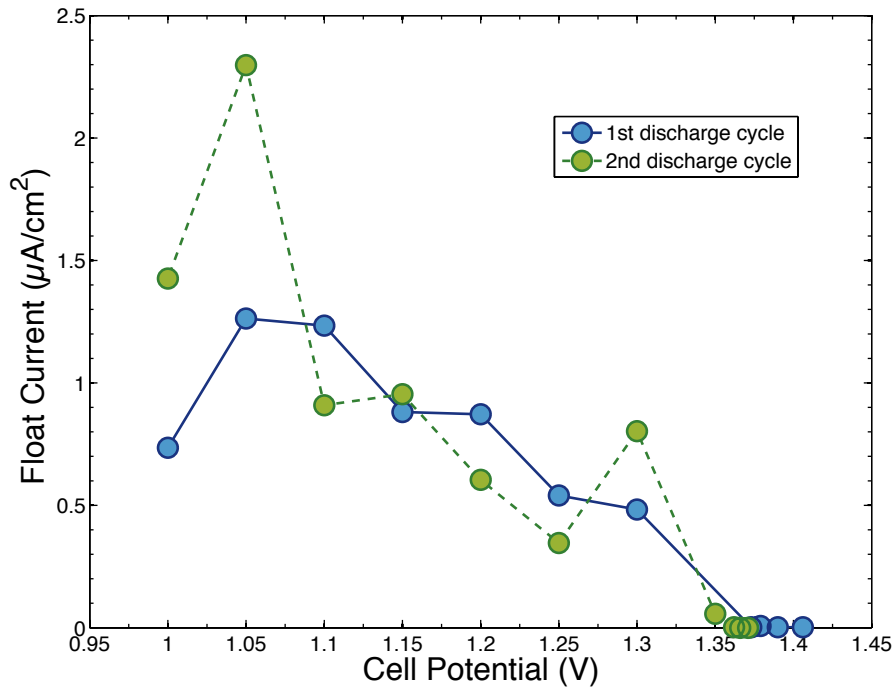


Figure 7.18. The float currents for two discharge cycles as a function of cell potential.

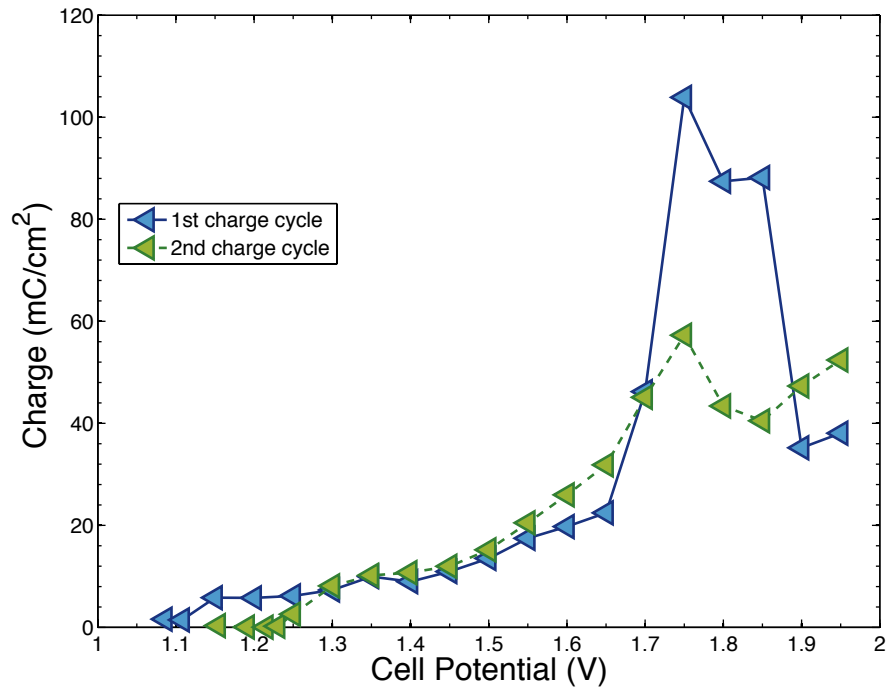


Figure 7.19. The charge passed due to leakage for two charge cycles as a function of cell potential. Measurements were extracted from float current measurements.

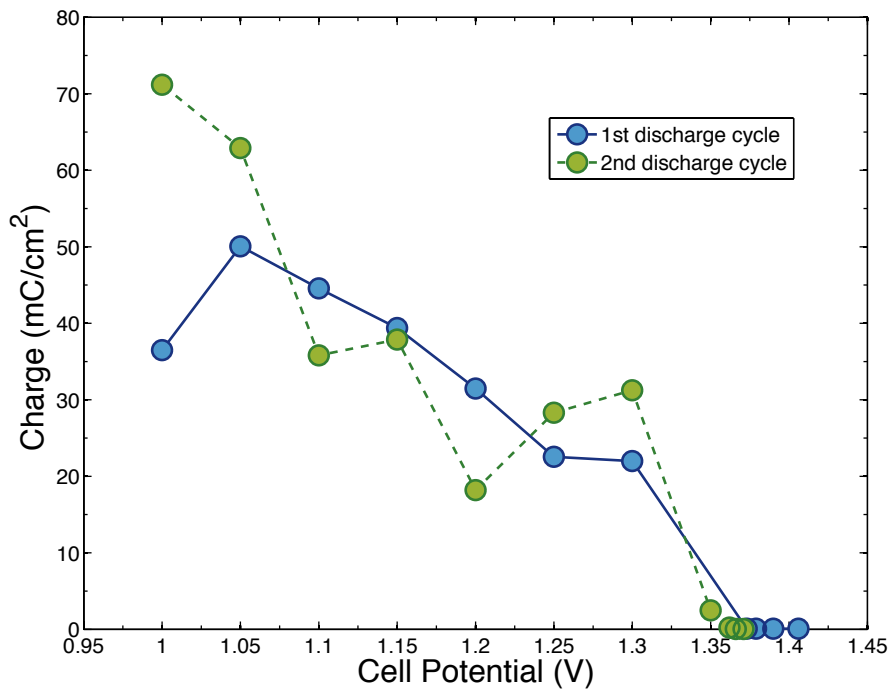


Figure 7.20. The charge passed due to leakage for two discharge cycles as a function of cell potential. Measurements were extracted from float current measurements.



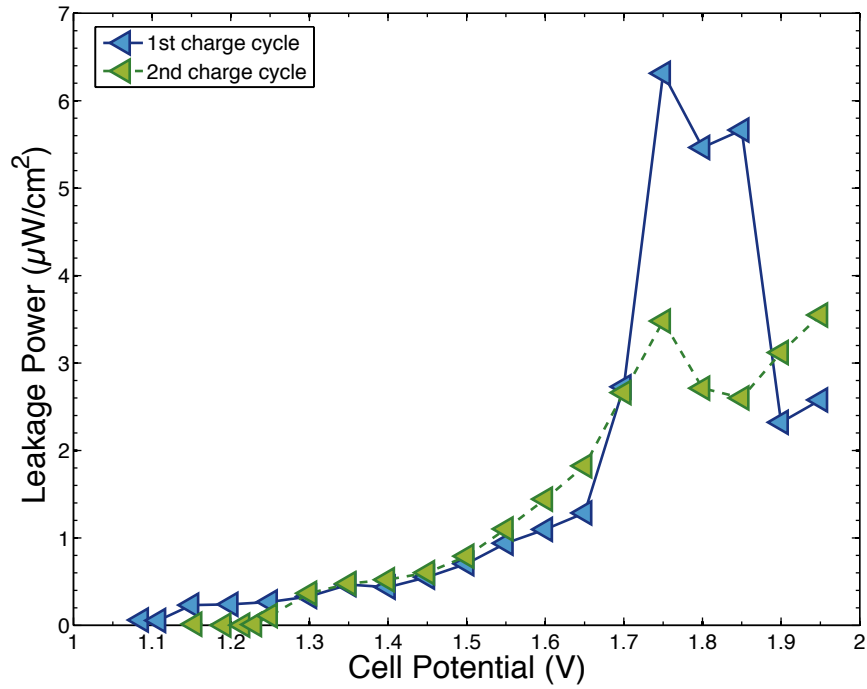


Figure 7.21. The leakage power for two charge cycles as a function of cell potential. Measurements were extracted from float current measurements.

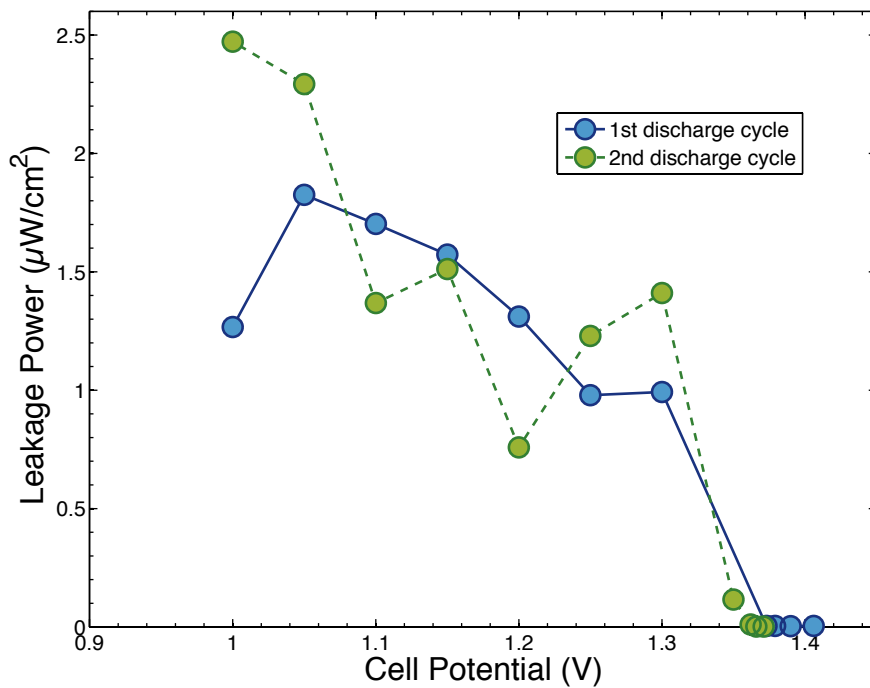


Figure 7.22. The leakage power for two discharge cycles as a function of cell potential. Measurements were extracted from float current measurements.

### 7.2.3 Preliminary Failure Analysis

Understanding the mechanisms of failure in a battery and determining usage and environmental conditions which mitigate the onset of these failure procedures are as critical as characterizing its performance metrics. Though the failure mechanisms in these printed batteries are difficult to isolate, there are a few intuitions that can be derived from observations seen in the previous studies. In Figure 7.23, unexpected failure of the printed batteries occurs in a galvanostatic experiment. The cell was able to successfully charge and discharge over 18 cycles, then at  $t = 47$  h, began to show erratic behavior. After  $t = 58$  h, the cell was unable to charge past 1.3 V. This failure behavior may stem from the presence of a side reaction(s) that eventually extracts most of the current applied to the cell. Side reactions that may occur in this printed battery system include the propagation of zinc dendrites, electrolyte decomposition, and redox reactions due to impurities. Though side reactions in batteries may initiate slowly, after a certain threshold, they become overwhelming factors contributing to the rapid failure of the battery. The detection of impurities is exceedingly difficult, and not discussed in this study.

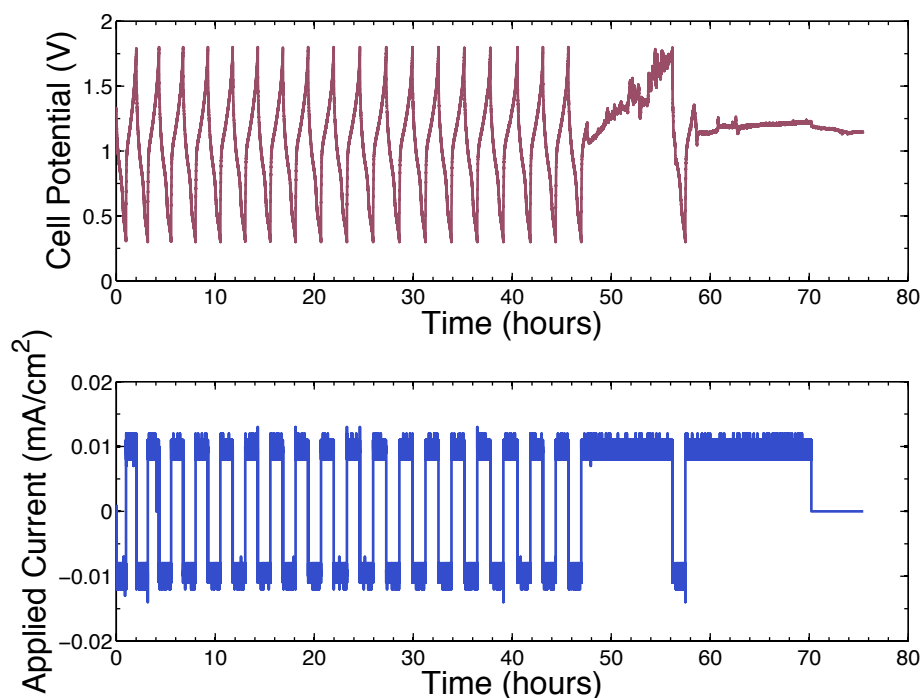


Figure 7.23. Galvanostatic cycling of a printed battery demonstrating unexpected behavior starting at  $t = 47$  h and subsequently followed by the failure of the device.

In section 4.1.3, zinc dendrite formation was discussed in detail, and may be a likely culprit in precipitating unforeseen failure. Due to difficulties in capturing zinc electrode morphology changes and dendrite propagation through the gel electrolyte, no visual confirmation of zinc dendrites in a printed battery has been collected. Carefully controlled in-situ microscopy experiments may provide an opportunity for detecting this in printed batteries. The decomposition of the electrolyte is likely to occur if the cell potential exceeds its electrochemical stability window. This can be a cause of concern

especially in applications that draw large pulses of power. If a battery varies in impedance depending on its state of charge, or ages with cycle life, its response to high power pulses can change. Without proper characterization or regulation with additional circuitry, this can go undetected, leading to the eventual deterioration of the battery's health. By applying a current causing the cell potential of a printed battery to greatly exceed 2 V, induced gel electrolyte decomposition was shown in micrographs in Figure 7.24. In this study, the cell potential approached 5 V. In Figure 7.24 (a-b), the gel electrolyte breakdown occurred near its interface with the printed electrode (at the top of the image). From the micrographs, dark and finger-like structures protrude from the interface. In Figure 7.24 (b), the dark regions possess similar morphology and are of similar size as the green gel electrolyte "grains". This suggests that the electrolyte decomposition due to the application of high currents causes the decomposition of either the polymer grain and/or its encapsulated liquid. As a result, irreversible damage to the gel electrolyte is incurred. In some samples, brown regions have been observed in printed batteries where cell failure was measured, oftentimes visible surrounding an electrode film's corners. These brown regions were imaged using an SEM in Figure 7.24 (c-d). In comparison to the images of fresh gel electrolytes seen in Figure 3.9, the gel no longer exhibits its porous grain morphology, but rather the micrographs suggest that the gel electrolyte had disintegrated. In Figure 7.24 (d) a 60  $\mu\text{m}$  hole is seen, which may be a damaged electrolyte region due to the local potential exceeding the gel's stability.

The inception of zinc dendrite formation and electrolyte breakdown may be a

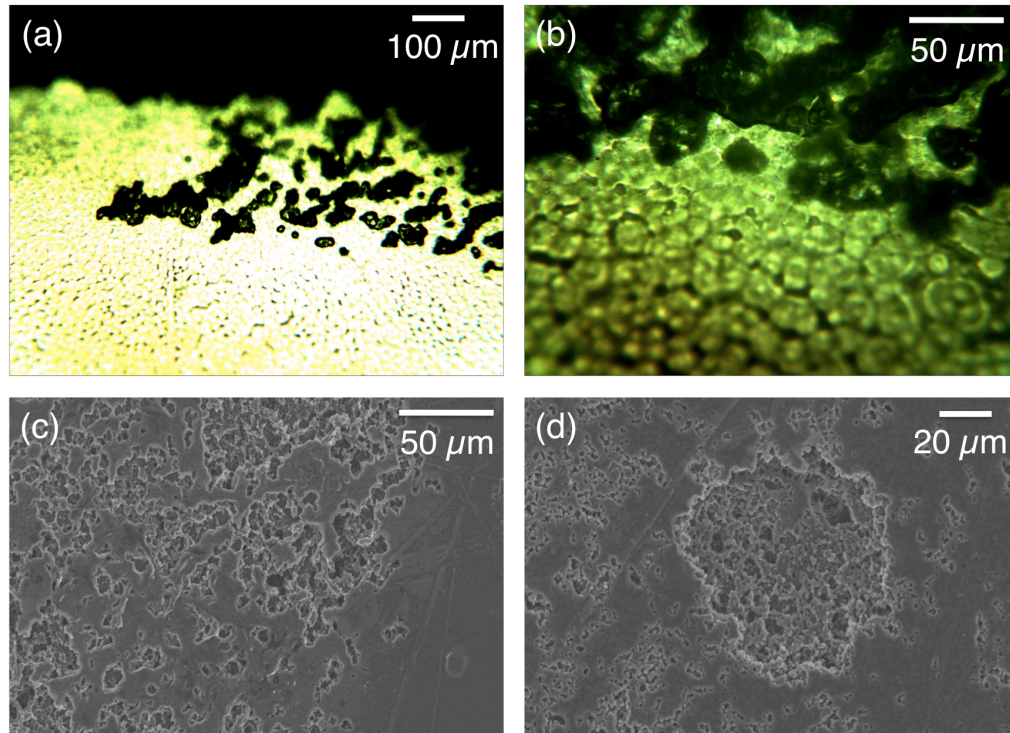


Figure 7.24. (a-b) Optical micrographs of gel electrolyte decomposition. (c-d) Scanning electron microscope (SEM) micrographs of gel electrolyte decomposition.

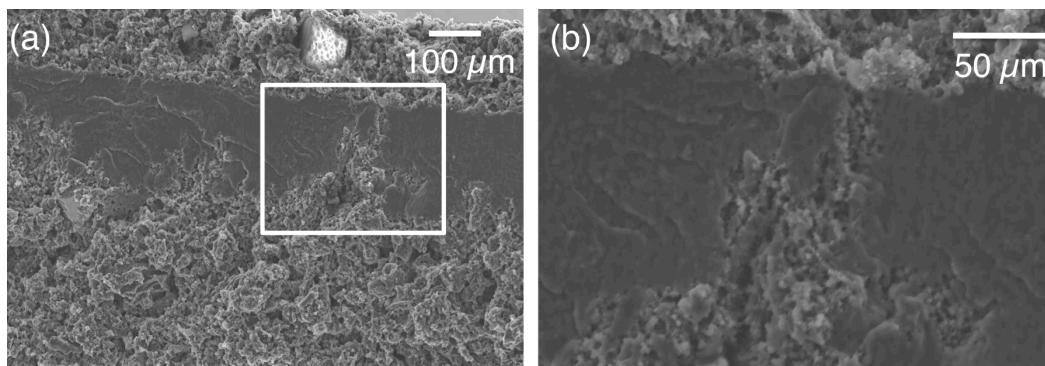


Figure 7.25. Pinholes in the gel electrolyte result in uneven electrode and electrolyte interfaces, which result in points of failure. Magnification of a pinhole boxed in (a) is displayed in (b).

consequence of inhomogenous electrode and electrolyte film morphologies. For example, as was observed in Figure 7.25, a printed gel electrolyte can contain pinholes that subsequently printed electrode ink can trickle into, creating an uneven interfacial configuration. As a result, the current pathways through the battery fail to distribute evenly, and because the electrode material in a pinhole is closer to the opposing electrode interface, current is more likely to flow through this path of low resistance. This localized concentration of current may exceed the stability limits of the electrolyte or promote zinc dendrite propagation, ultimately causing failure in the cell. Since the failure is concentrated to a small region within the battery, it is difficult to preventively detect. From this study, it has become apparent that the reduction of variability in dispenser printing and processing is critical to ensure widespread device fidelity for all batteries that are fabricated. Wright et al. developed a study that begins to quantify sources of processing errors and variability in dispenser printing [Wright, *et al.*, 2010], and further characterization should be explored.

### 7.3 Concluding Remarks

A printed microbattery with zinc and manganese dioxide electrodes sandwiching an ionic liquid gel electrolyte was fabricated using direct write dispenser printing. For an operating voltage between 1 to 2 V, the average measured areal capacity and energy density are  $1 \text{ mAh/cm}^2$  and  $1.2 \text{ mWh/cm}^2$ . Rate performance experiments showed that the microbattery exhibits an optimal capacity for a moderate range of power densities between  $0.05 - 1 \text{ mW/cm}^2$ . The maximum power density extracted from a printed microbattery was  $2 \text{ mW/cm}^2$ .

Table 7.1 summarizes the performance benchmarks of the printed microbattery for capacity, energy, and power with respect to area, volume and weight.

Table 7.1. Printed Microbattery Performance Summary – All values were derived from the maximum measured quantity in lab experiments.

<b>Normalization Metric</b>	<b>Capacity</b>	<b>Energy</b>	<b>Power</b>
<b>Area</b>	1 mAh/cm <sup>2</sup>	1.49 mWh/cm <sup>2</sup>	2 mW/cm <sup>2</sup>
<b>Volume</b>	100 mAh/cm <sup>3</sup>	149 mWh/cm <sup>3</sup>	200 mW/cm <sup>3</sup>
<b>Weight</b>	87 Ah/kg	130 Wh/kg	155 W/kg

The self-discharge characteristics of the printed microbattery were characterized using both open circuit decay and float current measurements. The open circuit decay of the battery was measured for both charge and discharge cycles for a range of cell potentials. The nature of the voltage decay (or recovery for the discharge cycle) as a function of time exhibited a logarithmic dependence, indicating the self-discharge mechanism can be attributed to parasitic faradaic reactions at the anode and cathode rather than diffusion phenomena. This leakage behavior was shown to be dependent on both the state of charge of the battery as well as the direction of current flow. When charging, the leakage power increased with increasing cell potential or state of charge; upon the discharge cycle, the leakage power decreased with decreasing cell potential. The average leakage power of the printed battery was 1.38  $\mu\text{W}/\text{cm}^2$ , but a maximum power of 6.4  $\mu\text{W}/\text{cm}^2$  was measured when charging, and 2.5  $\mu\text{W}/\text{cm}^2$  when discharging. Efforts to understand and mitigate this leakage phenomenon are required, especially for low power applications in which the input and output power densities are similar in magnitude to the leakage power measured in the printed battery.

A few proposed methods of failure in microbatteries, including zinc dendrite formation and electrolyte breakdown, were discussed. One possible reason for the onset of these types of failure may be due to processing variability, for example pinholes in films causing the uneven distribution of electrode and electrolyte layers through the thickness device. Inhomogeneous film morphology can result in uneven current density passage through the battery, causing some regions to experience electric fields or current densities exceeding their stability, or promote premature shorting through the cell. As improvements in printing accuracy and reliability are implemented, these concerns could be potentially be alleviated.

## 7.4 References

- Ho, C. C. (2007). *Pneumatic Dispenser Printed Electrochemical Capacitors*. Masters Thesis, University of California, Berkeley, Materials Science and Engineering.
- Niu, J., Conway, B. E., & Pell, W. G. (2004). Comparative Studies of Self-Discharge by Potential Decay and Float-Current Measurements at C Double-Layer Capacitor and Battery Electrodes. *Journal of Power Sources*, 135, 332-343.

Otis, B., Gambini, S., Shah, R., Steingart, D., Quevy, E., Rabaey, J., et al. (2007). Modelling and Simulation Techniques for Highly Integrated, Low-Power Wireless Sensor Networks. *IET Computer Digital Technology*, 1 (5), 528-536.

Wright, P. K., Dornfeld, D. A., Chen, A., Ho, C. C., & Evans, J. W. (2010). Dispenser Printing for Prototyping Microscope Devices. *Transactions of NAMRI/SME*, 38, pp. 555-561.

## Chapter 8

# Applications and Prospects for Dispenser Printed Microbatteries

The successful demonstration of a working printed microbattery creates an abundant number of opportunities for applications requiring integrated energy storage. The principal advantage of this process is its flexibility to pattern the electrochemical device into arbitrary geometries with precise lateral and thickness control onto virtually any substrate so that areas not typically accessible with other fabrication technologies can be used to store energy, and the performance of the electrochemical device can be optimized for a given application's power demands. Furthermore, the process is inexpensive and can be scaled up for mass manufacture. The ability to precisely pattern inks onto any substrate at ambient and room temperature conditions allows for the easy integration of batteries onto any devices. Areas that can be covered with an energy storage structure may include the regions adjacent to any other components on the substrate, as well as conformably coated above and below the components. The following sections show the versatility of the printing process and possible applications for the technology.

### 8.1 “Printing on Green”

On a crowded printed circuit board (PCB) with limited unoccupied substrate area, the dispenser printer has the ability to fill any open space with an energy storage component(s), effectively depositing an energy storage structure and electrical leads on typically unreachable areas within a crowded substrate. This concept, also known as “printing on green”, is illustrated in Figure 8.1. Note that this process is carried out under ambient conditions and mild post-processing temperatures ( $< 150^{\circ}\text{C}$ ), therefore it avoids damaging any neighboring components that might be sensitive to higher temperature or other gas or solvent exposure.

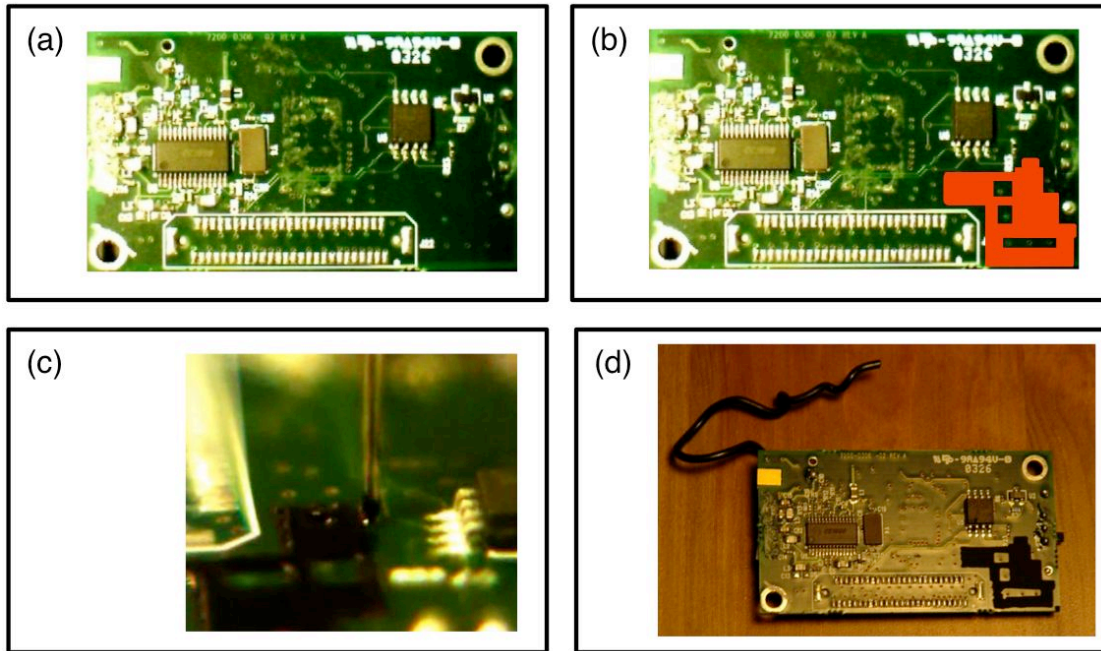


Figure 8.1. (a-d) “Printing on green” concept: (a) A crowded printed circuit board (PCB) has limited unoccupied substrate area, as is designated in red in (b). The dispenser printer is able to deposit a printed battery in this open space (c) and an energy storage device is integrated directly onto the PCB (adapted from [Steingart, 2006]).

## 8.2 Hybrid Micropower Supplies

For applications operating over long device lifetimes ( $> 10$  years without the ability to replace the power source if depleted), the incorporation of an energy harvester to convert ambient energy to useful electrical energy is a popular strategy for perpetual power supplies. Obstacles to the incorporation of energy harvesting technologies in current devices include their high cost and intermittency of power supplied. Dispenser printed microbatteries add inherent value to energy harvesting devices because of their simple integration procedure that enables versatile form factors and customizable performance properties. As most energy harvesters are materials-, processing-, and energy-intensive to fabricate, pairing these devices with a low-cost energy storage device that is easily integrated with minimal materials, waste, and energy inputs adds significant utility. More importantly, energy storage bridges discrepancies in power demands with the power supplied by the harvester. In most applications and environments, the combination of energy harvester and storage devices, known as a hybrid power supply, will be necessary. In Figure 8., dispenser printing was used to integrate an energy storage device on the substrate area surrounding MEMS vibration energy harvesters that were microfabricated onto a silicon die [Miller, *et al.*, 2009]. Note that the components were only physically integrated, and were not electrically connected with power regulation circuitry. The dispenser printer also offers the added benefit of being able to tailor the energy storage performance properties to be compatible with the power supplied by the energy harvester



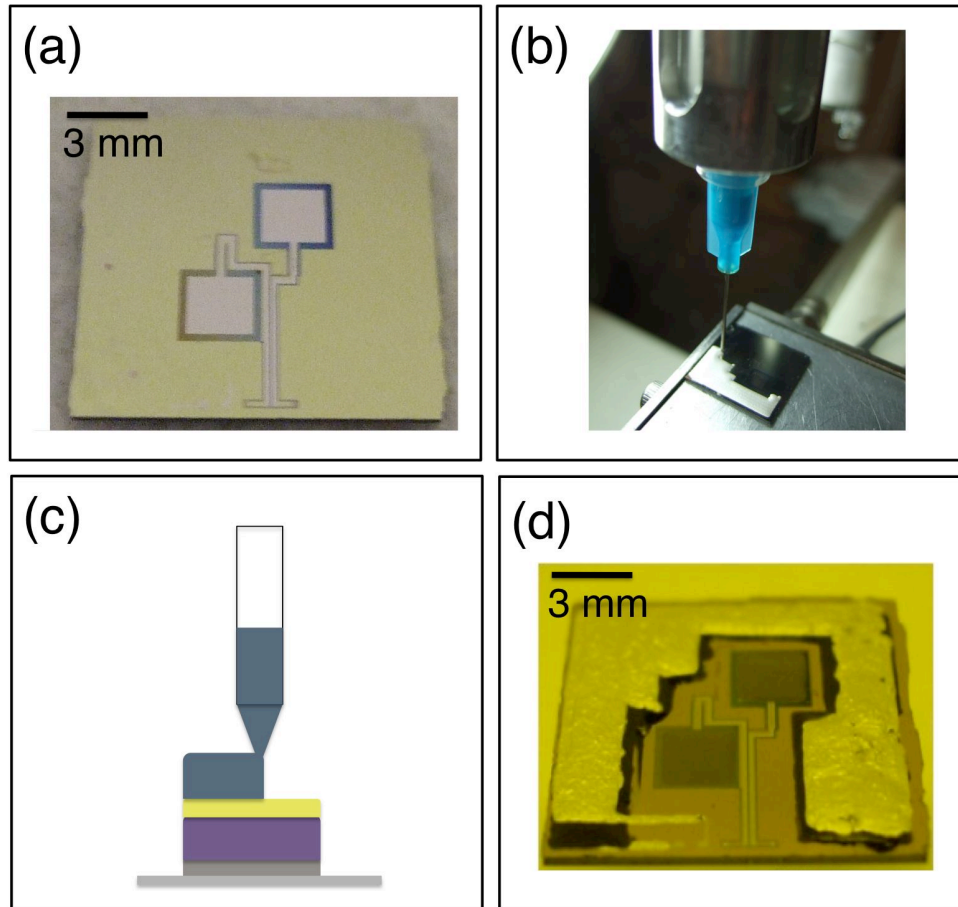


Figure 8.2. (a-d) An integrated hybrid power supply comprising of (a) MEMS vibration energy harvesters patterned on a silicon die. (b-d) The dispenser printer deposits a multilayer printed energy storage component in the open space surrounding the energy harvester (adapted from [Miller, *et al.*, 2009]).

as well as the power demanded by the load, which both can vary significantly with the environment it is calibrated in.

### 8.3 Conformal Printing

Along with being able to print in inaccessible areas on a crowded substrate, the dispenser printer is also capable of printing conformably on non-planar surfaces (see Figure 8.3 for a demonstration of this concept). This adds greater flexibility in where energy storage devices can be integrated on a device. On a crowded substrate, an electrically insulating layer can be printed on top of any components, and then conformably coated with a printed microbattery. Since all fabrication and post-processing of the microbattery occurs at ambient conditions and temperatures under 120°C, all neighboring components should not be damaged in the process.

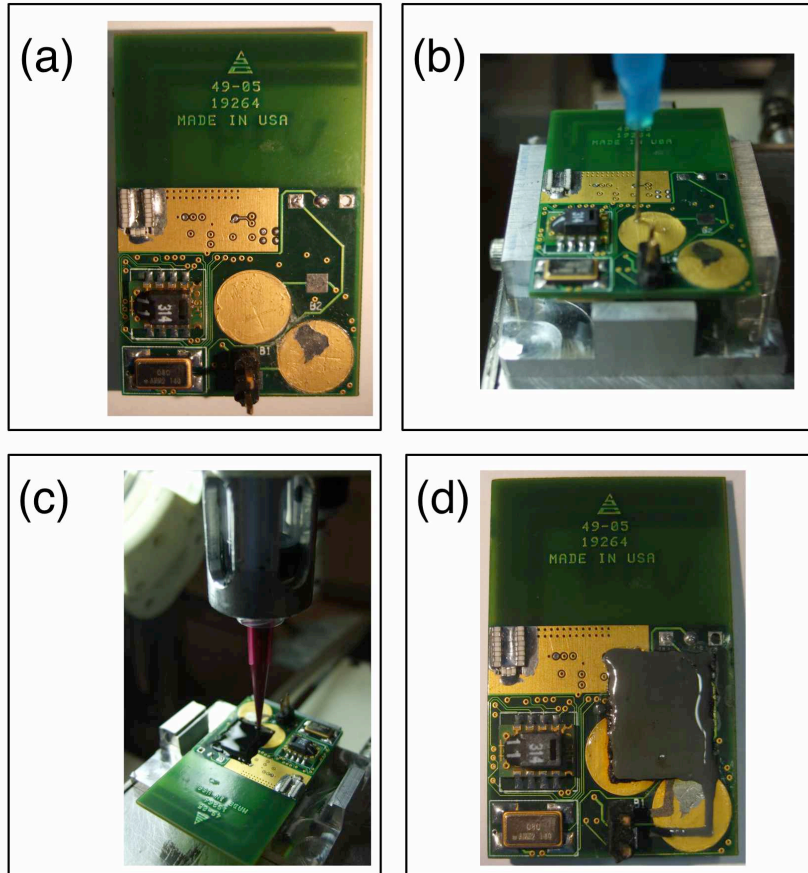


Figure 8.3. (a-d) The conformal printing of a microbattery on an integrated circuit board: (a) An integrated circuit board originally designed to be powered with two hearing aid batteries (connected by two gold circular traces) will be retrofit with a dispenser printed microbattery. (b) An electrical insulating layer is printed on top of the board on which (c-d) a printed microbattery is deposited.

## 8.4 Local Energy Storage – An Opportunity in Creating a New Design Paradigm

The capability of depositing custom microbatteries both in the open space as well as conformably on device components provides extensive possibilities for the on-demand fabrication of localized energy storage components. Traditionally, an electronic device obtains its power from a single source, such as a primary battery. If any of its components require different supply voltages, additional power circuitry is needed to convert the battery voltage to its required value. The efficiency of a voltage conversion operation will vary with the type of conversion method used; linear regulators are simple and low-cost, but are very inefficient for large voltage changes, resulting in unwanted heat dissipation. Switched-mode voltage converters (such as switched capacitors) can be designed to be very efficient (> 75%) and by using CMOS fabrication, the devices are less area intensive compared to linear regulators, however they are complex to design and integrate. In this

discussion it is assumed that a typical wireless sensor contains a microcontroller typically comprised of an oscillator and control unit, a communication component(s) such as a transceiver and/or receiver, a sensor(s), and a power supply. For most microdevices, various components require different supply voltages, requiring an intricate network of power converters, for example, UC Berkeley's low power wireless sensor prototype "picocube" required the conversion of a nickel metal hydride battery supply voltage of 1.2 V to 2.1 V for the sensor and microcontroller, and 0.65 V for the radio (Seeman, Sanders, & Rabaey, 2008). The use of micro energy storage devices as local supply voltages and power sources can mitigate the design complexities and conversion inefficiencies associated with power regulation as well as reduce the substrate area dedicated power circuitry. Added functionality and areal footprint efficiency is achieved by fabricating stacked series and parallel configurations of microbatteries and capacitors. This should be achievable using dispenser printing, but has yet to be fully demonstrated.

Localized energy storage components can be tailored according to their use; rather than pulsing a battery with a cumulatively high power draw derived from the sum of many components, a highly tailored energy storage device can be dedicated to each individual component. For example, a microcontroller unit typically draws a continual low power ( $< 10 \mu\text{W}$ ) and may be suitably powered by a local microbattery of the chemistry studied in this work. On the other hand, a transceiver requires infrequent high bursts of power. This behavior may be better addressed by an electrochemical capacitor or battery chemistry capable of handling high rates of discharge (such as zinc-silver oxide). By exploiting their advantages and separating the energy storage components, the overall cumulative health of the energy storage network may exceed that of traditional single battery powered system. To encourage this design paradigm change, simulations and demonstrations of this concept are needed.

## **8.5 Flexible Electronics**

Along with the applications discussed, flexible electronics provides a unique opportunity for printed microbatteries. Relevant markets include low-cost active RFID tags for asset management and printed media. By utilizing polymer-based materials, the zinc, gel electrolyte, and manganese dioxide microbatteries discussed in this work can be reasonably bent and conformed to non-planar substrates without damage. Furthermore, most flexible substrates are polymer materials which cannot be processed beyond 150-200°C. The dispenser printer enables near room temperature deposition and post-processing, and is compatible with these substrates. A demonstration of a flexible dispenser printed microbattery is shown in Figure 8.4.

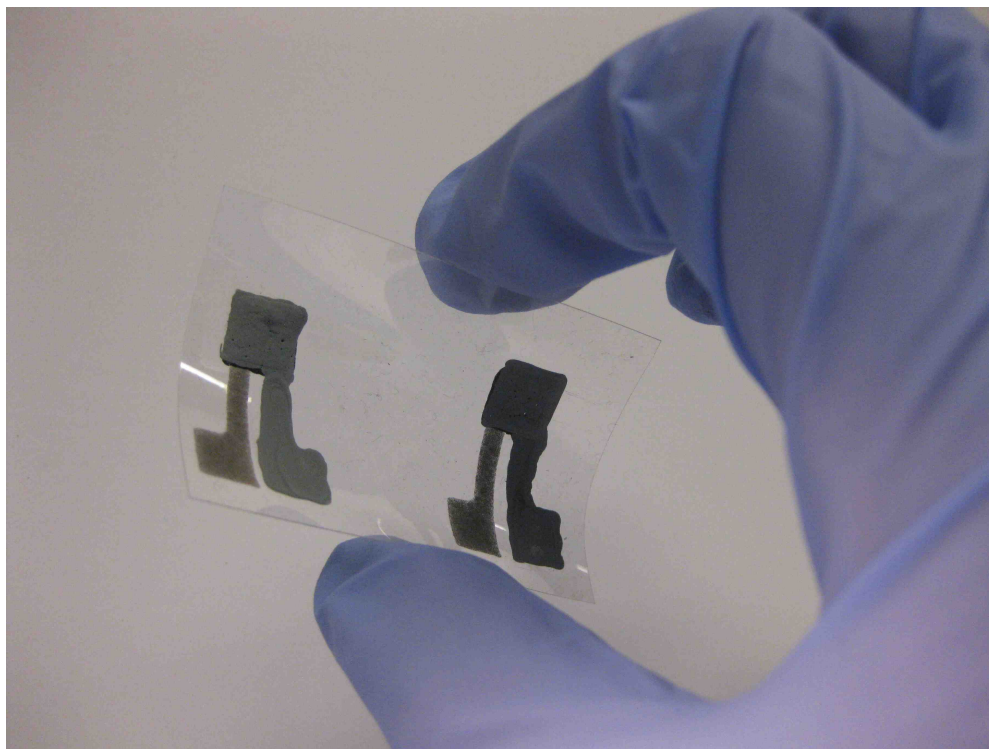


Figure 8.4. Flexible dispenser printed microbatteries on a polyimide substrate. The microbatteries are composed of a nickel current collector, manganese dioxide electrode, ionic liquid gel electrolyte, and zinc electrode/current collector.

## 8.6 Conclusions

Dispenser printing offers a simple method of integrating printed microbatteries on small devices by utilizing any open space on a substrate, or even conformably coating the device and its components. Rather than using a traditional single battery power source, small energy storage devices can be tailored to power a single component, and therefore provide efficient delivery of power locally. Because dispenser printing is straightforward and relatively materials or substrate indiscriminate, it can be applied to a variety of energy storage devices and corresponding chemistries. As a consequence, local energy storage components can be highly customized in supply voltage and output characteristics to best optimize its performance. Furthermore, this battery chemistry and printing process is highly compatible with flexible substrates. As has been demonstrated, the applications for dispenser printed microbatteries are varied and highly enabling.

## 8.7 References

Miller, L. M., Ho, C. C., Shafer, P. C., Wright, P. K., Evans, J. W., & Ramesh, R. (2009 йил 17-Jul). Integration of a Low Frequency, Tunable MEMS Piezoelectric Energy

Harvester and a Thick Film Micro Capacitor as a Power Supply System for Wireless Sensor Nodes. *Proceedings from IEEE-ECCE* , 2627-2634.

Seeman, M. D., Sanders, S. R., & Rabaey, J. M. (2008). An Ultra-Low-Power Power Management IC for Energy-Scavenged Wireless Sensor Nodes. *IEEE 2007 Custom Intergrated Circuits Conference (CICC)*, (pp. 925-931).

Steingart, D. A. (2006). *Printed On-Chip Electrochemical Storage*. PhD Dissertation, University of California, Berkeley, Materials Science and Engineering.

# Chapter 9

## Appendix: Experimental Methods and Derivations

This section describes in detail the experimental procedures, apparatus, and test cell configurations for the measurements presented in Chapters 3 through 8. Any necessary theoretical derivations are also included. This chapter is organized according to experimental equipment, characterization procedure, and test configurations.

### 9.1 Rheometry

#### 9.1.1 Rotating Parallel Plate Rheometer

A rotating parallel plate rheometer was used to characterize the viscosity of highly viscous polymer solutions and slurries. An example of the Rheometrics ARES parallel plate rheometer used in this work is included in Figure 9.1. Measurements are made using strain-controlled rheometry. Polymer solution or slurry is placed in the gap between the two plates. The bottom plate is rotated by a motor, applying strain or rotation to the polymer solution; the top plate is connected to a transducer which measures normal force and torque. The viscosity ( $\eta$ ) is the proportional relationship between the applied strain ( $\tau$ ) and the resulting force or stress ( $G$ ):

$$\tau = \frac{\eta}{G} \quad (\text{Equation 9.1})$$

The viscosity of the solutions and slurries were displayed as a function of shear rate (Figure 2.6).

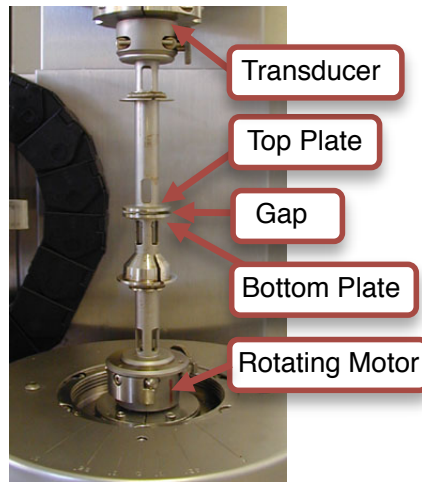


Figure 9.1. Rheometrics ARES parallel plate rheometer. Polymer solution or slurry is injected into the gap between the top and bottom plate [Rheometrics ARES Rheometer].

### 9.1.2 Cone-Plate Viscometer

A Brookfield DV-III+ viscometer [Brookfield] with small sample, small volume adapter was used to characterize the viscosities of ionic liquid samples (Section 3.2.2). It utilizes a cone-plate geometry, which unlike the rotating parallel plate viscometer, applies a uniform strain or strain rate and utilizes a fixed gap distance between the cone and plate.

### 9.1.3. Dispenser Printer Deposition Capabilities

To predict the feature sizes capable of being deposited by the dispenser printer, the ink viscosity behavior with respect to shear rate was correlated to the maximum shear rate applied by the dispenser printer to the ink upon deposition. This was determined by estimating the flow down a needle.

#### Derivation of the Maximum Shear Rate Experienced by a Solution Flowing Down a Needle

In Figure 9.2, a hollow cylinder with length  $L$  and radius  $R$  represents a syringe needle. Fluid flows down its length along the  $z$  coordinate axis. The radial axis is orthogonal to the  $z$ -axis. A differential shell is defined as a cylinder of radius  $r_s$  with a shell thickness of  $\delta r$ . The footprint area of the differential shell is  $2\pi r_s \delta r$ .

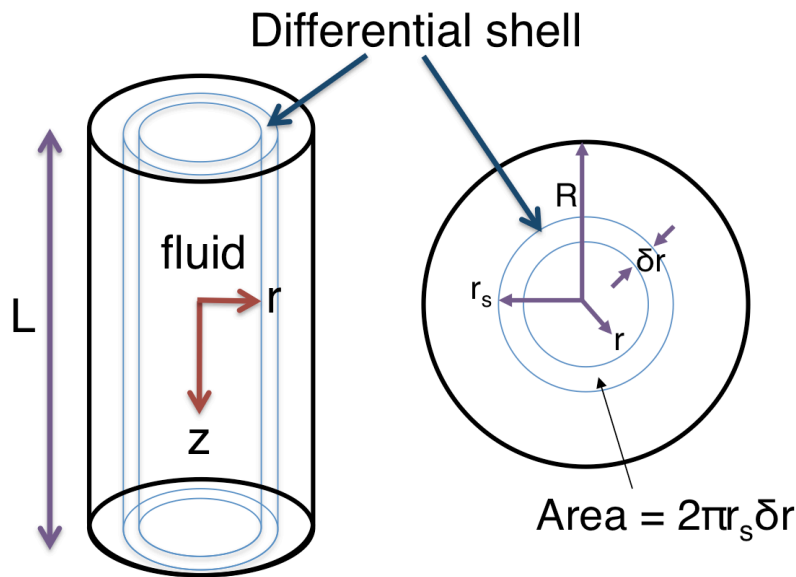


Figure 9.2. A schematic of the flow down a needle. A differential shell is defined, along with the coordinate system and relevant variables.

A differential shell momentum balance was performed for the flow down a needle (Poirier, *et al.*, 1994]. The force balance sums the downward and upward forces, as well as rate of inflow and outflow. At steady state, there is no accumulation in the needle. This calculation assumes the fluid is Newtonian.

Differential Shell Momentum Balance:

Downward drag near axis      Gravity      Pressure at top

$$\tau_{rz} 2\pi r L \Big|_{r_s} + \rho g 2\pi r_s \delta r L + 2\pi r_s \delta r P_{top} \dots$$

Upward drag at walls      Pressure at bottom

$$\dots - (\tau_{rz} 2\pi r L \Big|_{r_s + \delta r} + 2\pi r_s \delta r P_{bottom}) \dots$$

Rate of inflow      Rate of outflow

$$\dots + 2\pi r_s \delta r \rho V_z^2 \Big|_{top} - 2\pi r_s \delta r \rho V_z^2 \Big|_{bottom} = 0$$

(Equation 9.2)

where  $\tau$  is the shear stress,  $P$  is pressure, and  $V$  is the velocity. If the fluid density is assumed to be constant and the needle does not taper, the rate of inflow should exactly equal the rate of outflow, therefore the last two terms in Equation 9.2 should cancel out. The expression is rearranged and simplified:



$$\frac{r_s(P_{Top} - P_{Bottom})}{L} + r_s \rho g = \frac{1}{\delta r} \left[ r\tau_{rz} \Big|_{r_s + \delta r} - r\tau_{rz} \Big|_{r_s} \right] \quad (\text{Equation 9.3})$$

Letting the differential shell thickness,  $\delta r$  approach 0:

$$\frac{r_s(P_{Top} - P_{Bottom})}{L} + r_s \rho g = \frac{\delta(r\tau_{rz})}{dr} \Big|_{r_s} \quad \text{when } \delta r \rightarrow 0 \quad (\text{Equation 9.4})$$

The shell radius  $r_s$  is arbitrary, and the equation above is valid for all  $r < R$ .

$$\frac{r(P_{Top} - P_{Bottom})}{L} + r \rho g = \frac{\delta(r\tau_{rz})}{dr} \quad (\text{Equation 9.5})$$

Integrating Equation 9.5 results in the following expression:

$$\frac{r^2(P_{Top} - P_{Bottom})}{2L} + \frac{r^2}{2} \rho g = r\tau_{rz} + C_1 \quad (\text{Equation 9.6})$$

Newton's equation:  $\tau_{rz} = -\mu \frac{dV_z}{dr}$  (Equation 9.7)

$$\frac{r^2(P_{Top} - P_{Bottom})}{2L} + \frac{r^2}{2} \rho g = -r\mu \frac{dV_z}{dr} + C_1 \quad (\text{Equation 9.8})$$

At  $r=0$ ,  $\frac{dV_z}{dr} = 0$  because of symmetry,

$\tau_{rz} = 0$  at  $r = 0$  and  $C_1 = 0$

$$\frac{r}{2} \left[ \frac{(P_{top} - P_{bottom})}{L} + \rho g \right] = -\mu \frac{dV_z}{dr} \quad (\text{Equation 9.9})$$

By integrating the expression above:

$$\frac{r^2}{4} \left[ \frac{(P_{top} - P_{bottom})}{L} + \rho g \right] = -\mu V_z + C_2 \quad (\text{Equation 9.10})$$

at  $r = R$ ,  $V_z = 0$

$$C_2 = \frac{R^2}{4} \left[ \frac{(P_{top} - P_{bottom})}{L} + \rho g \right] \quad (\text{Equation 9.11})$$

$$\therefore \frac{r^2}{4} \left[ \frac{(P_{top} - P_{bottom})}{L} + \rho g \right] = -\mu V_z + \frac{R^2}{4} \left[ \frac{(P_{top} - P_{bottom})}{L} + \rho g \right] \quad (\text{Equation 9.12})$$

$$V_z = \left[ \frac{(P_{top} - P_{bottom})}{L} + \rho g \right] \left( \frac{R^2}{4\mu} \right) \left[ 1 - \left( \frac{r}{R} \right)^2 \right] \quad (\text{Equation 9.13})$$

Equation 9.13 exhibits a parabolic velocity profile and the maximum velocity occurs at  $r=0$ .

$$V_z = \left[ \frac{(P_{top} - P_{bottom})}{L} + \rho g \right] \left( \frac{R^2}{4\mu} \right) \quad (\text{Equation 9.14})$$

Volumetric flow rate:

$$\int_0^R V_z r 2\pi dr = \left[ \frac{(P_{top} - P_{bottom})}{L} + \rho g \right] \left( \frac{\pi R^4}{8\mu} \right) = \text{flow rate} \quad (\text{Equation 9.15})$$

Maximum shear rate:

$$\frac{dV_z}{dr} = \left( \frac{R}{2\mu} \right) \left[ \frac{(P_{top} - P_{bottom})}{L} + \rho g \right] \quad (\text{Equation 9.16})$$

$$\frac{dV_z}{dr} = \left( \frac{R}{2\mu} \right) \left[ \frac{(P_{top} - P_{bottom})}{L} + \rho g \right] \left( \frac{\pi R^4}{8\mu} \right) \left( \frac{8\mu}{\pi R^4} \right) \quad (\text{Equation 9.17})$$

$$\frac{dV_z}{dr} = \left( \frac{R}{2\mu} \right) [\text{flow rate}] \left( \frac{8\mu}{\pi R^4} \right) \quad (\text{Equation 9.18})$$

The flow rate will depend on the shot time and pressure applied, as well as the needle the ink is extruded through and the ink properties.

$$\text{flow rate} = \frac{\text{drop volume}}{\text{shot time}} \quad (\text{Equation 9.19})$$

The flow rate is calculated by estimating the drop volume of an ink through a needle for a pressure applied by the dispenser printer using imaging software and correlating it to the shot time applied by the dispenser printer.

$$\text{maximum shear} = \frac{4 \cdot \text{flow rate}}{\pi R^3} \quad (\text{Equation 9.20})$$

The maximum shear experienced by the ink is calculated from the flow rate and needle dimensions.

For a specific ink and needle size, the lowest and highest pressure applied by the dispenser printer can be measured. The dispenser printer can print a range of feature sizes by utilizing a variety of dispensing needles of varying cylinder radii. From the smallest and largest needles that can successfully deposit ink into a defined feature size, the ink droplet extruded from the needle is measured using imaging software (see section 2.2.1).

For a shot time of 10 ms, the flow rate can be correlated to this drop volume using Equation 9.19, and the maximum shear felt by the ink in that given needle can be calculated with Equation 9.20. The ranges of shear rates applied by the dispenser printer and resulting feature sizes for a polymer solution and composite slurry inks are featured in Figure 2.6.

## 9.2 Voltammetry

Voltammetry is a class of potentiodynamic electrochemical characterization methods where the cell voltage is scanned in a defined procedure, and the resulting cell current is measured. Linear sweep and cyclic voltammetry are used to determine various electrochemical properties. Both types of voltammetry experiments were conducted using a Gamry Reference 600 Potentiostat/Galvanostat/ZRA.

### 9.2.1 Linear Sweep Voltammetry

In linear sweep voltammetry (LSV) experiments, a sweeping potential is applied between a working electrode and a reference electrode. The potential is swept at a defined rate (mV/s), and any current detected at the working electrode is measured. Any inflections, peaks, or valleys detected could indicate a number of phenomena including the presence of redox reactions occurring at an applied potential or the change in the rate of a reaction occurring at adjacent potentials. The potential at which the sweep is terminated will be determined by the experimenter.

#### Electrochemical Potential Stability

LSV can be used to determine the range of potentials in which a material is electrochemically stable. In this work, LSV was used to determine the electrochemical potential stability window of ionic liquid electrolytes of varying zinc salt concentration. The counter electrode used was a zinc foil while the working electrode was a stainless steel shim. Stainless steel is nonreactive with the ionic liquid electrolyte, and is therefore known as a “blocking” electrode. The test cell is illustrated in Figure 9.4. To contain the ionic liquid electrolyte, a Swagelok cell was used, and a 100  $\mu\text{m}$  Teflon spacer ensured separation between the two electrodes.

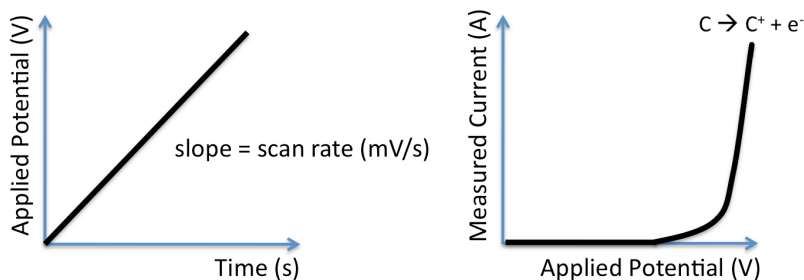


Figure 9.3. Schematic of linear sweep voltammetry showing an applied sweeping potential (left) and resulting measured current (right). The current rise corresponds to the oxidation or reduction reaction of an active species at a certain potential.

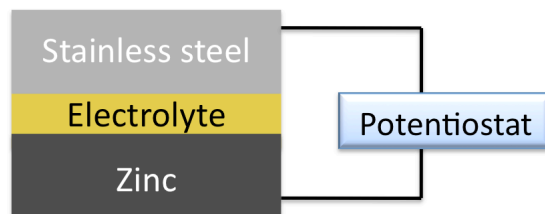


Figure 9.4. Test cell used to measure the electrochemical potential stability of ionic liquid electrolytes. Zinc is the counter electrode while stainless steel acts as the working electrode.

## 9.2.2 Cyclic Voltammetry

Cyclic voltammetry (CV) is similar in concept to LSV, except once reaching a pre-defined potential, the potential sweep is reversed until a terminal potential is approached. This experiment may be repeated over numerous cycles, hence its moniker.

### Electrodeposition and Dissolution

For electrochemically reactive, “non-blocking” electrodes, CV can be used to investigate the electrodeposition and dissolution of an active species through an electrolyte medium. A typical test cell is usually symmetric and contains two non-blocking electrodes sandwiching an electrolyte. An example of the stacked cell configuration used in sections 4.1.1 and 4.1.2 is shown in Figure 9.5. Zinc foil electrodes tested with ionic liquid electrolyte were set in a Swagelok cell and separated by a 100  $\mu\text{m}$  Teflon spacer. Zinc foil electrodes tested with gel electrolytes were constructed by printing gel electrolytes of defined areas directly onto the zinc foils; after drying the gels, two gel-covered foils were clipped together at 60°C for 1 hour. Afterwards, the cell was equilibrated at room temperature for 24 hours before testing. For the characterization of fully printed cells, printed zinc electrodes were patterned on a glass substrate adjacent to each other (as shown in Figure 9.6). The separation between the films was 1-2 mm. A gel electrolyte was printed on top of the electrodes, and the electrode areas covered with gel electrolyte defines the active area of the cell.

Parameters that can be extracted from the measurement include the cell potentials at which oxidation and reduction occur, the maximum magnitude of the cathodic and anodic peaks, and the shape of the voltammogram, especially the sharpness of the peaks (see Figure 9.7). Note that these parameters are dependent on scan rate, scan direction, and other experimental quantities. A comparison of the positive (increasingly positive cell

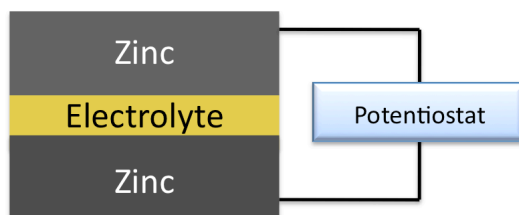


Figure 9.5. Symmetric cell probed by CV to determine properties of the electrodeposition and dissolution of zinc with the gel electrolyte.

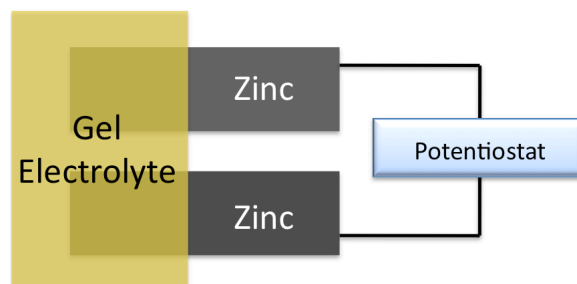


Figure 9.6. Printed symmetric cell probed by CV to determine properties of the electrodeposition and dissolution of printed zinc films with the gel electrolyte. Films were deposited adjacent to each other on a substrate such as glass and gel electrolyte was printed on top of the printed electrodes.

potential) and negative (increasingly negative cell potential) scans can indicate the reversibility of a redox reaction for certain scan rates, and repeating the experiment many times can probe its long-term cycling behavior.

### Electrochemical Insertion into a Material

A CV experiment can be used to determine if and at what cell potentials electrochemical intercalation reactions occur. Similar to electrochemical deposition and dissolution reactions, the insertion of active ions in a host material is accompanied by an oxidation or reduction reaction that outputs a detectable current density measurable by CV. In this work, electrochemical insertion of zinc into vanadium pentoxide ambigel and manganese dioxide composite cathodes was detected for a working potential range between 0 to 2

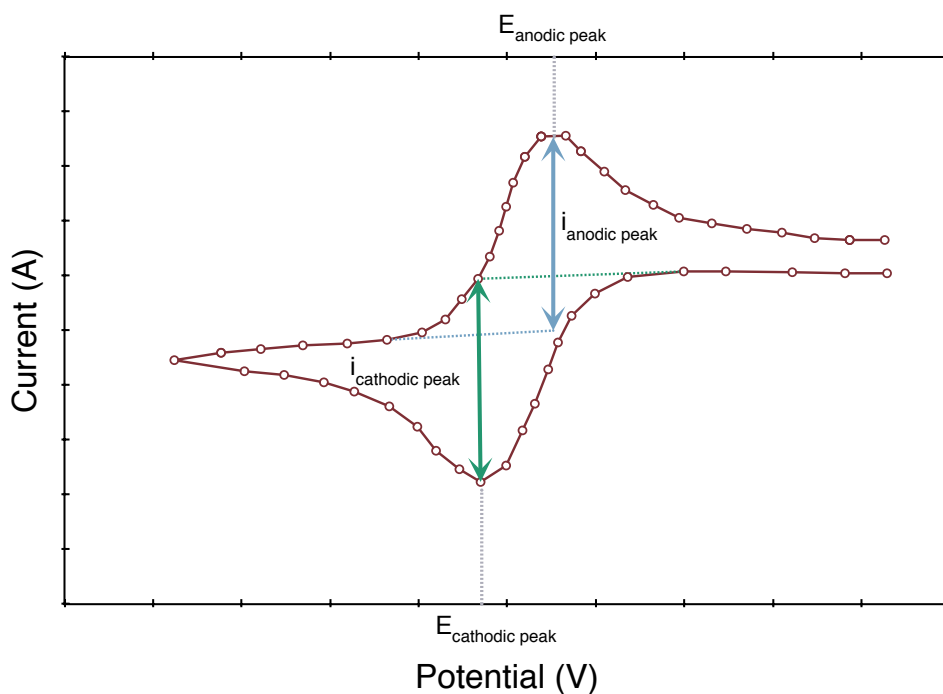


Figure 9.7. Example voltammogram with key parameters typically characterized using CV.

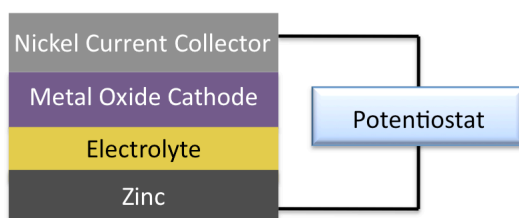


Figure 9.8. Test cell probed with CV used to test the electrochemical intercalation of zinc ions into a metal oxide host material.

V. Both cells were fabricated by printing the cathode inks onto nickel current collector foils. The inks were patterned into  $0.25 \text{ cm}^2$  square films and then covered with printed gel electrolyte layers. Gel electrolyte was printed on zinc foil counter electrodes. The zinc and metal oxide cathode structures were combined by aligning their gel films together, compressing the structure, then heating the cell to  $60^\circ\text{C}$  for one hour. Afterwards, the cell was equilibrated at room temperature for 24 hours before testing. The test structure consists of the cell components illustrated in Figure 9.8.

### Electrochemical Potential Stability

The compatibility of current collector material with gel electrolyte was tested using CV. CV was used instead of LSV because instabilities such as the formation of dendritic structures may manifest gradually with cyclic behavior. The test cells were fabricated with the same procedure discussed for the printed zinc electrodeposition and dissolution cells, and a representative cell is illustrated in Figure 9.9. The printed current collector inks included commercial silver in epoxy [ESL ElectroScience] and in-lab synthesized nickel slurries incorporating various commercial nickel powders.

## 9.3 Electrochemical Impedance Spectroscopy

Impedance is a metric used to quantify the ability of a circuit component to resist the flow of an electrical current. Resistance is the component of impedance that is independent of frequency. For an ideal resistor, Ohm's law states:

$$\text{Resistance} = \frac{\text{Voltage}}{\text{Current}} \quad (\text{Equation 9.21})$$

An ideal resistor would be invariant with input frequency. When exposed to an input AC current or voltage, an ideal resistor would output a corresponding in-phase signal. Non-ideal components display more complicated behavior, captured more accurately with impedance rather than these oversimplifying resistance properties.

Electrochemical impedance spectroscopy (EIS) is a common method used to differentiate impedances within an electrochemical cell. It is measured by applying a small AC potential to the cell and then measuring its induced AC current response. A small excitation potential ( $< 10 \text{ mV}$ ) is used to maintain a linear or pseudo-linear response so that the output current remains sinusoidal in morphology but shifted in phase. If the excitation potential,  $E(t)$ , is represented by the following expression:

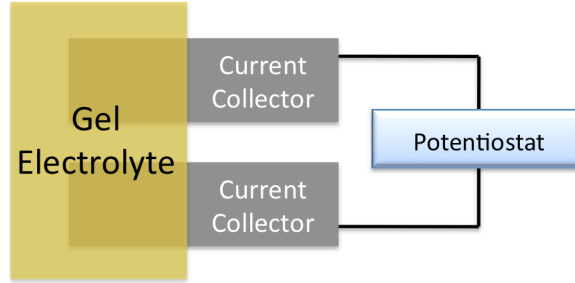


Figure 9.9. Printed symmetric cell probed by CV to determine the stability of printed current collector films with the gel electrolyte. Films were deposited adjacent to each other on a substrate such as glass, and gel electrolyte was printed on top of the printed electrodes.

$$E(t) = E_o \cos(\omega t) \quad (\text{Equation 9.22})$$

where  $t$  is time,  $E_o$  is the amplitude of the potential signal, and  $\omega$  is the radial frequency (rad/s), which is related to frequency ( $f$ ):

$$\omega = 2\pi f \quad (\text{Equation 9.23})$$

The resulting current for a linear response,  $I(t)$ , has a sinusoidal shape with an amplitude  $I_o$  and phase shifted by  $\phi$ :

$$I(t) = I_o \cos(\omega t - \phi) \quad (\text{Equation 9.24})$$

All expressions can be expressed as complex numbers by using Euler's function:

$$\exp(j\phi) = \cos\phi + j \sin\phi \quad (\text{Equation 9.25})$$

$$E(t) = E_o \exp(j\omega t) \quad (\text{Equation 9.26})$$

$$I(t) = I_o \exp(j\omega t - j\phi) \quad (\text{Equation 9.27})$$

The impedance is therefore the ratio between the input potential and output current:

$$Z = \frac{E(t)}{I(t)} = Z_o \exp(j\phi) = Z_o (\cos\phi + j \sin\phi) \quad (\text{Equation 9.28})$$

As can be seen in Equation 9.28, the impedance can be partitioned into real and imaginary components and visually represented in a Nyquist plot. The impedance vector  $|Z|$  is plotted with respect to the phase angle  $\phi$  and the horizontal axis. An example of the Nyquist plot displaying the impedance spectrum for an example electrochemical system known as a Randles cell is shown in Figure 9.10. The imaginary and real impedance points are plotted from lowest to highest radial frequencies from right to left of the graph. Typical properties to discern include any horizontal intercepts and the shape of the spectrum envelope. All electrochemical impedance tests were conducted using a Gamry Reference 600 Potentiostat/Galvanostat/ZRA.

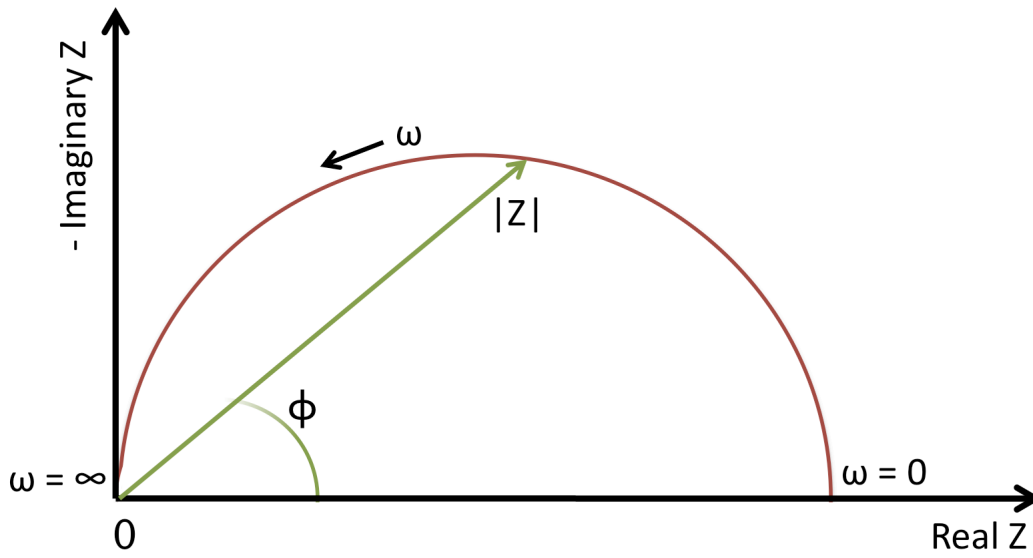


Figure 9.10. Nyquist plot displaying the real versus the imaginary components of the impedance of an example electrochemical system (known as Randles cell).

### 9.3.1 EIS Equivalent Electrical Circuit Modeling

All electrochemical impedance spectra can be fitted to an equivalent circuit model incorporating circuit components that represent physical entities in the electrochemical system. This section is an overview of the common circuit elements and their physical significance used to model electrochemical systems. Also for each circuit element, their impedance ( $Z$ ) will be defined according to its relationship between voltage and current:

$$V = IZ \quad (\text{Equation 9.29})$$

#### Resistor

An ideal resistor ( $R$ ) exhibits a voltage ( $E$ ) proportional to an electric current ( $I$ ) via the Ohm's Law:

$$E = IR \quad (\text{Equation 9.30})$$

The impedance of an ideal resistor is invariant with respect to input frequency and displays only a real impedance component, so that the current run through a resistor will always be in phase with the potential. The impedance of a resistor ( $Z$ ) can be represented as:

$$Z = R \quad (\text{Equation 9.31})$$

A resistor can be used to represent a few physical phenomena in an electrochemical cell.



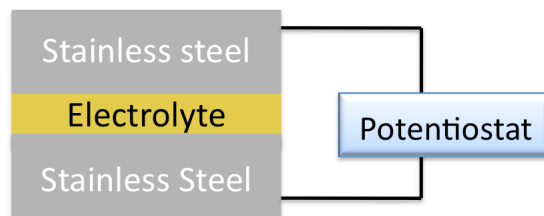


Figure 9.11. Cell used to determine the solution resistance of an electrolyte using EIS. For the electrolytes studied, the stainless steel terminals are blocking electrodes.

### *Solution Resistance*

Solution resistance of an ionic medium such as an electrolyte in an electrochemical cell depends the ionic medium, ion concentration, temperature, and the length ( $l$ ) and area ( $A$ ) of the cell being probed. From the solution resistance ( $R$ ), the ionic conductivity ( $\kappa$ ) can be determined as:

$$\kappa = \frac{l}{RA} \quad (\text{Equation 9.32})$$

The solution resistance is usually determined in the high frequency regime, extrapolated for  $\omega \rightarrow \infty$  from the horizontal intercept of an impedance spectrum plot.

Using EIS, the solution resistances of various electrolytes, liquid and gel, were determined by sandwiching the electrolyte between two blocking electrodes such as stainless steel. This configuration is illustrated in Figure 9.11.

### *Surface Resistance*

The resistance due to interfacial reactions and surface products between the electrode and electrolyte can be detected using EIS. Usually the surface resistance is associated with a double layer capacitance, and represented by a resistor and capacitor in parallel. If this element is placed in series with a resistor representing the solution's resistance, the resulting circuit model appears as a semi-circle (such as that depicted in Figure 9.10) with two horizontal intercepts at high and low radial frequencies corresponding to the solution and surface resistance. For any cells utilizing non-blocking electrodes, interfacial surface films are likely to be found, and therefore detectable with EIS. Explicit interfacial resistance tests were conducted by using symmetric cells such as Figure 9.5 and Figure 9.6, and the progression of interfacial reactions with elapsed time was detected by testing the same cell repeatedly until unchanging interfacial values were achieved.

### *Charge Transfer Resistance*

By forcing an electrode to a potential different from its equilibrium value at open circuit, the electrode is being polarized. As a result of polarization, there are induced electrochemical reactions that occur at the interface between the electrode and electrolyte that cause current to flow. The magnitude of this current is determined both by the

reaction kinetics at the electrode interface as well as the diffusion of reactants and products to and from the electrode, respectively.

When the polarization reaction can be estimated to be charge transfer limiting, the resulting current due to the overpotential, or the degree of polarization, can be estimated using the Butler-Volmer equation:

$$i = i_o \left[ \frac{C_{oxid}}{C_{oxid}^*} \exp\left(\frac{\alpha n F \eta}{RT}\right) - \frac{C_{red}}{C_{red}^*} \exp\left(\frac{-(1-\alpha)n F \eta}{RT}\right) \right] \quad (\text{Equation 9.33})$$

where the reaction current density ( $i$ ) depends on the exchange current density ( $i_o$ ), the concentration of the oxidant and reductant at the electrode surface ( $C_{oxid}$  and  $C_{red}$ , respectively), the bulk concentration of the oxidant and reductant in the bulk ( $C_{oxid}^*$  and  $C_{red}^*$ , respectively), the overpotential ( $\eta = E - E_o$ ), the transfer coefficient ( $\alpha$ ), the number of electrons passed ( $n$ ), the cell temperature ( $T$ ), and the gas constant ( $R$ ). When the concentrations of oxidants and reactants in the bulk are the same as at the surface of the electrode (for example when the electrolyte is being stirred to minimize diffusion effects), the system is solely charge transfer limited [Orazem, *et al.*, 2006] and can be simplified as:

$$i = i_o \left( e^{\frac{\alpha n F \eta}{RT}} - e^{\frac{-(1-\alpha)n F \eta}{RT}} \right) \quad (\text{Equation 9.34})$$

For small overpotentials, the Butler-Volmer equation can be simplified further to estimate the exchange current density, which indicates the inherent rate of electron transfer for an electrochemical reaction, from the charge transfer resistance ( $R_{\text{charge transfer}}$ ) measured using EIS. For small alternating current (AC) perturbations and a system at equilibrium (where no direct current (DC) bias is applied), the exchange current density can be expressed as:

$$i_o = \frac{RT}{nFR_{\text{charge transfer}}} \quad (\text{Equation 9.35})$$

Therefore, from determining the charge transfer resistance in an electrochemical cell using EIS, the exchange current density of a charge transfer reaction can be determined. The charge transfer resistance is not easily discerned from a Nyquist plot, and instead must be determined by fitting an equivalent circuit model for a system.

## Capacitor

An ideal capacitor ( $C$ ) demonstrates a linear change in voltage with respect to time with an applied current:

$$I = C \frac{dE}{dt} \quad (\text{Equation 9.36})$$

With an increased frequency, a capacitor's impedance diminishes. Its impedance exhibits only an imaginary component, and the current through a capacitor will be phase shifted - 90° with a voltage signal. The impedance of a capacitor can be represented as:

$$Z = \frac{1}{j\omega C} \quad (\text{Equation 9.37})$$

The physical phenomena of electrochemical systems that can be represented by capacitors are discussed in the following sections.

### *Double Layer Capacitance*

The double layer is an accumulation of charges, electrons in the electrode and ions in the electrolyte, along an interface. As a result of the separation of charge, a double layer capacitance is induced, and the magnitude of this capacitance is affected by the types of electrode material and ions, the concentration of ions, the electrode potential, temperature, interfacial morphology, and any oxide films or adsorbed impurities. Typically any surface resistances or charge transfer resistances occurring at the interface in an electrochemical system are accompanied by double layer capacitances associated with the charge build up along the interface. An equivalent circuit containing a resistor in parallel with a capacitor usually represents this. The output Nyquist plot resembles a semi-circle such as the Randles cell spectra shown in Figure 9.10.

### *Constant Phase Element*

Due to a variety of inhomogeneous properties, capacitors rarely exhibit ideal behavior, and are instead represented with a constant phase element (CPE). The variations across an interface may be due to a few phenomena, including surface roughness, varying electrode and electrolyte compositions, and heterogeneous reactions rates and current distributions across the interface. The impedance of a CPE is:

$$Z = A(j\omega)^{-\alpha} \quad (\text{Equation 9.38})$$

where A is a constant that is the inverse of capacitance ( $A=1/C$ ) and the exponent  $\alpha$  determines its degree of non-ideality. If the system acts as an ideal capacitor,  $\alpha=1$  and Equation 9.37 represents its impedance. If a capacitor in a Randle's cell is replaced with a CPE, the semi-circle appears depressed, depending on the degree of inhomogeneity in the electrochemical system.

### **Inductor**

An ideal inductor (L) shows the opposite behavior of a capacitor. The potential of an inductor is proportional to a linear change in current with respect to time:

$$E = L \frac{dI}{dt} \quad (\text{Equation 9.39})$$

The inductance of a circuit element increases with increased frequency and similar to capacitors, only displays an imaginary impedance component. The current through an inductor will be phase shifted 90° with a voltage signal. The impedance of an inductor can be represented as:

$$Z = j\omega L \quad (\text{Equation 9.40})$$

### Warburg Impedance

A Warburg impedance circuit element is able to capture the diffusion mechanisms within an electrochemical system. Because diffusion phenomena are time dependent, they are inherently frequency dependent; reactants that diffuse are only detectable over significant time lengths, and therefore are only observable by EIS at increasingly low frequencies.

The Warburg impedance of a system where the diffusion region is of infinite thickness is defined as:

$$Z = W(\omega)^{-1/2}(1 - j) \quad (\text{Equation 9.41})$$

where the Warburg coefficient (W) is expressed as:

$$W = \frac{RT}{n^2 F^2 A \sqrt{2}} \left( \frac{1}{C_o^* \sqrt{D_o}} + \frac{1}{C_R^* \sqrt{D_R}} \right) \quad (\text{Equation 9.42})$$

In this expression n is the number of electrons involved, A is the surface area of the electrode, C\* is the bulk concentration of the oxidant (O) or reactant (R), and D is the diffusion coefficient. For a Nyquist plot at low frequencies, the infinite Warburg impedance appears as a sloped line occurring at a 45° with the horizontal axis.

Most systems have bounded diffusion regions that are not infinite, and Equation 9.41 can be converted into the expression below:

$$Z = W\omega^{-1/2}(1 - j) \tanh \left[ \delta \left( \frac{j\omega}{D} \right)^{1/2} \right] \quad (\text{Equation 9.43})$$

where D is the average diffusion coefficient and δ is the Nernst diffusion layer thickness. For a Nyquist plot at low frequencies, a bounded Warburg impedance element appears as a sloped line with varying angle orientation depending on the nature of the system.

### Summary of Equivalent Circuit Elements

The table below displays common equivalent circuit elements used to model electrochemical systems and summarizes their corresponding impedance expressions.

Table 9.1. Equivalent circuit elements and their impedance expressions

<i>Equivalent Circuit Element</i>	<i>Impedance</i>
Resistor, R	$Z = R$
Capacitor, C	$Z = \frac{1}{j\omega C}$
Constant Phase Element, CPE	$Z = A(j\omega)^{-\alpha}$
Inductor, L	$Z = i\omega L$
Infinite Warburg, $W_{\text{infinite}}$	$Z = W(\omega)^{-1/2}(1 - j)$
Bounded Warburg, $W_{\text{finite}}$	$Z = W\omega^{-1/2}(1 - j) \tanh \left[ \delta \left( \frac{j\omega}{D} \right)^{1/2} \right]$

### Series and Parallel Configurations

Most electrochemical systems can only be described with a combination of circuit elements arranged in series and parallel with each other. A series of impedance elements ( $Z_a, Z_b, Z_c, \dots$ ) would contribute to an equivalent impedance ( $Z_{eq}$ ) with the expression below:

$$Z_{eq} = Z_a + Z_b + Z_c + \dots \quad (\text{Equation 9.44})$$

For elements arranged in parallel with each other, the equivalent impedance is:

$$\frac{1}{Z_{eq}} = \frac{1}{Z_a} + \frac{1}{Z_b} + \frac{1}{Z_c} + \dots \quad (\text{Equation 9.45})$$

### Equivalent Circuit Model Fitting

A cell's impedance spectrum was fitted with an equivalent circuit model using Gamry's EIS300 Electrochemical Impedance Spectroscopy Software. The Levenberg-Marquardt method was used to fit the model to the data. The equivalent circuit model is built according to empirical intuitions on the electrochemical system, then fit using the software. Values for each circuit element are estimated until a "best fit" is found.

For the experiments discussed in section 5.2.4, the parameters of the equivalent circuit model fits were recorded for groups of EIS measurements.

Table 9.2. Equivalent circuit model fit for printed MnO<sub>2</sub> electrode, gel electrolyte, and zinc foil cells . Measurements were taken during a discharge sweep. The EIS scans were recorded at the equilibrium potential of the cell ranging between 1.555 to 1.248 V with an AC input amplitude of 5 mV and a frequency sweep between 0.01 to 106 Hz.

	Open Circuit Voltage V	R <sub>solution</sub> Ω	Q <sub>surface</sub> S*s^a	a <sub>surface</sub> fit	R <sub>surface</sub> Ω	Q <sub>double layer</sub> S*s^a	a <sub>double layer</sub> fit	R <sub>charge transfer</sub> Ω	W <sub>diff</sub> S*s^(1/2)	R <sub>charge transfer</sub> ohm/cm^2	Exchange current density A/cm <sup>2</sup>
<b>Discharge</b>	1.555	239.6	6.73E-06	5.26E-01	9.86E+03	1.23E-05	7.11E-01	4.95E+04	3.53E-04	4.95E+04	2.60E-07
	1.484	233.3	6.62E-06	5.30E-01	1.01E+04	1.47E-05	6.71E-01	4.78E+04	4.26E-04	4.78E+04	2.69E-07
	1.441	228.1	6.80E-06	5.30E-01	9.83E+03	1.65E-05	6.34E-01	4.61E+04	4.71E-04	4.61E+04	2.78E-07
	1.407	228.2	6.86E-06	5.29E-01	9.87E+03	1.75E-05	6.11E-01	4.51E+04	4.91E-04	4.51E+04	2.85E-07
	1.379	203.6	1.41E-06	8.59E-01	1.66E+03	1.56E-05	4.50E-01	6.43E+04	1.39E-03	6.43E+04	2.00E-07
	1.357	204.7	1.54E-06	8.42E-01	1.79E+03	1.56E-05	4.48E-01	6.25E+04	9.65E-04	6.25E+04	2.05E-07
	1.338	204.4	1.66E-06	8.28E-01	1.88E+03	1.58E-05	4.47E-01	6.05E+04	7.99E-04	6.05E+04	2.12E-07
	1.319	206.8	1.82E-06	8.10E-01	2.07E+03	1.59E-05	4.45E-01	6.04E+04	7.02E-04	6.04E+04	2.12E-07
	1.301	206.7	1.87E-06	8.02E-01	2.13E+03	1.60E-05	4.44E-01	5.84E+04	5.99E-04	5.84E+04	2.20E-07
	1.287	217.6	2.20E-06	7.85E-01	2.39E+03	1.39E-05	4.52E-01	7.58E+04	1.80E-03	7.58E+04	1.69E-07
	1.28	213.8	2.44E-06	7.67E-01	2.60E+03	1.50E-05	4.48E-01	6.93E+04	1.00E-03	6.93E+04	1.85E-07
	1.269	208.4	2.53E-06	7.61E-01	2.66E+03	1.59E-05	4.45E-01	6.36E+04	7.84E-04	6.36E+04	2.02E-07
	1.258	207.7	2.73E-06	7.43E-01	2.94E+03	1.69E-05	4.41E-01	6.11E+04	6.81E-04	6.11E+04	2.10E-07
	1.248	206.5	2.91E-06	7.26E-01	3.26E+03	1.80E-05	4.38E-01	5.92E+04	6.00E-04	5.92E+04	2.17E-07

Table 9.3. Equivalent circuit model fit for printed MnO<sub>2</sub> electrode, gel electrolyte, and zinc foil cells . Measurements were taken during a charge sweep. The EIS scans were recorded at the equilibrium potential of the cell ranging between 1.267 to 1.62 V with an AC input amplitude of 5 mV and a frequency sweep between 0.01 to 106 Hz.

	Open Circuit Voltage V	R <sub>solution</sub> Ω	Q <sub>surface</sub> S*s^a	a <sub>surface</sub> fit	R <sub>surface</sub> Ω	Q <sub>double layer</sub> S*s^a	a <sub>double layer</sub> fit	R <sub>charge transfer</sub> Ω	W <sub>diff</sub> S*s^(1/2)	R <sub>charge transfer</sub> ohm/cm^2	Exchange current density A/cm <sup>2</sup>
<b>Charge</b>	1.267	176.2	2.11E-06	8.71E-01	463.6	2.20E-05	4.95E-01	5.50E+04	5.42E-03	5.50E+04	2.33E-07
	1.325	171.2	7.46E-07	9.67E-01	3.44E+02	2.82E-05	4.65E-01	6.38E+04	7.99E-04	6.38E+04	2.01E-07
	1.363	179.8	6.55E-06	6.50E-01	2.43E+03	2.13E-05	5.11E-01	5.64E+04	1.96E-04	5.64E+04	2.27E-07
	1.393	195.7	3.95E-06	6.13E-01	3.24E+03	9.99E-06	6.81E-01	7.07E+04	3.82E-04	7.07E+04	1.82E-07
	1.415	195.3	4.14E-06	6.04E-01	3.42E+03	9.83E-06	6.94E-01	6.39E+04	3.94E-04	6.39E+04	2.01E-07
	1.430	198	4.28E-06	5.96E-01	3.61E+03	9.36E-06	7.06E-01	6.49E+04	4.04E-04	6.49E+04	1.98E-07
	1.459	197.8	4.56E-06	5.88E-01	3.68E+03	9.18E-06	7.11E-01	6.58E+04	4.52E-04	6.58E+04	1.95E-07
	1.477	201.6	4.73E-06	5.81E-01	3.92E+03	9.05E-06	7.13E-01	6.67E+04	4.34E-04	6.67E+04	1.93E-07
	1.468	202.2	4.93E-06	5.76E-01	4.12E+03	9.04E-06	7.14E-01	6.56E+04	4.50E-04	6.56E+04	1.96E-07
	1.445	205.8	5.11E-06	5.70E-01	4.49E+03	8.91E-06	7.17E-01	6.60E+04	4.37E-04	6.60E+04	1.95E-07
	1.471	206.6	5.41E-06	5.63E-01	4.78E+03	8.88E-06	7.20E-01	6.50E+04	4.34E-04	6.50E+04	1.97E-07
	1.476	210.8	5.57E-06	5.58E-01	5.28E+03	8.93E-06	7.21E-01	6.42E+04	4.33E-04	6.42E+04	2.00E-07
	1.481	214.2	5.77E-06	5.53E-01	5.89E+03	8.81E-06	7.23E-01	6.37E+04	4.24E-04	6.37E+04	2.01E-07
	1.514	219	5.95E-06	5.48E-01	6.61E+03	8.82E-06	7.22E-01	6.52E+04	4.13E-04	6.52E+04	1.97E-07
	1.535	224	6.06E-06	5.44E-01	7.50E+03	8.74E-06	7.27E-01	6.63E+04	4.05E-04	6.63E+04	1.94E-07
	1.549	227.2	6.24E-06	5.40E-01	8.30E+03	8.80E-06	7.26E-01	6.97E+04	4.23E-04	6.97E+04	1.84E-07
	1.562	232.3	6.23E-06	5.38E-01	9.31E+03	8.52E-06	7.41E-01	7.19E+04	3.97E-04	7.19E+04	1.79E-07
	1.575	235.7	6.39E-06	5.35E-01	9.54E+03	8.60E-06	7.41E-01	7.26E+04	4.02E-04	7.26E+04	1.77E-07
	1.596	243.6	6.36E-06	5.32E-01	1.05E+04	8.49E-06	7.50E-01	7.45E+04	4.00E-04	7.45E+04	1.72E-07
	1.620	249.4	6.42E-06	5.29E-01	1.12E+04	8.51E-06	7.54E-01	7.67E+04	3.75E-04	7.67E+04	1.67E-07

## 9.4 Galvanostatic and Potentiostatic Techniques

Galvanostatic or constant current methods are pervasively used to characterize electrochemical systems. The magnitude of the applied current, the length of time of the current and interruptions, and the cyclic nature of the galvanostatic algorithms are all parameters that can be used to test electrochemical properties of a cell. A variety of galvanostatic characterization methods is discussed in detail in this section. The equipment used to conduct galvanostatic testing includes a custom potentiostat/galvanostat [Steingart, *et al.*, 2006], a Gamry Reference 600 Potentiostat/Galvanostat/ZRA, and a Maccor Series 4000 automated battery tester.

### 9.4.1 Galvanostatic Cycling

In this work, galvanostatic cycling refers to the application of current to a cell in both alternating directions. This corresponds to charging and discharging the cell. By adjusting the magnitude of the current and duration of its application, the resulting potential of an electrochemical cell can indicate quantities such as charge capacity, energy and power density, internal resistance, and other materials properties due to the morphology of the cell potential output. As most electrochemical systems exhibit evolving behavior with cycle life, many experiments apply these galvanostatic tests repeatedly for extended periods of times. The following galvanostatic test methods were used in this work, and their corresponding test parameters and test structures are discussed in detail.

#### Charge and Discharge Analysis

By polarizing an electrochemical cell using a constant current, the cell potential adjusts according to the magnitude of the current. Depending on the direction of current, the potential either increases or decreases, and correspondingly charges or discharges, respectively. In this work, current was applied in one direction until the cell reached a certain cutoff voltage, then the direction of current was switched. Cutoff voltages were established as the minimum and maximum state of charge of the electrochemical system. To compare the charge and discharge routines, the applied current magnitudes were kept identical.

An example of the output of an electrochemical cell tested using constant current cycling is shown in Figure 9.12. From this plot, various quantities can be characterized, including the charge and discharge time, the coulombic efficiency from a comparison of the times, the capacity from the product of the cycle times with the current, the energy from the area under the curves, and the power from dividing the area by the charge or discharge time. Furthermore the shapes of the cell potential curves can indicate the presence of phase changes, or when switching current directions, the internal resistance of the cell.

#### Cycle Life Analysis

If the galvanostatic charge and discharge currents are applied repeatedly to a cell, the properties that can be extracted from each cycle are recorded and compared. The



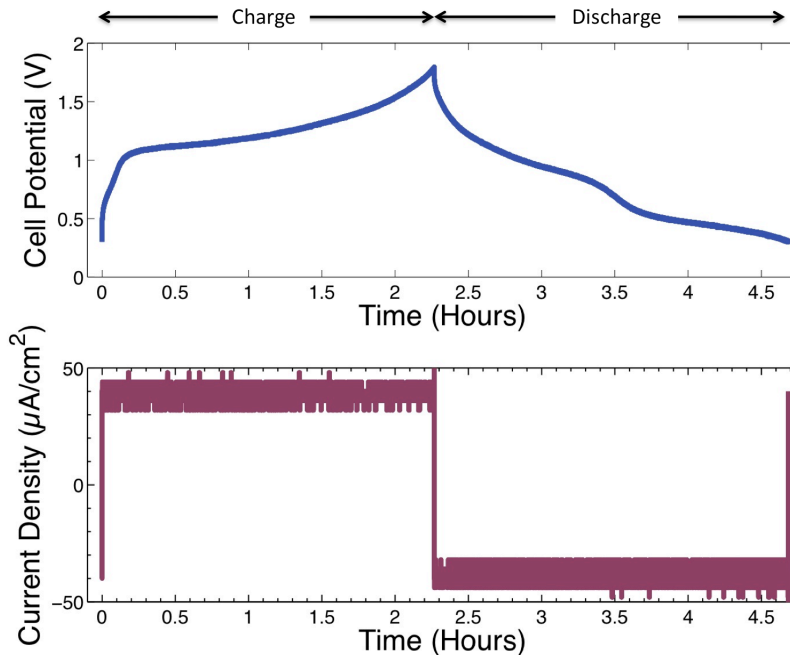


Figure 9.12. Galvanostatic charge and discharge of a test cell.

evolution of these properties can give more insight on the long-term cycle lives of the cells, which is especially important for secondary batteries.

#### *Accelerated Failure Testing*

Galvanostatic cycling can also be used to promote accelerated failure of the printed battery. To propagate dendrite formation, rapid cycling with high current densities was used. If the same experiment is conducted with current densities that cause the cell to reach potentials exceeding its electrolyte stability, the breakdown of the electrolyte and any other adverse side reactions can also be induced.

### **9.4.2 Restricted Diffusion Method**

The salt diffusion coefficient in a single-phase binary salt electrolyte can be detected using the restricted diffusion method described in detail by Ma et al. for a sodium ion conducting polymer electrolyte [Ma, *et al.*, 1995]. Restricted diffusion is a versatile method for accurately measuring salt diffusion coefficients for electrolytes of varying concentrations.

A symmetric cell (such as those illustrated in Figures 9.5 and 9.6) sandwiching the electrolyte of interest is subjected to a constant current for a sufficient time to create a concentration gradient, as shown in Figure 9.13. After substantial polarization, the current is interrupted, and at open circuit the cell potential is observed for an extended period of time (see Figure 9.14 a). The decreasing behavior of the cell potential reflects

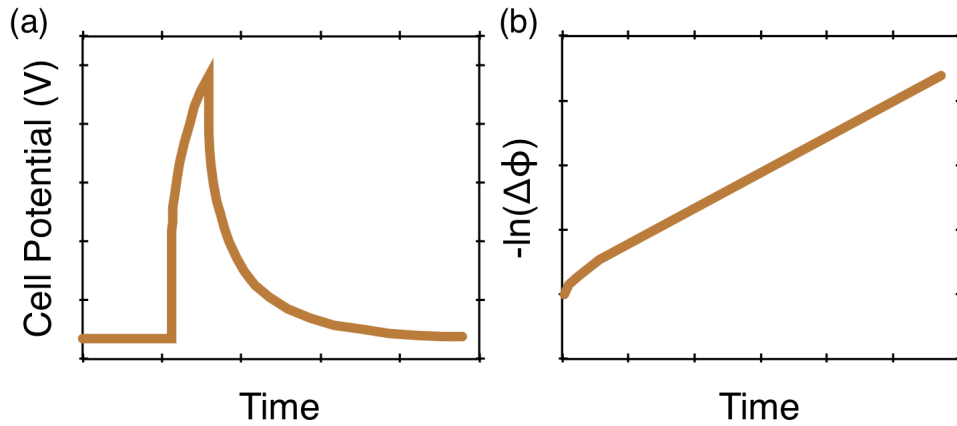


Figure 9.13. Restricted diffusion method measures (a) the cell potential during polarization (increasing cell potential) then when it is interrupted (exponentially decaying potential). The slope of the negative natural log of the open circuit cell potential  $[-\ln(\Delta\phi)]$  with respect to time is used to determine the salt diffusion coefficient within the electrolyte.

the concentration profile in the electrolyte relaxing. The potential decay is utilized to determine the effective salt diffusion coefficient using the following formula:

$$\Delta\phi = \exp\left(-\frac{\pi^2 D_{\text{salt}}}{L^2} t + A\right) \quad (\text{Equation 9.46})$$

where  $\phi$  is the cell potential,  $D_{\text{salt}}$  is the salt diffusion coefficient,  $L$  is the length or thickness of the electrolyte between the two electrodes,  $t$  is time, and  $A$  is an intercept value. From the expression, it is apparent that the cell potential decay should diminish exponentially with long times. If the natural log of the cell potential  $[\ln(\Delta\phi)]$  is plotted

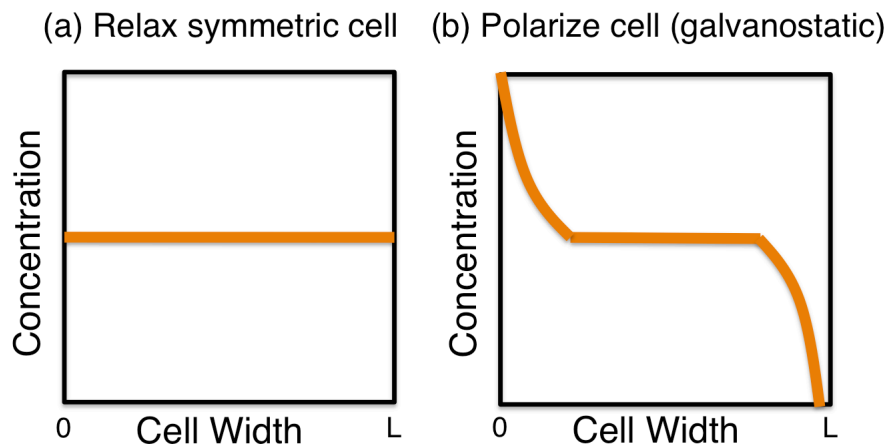


Figure 9.14 (a-b). Electrolyte concentration along the width of a cell (electrodes are situated at 0 and  $L$ ) during (a) equilibrium and (b) when polarizing the cell.

with respect to time, for long times the plot should appear linear (see Figure 9.14 b), and the slope can be used to determine the salt diffusion coefficient using the expression:

$$\text{slope} = -\frac{\pi^2 D}{L^2} \quad (\text{Equation 9.47})$$

From this method, the diffusion coefficient of zinc salt in an ionic liquid electrolyte was estimated. A symmetric cell of zinc foil electrodes and an ionic liquid electrolyte was assembled using a Swagelok cell. The electrodes were separated with a 100  $\mu\text{m}$  Teflon spacer. A constant current of 1  $\text{mA}/\text{cm}^2$  was applied to the cell for 15 minutes, and the cell was allowed to relax for 8 hours, upon which the diffusion coefficient could be determined. This experiment was repeated for various cells of varying zinc salt concentration in section 3.2.2.

### 9.4.3 Galvanostatic Intermittent Titration Technique (GITT)

GITT is an electrochemical measurement technique that uses a combination of transient and steady state measurements to derive kinetic and thermodynamic parameters for solid mixed-conducting materials (Weppner and Huggins 1977). For the incorporation of an electroactive species within a host crystal structure, the transport properties within the material depend greatly on the compositional variation within the system and how quickly it equilibrates to these changes. This equilibration process is usually reported as the chemical diffusion coefficient ( $\tilde{D}$  is typically reported in  $\text{cm}^2/\text{s}$ ). Because the cell voltage is associated with the thermodynamics of the system, an applied current can be used to derive kinetic information from the system. On its own, steady state measurements can be used to derive information about a material system's conductivity and also the product of the diffusion coefficient and concentration, while transient methods may be able to differentiate these quantities. By combining the steady state and transient measurements, kinetic properties such as chemical and component diffusion coefficients, mobility and component conductivity can be found with high precision. GITT eliminates any difficulties with resistance polarizations in a system, which typically hampers traditional potentiostatic characterization techniques. Moreover, the equipment needed to implement GITT experiments are a constant current source and a data acquisition system for measuring the evolution of voltage with time.

To conduct the measurement, a sample of known composition ( $A_{y+\delta}B$ ) is assembled into a galvanic cell. It is assumed that in this system one type of electroactive ion (A) and electrons are the only kinds of species contributing to the transport in the material. The Nernst equation states that the cell voltage (E) is a measure of the thermodynamic activity (a) of the species of interest (A) in the electrode ( $A_{y+\delta}B$ ) at the interface with the electrolyte with respect to its activity in the bulk electrolyte ( $A^\circ$ ).

$$E = \frac{kT}{z_A q} \ln \frac{a_A(A^\circ)}{a_A(A_{y+\delta}B)} \quad (\text{Equation 9.48})$$

After establishing thermoelectric equilibrium, the activities of all species in the electrode should be homogenous, and this composition will correspond to a cell voltage E.

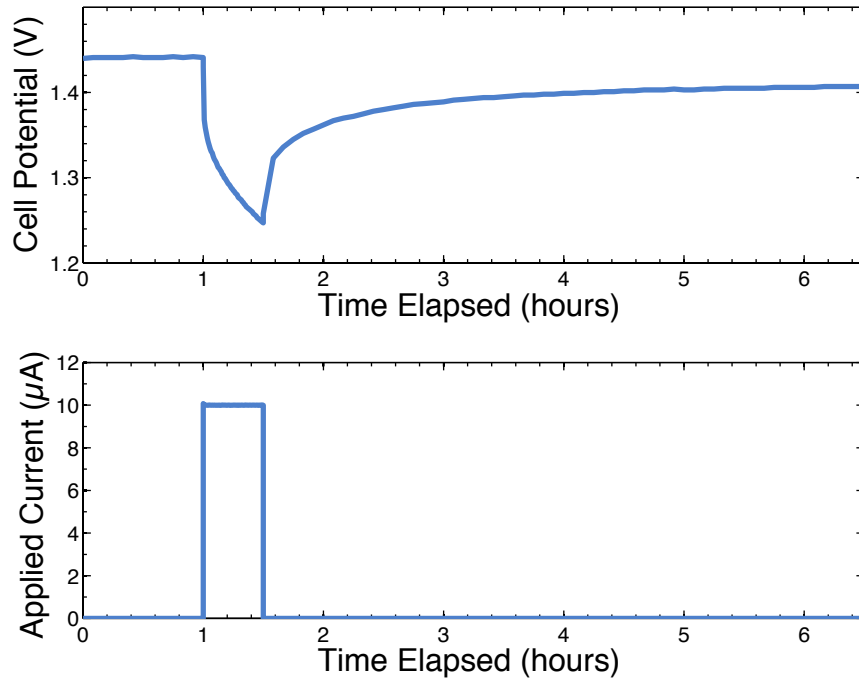


Figure 9.15. Galvanostatic intermittent titration technique (GITT) procedure: current is applied for 30 minutes to a cell, then held at open circuit for 5 hours while the cell potential is monitored.

As illustrated in Figure 9.15, a constant current  $I_0$  is applied to the cell; the magnitude of this current determines the transport of any mobile species at the boundary between the electrode and electrolyte ( $x=0$ ). The current is related to the chemical diffusion coefficient with the following expression:

$$I = -S z_i q \tilde{D} \left. \frac{\partial c}{\partial x} \right|_{x=0} \quad (\text{Equation 9.49})$$

where  $S$  is the interfacial area between the sample and electrolyte,  $z_i$  is the valence of the electroactive ion,  $q$  is the charge, and  $\left. \frac{\partial c}{\partial x} \right|_{x=0}$  is the concentration gradient at the phase

boundary between the electrode and electrolyte. The concentration gradient that is generated by the current is constant; for the electrode to maintain this concentration, its composition changes, resulting in a cell voltage change. Note that an ohmic drop or increase may occur when current is applied to the cell, but this IR drop acts as a constant that shifts the cell voltage and does not change its time dependent behavior. After a known amount of time ( $\tau$ ) has elapsed, the current is interrupted, and the electrode equilibrates, becoming homogenous through the diffusion of its mobile species. The amount of stoichiometric change ( $\Delta\delta$ ) in the electrode due to the applied current is:

$$\Delta\delta = \frac{I\tau M_{\text{host}}}{z_{\text{ion}} m_{\text{host}} F} \quad (\text{Equation 9.50})$$

where  $M_{\text{host}}$  is the atomic weight of the host material,  $z_{\text{ion}}$  is the valence of the electroactive ion,  $m_{\text{host}}$  is the mass of the host material, and  $F$  is Faraday's constant. As

this composition stabilizes, the cell voltage drifts to its new steady state voltage,  $E_{\text{steady state}}$ . Once the electrode reaches equilibrium, the procedure is repeated.

For small current pulses applied for short times, the chemical diffusion coefficient (also referred to as an interdiffusion coefficient) can be determined by solving for the cell potential's behavior with respect to time from Fick's second law:

$$\frac{\partial c_i(x,t)}{\partial t} = \tilde{D} \frac{\partial^2 c_i(x,t)}{\partial x^2} \quad (\text{Equation 9.51})$$

The initial and boundary conditions are stated below:

$$c_i(x,t=0) = c_o \quad (0 \leq x \leq L) \quad (\text{Equation 9.52})$$

$$-\tilde{D} \frac{\partial c_i}{\partial x} \Big|_{x=0} = \frac{I_o}{S z_i q} \quad (t \geq 0) \quad (\text{Equation 9.53})$$

$$\frac{\partial c_i}{\partial x} \Big|_{x=L} = 0 \quad (t \geq 0) \quad (\text{Equation 9.54})$$

The electrode spans from 0 to L along the x-axis, and it assumed to be impermeable at the side furthest from the electrolyte and electrode phase boundary. Using the initial and boundary conditions, the solution to Equation 9.51 at the interface (x=0) is:

$$c_i(x=0,t) = c_o + \frac{2I_o \sqrt{t}}{S z_i q \sqrt{\tilde{D}}} \sum_{n=0}^{\infty} \left( \text{ierfc} \left[ \frac{nL}{\sqrt{\tilde{D}t}} \right] + \text{ierfc} \left[ \frac{(n+1)L}{\sqrt{\tilde{D}t}} \right] \right) \quad (\text{Equation 9.55})$$

where the first integral of the complement error function is:

$$\text{ierfc}(\lambda) = \left[ \pi^{-1/2} \exp(-\lambda^2) \right] - \lambda + \left[ \lambda \text{erf}(\lambda) \right] \quad (\text{Equation 9.56})$$

For  $t \ll \frac{L^2}{\tilde{D}}$ , the infinite sum of Equation 9.55 can be approximated by its first term. The solution becomes simplified, and the derivative of the concentration with respect to the square root of time is:

$$\frac{dc_i(x=0,t)}{d\sqrt{t}} = \frac{2I_o}{S z_i q \sqrt{\tilde{D}} \pi} \left( t \ll \frac{L^2}{\tilde{D}} \right) \quad (\text{Equation 9.57})$$

The molar volume is assumed to change negligibly with concentration so the change in concentration with respect to stoichiometry can be approximated as:

$$dc_i = \frac{N_A}{V_M} d\delta \quad (\text{Equation 9.58})$$

$N_A$  is Avogadro's number while  $V_M$  is the mole volume of the sample. By inserting Equation 9.58 into equation 9.57 and multiplying the change in cell potential to the expression, the expression below emerges:

$$\frac{dE}{d\sqrt{t}} = \frac{2V_M I_o}{S F z_i \sqrt{\tilde{D}} \pi} \frac{dE}{d\delta} \quad (\text{Equation 9.59})$$

Equation 9.39 can be solved in terms of the diffusion coefficient,  $\tilde{D}$ :

$$\tilde{D} = \frac{4}{\pi} \left( \frac{V_M}{SFz_i} \right)^2 \left[ \frac{I_o \left( \frac{dE}{d\delta} \right)}{\left( \frac{dE}{d\sqrt{t}} \right)} \right]^2 \quad (\text{Equation 9.60})$$

If using a sufficiently small galvanostatic current, the change in cell potential  $dE$  can be simplified as  $\Delta E_{\text{steady state}} = (E_1 - E_0)$  while  $d\delta$  is approximated by the expression for  $\Delta\delta$  in

Equation 9.50. The expression  $\frac{dE}{d\delta}$  is simply  $\frac{\Delta E_{\text{steady state}}}{\Delta\delta}$ , and the equation for the diffusion coefficient is finally:

$$\tilde{D} = \frac{4}{\pi} \left( \frac{m_{\text{host}} V_M}{M_{\text{host}} S} \right)^2 \left[ \frac{\Delta E_{\text{steady state}}}{\tau \left( \frac{dE}{d\sqrt{t}} \right)} \right]^2 \quad (\text{Equation 9.61})$$

where  $\left( \frac{dE}{d\sqrt{t}} \right)$  is the slope of the transient cell potential with respect to the square root foot of time elapsed. The following equation relates the chemical diffusion coefficient to the component diffusion coefficient ( $D_{\text{component}}$ ):

$$\tilde{D} = D_{\text{component}} \frac{\partial \ln a_{\text{component}}}{\partial \ln c_{\text{component}}} \quad (\text{Equation 9.62})$$

The term modifying the component diffusion coefficient is known as the enhancement factor that is defined as:

$$\frac{\partial \ln a_{\text{component}}}{\partial \ln c_{\text{component}}} = - \frac{z_{\text{component}} q c_{\text{component}} V_M}{kTN_{\text{component}}} \left( \frac{dE}{d\delta} \right) \quad (\text{Equation 9.63})$$

By combining Equations 9.61-63, the component diffusion of a mobile ion species in a host material is expressed as:

$$D_{\text{component}} = - \frac{4kTm_{\text{host}} V_M I_o}{\pi c_{\text{ion}} z_{\text{ion}}^2 q^2 M_{\text{host}} S^2 \tau} \frac{\Delta E_{\text{steady state}}}{\left( \frac{dE}{d\sqrt{t}} \right)^2} \quad (\text{Equation 9.64})$$

These expressions are only valid in single-phase regions in which the steady state potential varies linearly with composition. Regions in which the steady state cell potential becomes invariant with composition indicate the presence of a phase change in the system (for an example, see Figure 9.16); the Gibbs Phase Rule dictates this phenomenon. Using Equation 9.50, the capacity of the cell from Figure 9.16 can be related to the stoichiometric change in electrode composition,  $\Delta\delta$ .

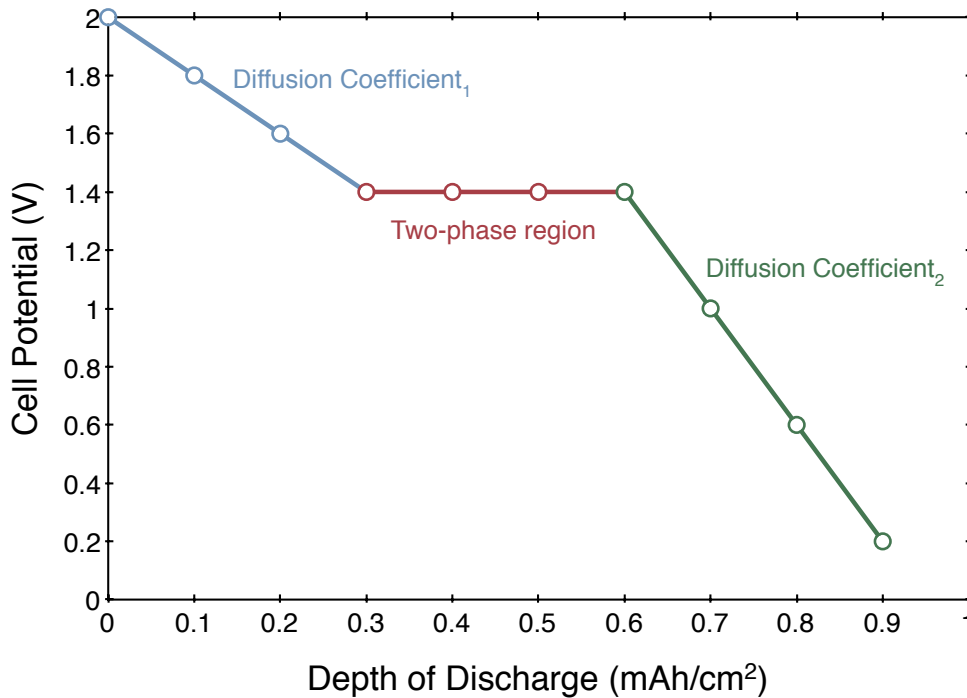


Figure 9.16. An example of the equilibrium cell potential of a battery using GITT protocol. Flat cell potential regions indicate phase changes in the host while diffusion coefficients can be extracted from sloped regions.

#### 9.4.4 Rate Performance

How a battery responds to different discharge rates can be quantified by galvanostatically cycling the battery using different discharge current densities. At moderate discharge rates, a battery will exhibit its maximum capacity. With increasing discharge rates, the battery becomes kinetically limited, unable to chemically convert reactants fast enough and therefore poorly utilizing its material constituents for extracting stored energy. High discharge rates may also promote injurious side reactions or inhomogeneous current and potential distributions through the battery. As a result the capacities achieved at these higher discharge rates are diminished. Typically a current density that reduces the output to 70% of its greatest capacity is deemed its peak discharge rate. Conversely, for low discharge rates, the battery will exhibit reduced capacities due to charge consumed by any leakage mechanisms, which manifest in self-discharge. The minimum discharge rate can be identified with the same criteria as that of the maximum. From this study, the integral of the constant current discharge curves can be used to determine the correlations between energy and power densities of an electrochemical cell, which can be visualized in a Ragone plot (Winter and Brodd 2004), and important maximum energy and power density parameters can be determined for the system.

#### 9.4.5 Self-Discharge

Self-discharge in an electrochemical battery is the progressive time dependent loss of charge, and can be attributed to parasitic interfacial activity. These processes and the magnitude of self-discharge can vary with the battery chemistry, impurities in the system,

charge and discharge rates, and state of charge of the cell. The mechanisms causing self-discharge and the galvanostatic and potentiostatic methods to characterize the processes will be discussed in this section. In this work, all battery samples in which self-discharge was detected resembled the cell illustrated in Figure 9.8 and all components were printed but the nickel current collector.

### Self-Discharge Mechanisms

Three common types of leakage mechanisms have been identified: (1) self-discharge due to coupled faradaic reactions which are kinetically limited by activation or charge transfer processes, (2) leakage reactions which are mass-transport limited, and (3) short circuit leakage between electrodes resulting in distinguishable ohmic polarization (Niu, Conway and Pell 2004). These processes are discussed in detail in the following sections, and they can be distinguished by observing the cell's potential decay behavior with time.

#### *Kinetically limited self-discharge*

Faradaic reactions resulting in leakage can be attributed to parasitic interfacial reactions at the anode and cathode. Examples include the oxidation and reduction of impurities at an interface or the decomposition of the electrolyte solution due to overcharge; in both examples the deleterious processes may continue to propagate even after removing the stimulus (such as polarization or temperature) that caused their onset. Depending on the charge transfer reaction, the process may be kinetically limited. The self-discharge current associated with a kinetically-limited faradaic reaction is described using the Butler-Volmer expression, which states that the current density ( $i$ ) changes exponentially with polarization ( $\eta$ ), or the cell's divergence from equilibrium:

$$i = i_o \left[ \exp\left(\frac{\alpha F \eta}{RT}\right) - \exp\left(\frac{-(1-\alpha)nF\eta}{RT}\right) \right] \quad (\text{Equation 9.65})$$

where  $i_o$  is the exchange current density,  $\alpha$  is the transfer coefficient or fraction of charge of  $\eta$  that leads to an adjustment of the charge transfer rate,  $F$  is Faraday's constant,  $R$  is the gas constant, and  $T$  is the temperature. If the expression is rearranged, the polarization shows a logarithmic dependence on current density, as stated by Tafel's equation for high overpotentials where the reverse reaction rate is negligible:

$$\eta = a - b \ln\left(\frac{i}{i_o}\right) \quad (\text{Equation 9.66})$$

where  $a$  and  $b$  are constants. If the self-discharge current is constant for a rate of potential decay with time ( $dV/dt$ ) and proportional to different  $dV/dt$  rates, its behavior can be approximated like that of a capacitor with capacitance  $C$ :

$$i = C \frac{dV}{dt} \quad (\text{Equation 9.67})$$

The expression above is equated with the Butler-Volmer expression and then integrated to solve for the time-dependence of the open circuit potential ( $V_t$ ):



$$V_t = -A \ln\left(\frac{i_o}{AC}\right) - A \ln(t + \theta) \quad (\text{Equation 9.68})$$

$$A = \frac{RT}{\alpha F} \quad (\text{Equation 9.69})$$

$$V_{initial} = -A \ln\left(\frac{i_o}{AC}\right) \quad (\text{Equation 9.70})$$

$$V_t = V_{initial} - A \ln(t + \theta) \quad (\text{Equation 9.71})$$

where  $\theta$  is the integration constant and the double layer capacitance  $C$  is assumed to remain unchanged as the cell potential varies. Equation 9.71 indicates that for faradaic self-discharge processes that are kinetically limited, the open circuit potential should exhibit a logarithmic decay with time.

#### *Mass Transport Limited Self-Discharge*

A parasitic faradaic reaction may require the movement of reactants to and from the reaction site in order to be sustained. An example is the oxidation and reduction of electroactive impurities from the electrolyte; since the relative concentration of impurities is low, the process relies on the diffusion of the impurities to the electrode surface in order to react. The reaction is described as mass transport limited. Diffusion processes are relatively slow and must be detected on longer time scales than kinetically limited processes.

For a mass transport limited process, the cell potential will have a square root dependence with time:

$$V_t = V_{initial} - \frac{2zFAD^{1/2}\pi^{1/2}c_o}{C}\sqrt{t} \quad (\text{Equation 9.72})$$

where  $z$  is the charge of the redox species,  $D$  is its diffusion coefficient,  $c_o$  is its initial concentration, and  $A$  is the interfacial area where the redox reactions occur. The equation can be simplified to more clearly reflect the cell potential's square-root relationship with the time:

$$B = \frac{2zFAD^{1/2}\pi^{1/2}c_o}{C} \quad (\text{Equation 9.73})$$

$$V_t = V_{initial} - B\sqrt{t} \quad (\text{Equation 9.74})$$

### Internal Short Circuit

In the event a short circuit occurs within the cell due to poor construction or mechanical failure, the third self-discharge mechanism can be easily distinguished from the first two. Internal ohmic self-discharge will depend on the resistance provided by the leakage pathway ( $R_{\text{leak}}$ ) due to the ohmic contact formed between the electrodes, and the cell potential is defined as:

$$\ln V_t = \ln V_{\text{initial}} - \frac{t}{R_{\text{leak}} C} \quad (\text{Equation 9.75})$$

### Measuring Open Circuit Potential Decay

By measuring the open circuit potential decay of a cell and discerning its relationship with respect to time, the mechanism of self-discharge can be easily determined. For this study, it is assumed that the printed batteries were fabricated without short circuit defects so that no ohmic leakage occurs. Therefore, only the first two mechanisms were considered contributors to any self-discharge phenomena.

Printed batteries were subject to a cyclic protocol of transient and steady state operations. A  $40 \mu\text{A}/\text{cm}^2$  constant current was applied for 30 minutes to the cell, and then interrupted for five hours as the cell potential was recorded at open circuit. An example of the open circuit potential decay of a battery is shown in Figure 9.17. This process was repeated as long as the cell's voltage was within the working potential of the cell. After positive charge currents, all cells initially showed decaying cell voltages, while for negative discharge currents, the initial open circuit potential of most cells showed an increase or charge recovery period. After determining the open circuit potential decay behavior with time, the slope of the linear plots was compared with respect to cell potential, which is identified as the voltage measured at current interruption at the beginning of a voltage decay routine.

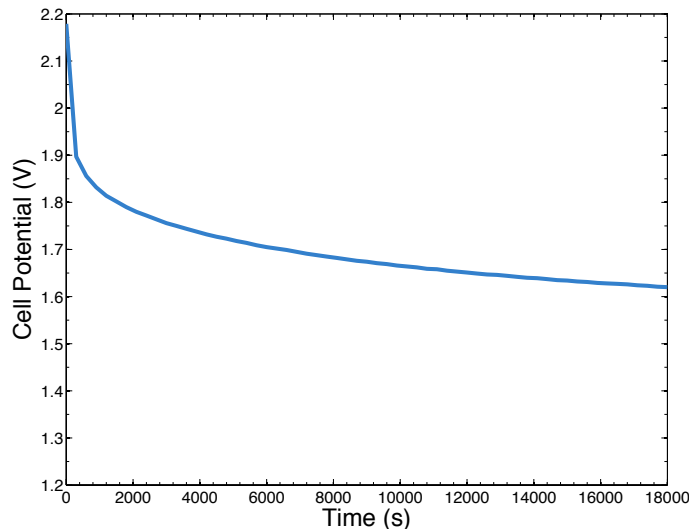


Figure 9.17. An example of the open circuit potential decay of a battery measured after polarization.

## Measuring Float Current

The float current characterization method allows the dependence of the self-discharge to be determined as a function of the cell's state of charge (Niu, Conway and Pell 2004). The float current is the current needed to maintain the electrodes at a cell potential. The float current exactly matches the magnitude of the spontaneous self-discharge current flowing in the cell and therefore prevents the parasitic currents from diminishing the cell's state of charge. To determine the voltage dependence of the printed battery's leakage, the cell's potential was held for eight hours and its current response was measured. At the onset of holding the cell at a certain voltage, the resulting current response exhibits its maximum value and then gradually decays over time until it reaches steady state. An example of the current measured in a printed battery held at 1.65 V is shown in Figure 9.18. The float current is estimated as the current measured after eight hours of holding the cell at a given potential, and assumed to be equal in magnitude to the leakage currents occurring spontaneously in the cell. The amount of charge passed due to these parasitic mechanisms is determined by integrating the area under the current response curves, and from this a leakage power as a function of cell potential can be calculated.

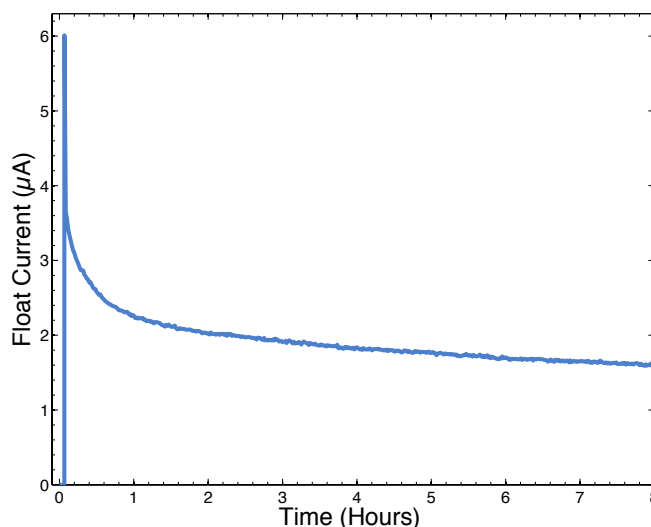


Figure 9.18. The current response to potentiostatic control of a printed battery. The float current is assumed to be the steady state current achieved after holding the cell at a certain potential for extended times.

## 9.5 X-Ray Diffraction

X-ray diffraction (XRD) is a class of characterization techniques used to determine the crystallography, structure, composition, and physical morphology of a material. It utilizes a beam of x-rays which is directed towards a material or structure of interest. The behavior of the x-rays scattered from the sample as well as their intensity can be used to

deduce the material's properties. All XRD work was conducted using a Siemens D5000 automated powder diffractometer.

A sample irradiated with x-rays is mounted onto a goniometer that adjusts its angular position so that a range of angles of scattered x-rays can be detected. The intensity and scattering angle data is used to identify a material (using a diffraction database) or compare the XRD output of a material over a variety of parameters. The shape of diffraction peaks can also reveal the morphology of a material, for example crystalline materials tend to have very sharp peaks while truly amorphous materials display no peaks. Poorly crystalline materials or materials with very small particle sizes tend to demonstrate broad diffraction peaks.

To test the x-ray diffraction of gel electrolyte, the gel samples were cast onto thin glass substrates. After drying, the films were carefully removed from the glass and transferred to an XRD sample holder. Double stick tape was used to immobilize the film.

## 9.6 Electrical Resistance

The electrical sheet resistance of a film was determined using Van der Pauw's method. From this, the resistivity of the material can be calculated after characterizing the film thickness. Samples are printed as 1 cm<sup>2</sup> squares with thicknesses ranging from 20-50 μm depending on the material. Four contacts are made to the corners of the material using electrical probe needles as illustrated in Figure 9.19.

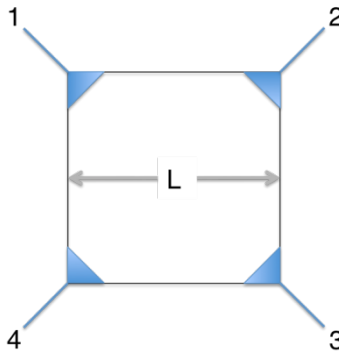


Figure 9.19. Test structure for measuring electrical sheet resistance using Van der Pauw's method. Contacts are made on the corners of the sample and are labeled 1-4.

Current (I) is applied to two of the contacts, while the other two contacts measure the potential (V) response. Using Ohm's Law, resistance is calculated. Current is flowed and potential is measured along a different pair of film edges, and another resistance measurement is taken. From these two measurements, the electrical sheet resistance ( $R_s$ ) can be computed using the following expressions:

$$R_{12,34} = \frac{V_{34}}{I_{12}} \quad (\text{Equation 9.76})$$

$$R_{23,41} = \frac{V_{41}}{I_{23}} \quad (\text{Equation 9.77})$$

$$\exp\left(-\pi \frac{R_{12,34}}{R_s}\right) + \exp\left(-\pi \frac{R_{23,41}}{R_s}\right) = 1 \quad (\text{Equation 9.78})$$

## 9.7 Electron Dispersive X-ray Spectroscopy

Electron dispersive x-ray spectroscopy (EDS) is used for elemental analysis of samples. An electron beam is focused onto a sample, generating the emission of characteristic x-rays unique to the elements in the sample. A spectrometer characterizes these x-rays according to their energy (keV), and elements in the sample are identified. All EDS measurements were taken using a JEOL JSM-6490LV Scanning Electron Microscope (JEOL).

Cathode samples for EDS were prepared by printing electrode inks on metal substrates. For fresh, untested electrodes, the samples were characterized on the metal backings. For electrochemically-tested samples, the electrodes were covered with printed gel electrolyte films. These structures were sandwiched with a zinc foil upon which galvanostatic cycling was conducted. The cycled electrodes and gel electrolyte were removed from metal foils and characterized using EDS. The gel films were kept attached to the electrode for structural support.

## 9.8 Imaging

All sample images were taken with a bench top microscope or scanning electron microscope (SEM). The SEM images were produced with a JEOL JSM-6490LV Scanning Electron Microscope (JEOL). Any image analysis was conducted using Image J software.

## 9.9 References

*Brookfield*. [www.brookfieldengineering.com](http://www.brookfieldengineering.com).

*ESL ElectroScience*. <http://www.electroscience.com/>.

JEOL. [www.jeol.com](http://www.jeol.com).

Ma, Yanping, Marc Doyle, TF Fuller, Marca M Doeff, LC D Jonghe, and J Newman. "The Measurement of a Complete Set of Transport Properties for a Concentrated Solid Polymer Electrolyte Solution." *Journal of The Electrochemical Society* 142, no. 6 (1995): 1859-1868.

Niu, Jianjun, Brian E Conway, and Wendy G Pell. "Comparative Studies of Self-Discharge by Potential Decay and Float-Current Measurements at C Double-Layer Capacitor and Battery Electrodes." *Journal of Power Sources* 135 (2004): 332-343.

Orazem, M.E, and B Tribollet. *Electrochemical Impedance Spectroscopy*. New York: Wiley-Interscience, 2006.

Poirier, D.R., and G.H. Geiger. *Transport Phenomena in Materials Processing*. Warrendale, Pennsylvania: The Minerals, Metals & Materials Society, 1994.

*Rheometrics*                      *ARES*                      *Rheometer*                      (1996).  
<http://felix.metsce.psu.edu/Colby/Research/ares.html>.

Steingart, DA, A Redfern, CC Ho, JW Evans, and PK Wright. "Jonny Galvo: A Small, Low Cost Wireless Galvanostat." *ECS Transactions* 1, no. 21 (2006): 17-22.

Weppner, W, and R.A Huggins. "Determination of the Kinetic Parameters of Mixed-Conducting Electrodes and Application to the System Li<sub>3</sub>Sb." *Journal of the Electrochemical Society* 124, no. 10 (1977): 1569-1578.

Winter, M, and RJ Brodd. "What Are Batteries, Fuel Cells, and Supercapacitors?" *Chem. Rev.* 104, no. 10 (Jun 2004): 4245-4269.